Matching Squark Production and Decay at Next-to-Leading Order Accuracy with Parton Showers

Zur Erlangung des akademischen Grades eines

DOKTORS DER NATURWISSENSCHAFTEN

von der Fakultät für Physik des
Karlsruher Instituts für Technologie (KIT)
genehmigte

DISSERTATION

von

Dipl.-Phys. Christian Hangst
aus Oberndorf am Neckar

Tag der mündlichen Prüfung: 23. Mai 2014

Referentin: Prof. Dr. Margarete Mühlleitner
Korreferent: Prof. Dr. Matthias Steinhauser

Abstract

The search for supersymmetric particles constitutes one of the main points of the physical program at the Large Hadron Collider. For the interpretation of the measured data precise theory predictions are mandatory. In the context of this thesis two complementary methods for the improvement of the predictions for the production of light-flavour squarks and the subsequent decays into a quark and the lightest neutralino are used and combined: higher-order corrections at fixed-order perturbation theory and parton showers.

In the first part the calculation of the NLO SUSY-QCD corrections to the on-shell production of a squark antisquark pair is presented. A similar calculation has been performed for squark pair production, however, only the points not included in a related thesis are explicitly discussed. The results are combined with the NLO predictions for the decay of the squarks into a quark and the lightest neutralino, applying the narrow-width approximation. Unlike the results implemented in the publicly available programs Prospino and Sdecay, the calculation is performed fully differentially, without any assumptions on the mass spectrum of the squarks.

In the second part the implementation of these NLO calculations in the program package Powheg-Box is described. This framework allows for a consistent combination of the fixed order results with parton showers by automating the Powheg matching scheme. The event samples generated with this implementation are interfaced in turn to the parton showers implemented in the Monte Carlo event generators Pythia 6 and Herwig++.

Zusammenfassung

Die Suche nach in supersymmetrischen Theorien vorhergesagten neuen Teilchen ist ein wichtiger Punkt auf der Agenda des Large Hadron Colliders. Von Seiten der Theorie sind hierfür möglichst genaue Vorhersagen nötig, welche durch die Berücksichtigung Terme höherer Ordnung in der Störungsreihe verbessert werden können. Ein komplementärer Ansatz ist die Verwendung von Partonschaueralgorithmen, welche eine Resummation logarithmisch verstärkter Terme zu allen Ordnungen in der Störungstheorie implizieren und eine genauere Simulation der im Experiment beobachteten Endzustände ermöglichen.

Im Rahmen dieser Arbeit werden diese beiden Ansätze konkret auf die Produktion und den Zerfall von Squarks der ersten beiden Generationen angewandt. Im ersten Teil wird die Berechnung der Korrekturen zur Produktion eines Squark-Antisquark Paares in nächst-führender Ordnung der QCD-Störungsreihe präsentiert. Auf eine ausführliche Diskussion der Resultate für Squark-Squark Produktion wird hier verzichtet, da diese bereits in einer unabhängigen Arbeit veröffentlicht wurden. Lediglich einige dort noch nicht berücksichtigte Punkte werden hier diskutiert. Ferner werden die Zerfälle der Squarks in Quarks und das leichteste Neutralino in nächstführender Ordnung der Störungstheorie berechnet und mit den beiden Produktionsprozessen verknüpft. Im Gegensatz zu den in den Programmen Prospino und Sdecay implementierten Berechnungen dieser Prozesse werden keine vereinfachenden Annahmen hinsichtlich der Massen der Squarks gemacht, ferner ist die Generierung beliebiger differentieller Verteilungen möglich.

Im zweiten Teil dieser Dissertation wird die Implementierung der berechneten Prozesse in das Programm Powheg-Box beschrieben, welches die konsistente Kombination dieser Resultate mit Partonschauern im Rahmen des Powheg-Formalismus ermöglicht. Die erzeugten Ereignisse werden mit verschiedenen Partonschaueralgorithmen aus den Monte Carlo Ereignisgeneratoren Pythia 6 und Herwig++ verknüpft.

CONTENTS

1. Introduction **1**

2. Theoretical basics **5**
2.1. Supersymmetry and the MSSM 5
2.1.1. Motivation 5
2.1.2. Supersymmetry 7
2.1.3. The Minimal Supersymmetric Standard Model 8
2.1.4. SUSY searches at hadron colliders 10
2.2. Higher order corrections and beyond 12
2.2.1. Hadronic collisions 13
2.2.2. Ingredients of NLO calculations 13
2.2.3. Parton showers 20
2.2.4. Combining NLO and parton showers - the POWHEG method 25

3. Squark production and decay at NLO **31**
3.1. Squark antisquark production at NLO 31
3.1.1. The LO contributions 32
3.1.2. The virtual contributions 34
3.1.3. The real contributions 37
3.1.4. Checks and comparisons 47
3.1.5. Results 50
3.2. Squark decays 65
3.2.1. Decay width for $\tilde{q} \to q\tilde{\chi}_1^0$ at NLO 66
3.2.2. The total squark width at NLO 69
3.3. Combination of production and decay 72
3.3.1. Formalism 72
3.3.2. Phenomenological results 74

4. Matching squark production and decay with parton showers **83**
4.1. Implementation of the processes in the POWHEG-BOX 83
4.1.1. Process-dependent ingredients 83
4.1.2. Implementation of the subtraction schemes for on-shell intermediate gluinos 85

4.2. Checks of the implementation . . . 88
4.3. Effects of different parton shower algorithms . . . 96
4.3.1. Setup and general remarks . . . 96
4.3.2. Results for undecayed squarks . . . 99
4.3.3. Including the decays $\tilde{q} \to q\tilde{\chi}_1^0$ . . . 102
4.4. Results for total rates . . . 106

5. Summary and outlook **109**

A. Calculational techniques **113**
A.1. Ghost subtraction . . . 113
A.2. Colour- and spin-correlated Born amplitudes squared . . . 114
A.3. Colour flow decomposition . . . 117

B. Input parameters for the Powheg-Box **121**

C. Sample input file for Herwig++ **125**

Bibliography **129**

Acknowledgments **139**

CHAPTER 1

INTRODUCTION

Alles Wissen und alles Vermehren unseres Wissens endet nicht
mit einem Schlußpunkt, sondern mit einem Fragezeichen.
Hermann Hesse

Basically all phenomena observed at particle colliders over the last decades can be explained by the Standard Model (SM) of particle physics. This model has been developed in the 1960s and 70s and describes the strong [1, 2], electromagnetic and weak interactions [3–5] in terms of a local gauge theory. The plethora of its successful predictions culminated in 2012 in the discovery of a candidate for the long-sought Higgs boson at the Large Hadron Collider (LHC) [6, 7]. This massive scalar particle is a remnant of the so-called Higgs mechanism [8–11], which describes the spontaneous breaking of the electroweak symmetry in the SM, allowing thus for a gauge invariant introduction of mass terms. However, despite all these successes there are still many fundamental questions for which the SM provides no solution, which has led to the development of numerous theories beyond the SM. The probably most appealing extensions of the SM are supersymmetric theories. Besides providing explanations for several phenomena not incorporated in the SM, this class of theories is from a theoretical point of view very interesting by itself, as the supersymmetric extension of the Poincaré algebra is the only possible extension leading to a consistent quantum field theory [12]. An unambiguous prediction of supersymmetric theories is the existence of additional particles, which differ from the corresponding SM particles by half a unit in spin, but are in all other properties carbon copies of their respective SM partner. In particular the masses of these superpartners, which are commonly denoted sparticles, should be identical. Therefore, the non-observation of sparticles immediately leads to the conclusion that supersymmetry (SUSY) cannot be an exact symmetry of nature, but has to be broken. However, for theoretical reasons the masses of at least some of them should lie in the TeV range and thus in reach of the LHC.

At hadron colliders the largest cross sections for the production of sparticles are to be expected for the strongly interacting ones. These comprise the scalar partners of the quarks, the squarks, and the fermionic partners of the gluon, the gluinos. The production rates for these particles at leading order (LO) in perturbation theory have been known for more than 30 years [13–16]. Almost 20 years ago the next-to-leading order (NLO) contributions in Quantum Chromodynamics

(QCD) have been calculated in [17]. These were found to be large and can increase the total cross section by up to 100% for specific parameter choices. The results of this calculation have been implemented in the publicly available FORTRAN program PROSPINO [18] and are nowadays used by the ATLAS and CMS collaborations in order to obtain the theoretical predictions for their analyses at NLO accuracy. However, this calculation is based on several simplifying assumptions: First of all, the masses of the squarks of the first two generations are assumed to be degenerate, i.e. the (usually different) squark masses are replaced by an averaged value. Second, the various contributing subchannels to squark production are not calculated independently, only the fully summed result is returned. In the more recent version PROSPINO2 this situation is improved by evaluating the LO contributions for each subchannel individually, keeping the full mass dependence. However, the NLO effects are still approximated by multiplying these LO results with a constant K-factor, which corresponds to the ratio of the total NLO and LO cross sections, calculated for a degenerate squark mass spectrum. Moreover, it is not possible to obtain the NLO corrections for arbitrary differential cross sections. So far these corrections are approximated by rescaling the LO distributions with a constant K-factor, thus implicitly assuming that the differential corrections are flat. Recently two independent groups have presented results without these assumptions at NLO accuracy for the production of squark pairs [19] and all production channels of squarks and gluinos [20], respectively. However, the resulting programs are not publicly available.

The produced squarks and gluinos are unstable and decay further into sparticles and SM particles. The higher-order QCD corrections to these decays can be sizeable and have been calculated in [21, 22] for squarks and in [23] for gluinos. The results of these calculations are implemented in the program SDECAY [24]. However, the masses of the squarks of the first two generations are again assumed to be degenerate. Moreover, only the results for the total branching ratios at NLO are available, hence a fully differential description of the decay products is not possible.

The first goal of this thesis consists in improving these theoretical predictions by calculating the SUSY-QCD NLO corrections to the production of squarks of the first two generations and their subsequent decay into a quark and the lightest neutralino fully differentially, without any assumptions on the mass spectrum.

Taking into account higher orders in fixed-order perturbation theory is only one possibility to obtain more precise predictions. A complementary approach is the simulation of the additional emission of quarks and gluons off the partons in the initial and final state. Formally these contributions are suppressed by higher powers in the strong coupling constant. However, in the limit of soft and/or collinear splittings they are logarithmically enhanced and an all-order resummation is mandatory. The simulation of these emissions is achieved by parton showers. Besides resumming the leading logarithms to all orders, this approach allows for a more realistic simulation of the event structure at colliders like the LHC: typical events show a large multiplicity of final-state particles, whereas fixed-order calculations are usually performed for only a comparatively small number of external particles. However, combining the all-order effects of a parton shower with processes calculated at NLO is non-trivial. In a naïve combination of these two steps certain terms would appear twice. In order to avoid a double counting of these contributions a dedicated matching prescription is required. The POWHEG method [25, 26] is one possible approach to perform such a matching. This method is applied in this thesis to match squark production and decay at NLO with several parton shower algorithms. To this end the POWHEG-BOX framework [27] is used, a FORTRAN program that automates several of the process-independent steps of the POWHEG method.

This thesis is organized as follows: In Ch. 2 the theoretical basics for the performed calculations are outlined. Section 2.1 contains a brief introduction to supersymmetry and the minimal supersymmetric SM. In Sec. 2.2 the technical prerequisites for the calculation of NLO corrections are introduced. These comprise details on the renormalization of ultraviolet divergences in the one-loop contributions and the treatment of infrared divergences. Moreover, the general concept of parton showers and the POWHEG method are explained.

Chapter 3 contains the details on the NLO calculation for squark production and decays. In Sec. 3.1 the results for squark antisquark production at NLO are presented. Moreover, the results for squark pair production published in [28] are extended to scenarios with a mass hierarchy $m_{\tilde{q}} < m_{\tilde{g}}$. Furthermore, this section includes numerical results for both total and differential cross sections, calculated for two benchmark scenarios. These outcomes are compared to the results obtained with the approximations used in PROSPINO2. Section 3.2 contains the results for the NLO contributions to the specific decay of a squark into a quark and the lightest neutralino, $\tilde{q} \to q\tilde{\chi}_1^0$. Moreover, the partial widths for all possible squark decay channels are determined at NLO accuracy, adapting the results given in the literature to the case of a non-degenerate mass spectrum. The NLO results for squark antisquark and squark pair production are combined with the decay $\tilde{q} \to q\tilde{\chi}_1^0$ at NLO accuracy in Sec. 3.3, using the narrow-width approximation.

The matching of the NLO results with parton showers is presented in Ch. 4. The implementation of the calculated results in the POWHEG-BOX is described in Sec. 4.1, followed by a discussion of the performed checks in Sec. 4.2. The results of different parton shower programs, namely PYTHIA 6 [29] and both the default shower and the DIPOLE-SHOWER [30, 31] implemented in the Monte Carlo event generator HERWIG++ [32], are presented in Sec. 4.3. In Sec. 4.4 the total rates obtained in a cut-based analysis are compared to the corresponding results determined with the setup used so far by the experiments. To this end the procedure specified in an analysis of the ATLAS collaboration, [33], is applied for two benchmark scenarios.

Chapter 5 summarizes the results and gives an outlook.

CHAPTER 2

THEORETICAL BASICS

In the following chapter the theoretical foundations of the calculations presented in the further course of this thesis are outlined. Section 2.1 is devoted to a brief overview of supersymmetry (SUSY) and the Minimal Supersymmetric Standard Model (MSSM). The second part deals with some technicalities required for the calculation of NLO corrections and their combination with parton showers.

2.1. Supersymmetry and the MSSM

2.1.1. Motivation

In order to understand the motivation for supersymmetric theories it is necessary to recapitulate the current status of elementary particle physics. Basically all experimental observations at particle colliders like the LHC, currently operating at CERN in Geneva, can be explained by the Standard Model of particle physics (SM). The SM is a quantum field theory (QFT) based on the principle of local gauge invariance with the underlying gauge group $SU(3)_C \times SU(2)_L \times U(1)_Y$. It comprises of Quantum Chromodynamics (QCD) [1, 2], which describes the strong interactions between quarks and gluons in terms of the $SU(3)_C$ gauge group, and the electroweak interactions [3–5], which are collectively described via the $SU(2)_L \times U(1)_Y$ group. The group $SU(2)_L \times U(1)_Y$ is spontaneously broken to $U(1)_{\mathrm{em}}$, the group of Quantum Electrodynamics (QED), by introducing a scalar field which acquires a non-vanishing vacuum expectation value. This mechanism of electroweak symmetry breaking (EWSB) is a fundamental prerequisite for the validity of the SM, as it generates the masses of the fermions and the heavy gauge bosons $W^{\pm}$ and Z in a gauge invariant way. It is nowadays referred to as the Higgs mechanism [8–11], the field introduced to trigger the EWSB is commonly known as the Higgs field. An immediate consequence of this approach is the prediction of a massive scalar particle, the Higgs boson. For almost 20 years this particle constituted the last missing puzzle piece of the SM, until the two largest experiments at the LHC, ATLAS and CMS, announced in July 2012 the discovery of a heavy resonance with mass 125-126 GeV, see [6, 7]. While the unraveling of the properties of this particle is still a topic of current research, all measurements of its quantum numbers and couplings are so far compatible with the SM predictions for the Higgs boson, namely a CP-even

scalar particle of even parity whose couplings to other particles are proportional to the respective particles' masses.

Over the last decades the SM has been challenged by countless experimental tests with unprecedented precision. However, so far no significant deviations have been found. After the discovery of the Higgs boson this raises the question why theories Beyond the SM (BSM) are relevant at all. Besides rather philosophical arguments like the large number of free parameters introduced in the SM there are several points suggesting that the SM cannot provide the ultimate description for all fundamental phenomena observed in nature. An obvious shortcoming of the SM is the lack of an explanation for the fourth fundamental force, the gravitational interaction between massive particles. In classical physics this is described with amazing precision by Einstein's theory of General Relativity as a consequence of the structure of space-time. However, so far no convincing embedding of this fundamental force in a QFT has been achieved. In addition to this technical point it is hard to believe that no additional effects occur between the TeV-scale investigated nowadays at colliders like the LHC and the typical scale of gravitational effects, which is given by the Planck mass $M_P \propto 10^{18}$GeV. A second experimental observation hinting at physics BSM is the existence of dark matter. The particle spectrum of the SM offers no candidate for this mysterious form of matter, which constitutes almost 25% of the energy content of our universe. Even more mysterious is the so-called dark energy, whose existence is postulated in order to explain the expansion of the universe and the structure of the cosmic microwave background. This so-far unexplained novel form of energy accounts for roughly 70% of the total energy content of the universe. A further experimental reason for the consideration of models BSM is the observation of neutrino oscillations, which inevitably require the neutrinos to be massive particles. The SM, however, includes no mass terms for the neutrinos.

Besides these obviously missing ingredients, some more theoretically motivated reasons point to the existence of physics BSM. First of all, in the SM the unification of the three forces is not possible. Considering the evolution of the three gauge couplings to high scales they approach each other in the vicinity of $Q \approx 10^{16}\,\text{GeV}$, but do not intersect in a single point. Furthermore, the calculation of the quantum corrections to the mass m_H of the Higgs boson in the SM reveals a high sensitivity to phenomena occurring at large scales. In order to understand this effect consider the one-loop contributions to m_H^2 induced by a massive Dirac fermion, e.g. the top quark. Following the discussion in [34], the calculation of these corrections Δm_H^2 requires the evaluation of a loop integral, which is divergent for large values of the loop momentum. Regularizing this divergence by introducing an upper cut-off scale Λ_{UV} one obtains

$$\Delta m_H^2 = -\frac{\lambda_f^2}{8\pi^2}\left[\Lambda_{\text{UV}}^2 + \dots\right] \tag{2.1}$$

with the Yukawa coupling λ_f of the fermion to the Higgs boson. The ellipses indicate further terms, which have at most a logarithmic dependence on Λ_{UV}. For large values of Λ_{UV} these corrections result in a value for m_H far above the one measured for the newly discovered resonance at the LHC, $m_H \approx 126\,\text{GeV}$. At first glance this is not a real problem in the sense of an inconsistency: the SM is known to be renormalizable, i.e. eventually the divergence regularized by Λ_{UV} is absorbed into a counterterm introduced in the renormalization procedure. However, interpreting this cut-off scale as the scale up to which the SM is valid and assuming that no new effects occur between the scale of EWSB, which is related to the vacuum expectation value $v \approx 246\,\text{GeV}$ of the Higgs field, and the Planck scale would require an enormous amount of 'fine-tuning' to adjust the counterterm such that m_H takes the 'correct' value. Similarly, the

corrections induced by a complex scalar field of mass m_s take the form

$$\Delta m_H^2 = \frac{\lambda_s}{16\pi^2}\left[\Lambda_{\mathrm{UV}}^2 + \dots\right], \tag{2.2}$$

where again the missing terms depend at most logarithmically on Λ_{UV}. Comparing the two types of corrections an immediate solution to this 'fine-tuning problem' emerges: if the number of bosonic and fermionic degrees of freedom of the particles in the two types of corrections is identical and the couplings fulfil $\lambda_s = \lambda_f^2$ the quadratic terms neatly cancel.

In order to achieve this cancellation to all orders of perturbation theory the introduction of a new kind of symmetry is required, which connects fermionic and bosonic degrees of freedom. This is achieved in supersymmetric theories [35–40]. For a pedagogic introduction and a detailed guide to the original literature see the review [34], which forms also the basis of the following two sections.

2.1.2. Supersymmetry

While it is possible to construct SUSY theories in such a way that the fine-tuning problem discussed in the last section is avoided, this is by far not the only motivation for this class of theories. Maybe one of the most profound arguments in favour of SUSY emerged from considerations of the maximal set of symmetries allowed for the $\mathcal{S}$-matrix within a consistent relativistic QFT. The no-go theorem by Coleman and Mandula [41] states that it is not possible to combine internal symmetries of the $\mathcal{S}$-matrix like gauge symmetries and the Poincaré symmetry in any but a trivial way, i.e. the only generators transforming tensorially under the Poincaré group are the generators of translations P^μ and Lorentz transformations $\mathcal{M}^{\mu\nu}$. However, the Coleman-Mandula theorem does not include anticommuting spinorial generators Q. It has been shown by Haag, Lopuszanski and Sohnius [12] that the Super-Poincaré algebra stated below in Eq. (2.4) is the only so-called graded Lie-algebra of symmetries of the $\mathcal{S}$-matrix which leads to a consistent relativistic QFT. Schematically, the spinorial operators Q turn a bosonic state into a fermionic one and vice versa:

$$Q\,|\mathrm{Boson}\rangle = |\mathrm{Fermion}\rangle\,, \quad Q\,|\mathrm{Fermion}\rangle = |\mathrm{Boson}\rangle\,. \tag{2.3}$$

Considering the simplest case of an extension of the Poincaré algebra by one such spinorial generator Q in form of a Weyl spinor, which is referred to as $N = 1$ SUSY, the generator Q and its hermitian conjugate $Q^\dagger$ have to fulfil the following (anti)commutation relations (see [42]):

$$\begin{aligned} \{Q, Q^\dagger\} &= 2\sigma_\mu P^\mu \\ \{Q, Q\} = \{Q^\dagger, Q^\dagger\} &= 0 \\ [Q, P^\mu] = [Q^\dagger, P^\mu] &= 0 \\ [Q, \mathcal{M}^{\mu\nu}] &= \sigma^{\mu\nu} Q\,, \end{aligned} \tag{2.4}$$

where $\sigma^\mu = \left(\mathbf{1}, \sigma^i\right)$ and $\sigma^{\mu\nu} = \frac{i}{4}\left(\sigma^\mu\bar{\sigma}^\nu - \sigma^\nu\bar{\sigma}^\mu\right)$ with $\bar{\sigma}^\mu = \left(\mathbf{1}, -\sigma^i\right)$ and the usual Pauli matrices σ^i $(i = 1, 2, 3)$. In combination with the commutation relations of the Poincaré algebra Eq. (2.4) forms the Super-Poincaré algebra. The generators P^μ, $\mathcal{M}^{\mu\nu}$, Q and $Q^\dagger$ commute with all generators of internal symmetries of the $\mathcal{S}$-matrix.

In order to construct a supersymmetric extension of the SM the particles of the SM and their predicted superpartners (commonly called sparticles) are arranged in irreducible representations

of the Super-Poincaré algebra, the so-called supermultiplets. Due to the fact that the internal symmetry generators commute with those of the Super-Poincaré algebra all particles in a supermultiplet share the same transformation behaviour under the respective gauge group, thus the couplings of the superpartners are identical to those of their respective SM partner. Moreover, the Casimir operator P^2 of the Poincaré algebra, whose eigenvalues correspond to the respective particle masses, commutes with the SUSY generators Q and $Q^\dagger$, hence the masses of all particles in a supermultiplet are identical. In addition, it can be shown that the number of bosonic and fermionic degrees of freedom in a supermultiplet is identical. Thus the structure of supersymmetric theories is indeed such that the fine-tuning problem introduced at the end of the last section is absent.

2.1.3. The Minimal Supersymmetric Standard Model

For the construction of the minimal supersymmetric extension of the SM only two types of supermultiplets are required. The first ones are the chiral supermultiplets, which contain each a complex scalar field and a Weyl fermion. The second building block are the gauge supermultiplets, which combine a massless vector boson and a Weyl fermion. Note that in both cases the number of bosonic and fermionic degrees of freedom is indeed identical.

In order to determine the particle content of the MSSM the particles of the SM and their superpartners have to be assigned to either a chiral or a gauge supermultiplet. An immediate consequence of this assignment is the fact that the thus predicted superpartners differ by half a unit in spin compared to the corresponding SM particle. The quarks and leptons have to be assigned to chiral supermultiplets, as only those allow for a different transformation behaviour of left- and right-handed components, which is an essential property of the electroweak theory. Hence the corresponding superpartners are scalar particles, which are called squarks and sleptons. A lower subscript L/R indicates the left/right chiral nature of the respective SM particle. As a scalar particle, the Higgs boson of the SM has to be part of a chiral supermultiplet, too. However, it turns out that one Higgs chiral supermultiplet is not sufficient to obtain a supersymmetric, anomaly-free theory. In the minimal supersymmetric extension of the SM two Higgs chiral supermultiplets have to be introduced, one with a weak hypercharge $Y = +1/2$ and one with $Y = -1/2$. Demanding invariance under SUSY transformations restricts the Yukawa couplings in such a way that the first one only couples to up-type quarks and the second one only to leptons and down-type quarks. Hence in order to obtain masses for both types of quarks and the leptons the introduction of both these Higgs chiral supermultiplets is inevitable. The particles in these two supermultiplets are indicated by a suffix u and d, respectively. The fermionic superpartners of the Higgs scalars are called Higgsinos. The resulting chiral supermultiplets for the MSSM are summarized with the corresponding transformation properties of the particles under the gauge group $SU(3)_C \times SU(2)_L \times U(1)_Y$ of the SM in Tab. 2.1. Only the first generation of (s)quarks and (s)leptons is given there, the other two generations only differ in names. Note that here, following the notation in [34], all chiral supermultiplets are defined in terms of left-chiral Weyl spinors, i.e. the conjugates of the right-handed fields occur in Tab. 2.1.

The gauge bosons of the SM have to be assigned to gauge supermultiplets, their superpartners are collectively called gauginos. In detail, the superpartner of the gluon is the gluino, while the partners of the W and B bosons are the winos and the bino. After EWSB the $\tilde{B}^0$ and $\tilde{W}^0$ mix to the zino and the photino, which have in unbroken SUSY the mass of the Z boson, m_Z, and the photon, $m_\gamma = 0$. The gauge supermultiplets of the MSSM are summarized in Tab. 2.2.

	Scalars	Fermions	$SU(3)_C$	$SU(2)_L$	$U(1)_Y$
Squarks & Quarks	$(\tilde{u}_L, \tilde{d}_L)$	(u_L, d_L)	3	2	$\frac{1}{6}$
	$\tilde{u}_R^*$	$u_R^\dagger$	$\bar{3}$	1	$-\frac{2}{3}$
	$\tilde{d}_R^*$	$d_R^\dagger$	$\bar{3}$	1	$\frac{1}{3}$
Sleptons & Leptons	$(\tilde{\nu}, \tilde{e}_L)$	(ν, e_L)	1	2	$-\frac{1}{2}$
	$\tilde{e}_R^*$	$e_R^\dagger$	1	1	1
Higgs & Higgsinos	(H_u^+, H_u^0)	$(\tilde{H}_u^+, \tilde{H}_u^0)$	1	2	$\frac{1}{2}$
	(H_d^0, H_d^-)	$(\tilde{H}_d^0, \tilde{H}_d^-)$	1	2	$-\frac{1}{2}$

Table 2.1.: The chiral supermultiplets of the MSSM. Only the (s)quarks and (s)leptons of the first generation are listed explicitly. The fermions are given in terms of left-chiral Weyl fermions. The last three columns indicate the transformation behaviour under the gauge group of the SM.

	Fermions	Vectors	$SU(3)_C$	$SU(2)_L$	$U(1)_Y$
Gluino & Gluon	$\tilde{g}$	g	8	1	0
Winos & W bosons	$\tilde{W}^\pm$ $\tilde{W}^0$	$W^\pm$ W^0	1	3	0
Bino & B boson	$\tilde{B}^0$	B^0	1	1	0

Table 2.2.: The gauge supermultiplets of the MSSM. The last three columns indicate the transformation behaviour under the gauge group of the SM.

This completes the particle content of the MSSM. However, as already observed above, an immediate consequence of the Super-Poincaré algebra in Eq. (2.4) is the equality of the masses of the superpartners in each supermultiplet. As moreover their gauge couplings are identical one can conclude immediately that SUSY is not an exact symmetry of nature, otherwise at least some of the superpartners of the SM would have been found. The mechanism for the breaking of SUSY is a priori unknown. However, taking again the fine-tuning problem as a guidance, the possible SUSY-breaking terms in the Lagrangian are not completely arbitrary. In order not to destroy the cancellation of the quadratic divergences SUSY is only 'softly' broken, i.e. the terms added to the Lagrangian which are not invariant under SUSY transformations contain either only mass terms or interaction terms with coupling parameters of positive mass dimension. This guarantees that the correction terms to m_H^2 are $\propto m_{\text{soft}}^2 \log(\Lambda_{\text{UV}}/m_{\text{soft}})$, with m_{soft} representing the largest mass scale occurring in the soft SUSY-breaking part of the Lagrangian. In order not to introduce a new source of fine-tuning this scale should not be chosen too large.

An immediate consequence of SUSY breaking is the fact that the superpartners of the SM particles introduced above are in general no longer the mass eigenstates of the theory. After EWSB the electroweak gauginos and Higgsinos with equal electrical charge mix with each other, leading to four massive neutral so-called neutralinos $\tilde{\chi}_i^0$ $(i = 1, \ldots, 4)$, which are by convention ordered by ascending mass, and two charged particles, $\tilde{\chi}_k^\pm$ $(k = 1, 2)$, the charginos. The same holds for the squark and slepton sector of the MSSM. However, in this case it is usually sufficient to consider only the mixing effects for sparticles of the third-generation, as the non-diagonal mixing matrix elements are zero in the limit of vanishing quark/lepton masses.

One further important point for phenomenological studies of the MSSM is the so-called R-

parity. In principle it is possible to introduce further terms in the Lagrangian of the MSSM, which are invariant under SUSY and gauge transformations, but violate the conservation of baryon or lepton number. So far no such processes have been observed, hence in order to fulfil the stringent experimental bounds (e.g. from the non-observation of the proton decay) the corresponding couplings have to be suppressed tremendously. These terms are completely eliminated by imposing an additional discrete symmetry, known as R-parity [43], which is a multiplicatively conserved quantum number defined for each particle as

$$\mathcal{P}_R = (-1)^{3(B-L)+2s}\,, \tag{2.5}$$

where B (L) corresponds to the respective baryon (lepton) number and s denotes the spin of the particle. A direct consequence of the fact that all SM particles differ by half a unit in spin from their superpartners is a difference in the sign of their respective $\mathcal{P}_R$ values. It is straightforward to show that

$$\begin{aligned} \mathcal{P}_R &= +1 \quad \text{for SM particles} \\ \mathcal{P}_R &= -1 \quad \text{for their superpartners}\,. \end{aligned} \tag{2.6}$$

As important phenomenological consequence the sparticles are only produced pairwise. Moreover, in theories with $\mathcal{R}$-parity conservation, the lightest supersymmetric particle (LSP) is stable. If the LSP corresponds to the lightest neutralino, $\tilde{\chi}_1^0$, it represents an ideal candidate for dark matter.

This concludes the brief introduction to SUSY and the MSSM. For further reading the reader is again referred to the more detailed introduction in [34] and the references given therein. The derivation of the Feynman rules applied in the various calculations presented in Ch. 3 is not repeated here, they have been taken from [44].

2.1.4. SUSY searches at hadron colliders

The search for evidences of sparticle production constitutes one of the main points of the physical program at the LHC. The unprecedented high centre-of-mass energy of $\sqrt{s} = 8\,\text{TeV}$ in the last proton-proton runs at the end of 2012 extends the accessible SUSY parameter space tremendously compared to the SUSY searches at the Tevatron or the Large Electron Positron collider.

The first step in direct searches for supersymmetric particles at hadron colliders consists in the search for squarks and gluinos, as the production cross sections for these strongly interacting particles are usually large compared to sleptons and other gauginos. The produced squarks and gluinos are unstable and decay into SM particles (i.e. quarks, leptons and neutrinos) and the LSP (i.e. usually the $\tilde{\chi}_1^0$). The presence of neutralinos in the final state gives rise to the first very characteristic signature of SUSY processes, namely an imbalance in the transverse energy of all visible particles, the missing transverse energy $\not{E}_T$. Of course, neutrinos also lead to $\not{E}_T$, however, the resulting values are usually much smaller, hence these contributions can be suppressed by suitably designed phase space cuts. The second element of a typical experimental signature for squark and gluino decays is the occurrence of several jets with high transverse momentum and, in case of longer cascade decays involving intermediate sleptons, comparatively hard leptons.

The two multipurpose experiments at the LHC, ATLAS and CMS, have been searching extensively for signatures of this type, however, so far no excess over the various SM background processes has been observed. Hence the experiments can only give lower limits on the masses

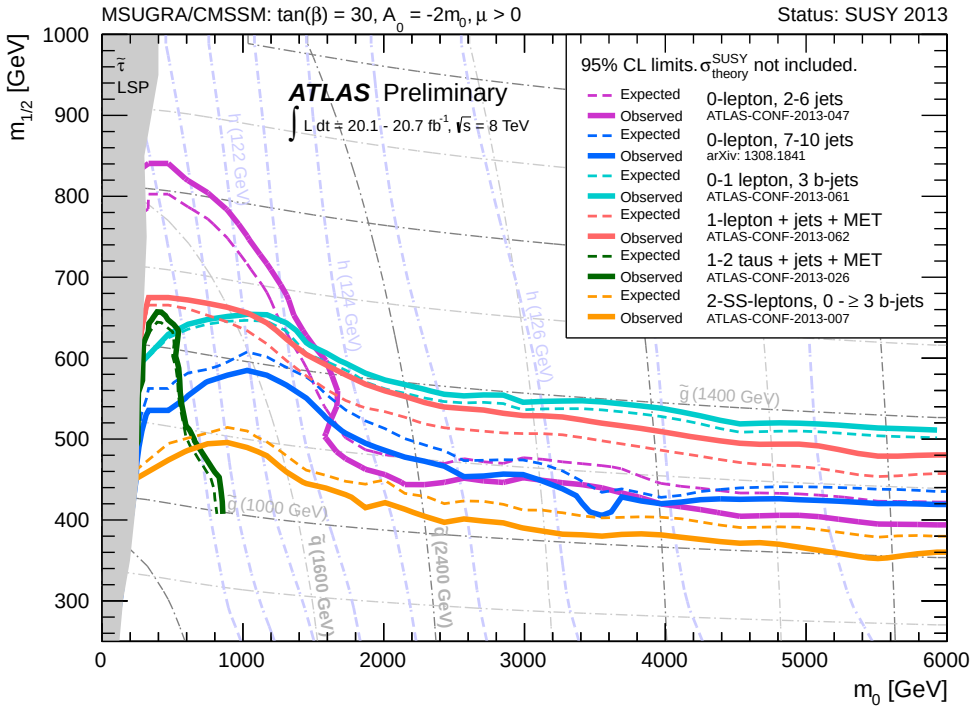

Figure 2.1.: Exclusion bounds from the ATLAS experiment in a mSUGRA scenario with $A_0 = -2m_0$, $\tan\beta = 30$ and $\mu > 0$ in the m_0-$m_{1/2}$ plane. The plot summarizes several analyses defined in the legend and has been taken from [55].

of the squarks and gluinos, [33, 45–48] and [49–54]. These exclusion bounds are obtained from various search channels with different multiplicities of jets and leptons in the final state. However, due to the large number of free parameters in the most general version of the MSSM with soft SUSY breaking it is impossible to determine lower limits for all parameters simultaneously. Therefore, as a first step in the analyses performed by the experiments this number is reduced to a manageable amount by applying some simplifying assumptions.

This can be achieved by considering specific models for the mechanism of SUSY breaking. One such model is minimal SUperGRAvity (mSUGRA), which is also used for the numerical analysis of the analytical results calculated in this thesis. This model is defined in terms of five parameters determined at a high energy scale, namely the soft SUSY breaking masses m_0 for the scalars and $m_{1/2}$ for the gauginos, the trilinear coupling A_0, the ratio of the vacuum expectation values of the two Higgs doublets, $\tan\beta$, and the sign of the μ parameter introduced in the superpotential. These parameters in turn determine all masses and the mixing patterns of the sparticles at lower energy scales by means of the renormalization group equations (RGEs). The exclusion bounds given by the ATLAS collaboration for a specific mSUGRA model with fixed values $A_0 = -2m_0$, $\tan\beta = 30$ and $\mu > 0$ are shown in the m_0-$m_{1/2}$ plane in Fig. 2.1. The various exclusion bounds have been obtained from the different search channels defined in the legend. The corresponding masses of the squarks and the gluinos are indicated by the dash-dotted grey lines. This allows for a direct interpretation in terms of lower limits for squark and gluino masses. For example the analysis in [33] (which corresponds to the magenta coloured lines in Fig. 2.1) excludes scenarios with $m_{\tilde{q}} = m_{\tilde{g}} \lesssim 1700\,\text{GeV}$ for this specific mSUGRA model.

A slightly different approach to determine exclusion limits for squark and gluino masses is the

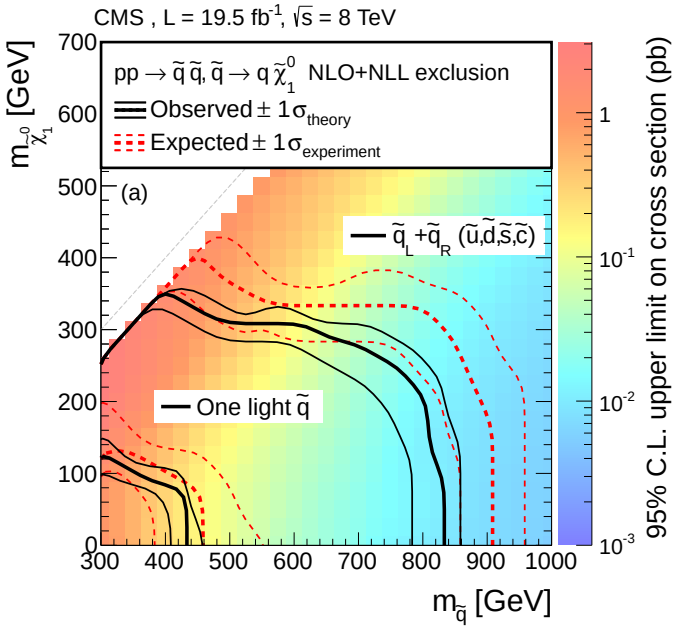

Figure 2.2.: Exclusion bounds from the CMS collaboration on the squark and lightest neutralino masses in simplified models as described in the text. The plot has been taken from [54].

consideration of simplified models. The latest bounds for such a model obtained by the CMS experiment for the production of a squark pair with squarks of the first two generations are shown in Fig. 2.2. The model considered here assumes that the produced squarks decay exclusively to a quark and the lightest neutralino, i.e. the experimental signature consists of several jets (in the analysis the effects of additional parton radiation on top of the pure squark pair production process are taken into account) and missing transverse energy. Moreover, the gluino mass is eliminated by setting it to a "very large" value. The exclusion limits shown in the plot in the $m_{\tilde{q}}$-$m_{\tilde{\chi}_1^0}$ plane have been obtained for two scenarios: either all squarks of the first two generations are assumed to share a common mass (this case is called $\tilde{q}_L + \tilde{q}_R$ in the figure), or only one squark is sufficiently light to be accessible at the LHC. In the first scenario values of $m_{\tilde{q}} < 780\,\text{GeV}$ are excluded for $m_{\tilde{\chi}_1^0} < 200\,\text{GeV}$, while with the second assumption the lower limit on the mass of the light squark is given by $m_{\tilde{q}} = 400\,\text{GeV}$ for $m_{\tilde{\chi}_1^0} < 80\,\text{GeV}$.

2.2. Higher order corrections and beyond

The following chapter summarizes several methods used in the calculations performed in Ch. 3 and 4. After establishing the connection of hadronic and partonic cross sections in Sec. 2.2.1, the treatment of ultraviolet and infrared divergences occurring in next-to-leading order (NLO) calculations is discussed in Sec. 2.2.2. Realistic simulations for the structure of events at (hadron) colliders require the supplement of a parton shower to the results obtained at fixed order. The general idea of parton showers is outlined in Sec. 2.2.3. However, the combination of NLO results with parton showers turns out to be a non-trivial task. The POWHEG method [25, 26] constitutes one approach to perform this so-called matching in a consistent manner, its basic idea is described in Sec. 2.2.4. This last section also introduces the program package POWHEG-BOX [27], which automates the process-independent steps of the POWHEG method and forms the basis for the implementation of all processes considered in this thesis.

2.2.1. Hadronic collisions

The theoretical predictions for specific observables at hadron colliders like the LHC are usually calculated for partonic interactions, i.e. reactions with quarks and gluons in the initial and final state. However, in nature no free partons occur due to the confinement of QCD. Hence to obtain realistic predictions for measurable quantities at experiments the connection between the scattered or produced hadrons and the calculated partonic reactions has to be established, which is achieved in the parton model (see e.g. [56] for a detailed discussion). The transition from partons to hadrons is subject to non-perturbative effects, which cannot be calculated, but have to be determined from experiments.

For the collision of two hadrons (e.g. two protons at the LHC) the connection between the differential hadronic cross section $\mathrm{d}\sigma_{\mathrm{had}}$ and the differential cross section $\mathrm{d}\hat{\sigma}_{ij\to n}$ for the scattering of two partons i, j to a final state with n particles is given by

$$\mathrm{d}\sigma_{\mathrm{had}} = \int_0^1 \mathrm{d}x_1 \int_0^1 \mathrm{d}x_2 \sum_{i,j} f_i(x_1,\mu_F) f_j(x_2,\mu_F) \mathrm{d}\hat{\sigma}_{ij\to n} \left(p_i + p_j = \sum_{a=1}^{n} k_a \right). \tag{2.7}$$

The momenta p_i/p_j of the two partons are related to those of the two colliding hadrons, P_1/P_2, via $p_i = x_1 P_1$ and $p_j = x_2 P_2$ ($x_k \in [0,1]$), respectively. The momenta of the n particles in the final state are denoted k_a. The experimentally determined parton distribution function (PDF) $f_i(x_1, \mu_F)$ denotes the probability of finding a parton of type i in the first hadron with a momentum fraction x_1 of the total hadron momentum P_1 at the factorization scale μ_F, which separates the non-perturbative and perturbative effects. The sum in Eq. (2.7) runs over all partons contributing to the process $ij \to n$. The differential partonic cross section $\mathrm{d}\hat{\sigma}_{ij\to n}$ is calculated in perturbation theory by evaluating the matrix elements squared for the respective partonic processes to the desired order in the perturbative expansion. These results have to be multiplied by the flux factor $1/(2\hat{s})$ for the incoming partons and the Lorentz-invariant phase space element $\mathrm{d}\Phi_n$ for a $2 \to n$ process, yielding

$$\mathrm{d}\hat{\sigma}_{ij\to n} = \frac{1}{2\hat{s}} \mathrm{d}\Phi_n \left| \mathcal{M}_{ij\to n} \right|^2 \tag{2.8}$$

with the partonic centre-of-mass energy squared $\hat{s} = 2p_i \cdot p_j$ and the matrix element $\mathcal{M}_{ij\to n}$ of the process considered. The n-particle phase space element takes the form

$$\mathrm{d}\Phi_n = (2\pi)^4 \delta^{(4)} \left(p_i + p_j - \sum_{a=1}^{n} k_a \right) \prod_{a=1}^{n} \frac{\mathrm{d}\vec{k}_a^{\,3}}{(2\pi)^3 2k_a^0}\,. \tag{2.9}$$

2.2.2. Ingredients of NLO calculations

Besides the evaluation of the Born matrix elements squared, the calculation of higher-order corrections requires the computation of loop integrals. For the NLO corrections calculated in the context of this thesis only one-loop contributions are relevant. The integration over the loop momenta is not restricted to a certain range and can lead to ultraviolet (UV) and/or infrared (IR) divergences. The latter ones also occur in the real emission of partons if a radiated gluon gets soft and/or collinear to a massless emitting parton or if a gluon splits into a collinear quark-antiquark pair. The IR divergences occurring in the virtual and the real contributions mutually cancel, as will be discussed in the last paragraph of this section. The UV divergences, however, have to be removed via a reinterpretation of the quantities in the Lagrangian of the theory.

2.2.2.1. Regularization and renormalization

Before being able to perform any meaningful calculation it is inevitable to isolate the divergences occurring in the loop integrals. This is achieved by defining a regularization scheme, the most commonly used one being Dimensional Regularization (DR) [57]. The basic idea of DR consists in performing the integration no longer in four space-time dimensions, but in $d = 4-2\epsilon$ dimensions. Formally this amounts to the replacement

$$\int \frac{\mathrm{d}^4 q}{(2\pi)^4} \to \mu^{4-d} \int \frac{\mathrm{d}^d q}{(2\pi)^d}\,, \tag{2.10}$$

where μ is the 't Hooft scale introduced here to preserve the correct mass dimensions. This scheme is known to respect both gauge and Lorentz invariance, moreover it is possible to regularize both UV and IR divergences. These divergences lead to poles for $\epsilon \to 0$, which emerge at NLO as $1/\epsilon_{\mathrm{UV}}$ and $1/\epsilon_{\mathrm{IR}}$ ($1/\epsilon^2_{\mathrm{IR}}$) for soft or (and) collinear divergences.

At one-loop level it is possible to separate the $1/\epsilon_{\mathrm{IR}}$ and $1/\epsilon_{\mathrm{UV}}$ poles, as the resulting scalar loop integrals have either a UV or an IR divergence. The only exception is the scalar two-point function $B_0(p^2, m_1^2, m_2^2)$ for the special case $p^2 = m_1^2 = m_2^2 = 0$, which reads

$$B_0(0,0,0) = \frac{1}{\epsilon_{\mathrm{UV}}} - \frac{1}{\epsilon_{\mathrm{IR}}} + \log \frac{\mu^2_{\mathrm{UV}}}{\mu^2_{\mathrm{IR}}}. \tag{2.11}$$

It is possible to set $B_0(0,0,0) = 0$ if the UV and IR divergences have been cancelled correctly by means of renormalization and e.g. a subtraction formalism, respectively. However, when checking UV and IR finiteness of a result separately this case has to be kept in mind, see Sec. 3.1.4.

A drawback of the DR scheme in the context of higher-order calculations in SUSY theories is the fact that it explicitly breaks SUSY. In conventional DR all quantities are continued to d dimensions, i.e. massless gauge bosons have $d-2$ degrees of freedom (dofs) instead of two. Majorana spinor fields and hence the gaugino fields, in contrast, still have two dofs. Consequently, one of the most profound properties of SUSY theories, the equality of bosonic and fermionic dofs, is violated due to this mismatch. A direct manifestation of this imbalance is the violation of the equivalence of the Yukawa couplings $\hat{g}$ and the gauge couplings g. One possibility to avoid this problem is the use of a modified scheme known as Dimensional Reduction [58, 59]. In this scheme the momenta are continued to d dimensions, as in conventional DR, but the vector fields remain four-dimensional. Another possible approach, which is also used in the following, consists in performing the calculation in conventional DR and restoring the relation $\hat{g} = g$ by hand. This requires the introduction of a 'SUSY restoring counterterm' constructed such that the additional dofs introduced in DR are subtracted.

After the isolation of the UV poles a meaningful calculation still requires an interpretation of the formally divergent results. This is subject of the renormalization procedure. The key idea of renormalization is the reinterpretation of the fields and parameters like masses and couplings in the Lagrangian $\mathcal{L}$. At tree level they can be set in a direct correspondence to measurable quantities in nature. Higher order corrections, however, destroy these direct relations, as they shift e.g. the real parts of the poles of the propagators, which correspond at tree level to the physical masses of the particles. In order to relate these so-called bare parameters and fields (indicated in the following by a lower index 0) to observable quantities, they are replaced by the product of their (finite) renormalized equivalent and (divergent) renormalization constants Z_i. With this approach, known as multiplicative renormalization, no new terms are introduced

in $\mathcal{L}$. The renormalization constants can be expanded as $Z_i = 1 + \delta Z_i$ with the counterterms δZ_i. For the parameters and fields required in the NLO calculation of squark production and decay this leads to

$$\begin{aligned} A_0^\mu &= (1 + \frac{1}{2}\delta Z_g) A^\mu \,, \\ \Psi_{q/\tilde{g},0} &= (1 + \frac{1}{2}\delta Z_{q/\tilde{g}}) \Psi_{q/\tilde{g}} \,, \\ \phi_{\tilde{q},0} &= (1 + \frac{1}{2}\delta Z_{\tilde{q}}) \phi_{\tilde{q}} \,, \\ g_{s,0} &= g_s + \delta g_s \,, \\ m_{\tilde{g},0} &= m_{\tilde{g}} + \delta m_{\tilde{g}} \,, \\ m^2_{\tilde{q},0} &= m^2_{\tilde{q}} + \delta m^2_{\tilde{q}} \,, \end{aligned} \tag{2.12}$$

with the gluon field A_μ, the spinorial field Ψ for the quarks and the gluino, the scalar squark field $\phi_{\tilde{q}}$, the strong coupling g_s and the masses of the squark, $m_{\tilde{q}}$, and the gluino, $m_{\tilde{g}}$. These expressions are then inserted into the bare Lagrangian, which can be rewritten as

$$\mathcal{L}_0 = \mathcal{L} + \delta\mathcal{L} \,, \tag{2.13}$$

where $\mathcal{L}$ is identical to $\mathcal{L}_0$ with renormalized fields, masses, couplings, etc. and all counterterm contributions are contained in the counterterm Lagrangian $\delta\mathcal{L}$. The Feynman rules obtained for $\mathcal{L}_0$ are still valid for $\mathcal{L}$, however, $\delta\mathcal{L}$ leads to additional rules which have to be taken into account in calculations beyond LO. The concrete form of these counterterms is in principle arbitrary, as long as they cancel the UV divergences present in $\mathcal{L}_0$. Their finite part is determined by renormalization conditions. The results for physical observables calculated to all orders in perturbation theory do not depend on these finite parts. However, if the perturbation theory is truncated, different renormalization conditions may give different results.

In the NLO calculations performed in the context of this thesis two renormalization schemes are applied: the on-shell scheme is used for the renormalization of all fields and masses, while the strong coupling constant is renormalized in the $\overline{\text{MS}}$ scheme.

On-shell scheme

In the on-shell scheme the counterterms are determined such that the renormalized masses correspond to the physical ones, i.e. to the real parts of the poles of the respective propagators. Moreover, the residues of the renormalized propagators shall be one, hence no corrections to external on-shell legs have to be taken into account. In order to obtain the counterterms in Eq. (2.12) such that they fulfil these conditions, the renormalized one-particle-irreducible two-point functions for the quark, squark, gluon and gluino have to be considered. Adapting the definitions of [44] and [60] these can be cast into the form

$$\begin{aligned} \hat{\Gamma}^q(k) &= i(\not{k} - m_q) + i\left[\not{k}\hat{\Sigma}^{q,V}(k^2) + m_q\hat{\Sigma}^{q,S}(k^2)\right] \,, \\ \hat{\Gamma}^{\tilde{q}}(k) &= i(k^2 - m^2_{\tilde{q}}) + i\hat{\Sigma}^{\tilde{q}}(k^2) \,, \\ \hat{\Gamma}^g_{\mu\nu}(k) &= -ig_{\mu\nu}k^2 - i\left(g_{\mu\nu} - \frac{k_\mu k_\nu}{k^2}\right)\hat{\Sigma}^g_T(k^2) - i\frac{k_\mu k_\nu}{k^2}\hat{\Sigma}^g_L(k^2) \,, \\ \hat{\Gamma}^{\tilde{g}}(k) &= i(\not{k} - m_{\tilde{g}}) + i\left[\not{k}\hat{\Sigma}^{\tilde{g},V}(k^2) + m_{\tilde{g}}\hat{\Sigma}^{\tilde{g},S}(k^2)\right] \,, \end{aligned} \tag{2.14}$$

where the longitudinal term $\hat{\Sigma}^g_L(k^2)$ vanishes due to a Ward identity. Note that in the following no flavour changing interactions occur, i.e. it is not necessary to use the more general expressions

given in [60] for the quarks. Likewise, no flavour changing effects in the two-point functions of the squarks have to be considered. Moreover, in the calculation all external quarks are assumed to be massless, as only contributions of first- and second-generation quarks are taken into account, i.e. $m_q = 0$.

Imposing the conditions of the on-shell scheme leads to the following relations for the renormalized self-energy contributions $\hat{\Sigma}^i$:

- **Squarks:**

$$\begin{aligned} &\mathrm{Re}\,\hat{\Gamma}^{\tilde{q}}(k)\Big|_{k^2=m_{\tilde{q}}^2} = 0 \quad \Rightarrow \quad \mathrm{Re}\,\hat{\Sigma}^{\tilde{q}}(m_{\tilde{q}}^2) = 0\,, \\ &\lim_{k^2\to m_{\tilde{q}}^2} \frac{\mathrm{Re}\,\hat{\Gamma}^{\tilde{q}}(k)}{k^2 - m_{\tilde{q}}^2} = i \quad \Rightarrow \quad \mathrm{Re}\,\frac{\partial\hat{\Sigma}^{\tilde{q}}(k^2)}{\partial k^2}\Big|_{k^2=m_{\tilde{q}}^2} = 0\,, \end{aligned} \tag{2.15}$$

- **Quarks:**

$$\lim_{k^2\to 0} \frac{\not{k}}{k^2}\mathrm{Re}\,\hat{\Gamma}^{q}(k)u(k) = iu(k) \quad \Rightarrow \quad \mathrm{Re}\,\hat{\Sigma}^{q,V}(0) = 0\,, \tag{2.16}$$

- **Gluon:**

$$\lim_{k^2\to 0} \frac{1}{k^2}\epsilon^{\rho}(k)\mathrm{Re}\,\hat{\Gamma}^{g}_{\rho\nu}(k) = -i\epsilon_{\nu}(k) \quad \Rightarrow \quad \mathrm{Re}\,\frac{\partial\hat{\Sigma}^{g}_{T}(k^2)}{\partial k^2}\Big|_{k^2=0} = 0\,, \tag{2.17}$$

- **Gluino:**

$$\begin{aligned} &\mathrm{Re}\,\hat{\Gamma}^{\tilde{g}}(k)u(k)\Big|_{k^2=m_{\tilde{g}}^2} = 0 \quad \Rightarrow \quad \mathrm{Re}\left(\hat{\Sigma}^{\tilde{g},V}(m_{\tilde{g}}^2) + \hat{\Sigma}^{\tilde{g},S}(m_{\tilde{g}}^2)\right) = 0\,, \\ &\lim_{k^2\to m_{\tilde{g}}^2} \frac{\not{k} + m_{\tilde{g}}}{k^2 - m_{\tilde{g}}^2}\mathrm{Re}\,\hat{\Gamma}^{\tilde{g}}(k)u(k) = iu(k) \\ &\qquad \Rightarrow \quad \mathrm{Re}\,\hat{\Sigma}^{\tilde{g},V}(m_{\tilde{g}}^2) + 2m_{\tilde{g}}^2\mathrm{Re}\left(\frac{\partial\hat{\Sigma}^{\tilde{g},V}(k^2)}{\partial k^2} + \frac{\partial\hat{\Sigma}^{\tilde{g},S}(k^2)}{\partial k^2}\right)\Big|_{k^2=m_{\tilde{g}}^2} = 0\,, \end{aligned} \tag{2.18}$$

where $u(k)$ corresponds to the quark/gluino spinor and ϵ^{μ} is the gluon polarization vector. With the conditions Eqs. (2.15) through (2.18) the counterterms can be expressed in terms of the unrenormalized quark, squark and gluino self-energy contributions Σ^i (see [44]):

$$\begin{aligned} \delta m_{\tilde{q}}^2 &= \mathrm{Re}\,\Sigma^{\tilde{q}}(m_{\tilde{q}}^2)\,, \\ \delta m_{\tilde{g}} &= m_{\tilde{g}}\mathrm{Re}\left(\Sigma^{\tilde{g},V}(m_{\tilde{g}}^2) + \Sigma^{\tilde{g},S}(m_{\tilde{g}}^2)\right)\,, \\ \delta Z_q &= -\mathrm{Re}\,\Sigma^{q}(0)\,, \\ \delta Z_{\tilde{q}} &= -\mathrm{Re}\,\frac{\partial\Sigma^{\tilde{q}}(k^2)}{\partial k^2}\Big|_{k^2=m_{\tilde{q}}^2}\,, \\ \delta Z_{\tilde{g}} &= -\mathrm{Re}\,\Sigma^{\tilde{g},V}(m_{\tilde{g}}^2) - 2m_{\tilde{g}}^2\mathrm{Re}\left(\frac{\partial\Sigma^{\tilde{g},V}(k^2)}{\partial k^2} + \frac{\partial\Sigma^{\tilde{g},S}(k^2)}{\partial k^2}\right)\Big|_{k^2=m_{\tilde{g}}^2}\,, \\ \delta Z_g &= -\mathrm{Re}\,\frac{\partial\Sigma^{g}_{T}(k^2)}{\partial k^2}\Big|_{k^2=0}\,. \end{aligned} \tag{2.19}$$

$\overline{\text{MS}}$ scheme

In the $\overline{\text{MS}}$ scheme [61] only the UV poles (and some universal constants) are absorbed in the counterterm for the strong coupling:

$$\delta g_s^{\overline{\text{MS}}} = \frac{\alpha_s}{8\pi}\beta_0 \left(-\Delta + \log\frac{\mu_R^2}{\mu^2}\right) \tag{2.20}$$

with the renormalization scale μ_R and $\Delta = \frac{1}{\epsilon} - \gamma_E + \log 4\pi$, where γ_E is the Euler-Mascheroni constant. The one-loop coefficient of the β-function, β_0, reads

$$\beta_0 = \underbrace{\left[\frac{11}{3}C_A - \frac{4}{3}T_F n_f^{\text{light}}\right]}_{\beta_0^{\text{light}}} + \underbrace{\left[-\frac{4}{3}T_F - \frac{2}{3}C_A - \frac{2}{3}T_F n_{\tilde{q}}\right]}_{\beta_0^{\text{heavy}}}, \tag{2.21}$$

with $T_F = 1/2$, $C_A = 3$, the number of squarks $n_{\tilde{q}} = 6$ and the number of light quarks $n_f^{\text{light}} = 5$. The first contribution, β_0^{light}, comprises the contributions of the gluon and the light quarks, whereas all contributions of heavy particles, i.e. the top quark, the gluino and the squarks, are subsumed in β_0^{heavy}.

The dependence of the strong coupling constant $\alpha_s = g_s^2/4\pi$ in the $\overline{\text{MS}}$ scheme, $\alpha_s^{\overline{\text{MS}}}$, on μ_R is determined by β_0 and thus by both the heavy and the light particles. As can be inferred directly from Eq. (2.21) this 'running' of $\alpha_s^{\overline{\text{MS}}}$ only depends on the number of particles, but not on their masses, i.e. they do not decouple automatically. This may lead to large logarithms if the scale of a process and (some of) the masses are widely separated. To avoid these artificial large logarithms the heavy particles have to be explicitly decoupled from the running of $\alpha_s^{\overline{\text{MS}}}$. At NLO, this is accomplished by replacing the (renormalized) coupling constant $\alpha_s^{\overline{\text{MS}}}$ with

$$\alpha_s^{(5),\overline{\text{MS}}}(\mu_R) = \alpha_s^{\overline{\text{MS}}}(\mu_R)\left[1 + \frac{\alpha_s^{\overline{\text{MS}}}(\mu_R)}{\pi}\left(\frac{2}{3}\log\frac{m_t^2}{\mu_R^2} + 2\log\frac{m_{\tilde{g}}^2}{\mu_R^2} + \frac{1}{3}\sum_{i=1}^{12}\log\frac{m_{\tilde{q}_i}^2}{\mu_R^2}\right)\right], \tag{2.22}$$

where in $\alpha_s^{(5),\overline{\text{MS}}}(\mu_R)$ only the five light-flavour quarks contribute to the μ_R dependence (see e.g. [62]). Technically, this modification is introduced into the calculation by modifying the counterterm δg_s,

$$\delta g_s^{\overline{\text{MS}}} \to \delta g_s^{\overline{\text{MS}}} - \frac{\alpha_s^{(5),\overline{\text{MS}}}}{8\pi}\left[\frac{2}{3}\log\frac{m_t^2}{\mu_R^2} + 2\log\frac{m_{\tilde{g}}^2}{\mu_R^2} + \frac{1}{3}\sum_{i=1}^{12}\log\frac{m_{\tilde{q}_i}^2}{\mu_R^2}\right]. \tag{2.23}$$

With this replacement the evolution of the strong coupling is described by

$$\frac{\partial g_s^2(\mu_R^2)}{\partial \log\mu_R^2} = -\alpha_s^2(\mu_R^2)\left[\beta_0 - \left(-\frac{2}{3} - \frac{6}{3} - 2\right)\right] = -\alpha_s^2(\mu_R^2)\beta_0^{\text{light}} \tag{2.24}$$

and consequently only the light-flavour quarks contribute to the running of α_s, as intended. In the calculations presented in the following chapter this decoupling is strictly speaking not necessary, as only processes with scales in the vicinity of the squark and gluino masses are considered, hence no artificially large logarithms occur. However, these calculations are implemented in an existing program (see Sec. 2.2.4) which relies on $\alpha_s^{(5),\overline{\text{MS}}}$. Thus applying the decoupling requires no changes to this code.

The last subtlety in the context of the renormalization of the strong coupling concerns the violation of SUSY by applying conventional DR. As already mentioned this destroys the identity of the gauge couplings g and the Yukawa couplings $\hat{g}$ beyond LO, hence $\hat{g}^{\overline{\text{MS}}} \neq g^{\overline{\text{MS}}}$. This mismatch can be corrected by adding a finite 'SUSY restoring counterterm' to the Yukawa-coupling, which has to be determined order by order. At NLO this has been done in a general fashion in [63], where it is shown that the relation

$$\hat{g_s}^{\overline{\text{MS}}} = g_s^{\overline{\text{MS}}} \left[1 + \frac{\alpha_s^{\overline{\text{MS}}}}{4\pi} \left(\frac{2}{3} N - \frac{1}{2} C_F \right) \right] \tag{2.25}$$

with $N = 3$ and the Casimir invariant $C_F = 4/3$ holds. In the calculation of squark (anti)squark production this affects the squark-quark-gluino vertex, whose coupling is related to the gauge-coupling according to Eq. (2.25) via $\hat{g}_s^{\overline{\text{MS}}} = g_s^{\overline{\text{MS}}} \left[1 + \frac{\alpha_s}{3\pi} \right]$. In the actual calculation this correction is taken into account by distinguishing between the Yukawa and the gauge coupling in the virtual contributions and modifying the counterterm of the Yukawa coupling,

$$\delta \hat{g}_s^{\overline{\text{MS}}} = \delta g_s^{\overline{\text{MS}}} + \frac{\alpha_s}{3\pi}. \tag{2.26}$$

2.2.2.2. Infrared divergences and how to deal with them

Besides the UV divergences occurring for very large loop momenta, the virtual contributions $\tilde{\mathcal{V}}$ comprise also IR divergences. Due to the Kinoshita-Lee-Nauenberg (KLN) theorem [64, 65] these cancel against the soft/collinear singularities occurring in the real matrix elements squared, $\mathcal{R}$, for sufficiently inclusive observables. Consequently the full NLO cross section for a process with n final-state particles (respectively $n+1$ for the real contributions),

$$\sigma_{\text{NLO}} = \int \mathrm{d}\Phi_n \left[\mathcal{B}(\Phi_n) + \tilde{\mathcal{V}}(\Phi_n) + \int \mathrm{d}\Phi_{\text{rad}} \mathcal{R}(\Phi_{n+1}) \right], \tag{2.27}$$

with the n particle phase space element $\mathrm{d}\Phi_n$ and the real phase space $\Phi_{n+1} = (\Phi_n, \Phi_{\text{rad}})$, is free of IR divergences. The Born matrix elements squared are denoted here and in the following $\mathcal{B}$.

However, the actual numerical evaluation of Eq. (2.27) is rather involved, as this cancellation takes place between terms with different final-state multiplicities, i.e. the (divergent) integrations for the real and the virtual contributions have to be performed separately. One possibility to overcome this problem, which is especially useful for Monte Carlo event generators, is the subtraction formalism. The basic idea of this approach consists in the introduction of a suitable 'counterterm' $\mathcal{C}(\Phi_{n+1})$, which has the same pointwise singular behaviour as the real contributions, i.e. $\mathcal{C} \to \mathcal{R}$ in the soft and/or collinear limit. Furthermore, $\mathcal{C}$ has to be integrated analytically over the one-particle phase space Φ_{rad}, i.e. the form has to be chosen such that this integration is feasible. This term is then subtracted and added in Eq. (2.27) as follows:

$$\sigma_{\text{NLO}} = \int \mathrm{d}\Phi_n \left[\mathcal{B}(\Phi_n) + \tilde{\mathcal{V}}(\Phi_n) + \int \mathrm{d}\Phi_{\text{rad}} \mathcal{C}(\Phi_{n+1}) + \int \mathrm{d}\Phi_{\text{rad}} \left(\mathcal{R}(\Phi_{n+1}) - \mathcal{C}(\Phi_{n+1}) \right) \right], \tag{2.28}$$

hence the total NLO result is left unaltered by these additional terms. As in case of the UV divergences any meaningful calculation requires a regularization of the IR divergences. Similar to that case the most convenient regularization scheme is Dimensional Regularization, i.e. the loop integrals in $\tilde{\mathcal{V}}$ are continued to $d = 4 - 2\epsilon$ dimensions. Likewise, the analytical integration

of the subtraction term over the one-particle emission phase space, $\int \mathrm{d}\Phi_{\mathrm{rad}}\mathcal{C}(\Phi_{n+1})$, is performed in d dimensions. With this approach the IR divergences can be extracted analytically as poles in $1/\epsilon$ and $1/\epsilon^2$ and cancel the corresponding poles occurring in the virtual contributions, i.e. $\tilde{\mathcal{V}}(\Phi_n)+\int \mathrm{d}\Phi_{\mathrm{rad}}\mathcal{C}(\Phi_{n+1})$ is free of IR divergences and the integration over the n-particle phase space can be performed numerically. The integral $\int \mathrm{d}\Phi_{n+1}\left(\mathcal{R}(\Phi_{n+1})-\mathcal{C}(\Phi_{n+1})\right)$ is integrable by construction, as the IR divergences are cancelled pointwise, hence this term can be evaluated numerically, too.

The explicit construction of the counterterms is always based on the factorization of QCD amplitudes in the soft/collinear limit. However, there are several methods differing in the organization of the actual subtraction. The most widely used approaches are the dipole subtraction formalism introduced by Catani and Seymour (see [66]; [67] extends the results given there to the case of massive dipoles) and the method by Frixione, Kunszt and Signer (FKS) [68]. The automated version of the FKS method implemented in the program package POWHEG-BOX [27] is used in this thesis and is therefore briefly discussed in the following.

The basic idea of the FKS method consists in a partition of the real contributions into a sum of terms such that each summand contains at most one collinear and/or one soft singularity. Following closely the discussion in [26] this can be achieved by introducing a set of so-called $\mathcal{S}$ functions:

$$\mathcal{R} = \sum_i \mathcal{R}_i + \sum_{ij} \mathcal{R}_{ij} \equiv \sum_i \mathcal{R}\mathcal{S}_i + \sum_{ij} \mathcal{R}\mathcal{S}_{ij}\,, \tag{2.29}$$

where the first sum contains all singular regions in which the final-state parton i becomes soft/collinear to an initial-state parton. The second sum comprises all divergent combinations where the parton i is soft/collinear to a final-state parton j. Obviously, the $\mathcal{S}$ functions have to fulfil

$$\sum_i \mathcal{S}_i + \sum_{ij} \mathcal{S}_{ij} = 1\,. \tag{2.30}$$

The $\mathcal{S}$ functions are chosen such that they are non-zero only if the combination of partons can result in a singularity, e.g. $\mathcal{S}_{ij} = 0$ if i is a quark and j corresponds to a gluon, as there is no singularity associated to the case of a quark i becoming soft (in this case $\mathcal{S}_{ji}$ has to be non-zero to select the region where the gluon is soft and/or collinear to the quark). These contributions are explicitly excluded from the sum. Moreover, the $\mathcal{S}$ functions select only one singular region at a time, i.e. their defining properties are the following:

- If parton a is soft, all $\mathcal{S}_i$ and all $\mathcal{S}_{ij}$ for $i \neq a$ are zero, i.e. taking into account Eq. (2.30)

$$\lim_{p_a^0 \to 0} \left(\mathcal{S}_i + \sum_j \mathcal{S}_{ij} \right) = \delta_{ia}. \tag{2.31}$$

- If parton a is collinear to an initial-state parton, i.e. $\vec{p}_a \parallel \vec{k}_{1/2}$, only $\mathcal{S}_a \neq 0$ and

$$\lim_{\vec{p}_a \parallel \vec{k}_{1/2}} (\mathcal{S}_i) = \delta_{ia}. \tag{2.32}$$

- If parton a is collinear to a final-state parton b, only $\mathcal{S}_{ab}$ and $\mathcal{S}_{ba}$ can be non-zero:

$$\lim_{\vec{p}_a \parallel \vec{p}_b} (\mathcal{S}_{ij} + \mathcal{S}_{ji}) = \delta_{ia}\delta_{jb} + \delta_{ja}\delta_{ib}. \tag{2.33}$$

The concrete form of the $\mathcal{S}$ functions is in principle arbitrary, as long as these analytical properties are guaranteed. However, in the context of Monte Carlo event generators smooth functions are preferable; for the functions used in the POWHEG-BOX see [27].

The subtraction terms for the different singular regions are then obtained from the process-independent form of the real contributions in the respective limits. In the soft approximation the real matrix element squared takes the well-known eikonal structure, see [27]:

$$\mathcal{R} = 4\pi\alpha_s\mu_R^{2\epsilon}\left(\sum_{m\neq n}\mathcal{B}_{mn}\frac{k_m\cdot k_n}{(k_m\cdot k)(k_n\cdot k)} - \mathcal{B}\sum_n C_n\frac{k_n^2}{(k_n\cdot k)^2}\right) + \mathcal{R}_{\text{fin}}. \tag{2.34}$$

Here, k corresponds to the momentum of the emitted parton, k_m and k_n are the momenta of coloured particles of the underlying Born process[1] and $\mathcal{R}_{\text{fin}}$ is the finite remainder. The factor C_n is the Casimir invariant of the n^{th} leg and the second term in Eq. (2.34) is non-zero only for massive particles. For a definition of the so-called colour-correlated Born amplitudes squared, B_{mn}, see App. A.2. It is important to note that this structure is independent of the spin of the emitting particle, i.e. it holds for both scalars and fermions (and hence for both squarks and quarks).

These terms have to be integrated analytically over the one-particle phase space of the radiated parton in $d = 4-2\epsilon$ dimensions, as indicated in Eq. (2.28). The finite terms are then added back to the virtual part, yielding $\mathcal{V}(\Phi_n) \equiv \tilde{\mathcal{V}}(\Phi_n) + \int \mathrm{d}\Phi_{\text{rad}}\mathcal{C}(\Phi_{n+1})$. The results for these integrals are given in Appendix A of [27].

The collinear limits of the real amplitudes squared can be obtained in terms of the Altarelli-Parisi splitting kernels [69] and are also listed in the appendix of [27]. Besides the usual Born amplitudes squared, the expressions involving a gluon connected to the underlying Born process require the process-dependent spin-correlated Born amplitudes squared, which are defined in App. A.2.

2.2.3. Parton showers

Quarks and gluons both in the initial and the final state can in principle radiate further gluons and (in case of gluons) split into quark-antiquark pairs. The produced partons can split further, leading to a whole cascade of partons. Formally, these branchings are suppressed by the coupling constant α_s. However, for specific kinematic configurations where a gluon is soft and/or collinear to a quark (respectively a gluon splits into a collinear quark-antiquark pair) this suppression can be overcome due to a logarithmic enhancement. These logarithms have to be resummed to all orders to obtain reliable results. A simulation of these exclusive final states and a resummation of the (leading) logarithmic terms can be achieved by applying a parton shower to the fixed-order result.

The mechanism used for the generation of the subsequent parton splittings still relies on perturbation theory, hence this step of the simulation is only valid above typical hadronic scales Q_{had}, where $\alpha_s \log(Q_{\text{had}}/Q_{\text{proc}}) = \mathcal{O}(1)$ and the perturbative approach breaks down. Here, Q_{proc} is the scale of the hard process. For the description of the effects below these scales (which are typically $\mathcal{O}(1\,\text{GeV})$) one has to rely on models describing the transition from the final set of partons to (usually unstable) hadrons and their subsequent decays, leading to stable hadrons which

[1] The underlying Born process for a real flavour configuration is obtained by replacing the partons i and j chosen by the respective $\mathcal{S}$ function with a parton of the appropriate type and flavour.

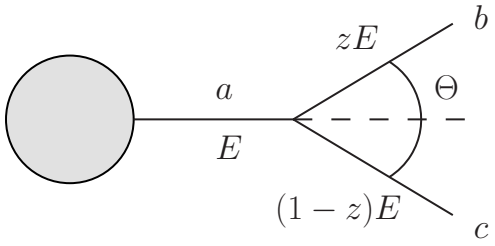

Figure 2.3.: Kinematics for a final-state splitting $a \to bc$. The circle indicates the hard process.

are then observable in the detector. Moreover, a reliable simulation of scattering processes at hadron colliders requires a dedicated simulation of the interactions of the beam remnants (i.e. the remainders of the protons after the 'extraction' of the reacting partons). These remnants contain a partonic substructure, which allows for further partonic interactions, so-called multi-parton interactions (MPI). Furthermore, at high luminosities the effects of pile-up, i.e. the simultaneous scattering of several protons in a single bunch crossing, have to be modelled correctly. In the further course of this thesis only the simulation of the hard process and the combination with the subsequent parton shower will be considered, i.e. hadronization effects, MPI and other effects of soft physics will not be discussed. An introduction to these topics can be found e.g. in [70].

In the remainder of this section some basic ideas of parton showers are sketched. This part is based on the discussions in [70] and [71], where further details can be found.

Collinear branching

Consider as a starting point the splitting of a parton a, which is produced in a hard process, into two partons b and c, as depicted in Fig. 2.3. If the angle Θ between b and c goes to zero the mathematical expression becomes formally divergent (for vanishing masses $m_b = 0$, $m_c = 0$), as the virtuality of parton a in the denominator of the corresponding propagator vanishes,

$$|\mathcal{M}|^2 \propto \frac{1}{(p_b + p_c)^2} = \frac{1}{2p_b \cdot p_c} = \frac{1}{z(1-z)E^2(1-\cos\Theta)} \overset{\Theta\to 0}{\longrightarrow} \infty\,, \tag{2.35}$$

where E is the energy of the splitting parton a and zE corresponds to the energy carried away by b. In the limit of such a collinear final-state splitting $a \to bc$ (corresponding to either $g \to gg$, $q \to gq$ or $g \to q\bar{q}$) the matrix element squared can be factorized for an arbitrary hard process involving $n+1$ external partons as follows:

$$|\mathcal{M}_{n+1}|^2 \approx |\mathcal{M}_n|^2 \frac{\alpha_s}{2\pi}\frac{\mathrm{d}t}{t}\mathrm{d}z P_{ba}(z)\,, \tag{2.36}$$

where the splitting kernels are defined as

$$\begin{aligned}
P_{gg}(z) &= C_A\left[\frac{z}{1-z} + \frac{1-z}{z} + z(1-z)\right]\,,\\
P_{qq}(z) &= C_F\frac{1+z^2}{1-z}\,,\\
P_{gq}(z) &= C_F\frac{1+(1-z)^2}{z}\,,\\
P_{qg}(z) &= T_F\left(z^2 + (1-z)^2\right)
\end{aligned} \tag{2.37}$$

and $\mathcal{M}_n$ corresponds to the matrix element of the underlying n-particle process. The indices indicate the type of the splitting: in P_{ba} the parton a corresponds to the emitting particle and b is the emitted, resolved parton. The kinematic quantities t and z describe the splitting process, the azimuthal angle ϕ has been integrated out here and is not stated explicitly in the following.[2] The concrete form of t and z is to some extent arbitrary and in fact represents one of the most important points wherein the various shower algorithms differ. However, in all formulations the variable t, which is time-like for final-state radiation, has to vanish in the collinear limit. Possible choices for t are

- the virtuality: $t = (p_b + p_c)^2 = 2p_b \cdot p_c \approx E^2 z(1-z)\Theta^2$,
- the transverse momentum: $t = p_{b,T}^2 = p_{c,T}^2 \approx E^2 z^2 (1-z)^2 \Theta^2$,
- the angle: $t = E^2\Theta^2$.

The quantity z corresponds in the collinear limit to the momentum fraction carried away by the parton b after the branching. Note that P_{gg}, P_{qq} and P_{gq} are divergent for $z \to 1$ and/or $z \to 0$. These configurations correspond to the case of a final-state gluon becoming soft. This additional source of divergences will be discussed at the end of this section.

The factorization sketched in Eq. (2.36) is valid as long as the minimal value of t evaluated for all possible combinations of external partons is smallest for the two partons b and c. In order to obtain the 'most singular' behaviour of a process the splitting described in Eq. (2.36) can be iterated. For n splittings (e.g. n radiations of a gluon off a quark), strictly ordered in t, the total contribution is proportional to

$$\alpha_s^n \int \frac{\mathrm{d}t_1}{t_1}\frac{\mathrm{d}t_2}{t_2}\ldots\frac{\mathrm{d}t_n}{t_n}\Theta(Q^2 > t_1 > t_2 > \cdots > t_n > Q_0^2) = \frac{1}{n!}\alpha_s^n \log^n \frac{Q^2}{Q_0^2}\,, \tag{2.38}$$

where the Θ function is one if the argument is true and zero otherwise. The scale of the hard process is denoted Q, and Q_0 is an infrared cutoff below which no further splitting is possible. This cutoff is chosen of the order of typical hadronic scales, where non-perturbative effects take over and the perturbative expansion breaks down. It can be interpreted as a resolution criterion (e.g. a minimal p_T) for which two partons can still be distinguished. This form clearly reflects the logarithmic behaviour and explains why the collinear approximation is commonly denoted 'leading-log' approximation.

In order to describe the development of all subsequent splittings in a shower Monte Carlo program, a probabilistic interpretation of these branchings is required. The probability to create a splitting of the parton a in a range between t and $t + \mathrm{d}t$ for the ordering variable (i.e. the transverse momentum, the angle, ...) is given by

$$\mathrm{d}\mathcal{P}_a = \frac{\alpha_s(t)}{2\pi}\frac{\mathrm{d}t}{t}\int_{Q_0^2/t}^{1-Q_0^2/t}\sum_b P_{ba}(z)\mathrm{d}z, \tag{2.39}$$

where the sum includes all possible splittings. Note that the integration range for the z integration depends on the infrared cutoff Q_0, hence the (potential) soft singularities for $z = 0$ and $z = 1$ are excluded from the integral.

[2] In principle the P_{ba} depend on the azimuthal angle, see e.g. [56]. Upon averaging over ϕ the corresponding terms vanish. This point is ignored here for the sake of simplicity, however, some parton shower algorithms take this angular correlation into account.

Taking into account unitarity, i.e. the fact that either a branching occurs or not, the probability that no branching occurs at $t' \in [t, t+dt]$ is simply $(1 - \mathrm{d}\mathcal{P}_a)$. Extending this interval to a finite one for the evolution from a high scale t_1 to a lower one t_2, the non-branching probability can be expressed in terms of N infinitesimal subintervals:

$$\begin{aligned}\mathcal{P}_{\text{non.branch}} &= \lim_{N\to\infty} \prod_{n=1}^{N} \left(1 - \frac{\alpha_s(t'_n)}{2\pi} \frac{\mathrm{d}t'}{t'_n} \int_{Q_0^2/t'_n}^{1-Q_0^2/t'_n} \sum_b P_{ba}(z)\mathrm{d}z\right) \\ &= \exp\left[-\int_{t_2}^{t_1} \frac{\mathrm{d}t}{t} \frac{\alpha_s(t)}{2\pi} \int_{Q_0^2/t}^{1-Q_0^2/t} \sum_b P_{ba}(z)\mathrm{d}z\right] \\ &\equiv \Delta_a(t_1, t_2).\end{aligned} \tag{2.40}$$

The quantity $\Delta_a(t_1, t_2)$ is known as Sudakov form factor. It is by construction an all-order quantity which resums the leading virtual contributions. The Sudakov form factor is the main building block for the shower evolution.

Applying Eqs. (2.39) and (2.40) the probability to observe the first resolvable splitting of a parton a in the infinitesimal interval $\mathrm{d}t$, starting from a scale $t_1 > t$ without any splitting in the range $t_1 \to t$, reads

$$\mathrm{d}\mathcal{P}_{\text{branch}} = \Delta_a(t_1, t) \frac{\alpha_s(t)}{2\pi} \frac{\mathrm{d}t}{t} \int_{Q_0^2/t}^{1-Q_0^2/t} \sum_b P_{ba}(z)\mathrm{d}z = \mathrm{d}\Delta_a(t_1, t)\,. \tag{2.41}$$

With these results the implementation of a final-state shower in a Monte Carlo program takes the following structure:

1. First a configuration of the hard process according to the corresponding partonic cross section is generated at a scale Q, which is typical for the respective process.
2. For each parton a in the final state the collinear splittings are set up as follows, starting from $t_1 = Q^2$:
   - A random number $r \in [0, 1]$ is chosen.
   - With this random number $\Delta_a(t_1 = Q^2, t) = r$ is solved for t. If the solution fulfils $t > Q_0^2$, i.e. t is above the infrared cutoff Q_0^2, a resolvable emission occurs, otherwise the shower is terminated.
   - If a resolvable emission occurs, the splitting $a \to bc$ and the momentum fraction z are generated according to $P_{ba}(z)$ (allowing for all possible splittings). Furthermore, an azimuthal angle $\phi \in [0, 2\pi]$ is chosen and the energies and momenta of the resulting partons b and c are determined from t, z and ϕ.
   - For the resulting partons b and c this procedure is repeated, using $t_1 = t$ as starting scale for the further branchings.

While these points describe in principle a final-state shower for the collinear splittings, several points have been left out in the discussion so far:

- The partons produced in the hard process are on shell, i.e. $p_a^2 = 0$. However, generating a resolvable splitting $a \to bc$ destroys this relation. In order to restore it the energies and momenta of the produced particles have to be reshuffled in a suitable manner. The concrete procedure is arbitrary, as long as the leading-log structure of the result is preserved, and is another point where the different parton shower algorithms differ.

- In hadronic scattering processes partons do not only occur in the final, but also in the initial state. The approach for an initial-state shower is in principle identical to the final-state case, however, an efficient implementation is much more involved. In this case the situation is kind of 'inverted' to the final-state shower, as the parton connected to the hard process is not the origin, but the result of (in general) many branchings. The virtuality of this parton is space-like in this case. Using the same approach as for the final-state shower would amount to set up an initial-state shower by starting with a parton extracted from the colliding hadron and generating subsequent splittings as sketched above. The branchings could be generated using the same expression for the Sudakov as before, starting from a scale $-Q_0$ and evolving to scales $-Q' < -Q_0$ until the parton entering the hard process at the scale $-Q$ is produced. However, generating these splittings starting from the original parton in such a forward evolution would be very inefficient, as most of the generated configurations would not result in the required one with a specific parton entering the hard process at a given scale. To circumvent this problem the evolution can be performed backwards, starting from the hard process at the lower scale $-Q$ and evolving towards the higher scale $-Q_0$. In this approach the form factors involve ratios of PDFs at different scales, see [56], rendering the implementation of such a backward initial-state shower more complicated.
- In the discussion so far the soft divergences occurring in gluon radiation have been ignored. However, these divergences are equally important as the collinear ones and might even occur at the same time, leading to a double-logarithmic singularity. Similar to the case of collinear divergences the structures can be factorized from the hard process, albeit for the soft divergences this factorization is only possible at the level of individual amplitudes, i.e. before forming the matrix element squared. A priori this leads to interference effects between gluons emitted from different parts of an event. Therefore, a sequential construction of the exclusive final states, treating the gluon emissions independently as described above, seems to be doomed to fail from the very beginning. However, a phenomenon known as colour coherence reconciles the picture of independent parton evolution and soft gluon radiation. In essence, it turns out that the interference effects are to a large extent destructive if the emission angle of the softest gluon is larger than all angular separations between partons resulting from further splittings, see [56] for a detailed discussion. In other words, a soft gluon emitted at an angle Θ_s cannot resolve the individual partons emitted in a cone with $\Theta < \Theta_s$, it 'sees' only the colour charge of all partons combined and is not affected by subsequent splittings at smaller angles. This effect allows again for an independent evolution of the different splittings if the branchings are ordered in the splitting angles (see [72, 73]). As an immediate consequence this implies that the first emission, i.e. the one with the largest splitting angle, is not the hardest one.

Adding further radiation to the initial- and final-state partons of an arbitrary hard process with a parton shower as described above improves the predictions for observables describing the soft/collinear region in phase space. The emission of harder partons, however, is not simulated correctly in this approach, as the probability for such a splitting, which is proportional to the splitting kernels in Eq. (2.37), is rather small. A correct treatment of this type of radiation can be achieved by combining fixed-order calculations of different parton multiplicities with a parton shower. Performing an event generation for these two steps is highly non-trivial, as a naïve combination would lead to a double counting of contributions which can be created by both the fixed-order matrix elements and the parton shower. There exist several prescriptions for the so-called 'merging' of these two simulation steps (see e.g. [70] for an overview), however

this approach will not be used in this thesis and is therefore not further discussed at this point. A second way to improve the predictions for a specific process consists in taking into account higher-order corrections in the calculation of the hard process. These reduce the dependence on the unphysical renormalization and factorization scales introduced in the evaluation of virtual contributions and the folding with the PDFs, respectively, and provide a more accurate description for inclusive quantities. Again, the combination of a process calculated at NLO and a parton shower requires some care to avoid the double counting of contributions occurring in the matrix elements and the shower. This so-called 'matching' procedure is discussed in the next section.

2.2.4. Combining NLO and parton showers - the Powheg method

The double counting problem

In order to illustrate the essence of the double counting problem consider an infrared safe observable $\mathcal{O}_i \equiv \mathcal{O}(\Phi_i)$, i.e. a quantity with i resolvable partons in the final state, which is insensitive to both the addition of any number of arbitrarily soft particles and the splitting of any external particle into two collinear ones. Starting from the hard process with n external particles, calculated at LO, the expectation value of this observable after one branching in the shower is given by

$$\langle \mathcal{O} \rangle_{\mathrm{LO}}^{\mathrm{PS}} = \int \mathrm{d}\Phi_n \mathcal{B}(\Phi_n) \Big[\overbrace{\mathcal{O}_n \Delta(t_0)}^{\text{no emission}} + \overbrace{\int\limits_{t_{\max} > t > t_0} \mathrm{d}\Phi_{\mathrm{rad}} \mathcal{O}_{n+1} \Delta(t) \frac{\alpha_s(t)}{2\pi} K(z,t)}^{\text{one emission with } t_{\max} > t > t_0} \Big], \tag{2.42}$$

with a compact notation for the Sudakov form factor, suppressing the starting scale $t_{\max}$ and making the sum over all possible splittings implicit, i.e.

$$\begin{aligned} \Delta(t) &= \exp\Big[- \int \mathrm{d}\Phi'_{\mathrm{rad}} \frac{\alpha_s(t')}{2\pi} K(z',t') \Theta(t'-t) \Big] \\ &= 1 - \int \mathrm{d}\Phi'_{\mathrm{rad}} \frac{\alpha_s(t')}{2\pi} K(z',t') \Theta(t'-t) + \mathcal{O}(\alpha_s^2). \end{aligned} \tag{2.43}$$

The other parameters are identical to those in Eq. (2.40), notably t is again the ordering variable of the shower, t_0 is the infrared cutoff, i.e. the scale where the shower stops and hadronization effects set in, and the one-particle radiation phase space is defined as $\mathrm{d}\Phi_{\mathrm{rad}} = \mathrm{d}t\, \mathrm{d}z\, \frac{\mathrm{d}\phi}{2\pi}$. The splitting kernels introduced in Eq. (2.36) in order to describe the collinear splittings have been replaced by the more general form $K(z,t)$ (e.g. in modern dipole showers as [30, 31] these kernels can be constructed from Catani-Seymour dipoles). Taking a closer look at the two terms in Eq. (2.42) it is obvious that the first term corresponds to the case of no additional emission between the starting scale and the IR cutoff, while the second term describes at least one emission. A realistic shower description would iterate from here, adding further splittings to the resulting partons after this first splitting. However, these terms are formally beyond NLO and not relevant at this point.

Inserting the expanded expression for the Sudakov form factor given in Eq. (2.43) into Eq. (2.42) yields terms which are formally of NLO:

$$\langle \mathcal{O} \rangle_{\mathrm{LO}}^{\mathrm{PS}} = \int \mathrm{d}\Phi_n \mathcal{B}(\Phi_n) \Bigg\{ \mathcal{O}_n + \int\limits_{t_{\max} > t > t_0} \mathrm{d}\Phi_{\mathrm{rad}} \left[\mathcal{O}_{n+1} \frac{\alpha_s(t)}{2\pi} K(z,t) - \mathcal{O}_n \frac{\alpha_s(t)}{2\pi} K(z,t) \right] \Bigg\} + \mathcal{O}(\alpha_s^2). \tag{2.44}$$

The same observable $\mathcal{O}$ has in a pure NLO calculation, i.e. before adding any further branchings, the expectation value

$$\langle\mathcal{O}\rangle_{\mathrm{NLO}} = \int \mathrm{d}\Phi_n \Big[\mathcal{O}_n \left[\mathcal{B}(\Phi_n) + \mathcal{V}(\Phi_n)\right] + \int \left[\mathcal{O}_{n+1}\mathcal{R}(\Phi_{n+1}) - \mathcal{C}(\Phi_{n+1})\mathcal{O}_n\right] \mathrm{d}\Phi_{\mathrm{rad}}\Big] \tag{2.45}$$

with the virtual contributions $\mathcal{V}$ (including both the correctly renormalized interference terms of the one-loop with the Born contributions and the terms added in the subtraction method, $\int \mathcal{C}(\Phi_{n+1})\mathcal{O}_n d\Phi_{\mathrm{rad}}$, see the discussion in Sec. 2.2.2), the subtraction counterterms $\mathcal{C}$ and the real amplitudes squared $\mathcal{R}$.

Applying a parton shower directly to Eq. (2.45) would lead to a double counting of the terms $\propto \alpha_s$ in Eq. (2.44). In order to perform a consistent matching of the NLO result and a parton shower the double counted terms have to be subtracted, yielding

$$\begin{aligned}\langle\mathcal{O}\rangle^{\mathrm{sub}}_{\mathrm{NLO}} = \int \mathrm{d}\Phi_n \Big\{\mathcal{O}_n \left[\mathcal{B} + \mathcal{V}\right] + \int \mathrm{d}\Phi_{\mathrm{rad}} \Big[\left(\frac{\alpha_s(t)}{2\pi}\mathcal{B}K(z,t) - \mathcal{C}\right)\mathcal{O}_n \\ + \left(\mathcal{R} - \frac{\alpha_s(t)}{2\pi}\mathcal{B}K(z,t)\right)\mathcal{O}_{n+1}\Big]\Big\}.\end{aligned} \tag{2.46}$$

Acting on this expression with a parton shower preserves the NLO accuracy for inclusive observables by construction, up to corrections of $\mathcal{O}(\alpha_s^2)$. The equation simplifies if one of the brackets involving the subtracted terms vanishes. One possibility to achieve such a simplification amounts to generating the first emission with

$$\frac{\mathcal{R}}{\mathcal{B}} = \frac{\alpha_s(t)}{2\pi}K(z,t) \tag{2.47}$$

instead of the shower specific splitting kernel. This is the key idea of the POWHEG method described in the next paragraph.

The Powheg method

The POWHEG method (POsitive Weight Hardest Emission Generator) was first proposed in [25] and is extensively discussed in [26].

In essence this approach aims at the generation of the first emission using the ratio of the real matrix element squared and the Born expression as splitting kernel, see Eq. (2.47). The ordering variable t in this splitting is the transverse momentum of the radiated parton with respect to the emitting particle. All subsequent radiation is then generated with a usual parton shower program, i.e. this approach can in principle be supplemented by any shower (in contrast to other matching schemes like MC@NLO [74], which need to be adapted to the respective parton shower program). However, using p_T as splitting criterion enforces all subsequent radiation steps to be performed at smaller values of the transverse momentum, i.e. the first emission created according to the POWHEG prescription discussed below with transverse momentum k_T has to be the hardest one in the whole event. In principle this is no problem, as almost all parton shower programs include the possibility to simply veto subsequent splittings with larger p_T. However, for an angular-ordered shower this is not sufficient, as in this case the first emission is not necessarily the one with the largest p_T, i.e. in the matched sample emissions with larger angles, but smaller p_T are absent. To compensate for these missing emissions a so-called vetoed truncated shower has to be introduced, see [25], which depends again on the respective shower algorithm.

The actual generation of the first radiation in the POWHEG approach can be performed in close analogy to the first step of a usual parton shower, sketched in Eq. (2.42). To this end the Born amplitude squared in Eq. (2.42) has to be replaced by the NLO contributions and Eq. (2.47) has to be used for the splitting. Performing these modifications leads to the POWHEG master formula:

$$\mathrm{d}\sigma_{PWG} = \overline{\mathcal{B}}(\Phi_n)\,\mathrm{d}\Phi_n \left[\Delta(\Phi_n, p_T^{\min}) + \Delta(\Phi_n, k_T)\frac{\mathcal{R}(\Phi_n, \Phi_{\mathrm{rad}})}{\mathcal{B}(\Phi_n)}\theta(k_T - p_T^{\min})\mathrm{d}\Phi_{\mathrm{rad}}\right], \tag{2.48}$$

where the scale $p_T^{\min}$ corresponds again to the IR cutoff which determines the lower limit for the k_T of the radiated parton. The two main ingredients in Eq. (2.48) are the $\overline{\mathcal{B}}$ function, which ensures the NLO accuracy of the method and comprises the typical elements of a NLO calculation,

$$\overline{\mathcal{B}}(\Phi_n) = \Big[\mathcal{B}(\Phi_n) + \mathcal{V}(\Phi_n) + \int \left(\mathcal{R}(\Phi_{n+1}) - \mathcal{C}(\Phi_{n+1})\right)\mathrm{d}\Phi_{\mathrm{rad}}\Big], \tag{2.49}$$

and the POWHEG Sudakov form factor

$$\Delta(\Phi_n, p_T) = \exp\left[-\int \mathrm{d}\Phi'_{\mathrm{rad}}\frac{\mathcal{R}(\Phi_n, \Phi'_{\mathrm{rad}})}{\mathcal{B}(\Phi_n)}\theta(k_T(\Phi_n, \Phi'_{\mathrm{rad}}) - p_T)\right]. \tag{2.50}$$

The phase space point Φ_n characterizes the underlying Born process, the phase space for the real emission is again constructed from Φ_n and the radiation variables Φ_{rad}, thus $\Phi_{n+1} = (\Phi_n, \Phi_{\mathrm{rad}})$.

Before discussing the fundamental properties of the POWHEG master formula further it should be noted that Eq. (2.48) is not the most general form, see [25] and [27]. In fact, the real amplitude squared can be split into a part comprising the IR singularities, $\mathcal{R}_s$ with $\mathcal{R}_s \to \mathcal{R}$ in the soft/collinear limit, and a hard part $\mathcal{R}_h$,

$$\mathcal{R} = \mathcal{R}_s + \mathcal{R}_h\,. \tag{2.51}$$

The generation of the first event can then be performed using only the singular part $\mathcal{R}_s$, whereas events involving hard radiation are generated with usual Monte Carlo methods according to $\mathcal{R}_h$. The POWHEG master formula in Eq. (2.48) takes in this case the more complicated form

$$\begin{aligned}\mathrm{d}\sigma_{PWG} = {} & \overline{\mathcal{B}}_s(\Phi_n)\,\mathrm{d}\Phi_n \left[\Delta_s(\Phi_n, p_T^{\min}) + \Delta_s(\Phi_n, k_T)\frac{\mathcal{R}_s(\Phi_n, \Phi_{\mathrm{rad}})}{\mathcal{B}(\Phi_n)}\theta(k_T - p_T^{\min})\mathrm{d}\Phi_{\mathrm{rad}}\right] \\ & + (\mathcal{R} - \mathcal{R}_s)\mathrm{d}\Phi_{n+1},\end{aligned} \tag{2.52}$$

where the real amplitude squared in the $\overline{\mathcal{B}}$ function and the Sudakov form factor is also replaced by $\mathcal{R}_s$, i.e.

$$\overline{\mathcal{B}}_s(\Phi_n) = \Big[\mathcal{B}(\Phi_n) + \mathcal{V}(\Phi_n) + \int \left(\mathcal{R}_s(\Phi_{n+1}) - \mathcal{C}(\Phi_{n+1})\right)\mathrm{d}\Phi_{\mathrm{rad}}\Big] \tag{2.53}$$

and

$$\Delta_s(\Phi_n, p_T) = \exp\left[-\int \mathrm{d}\Phi'_{\mathrm{rad}}\frac{\mathcal{R}_s(\Phi_n, \Phi'_{\mathrm{rad}})}{\mathcal{B}(\Phi_n)}\theta(k_T(\Phi_n, \Phi'_{\mathrm{rad}}) - p_T)\right]. \tag{2.54}$$

Choosing $\mathcal{R} = \mathcal{R}_s$ obviously simplifies the expression, but in some cases a different choice is more appropriate, as will be discussed in Ch. 4. Moreover, as shown e.g. in [75], it is possible to relate this generalized version of the POWHEG method to the MC@NLO approach by choosing $\mathcal{R}_s$ according to the splitting kernels $K(z,t)$ of the respective shower program. If moreover the

subtraction terms $\mathcal{C}$ in Eq. (2.46) can be chosen identical to the splitting kernels the whole expression simplifies tremendously. However, the MC@NLO method has some immediate technical shortcomings: first of all it has to be adapted to every parton shower algorithm individually. Furthermore, the terms $\mathcal{R} - \mathcal{R}_s$ are only non-singular if the splitting kernels reproduce all singularities of $\mathcal{R}$ exactly. And finally, events generated according to the thus obtained modified version of Eq.(2.52) can in general have negative weights.

In the following the POWHEG approach is used to match the NLO corrections calculated in Ch. 3 to parton showers. Some very basic checks for the correctness of this matching consist in testing the validity of several fundamental properties of the POWHEG master formula:

- The generated events have positive weights, as these are determined by $\overline{\mathcal{B}}$, which is (at least if the perturbative expansion holds) positive. However, as will be discussed in Sec. 4.3, this is a priori not necessarily true for every individual point in phase space, especially not if the refined version of the POWHEG master formula with $\mathcal{R} \neq \mathcal{R}_s$ is used.
- The NLO accuracy of inclusive observables is preserved by construction.
- For hard emissions the NLO accuracy[3] is preserved, too. This statement can be directly verified by considering Eq. (2.52) in the limit $k_T \gg 1$:

$$\begin{aligned} \mathrm{d}\sigma_{PWG} \to \left(\frac{\overline{\mathcal{B}}_s}{\mathcal{B}} \mathcal{R}_s + (\mathcal{R} - \mathcal{R}_s) \right) \mathrm{d}\Phi_{n+1} &= \left[(1 + \mathcal{O}(\alpha_s)) \mathcal{R}_s + (\mathcal{R} - \mathcal{R}_s) \right] \mathrm{d}\Phi_{n+1} \\ &= \mathcal{R} \mathrm{d}\Phi_{n+1} + \mathcal{O}(\alpha_s^2), \end{aligned} \tag{2.55}$$

  as $\Delta_s(\Phi_n, p_T^{\min}) \to 0$ and $\Delta_s(\Phi_n, k_T) \to 1$.
- The leading logarithmic accuracy of the parton shower is not spoiled by the POWHEG step, as in the limit $k_T \to 0$

$$\frac{\mathcal{R}_s(\Phi_n, \Phi_{\mathrm{rad}})}{\mathcal{B}(\Phi_n)} \approx \frac{\alpha_s}{2\pi} \frac{1}{t} P(z) \mathrm{d}\Phi_{\mathrm{rad}}. \tag{2.56}$$

The Powheg-Box

Several steps of the POWHEG method described in the previous paragraph are process-independent and can thus be coded once and for all. The public program package POWHEG-BOX [27] provides such a framework, which allows for the implementation of arbitrary processes. In detail this FORTRAN program contains an automated version of the FKS method described in Sec. 2.2.2 and generates the real phase space Φ_{n+1} accordingly, starting from Born phase space points Φ_n. Moreover, it performs the generation of the hardest emission according to the POWHEG master formula, Eq. (2.52), fully automatically and writes the obtained events according to the Les Houches Event (LHE) standard [76] into files, which in turn serve as input for an arbitrary parton shower program. As a by-product the evaluation of arbitrary NLO distributions is possible, since the event generation according to Eq. (2.52) requires a Monte Carlo integration of the $\overline{\mathcal{B}}$ function, which corresponds essentially to the usual NLO expression. This feature is used in Ch. 3.1 to obtain NLO results for squark antisquark production. In the most recent version (POWHEG-BOXV2) it is also possible to include NLO corrections to the decays of resonant particles in the narrow-width approximation, a feature which is used in Ch. 3.3 to evaluate the decays of the produced (anti)squarks at NLO.

[3] This is in fact only a LO prediction for the hard process plus one additional final-state parton, which is incorporated in $\mathcal{R}$.

The process-specific ingredients, which have to be provided by the user in order to implement a process into the POWHEG-BOX, are:

- **Flavour structures:** The user has to define all possible flavour structures contributing to the Born and the real processes. These are defined in terms of the usual PDG Monte Carlo particle numbering scheme [77], e.g. for $ud \to \tilde{u}_L \tilde{d}_L$ the Born structure reads $(2, 1, 1000002, 1000001)$.
- **Phase space:** The phase space for the Born process has to be implemented.
- **Matrix elements squared:** Besides the Born, virtual and real matrix elements squared the POWHEG-BOX requires the colour-correlated and the spin-correlated Born amplitudes squared as process-specific building blocks for the implemented FKS method.
- **Colour flows:** For the output to an LHE file the information regarding the colour flow in each event is required. To that end the user has to provide the colour information for the Born process, which is used in turn by the POWHEG-BOX to assign a colour flow to events both with and without additional emission.

The POWHEG-BOX already includes a large number of processes, however, so far almost exclusively SM processes have been implemented. The only implemented BSM processes are slepton pair production [78] and tH^- production [79]. In both cases the BSM particles are not strongly interacting and therefore do not affect the generation of additional QCD radiation. Hence before implementing the squark production processes considered in this thesis it has been necessary to make sure that all parts of the code are suitable for the consideration of this type of processes. To this end, the following aspects of the POWHEG-BOX had to be considered:

- As already mentioned the POWHEG-BOX includes an automated version of the FKS method, which could be affected by the presence of massive coloured BSM particles. The implemented algorithm is constructed such that in the initialization phase of the program all singular regions of the contributing flavour structures are identified by looping over pairs of massless partons. The presence of massive squarks in the final state does not spoil this procedure.

  The subtraction terms used in the FKS method consist of the eikonal factors for the soft singularities, see Eq. (2.34), and the factorization formulae for the collinear singularities. In case of the production of massive particles collinear singularities occur solely in initial-state radiation, hence it has not been necessary to adapt these terms. Soft singularities, however, occur also in the radiation of gluons off the final-state squarks, but as the eikonal factors do not depend on the spin of the emitting particle only minor changes to the code have been necessary. Correspondingly, the implemented formulae for the soft-virtual cross section have had to be adapted.

- The generation of the hardest emission according to the POWHEG formalism as implemented in the code is not affected by the presence of massive coloured particles in the final state.

- The POWHEG-BOX provides several additional routines for the calculation of α_s, calling PDF libraries, writing out LHE files, performing simple analyses etc. Besides some minor changes in the output routines for the LHE files only the implemented formula for α_s could be problematic. In the POWHEG-BOX the $\overline{\text{MS}}$ scheme with five active flavours is used. However, as all heavy (s)particles are decoupled from the running of α_s in the

calculation of the virtual corrections (see Sec. 2.2.2), no changes have been necessary at this point.

The thus modified version of the POWHEG-BOX serves in the following as basis for the implementation of the NLO corrections to squark pair and squark antisquark production and the subsequent decays $\tilde{q} \to q\tilde{\chi}_1^0$. The calculation and numerical evaluation of the fixed-order NLO processes is discussed in the next chapter, while some details on the actual implementation of these processes in the POWHEG-BOX and the actual matching to parton showers follow in Ch. 4.

CHAPTER 3

SQUARK PRODUCTION AND DECAY AT NLO

This chapter focuses on the fixed order results for the production of squark pairs, both squark squark and squark antisquark, at hadron colliders and their decays into the lightest neutralino and a quark. Both the production and the decay part are calculated at NLO in SUSY-QCD for squarks of the first two generations. The calculation is performed for a completely general SUSY mass spectrum and allows for predictions of arbitrary distributions. Section 3.1 mainly contains the discussion of the production of a squark antisquark pair. The approach for squark pair production is in many respects very similar and has already been discussed extensively in [28]. In the context of this thesis, an independent calculation for this process has been performed and mutually cross checked, sharing only the virtual amplitudes with [28]. However, the results presented there do not include the decays of the squarks and are only valid for mass spectra with $m_{\tilde{q}} > m_{\tilde{g}}$. These missing ingredients are provided in the following chapter, too.

Section 3.2 deals with the NLO corrections to the decay $\tilde{q} \to \tilde{\chi}_1^0 q$ and the total squark widths. The results for production and decay are combined and discussed in Sec. 3.3.

3.1. Squark antisquark production at NLO

In this section the NLO predictions to squark antisquark production are discussed in detail. After presenting the analytical results for the LO process, a description of the calculation of the virtual and real contributions follows. In this context a detailed discussion of real contributions with intermediate on-shell gluinos and the different methods how to deal with them is given, a point which is also relevant for squark pair production with $m_{\tilde{q}} < m_{\tilde{g}}$. Afterwards, some comments on the numerous checks performed in order to ensure the correctness of the calculation are made. The last part discusses numerical results for total and differential cross sections, both at LO and NLO, focusing on the question to which extent a fully differential description without any assumptions on the mass spectrum might alter the predictions for phenomenological studies of squark production at the LHC compared to the most up to date and publicly available tools.

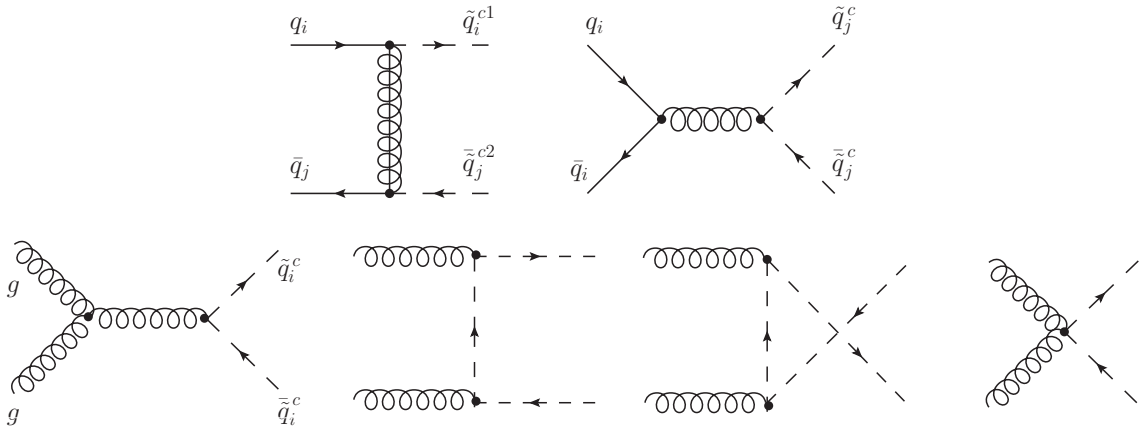

Figure 3.1.: Feynman diagrams contributing to squark antisquark production at LO.

3.1.1. The LO contributions

The amplitudes for the hadronic production of a squark antisquark pair depend on the flavour and chirality of the produced squarks. For the production of squarks of the first two generations this leads to 64 possible combinations in the final state. This number reduces if invariance under charge conjugation is taken into account, i.e. exploiting the fact that the results for $\tilde{q}_1\bar{\tilde{q}}_2$ production are identical to those for $\tilde{q}_2\bar{\tilde{q}}_1$ leaves 36 independent channels.

For these different subchannels there are in principle two possible production modes,

$$\begin{aligned} q_i\,\bar{q}_j &\to \tilde{q}_k^{c1}\,\bar{\tilde{q}}_l^{c2}\,, \\ g\,g &\to \tilde{q}_i^{c}\,\bar{\tilde{q}}_i^{c}\,, \end{aligned} \tag{3.1}$$

where the lower indices refer to the flavour of the respective (s)quark and the upper indices correspond to the chirality of the squarks. The Feynman diagrams for these processes are depicted in Fig. 3.1. Note that due to the flavour and chirality conserving structure of the occurring vertices the gg-channel and the s-channel graph for the $q\bar{q}$-channel only contribute to the production of squarks with identical flavour and chirality.

In the calculation of the matrix elements squared the masses of the initial-state quarks are set to zero and the final-state squarks are assumed to be produced on shell. Moreover, in the following considerations only the strong production modes are taken into account.

The matrix elements squared can be expressed in terms of the usual Mandelstam variables

$$\begin{aligned} s &= (p_q + p_{\bar{q}})^2 = (p_{\tilde{q}} + p_{\bar{\tilde{q}}})^2\,, \\ t &= (p_q - p_{\tilde{q}})^2 = (p_{\bar{q}} - p_{\bar{\tilde{q}}})^2\,, \\ u &= (p_q - p_{\bar{\tilde{q}}})^2 = (p_{\bar{q}} - p_{\tilde{q}})^2\,. \end{aligned} \tag{3.2}$$

The corresponding quantities for the gg-channel are obtained by replacing p_q and $p_{\bar{q}}$ with the two gluon momenta.

$q\bar{q}$-channels

The matrix elements for the $q\bar{q}$-channels contribute to different combinations of flavour and chirality. After summing over the final-state colours and averaging over the spin and the colour of the initial-state quarks one obtains the following results:

- **Different chirality ($c1 \neq c2$):** In this case only the t-channel graph contributes, thus

$$|\mathcal{M}_{q\bar{q}}|^2 = \frac{g_s^4}{4 \cdot 9} F_1 \frac{4 m_{\tilde{g}}^2 s}{\left(t - m_{\tilde{g}}^2\right)^2}, \tag{3.3}$$

  where F_1 is defined in Eq. (3.7) below.

- **Same chirality ($c1 = c2$), different flavour ($k \neq l$)**: Again, only the t-channel graph is relevant:

$$|\mathcal{M}_{q\bar{q}}|^2 = \frac{g_s^4}{4 \cdot 9} F_1 \frac{4\left(tu - m_{\tilde{q}}^2 m_{\bar{\tilde{q}}}^2\right)}{\left(t - m_{\tilde{g}}^2\right)^2}. \tag{3.4}$$

- **Same chirality ($c1 = c2$) and same flavour($k = l$)**: In this case either both graphs are non-zero (if the flavour of the initial-state quarks is identical to the squark flavour, i.e. $i = j = k = l$), resulting in

$$|\mathcal{M}_{q\bar{q}}|^2 = \frac{g_s^4}{4 \cdot 9} 8\left(tu - m_{\tilde{q}}^2 m_{\bar{\tilde{q}}}^2\right) \left[\frac{F_1}{s^2} + \frac{F_1}{2\left(t - m_{\tilde{g}}^2\right)^2} + \frac{F_2}{s\left(t - m_{\tilde{g}}^2\right)}\right], \tag{3.5}$$

  or only the s-channel graph contributes (for $i = j \neq k = l$), yielding

$$|\mathcal{M}_{q\bar{q}}|^2 = \frac{g_s^4}{4 \cdot 9} F_1 \frac{8\left(tu - m_{\tilde{q}}^2 m_{\bar{\tilde{q}}}^2\right)}{s^2}. \tag{3.6}$$

The colour factors F_i are given by

$$\begin{aligned} F_1 &= \mathrm{Tr}\left[T^a T^b\right]^2 = 8 T_F^2 = 2, \\ F_2 &= \mathrm{Tr}\left[T^a T^b T^a T^b\right] = -\frac{2}{3}, \end{aligned} \tag{3.7}$$

where the T^a correspond to the generators of $SU(3)_C$, the summation over repeated indices of the adjoint representation is implicit, i.e. a ranges from 1 through 8, and the normalization $\mathrm{Tr}\left[T^a T^b\right] = T_F \delta_{ab} = \frac{1}{2} \delta_{ab}$ is used.

gg-channels

The gg-channels contribute only to same-flavour and same-chirality squark antisquark production. The internal gluon propagator is evaluated in Feynman gauge, for the external gluons only the (physical) transverse degrees of freedom are taken into account. To exclude the unphysical contributions of longitudinally polarized gluons in the calculation a simple calculational method known as 'ghost subtraction' can be applied, for a discussion see [17] and App. A.1.

After summing/averaging over colours/spins of the external particles the result for the matrix elements squared reads

$$
\begin{aligned}
|\mathcal{M}_{gg}|^2 = \frac{g_s^4}{4\cdot 64}\Bigg[& F_3 \frac{2(u-t)^2 + 4s\left(4m_{\tilde{q}}^2 - s\right)}{s^2} + F_4 \frac{4\left(t+m_{\tilde{q}}^2\right)^2}{\left(t-m_{\tilde{q}}^2\right)^2} + F_5 \frac{4\left(u+m_{\tilde{q}}^2\right)^2}{\left(u-m_{\tilde{q}}^2\right)^2} \\
& + 4F_6 + 2\Bigg(-F_7 \frac{\left(4m_{\tilde{q}}^4 + 2m_{\tilde{q}}^2(t-u) - 5/2\, t^2 - tu - u^2/2\right)}{s\left(t-m_{\tilde{q}}^2\right)} \\
& - F_8 \frac{\left(4m_{\tilde{q}}^4 + 2m_{\tilde{q}}^2(u-t) - 5/2\, u^2 - tu - t^2/2\right)}{s\left(u-m_{\tilde{q}}^2\right)} \\
& + F_9 \frac{\left(s-4m_{\tilde{q}}^2\right)^2}{\left(t-m_{\tilde{q}}^2\right)\left(u-m_{\tilde{q}}^2\right)} - F_{10} \frac{4m_{\tilde{q}}^2 + 4t - s}{2\left(t-m_{\tilde{q}}^2\right)} - F_{11} \frac{4m_{\tilde{q}}^2 + 4u - s}{2\left(u-m_{\tilde{q}}^2\right)} \Bigg)\Bigg]
\end{aligned}
\tag{3.8}
$$

with the colour-factors

$$
\begin{aligned}
F_3 &= T_F f_{abc} f_{abc} = 12\,, \\
F_4 &= F_5 = \mathrm{Tr}\left[T^a\, T^b\, T^b\, T^a\right] = \frac{16}{3} \\
F_6 &= 2\mathrm{Tr}\left[T^a\, T^b\, T^a\, T^b\right] + 2\mathrm{Tr}\left[T^a\, T^b\, T^b\, T^a\right] = \frac{28}{3}\,, \\
F_7 &= F_8 = -i f_{abc} \mathrm{Tr}\left[T^c\, T^b\, T^a\right] = -6\,, \\
F_9 &= F_2 = -\frac{2}{3}\,, \\
F_{10} &= F_{11} = \frac{F_6}{2} = \frac{14}{3}\,,
\end{aligned}
\tag{3.9}
$$

where f_{abc} denote the structure constants of $SU(3)$.

To obtain the (differential) hadronic cross section the matrix elements squared have to be folded with the PDFs and (partially) integrated over the phase space as explained in Sec. 2.2.1.

3.1.2. The virtual contributions

The calculation of the virtual contributions has been performed using the MATHEMATICA packages FEYNARTS 3.8 [80, 81] and FORMCALC 6.1 [82]. The applied renormalization scheme has already been discussed extensively in Sec. 2.2.2. The package FEYNARTS generates the Born and one-loop amplitudes contributing to a specific process. The Feynman rules implemented in the MSSM model file of the version used here do not include the SUSY-QCD counterterms. These have been added according to the renormalization prescriptions outlined in Sec. 2.2.2. The obtained amplitudes are then calculated with FORMCALC[4], which creates FORTRAN subroutines for the numerical evaluation of the matrix elements.

In order to produce an efficient code the number of explicitly generated processes has been minimized as much as possible, i.e. only the NLO contributions for $u\bar{u} \to \tilde{u}_L \bar{\tilde{u}}_L$, $u\bar{u} \to \tilde{u}_L \bar{\tilde{u}}_R$,

[4]Evaluating the quark counterterm δZ_q as defined in Eq. (2.19) with FORMCALC leads to an incorrect additional finite term, which has to be removed manually.

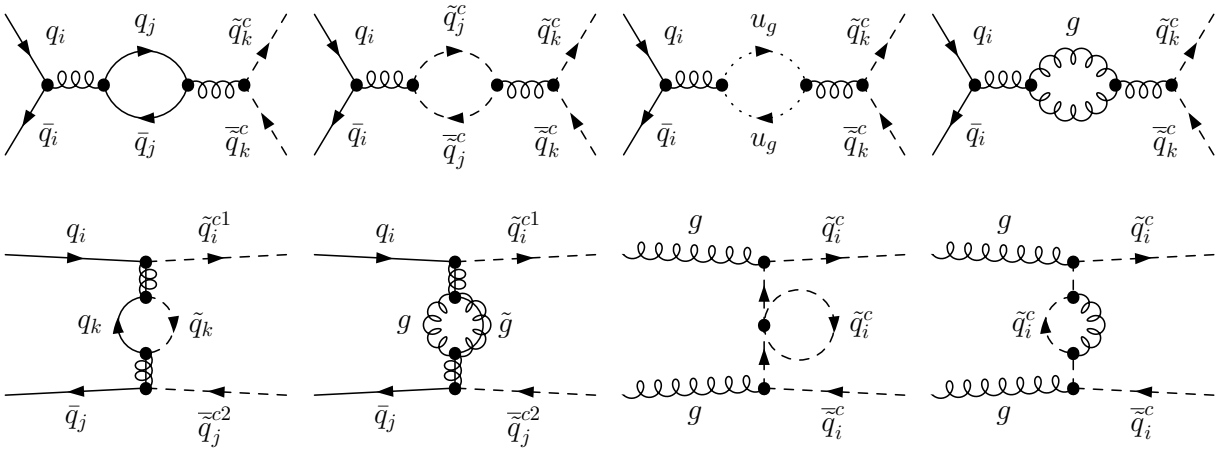

Figure 3.2.: Example diagrams for self-energy corrections to the gluon, gluino and squark propagators.

$u\bar{d} \to \tilde{u}_L\bar{\tilde{d}}_L$, $d\bar{d} \to \tilde{u}_L\bar{\tilde{u}}_L$ and $gg \to \tilde{u}_L\bar{\tilde{u}}_L$ have been calculated. All other possible flavour structures can be derived from the obtained results by appropriately replacing the masses of the internal squarks according to the external particles. Compared to the calculation of squark pair production, where it is sufficient to simply replace all internal squark masses in the vertex corrections and the box contributions with the masses of the final-state squarks, this generalization is more involved in the case at hand.

The self-energy corrections of the gluon and the gluino (see Fig. 3.2 for sample diagrams) do not require any generalization, as the internal quarks and squarks are obviously not connected to the final-state squarks. Hence in the generated FeynArts expressions only the occurring elements of the squark mixing matrices are simplified (recall that in the limit $m_q \to 0$ the corresponding mixing matrix becomes diagonal). Due to this diagonal structure the squark self-energy gets only contributions with identical internal and final-state squarks. Hence the masses of the squarks occurring in the loop functions (and propagators) of the last two diagrams in Fig. 3.2 have to be modified accordingly.

The vertex corrections, in contrast, are more involved. The internal squarks in the sample diagrams depicted in the first two rows of Fig. 3.3 are unambiguously connected to either one of the external squarks. Due to the flavour and chirality conserving structure of the occurring vertices and the diagonal squark mixing matrices the corresponding masses have to be replaced in order to generalize these contributions. Likewise, in the gg-channels the masses in diagrams like those shown in the first row of Fig. 3.4 have to be adapted. The diagrams shown in the last rows of the two figures, however, require a different treatment. While the internal squarks in the last row of Fig. 3.3 are connected to the initial-state quarks, i.e. the flavour of the squarks in these loops (and thus their mass) has to be made compliant with the respective quark flavour, the loops in Fig. 3.4 have to be left unaltered. The diagram in Fig. 3.4 including a four-squark vertex exhibits another peculiarity: for four identical squarks the corresponding Feynman rule gets an additional contribution (see e.g. App. A in [44]). This has to be taken into account when generalizing the result to arbitrary final-state configurations.

The box contributions to the $q\bar{q}$- and gg-channels require similar distinctions. In the sample diagrams in the upper rows of Figs. 3.5 and 3.6, respectively, the internal squarks are directly connected to those in the final state and thus the masses occurring in the loops have to be

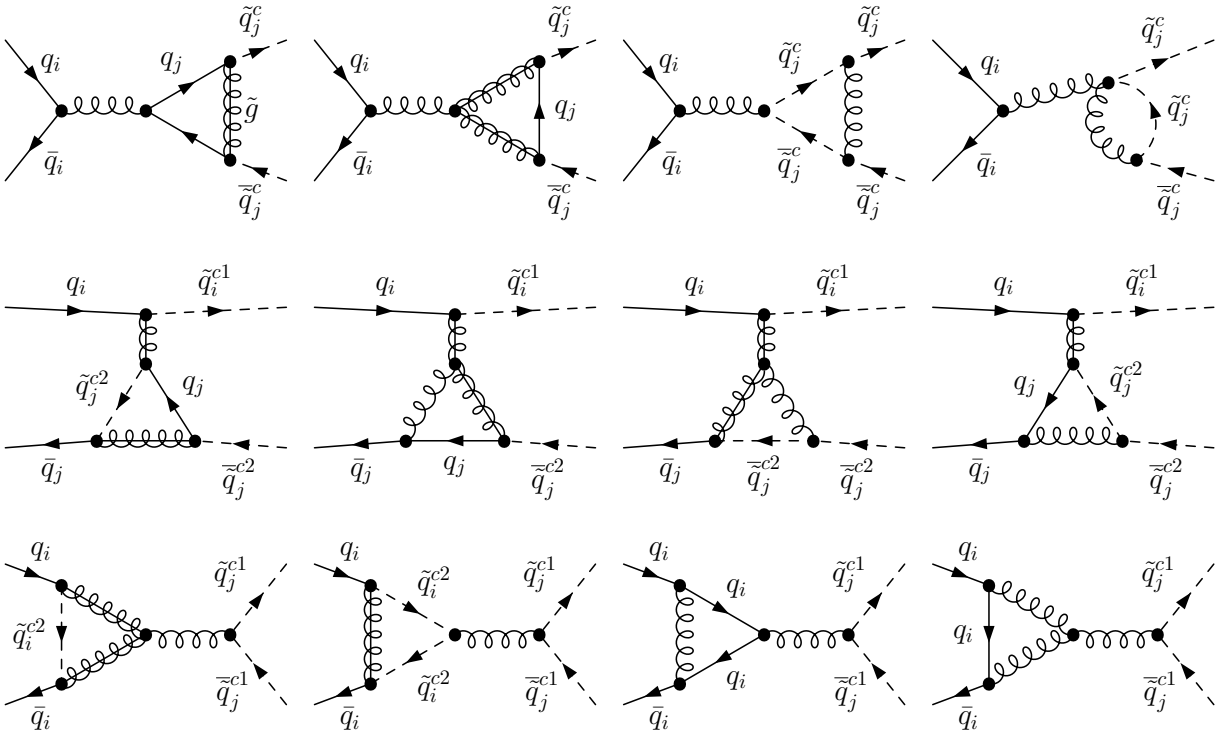

Figure 3.3.: Example diagrams for the vertex corrections to the $q\bar{q}$-channels.

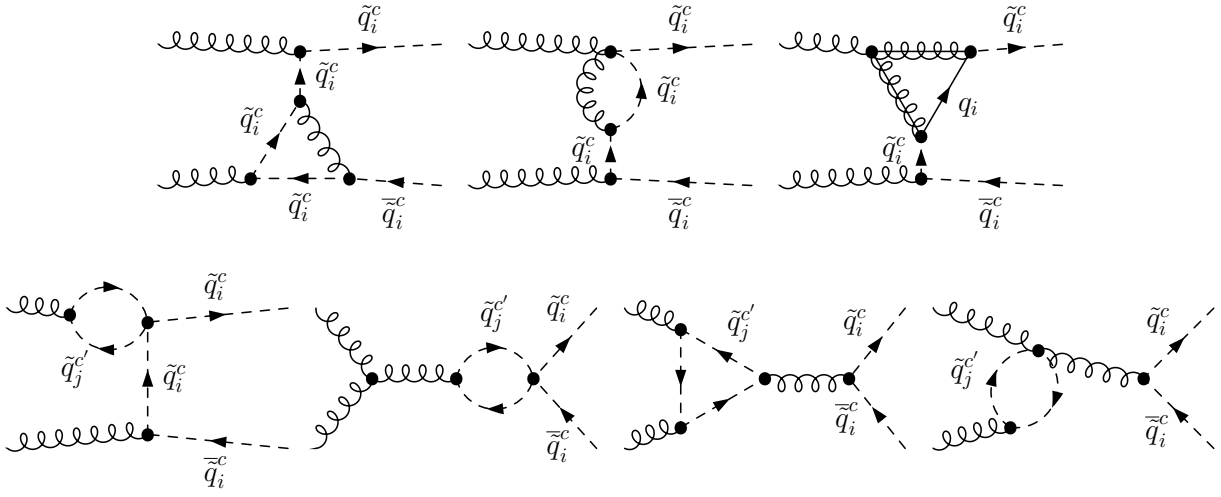

Figure 3.4.: Example diagrams for the vertex corrections to the gg-channels.

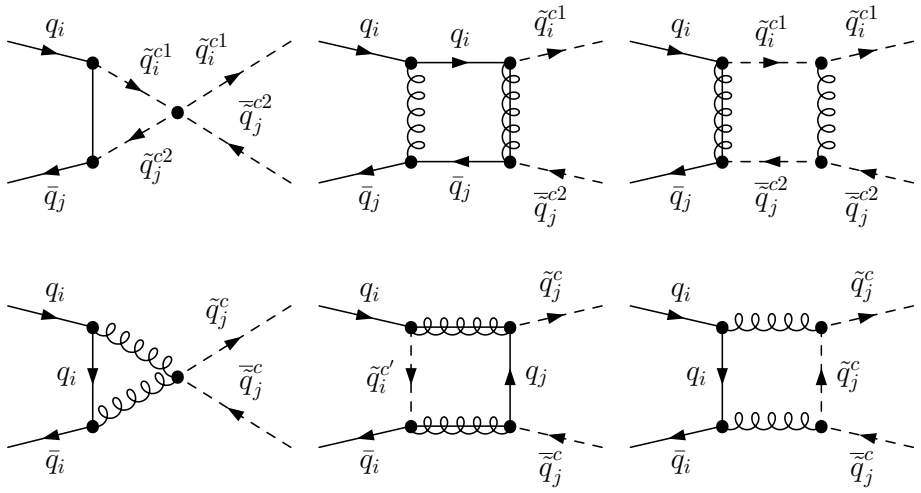

Figure 3.5.: Example diagrams for box corrections to the $q\bar{q}$-channels.

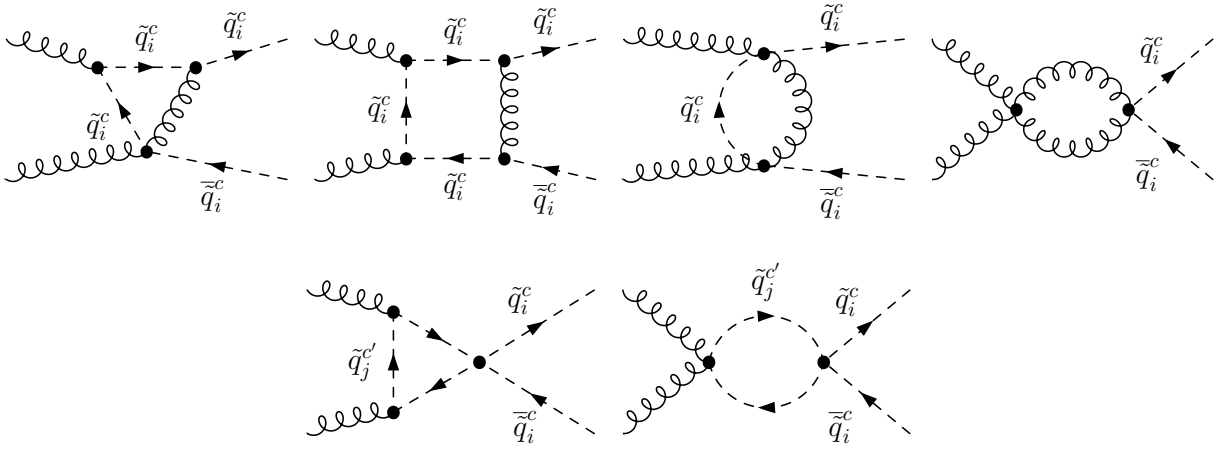

Figure 3.6.: Example diagrams for box corrections to the gg-channels.

adapted accordingly. In the second diagram shown in the lower row of Fig. 3.5 the internal squark is again connected to the initial-state, while the squark-loops in the lower row of Fig. 3.6 comprise all squarks and have to be left unaltered (modulo the changes regarding the four squark vertex, see the comment above).

For the numerical evaluation of the loop integrals in the created FORTRAN routines the package LOOPTOOLS 2.7 [83, 84] has been used.

3.1.3. The real contributions

The real corrections to squark antisquark production consist of two different topologies. The first one is characterized by an additional gluon in the final state. The flavour structures can be directly derived starting from the Born configurations stated in Eq. (3.1) by adding an additional gluon to the final state,

$$\begin{aligned} q_i\,\bar{q}_j &\to \tilde{q}_k^{c1}\,\bar{\tilde{q}}_l^{c2}\,g\,, \\ g\,g &\to \tilde{q}_i^{c}\,\bar{\tilde{q}}_i^{c}\,g\,. \end{aligned} \tag{3.10}$$

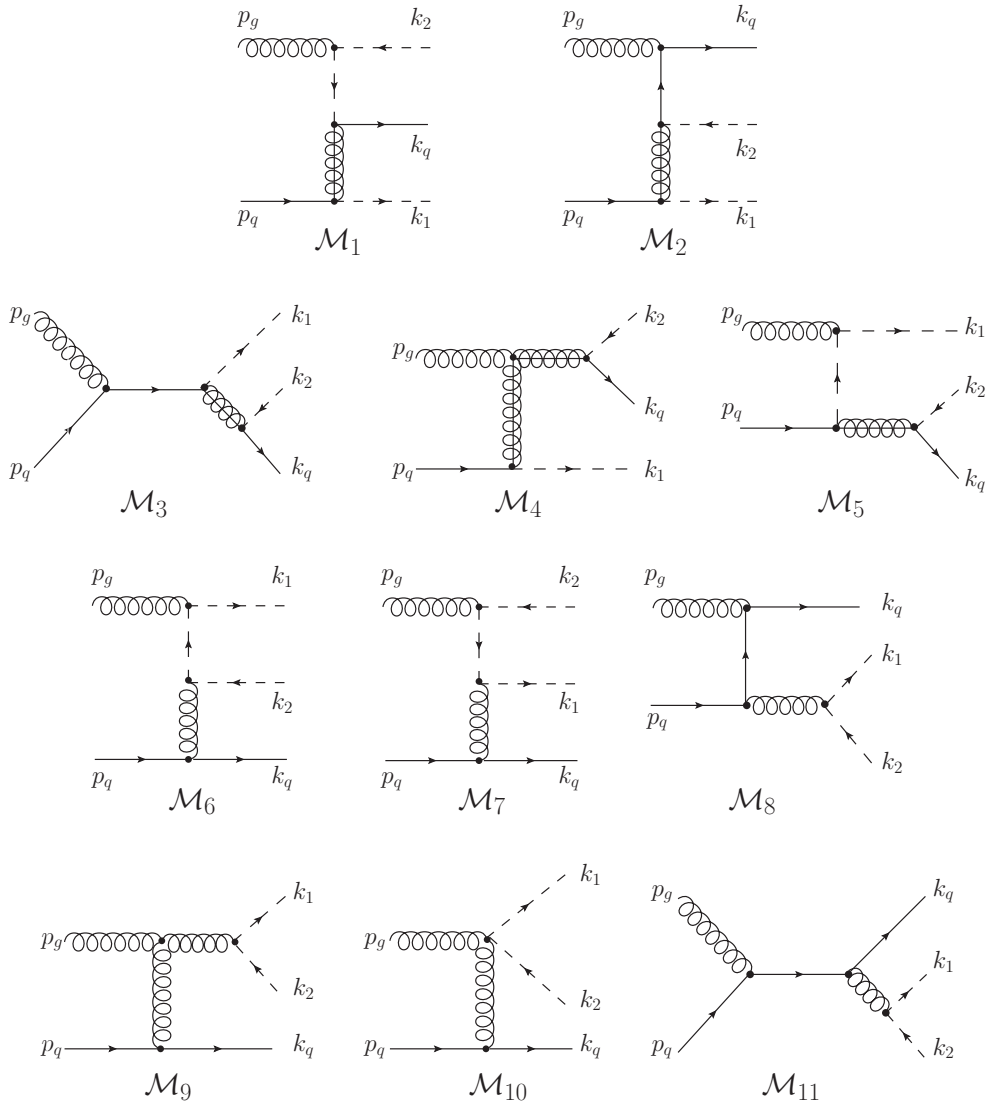

Figure 3.7.: Feynman diagrams contributing to the real corrections $q_i\, g \to \tilde{q}_k^{c1}\, \bar{\tilde{q}}_l^{c2} q_j$.

The second topology comprises channels with an additional (anti)quark in the final state,

$$\begin{aligned} q_i\, g &\to \tilde{q}_k^{c1}\, \bar{\tilde{q}}_l^{c2} q_j\,, \\ g\, \bar{q}_j &\to \tilde{q}_k^{c1}\, \bar{\tilde{q}}_l^{c2} \bar{q}_i\,. \end{aligned} \tag{3.11}$$

This topology is related to the $q_i\bar{q}_j$-channels from above by crossing symmetry. Taking into account the invariance under charge conjugation it is sufficient to calculate all possible contributions to either the $q_i\bar{q}_j$-, q_ig- or $g\bar{q}_j$-channels and construct the other combinations by either crossing the gluon or by charge conjugating the respective process. Here, the calculation has been performed explicitly for the $q_i\, g \to \tilde{q}_k^{c1}\, \bar{\tilde{q}}_l^{c2} q_j$ subprocesses. The contributing Feynman diagrams are shown in Fig. 3.7, where the momenta of the initial-state partons are p_q and p_g, while those of the final-state particles are denoted k_1 (k_2) for the squark (antisquark) and k_q for the quark.

Hence in total 11 distinct matrix elements have to be calculated. However, these do not contribute to all flavour/chirality combinations:

- $\mathcal{M}_1$ to $\mathcal{M}_5$ contribute to all channels $q_i\, g \to \tilde{q}_i^{c1}\, \bar{\tilde{q}}_j^{c2}\, q_j$ for all combinations of same/different flavour/chiralities.
- $\mathcal{M}_6$ to $\mathcal{M}_{11}$ contribute only to the subprocesses $q_i\, g \to \tilde{q}_j^c\, \bar{\tilde{q}}_j^c\, q_i$, regardless whether $i = j$ or $i \neq j$.

These matrix elements have been calculated analytically, using the MATHEMATICA package FEYNCALC 8.2 [85] for the evaluation of the occurring traces. For the internal gluon propagators Feynman gauge has been used. The sum over the polarization of the external gluon has been performed using two different gauges:

- **Feynman gauge:** In this gauge the polarization sum is simply

$$P^{\mu\nu} = \sum \epsilon^{\mu\,*}(p_g)\epsilon^{\nu}(p_g) = -g^{\mu\nu}. \tag{3.12}$$

  Since in case of the $q_i g$-channels only one external gluon occurs, it is not necessary to take care of the unphysical longitudinal degrees of freedom, i.e. no 'ghost subtraction' is needed here.

- **Axial gauge:** In axial gauges the most general formula for the gluon polarization sum is more sophisticated:

$$P^{\mu\nu} = \sum \epsilon^{\mu\,*}(p_g)\epsilon^{\nu}(p_g) = -g^{\mu\nu} + \frac{n^\mu p_g^\nu + n^\nu p_g^\mu}{n \cdot p_g} - \frac{n^2 p_g^\mu p_g^\nu}{(n \cdot p_g)^2}\,, \tag{3.13}$$

  with an arbitrary four vector n^μ defined such that $n^\mu \neq p_g^\mu$. Here, this vector has been chosen such that $n^2 = 0$ (this class of axial gauges is known as lightcone gauges, see e.g. [86]):

$$(n_0, n_1, n_2, n_3)^T = \left(\frac{1}{2}, 0, 0, -\mathrm{sgn}(p_{g,3})\frac{1}{2}\right)^T, \tag{3.14}$$

  with $\mathrm{sgn}(x) = \pm 1$ for $x \gtrless 0$. This specific choice is identical to the one used in the program MADGRAPH [87, 88], which has been used to test the analytical calculation numerically.

After adding up all contributions the results obtained in both gauges perfectly agree, as expected for a gauge-independent result.

The resulting expressions are rather lengthy and therefore not shown here. They have been converted to a set of FORTRAN routines which allow for a calculation of each individual contribution $\mathrm{Re}\,(\mathcal{M}_a^* \mathcal{M}_b)$ to the total matrix element squared. To obtain the $\bar{q}g$-channel it is sufficient to form the charge conjugate process for the different flavour structures, i.e. the momenta and masses of the squark and antisquark have to be interchanged in the corresponding routines. The results for the channels $q_i\, \bar{q}_j \to \tilde{q}_k^{c1}\, \bar{\tilde{q}}_l^{c2}\, g$ are obtained by means of crossing. The crossing of one fermion implies an overall minus sign for the matrix elements squared. Moreover, the momenta of the final-state quark and the initial-state gluon have to be interchanged, $p_g \leftrightarrow -k_q$.

The remaining channels $g\, g \to \tilde{q}_i^c\, \bar{\tilde{q}}_i^c\, g$ have to be calculated separately, see Fig. 3.8 for some sample Feynman diagrams. This calculation has not been performed analytically, as the analytical result is not needed in the following. Instead, the program MADGRAPH 5.1.3.1 [89] has been used to generate the code for the matrix elements squared automatically for one specific

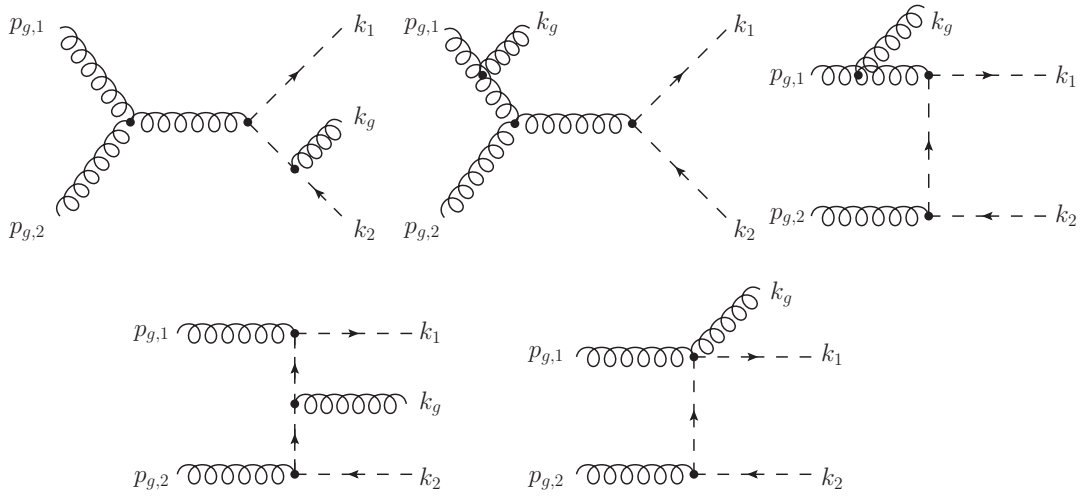

Figure 3.8.: Sample Feynman diagrams contributing to the real corrections $g\,g \to \tilde{q}_i^{\,c}\,\bar{\tilde{q}}_i^{\,c}\,g$.

production channel, $g\,g \to \tilde{u}_L\,\bar{\tilde{u}}_L\,g$. The output of this program is based on the helicity amplitude formalism [90] and provides the calls to the different HELAS subroutines relevant for the process at hand. These calls have been generalized to the case $g\,g \to \tilde{q}_i^{\,c}\,\bar{\tilde{q}}_i^{\,c}\,g$ by replacing the masses $m_{\tilde{u}_L}$ with $m_{\tilde{q}_i^c}$ in the routines. Moreover, the occurring squark propagators are by default evaluated for non-zero squark widths. As the widths are set to zero in all other parts of the calculation, these parts had to be adapted, too.

3.1.3.1. Infrared and on-shell singularities

Both the qg-channels and the gg-channels are infrared divergent. While in the qg case only collinear divergent matrix elements occur (namely $\mathcal{M}_2$ and $\mathcal{M}_8$ in Fig. 3.7), the $q\bar{q}$- and gg-channels with an additional gluon in the final state contain also soft singularities (e.g. the first graph in Fig. 3.8) and soft-collinear ones (e.g. the second and third graph in Fig. 3.8). These divergences are cancelled via the FKS method which is described in Sec. 2.2.2.2 and automated for arbitrary processes in the POWHEG-BOX. The only process-dependent ingredients are the colour- and spin-correlated Born amplitudes squared, $\mathcal{B}_{ij}$ and $\mathcal{B}_{\mu\nu}$. The calculation of these amplitudes and the results for squark antisquark production are summarized in App. A.2.

Besides these IR divergences, which are a common feature of NLO (SUSY)-QCD calculations, the gluon-initiated channels $q_i\,g \to \tilde{q}_i^{\,c1}\,\bar{\tilde{q}}_j^{\,c2}\,q_j$ give rise to another type of singularity: for $m_{\tilde{q}} < m_{\tilde{g}}$ the intermediate gluino in the diagrams $\mathcal{M}_3$, $\mathcal{M}_4$ and $\mathcal{M}_5$ in Fig. 3.7 can be produced on shell.[5] In principle, the resulting divergence originating from the gluino propagator can be cured by introducing a finite width $\Gamma_{\tilde{g}}$,

$$\frac{1}{(p_{\bar{\tilde{q}}_j} + p_{q_j})^2 - m_{\tilde{g}}^2} \to \frac{1}{(p_{\bar{\tilde{q}}_j} + p_{q_j})^2 - m_{\tilde{g}}^2 + i m_{\tilde{g}} \Gamma_{\tilde{g}}} \quad . \tag{3.15}$$

However, looking at these resonant contributions from a different point of view, they correspond to the LO production $q_i g \to \tilde{q}_i \tilde{g}$, followed by the decay $\tilde{g} \to \bar{\tilde{q}}_j q_j$. Keeping it as part of the real corrections to squark antisquark production would spoil the predictive power of the NLO

[5] The same problem arises in the $\bar{q}g$-channels for $m_{\tilde{q}} < m_{\tilde{g}}$. This situation will not be discussed explicitly in the following, as adapting the results is straightforward.

calculation, as for a very large region in the parameter space this resonant contribution easily exceeds the full NLO corrections. Moreover, considering all SUSY-QCD pair production channels (notably $\tilde{q}\tilde{g}$ production) and the subsequent decays, these channels would be double counted. Therefore, these contributions have to be removed in a consistent way.

This type of singularity also occurs in squark pair production and has not yet been considered in [28]. In this case the singular structure is more involved, as there are subprocesses where both produced squarks can originate simultaneously from on-shell gluinos. Therefore, the following discussion of these types of singularities also contains results for squark pair production and thus completes the calculation of the NLO SUSY-QCD corrections to this process presented in [28] with regard to scenarios in which $m_{\tilde{q}} < m_{\tilde{g}}$. The real contributions to squark pair production are briefly summarized in the next paragraph.

3.1.3.2. Real corrections to squark pair production - an interlude

Squark pair production at LO is mediated via a t-channel gluino exchange, similar to the first graph in Fig. 3.1. The different production modes

$$q_i\, q_j \to \tilde{q}_i^{c1}\, \tilde{q}_j^{c2} \tag{3.16}$$

can be categorized into four classes: For squarks with identical flavours, $i = j$, the chiralities can either be identical or different. In either case, the t-channel gluino exchange graph depicted in Fig. 3.1 has to be supplemented by the corresponding u-channel contribution. Note that due to the chirality conserving structure of the squark-quark-gluino vertex the interference between these two terms vanishes for squarks with different chiralities. If the flavour of the squarks is different, $i \neq j$, they can still have either the same or different chirality. For this configuration, however, only the t-channel graph contributes.

Similar to squark antisquark production, the real contributions in the squark pair case consist of topologies with an additional gluon in the final state and new channels with a quark and a gluon in the initial state and a final-state antiquark. Only the latter ones contain resonant intermediate gluinos. The contributing Feynman diagrams are identical to $\mathcal{M}_1$ to $\mathcal{M}_5$ in Fig. 3.7 after replacing the final-state quark with the corresponding antiquark ($k_q \to k_{\bar{q}}$) and the antisquark with the respective squark. As in the LO case these five diagrams have to be supplemented by an identical set with $\tilde{q}_1 \leftrightarrow \tilde{q}_2$ for channels involving same-flavour squarks. Again, the interference terms between these two sets are non-zero only if additionally the squark chiralities are identical.

This 'doubling' of the diagrams involving potentially on-shell intermediate gluinos in the same-flavour case is the reason for the higher complexity in squark pair production, as they involve two singular momentum configurations, which have to be handled simultaneously.

3.1.3.3. Subtraction of on-shell intermediate gluinos

The considerations presented in this section have been published for squark pair production in [91]. In order to discuss both squark antisquark and squark pair production simultaneously, the momenta of the final-state particles are generically denoted as follows:

- k_1 corresponds to the momentum of the squark in case of squark antisquark production and to the first squark for squark pair production, the corresponding mass is m_1. Only for the pair production of same-flavour squarks this squark is connected to a potentially on-shell gluino.

- k_2 is the momentum of the antisquark or of the second squark in case of the production of a squark pair, respectively. The corresponding mass is denoted m_2.
- k_3 denotes the momentum of the (anti)quark.

For the discussion of the subtraction of the resonant gluino contributions it is convenient to organize these momenta in terms of invariants,

$$\begin{aligned} s_{1g} &\equiv (k_1 + k_3)^2 - m_{\tilde{g}}^2 \,, \\ s_{2g} &\equiv (k_2 + k_3)^2 - m_{\tilde{g}}^2 \,. \end{aligned} \tag{3.17}$$

The general structure of the qg-channels can be written as

$$|\mathcal{M}_{\text{tot}}|^2 = |\mathcal{M}_{\text{nr}}|^2 + 2\,\text{Re}(\mathcal{M}_{\text{r}}\mathcal{M}_{\text{nr}}^*) + |\mathcal{M}_{\text{r}}|^2, \tag{3.18}$$

where $\mathcal{M}_{\text{nr}}$ comprises the non-resonant diagrams (thus all contributing matrix elements $\mathcal{M}_i$ with $i \neq 3, 4, 5$ in Fig. 3.7), whereas the resonant ones are combined in $\mathcal{M}_{\text{r}}$. In case of the production of two squarks with identical flavour both squarks can lead to a resonant behaviour (if both $m_{\tilde{q}_1} < m_{\tilde{g}}$ and $m_{\tilde{q}_2} < m_{\tilde{g}}$) and $\mathcal{M}_{\text{r}}$ reads

$$(\mathcal{M}_3 + \mathcal{M}_4 + \mathcal{M}_5) + (\mathcal{M}_3 + \mathcal{M}_4 + \mathcal{M}_5)_{k_1 \leftrightarrow k_2} \equiv \mathcal{M}_{\text{r},s_{2g}} + \mathcal{M}_{\text{r},s_{1g}} \,, \tag{3.19}$$

hence after forming the matrix element squared the resonant contributions read

$$|\mathcal{M}_{\text{r}}|^2 = |\mathcal{M}_{\text{r}}|^2_{s_{1g}} + |\mathcal{M}_{\text{r}}|^2_{s_{2g}} + 2\text{Re}\left(\mathcal{M}^*_{\text{r},s_{1g}}\mathcal{M}_{\text{r},s_{2g}}\right)\delta_{c1c2} \,. \tag{3.20}$$

On-shell intermediate states which require a subtraction formalism are not a unique feature of SUSY-QCD pair production processes, but occur in other processes, too. Several methods to cope with them exist, the most relevant ones for Monte Carlo event generators being the following:

- **Diagram Removal - type I (DR-I):** This approach was first used in the context of tW production, see [92]. It simply amounts to leave out all resonant diagrams, i.e. not only $|\mathcal{M}_{\text{r}}|^2$ but also the interference term $2\,\text{Re}(\mathcal{M}_{\text{r}}\mathcal{M}_{\text{nr}}^*)$ is completely removed.
- **Diagram Removal - type II (DR-II):** This method was proposed in a recent calculation of the NLO corrections to squark pair production [19]. Here, only the $|\mathcal{M}_{\text{r}}|^2$ part is dropped, whereas the interference term is kept. The interference terms between contributions originating from two resonant regions, $2\text{Re}\left(\mathcal{M}^*_{\text{r},s_{1g}}\mathcal{M}_{\text{r},s_{2g}}\right)$ in Eq. (3.20), are taken into account.

Both approaches are easily implemented in a Monte Carlo event generator. However, omitting diagrams breaks gauge invariance and therefore leads to in principle arbitrary results as it is not guaranteed that the neglected terms are small.

- **Diagram Subtraction (DS):** In this approach a 'counterterm' is introduced which removes the resonant parts for $s_{jg} \to 0$ locally, i.e. only the contributions originating from on-shell gluinos are subtracted, see [92]. This method retains both the interference terms and off-shell contributions of $|M_{\text{r}}|^2$. Furthermore, by construction it allows for a pointwise subtraction and thus represents an ideal method for Monte Carlo event generators. Usually, the width $\Gamma_{\tilde{g}}$ introduced in order to regularize the singular behaviour is not set to the physical value, but considered as an artificial regularization parameter. However, if this parameter is introduced by simply replacing the resonant propagator, see Eq. (3.15), the full result is only gauge-invariant in the limit $\Gamma_{\tilde{g}} \to 0$.

To obtain a fully gauge-invariant result, the DS method has to be modified such that the (gauge-dependent) matrix elements are no longer used as building blocks. Considering for the moment only the case of one singular region, the poles (in s_{2g}) are extracted instead analytically after choosing a specific phase space parametrization in terms of invariants (this approach is similar to the 'pole expansion' proposed in the context of $e^+e^- \to Z^* \to f\bar{f}$, see [93]):

$$|\mathcal{M}_{\text{tot}}|^2 = \frac{f_0}{s_{2g}^2} + \frac{f_1}{s_{2g}} + f_2(s_{2g}). \tag{3.21}$$

The coefficients f_k ($k = 0, 1, 2$) are gauge-invariant quantities, i.e. introducing a regulator $\Gamma_{\tilde{g}}$ at this point preserves gauge invariance and one obtains

$$|\mathcal{M}_{\text{tot}}|^2 = \frac{f_0}{s_{2g}^2 + m_{\tilde{g}}^2\Gamma_{\tilde{g}}^2} + \frac{s_{2g}}{s_{2g}^2 + m_{\tilde{g}}^2\Gamma_{\tilde{g}}^2} f_1 + f_2(s_{2g}). \tag{3.22}$$

Note that this regulator occurs only in diagrams which are not IR divergent, thus the cancellation of IR divergences against the FKS counterterms is still guaranteed. Comparing the expression (3.22) with the one obtained by introducing $\Gamma_{\tilde{g}}$ at the level of matrix elements it is possible to quantify the difference $\Delta(\Gamma_{\tilde{g}}, s_{2g})$ between the two methods, which gives indirectly a measure for the 'gauge dependence' of the result:

$$\Delta(\Gamma_{\tilde{g}}, s_{2g}) = \tilde{f}_2(s_{2g}) \frac{m_{\tilde{g}}^2\Gamma_{\tilde{g}}^2}{s_{2g}^2 + m_{\tilde{g}}^2\Gamma_{\tilde{g}}^2}, \tag{3.23}$$

where $\tilde{f}_2(s_{2g})$ comprises the parts of $f_2(s_{2g})$ originating from $2\,\text{Re}(\mathcal{M}_{\text{r}}\mathcal{M}_{\text{nr}}^*) + |\mathcal{M}_{\text{r}}|^2$. For $\Gamma_{\tilde{g}} \to 0$ the results are equivalent, but close to the resonant region the discrepancy is solely determined by the gauge-dependent quantity $\tilde{f}_2(s_{2g})$.

As mentioned above, the results for the pair production of same-flavour squarks can be obtained by taking these terms with $\tilde{q}_1 \leftrightarrow \tilde{q}_2$ into account twice. The additional interference terms between these two contributions for identical squarks in Eq. (3.20) lead to terms $\propto 1/(s_{1g}s_{2g})$. They do not require any subtraction. However, the singular structure necessitates again the introduction of a regularizing width $\Gamma_{\tilde{g}}$. To this end these terms are expanded both in $1/s_{1g}$ and $1/s_{2g}$ before this regulator is introduced:

$$\begin{aligned} 2\,\text{Re}\left(\mathcal{M}_{\text{r},s_{1g}}^* \mathcal{M}_{\text{r},s_{2g}}\right) = {} & \frac{s_{1g}s_{2g} + m_{\tilde{g}}^2\Gamma_{\tilde{g}}^2}{(s_{1g}^2 + m_{\tilde{g}}^2\Gamma_{\tilde{g}}^2)(s_{2g}^2 + m_{\tilde{g}}^2\Gamma_{\tilde{g}}^2)}\, g_0 + \frac{s_{1g}}{s_{1g}^2 + m_{\tilde{g}}^2\Gamma_{\tilde{g}}^2}\, \tilde{g}_1(s_{2g}) \\ & + \frac{s_{2g}}{s_{2g}^2 + m_{\tilde{g}}^2\Gamma_{\tilde{g}}^2}\, \tilde{g}_2(s_{1g}) + \tilde{g}_3(s_{1g}, s_{2g})\,. \end{aligned} \tag{3.24}$$

Correspondingly, the additional interference terms between the non-resonant and the resonant terms are expanded in either $1/s_{1g}$ or $1/s_{2g}$, depending on the type of the singular structure. Together with the interference terms from non-resonant contributions the expansion coefficients obtained in this way render the expressions $\propto \tilde{g}_{1,2,3}$ gauge invariant.

Considering again the difference between this expanded gauge-invariant expression and the one obtained by performing the replacement Eq. (3.15) directly in the matrix elements, the contribution Eq. (3.24) yields additional terms. In total, for identical squarks this difference takes the

form

$$\begin{aligned}\Delta(\Gamma_{\tilde{g}}, s_{1g}, s_{2g}) = \Delta(\Gamma_{\tilde{g}}, s_{2g}) + \Delta|_{\tilde{q}_1 \leftrightarrow \tilde{q}_2}(\Gamma_{\tilde{g}}, s_{1g}) \\ + \frac{m_{\tilde{g}}^2\Gamma_{\tilde{g}}^2(m_{\tilde{g}}^2\Gamma_{\tilde{g}}^2 + s_{1g}^2 + s_{2g}^2 - s_{1g}s_{2g})}{(s_{1g}^2 + m_{\tilde{g}}^2\Gamma_{\tilde{g}}^2)(s_{2g}^2 + m_{\tilde{g}}^2\Gamma_{\tilde{g}}^2)}\,\tilde{g}_3(s_{1g}, s_{2g}) \\ + \frac{m_{\tilde{g}}^2\Gamma_{\tilde{g}}^2(s_{2g} - s_{1g})}{s_{2g}(s_{1g}^2 + m_{\tilde{g}}^2\Gamma_{\tilde{g}}^2)}\,\tilde{g}_2(s_{1g}) + \frac{m_{\tilde{g}}^2\Gamma_{\tilde{g}}^2(s_{1g} - s_{2g})}{s_{1g}(s_{2g}^2 + m_{\tilde{g}}^2\Gamma_{\tilde{g}}^2)}\,\tilde{g}_1(s_{2g}),\end{aligned} \tag{3.25}$$

with $\Delta(\Gamma_{\tilde{g}}, s_{2g})$ defined in Eq. (3.23). Qualitatively, the effect of these terms is the same as in Eq. (3.23): For $\Gamma_{\tilde{g}} \to 0$ they vanish as expected, however, close to the resonant region the difference is determined solely by the gauge-dependent coefficients $\tilde{g}_{1,2,3}$.

This modified DS method (in the following denoted DS*) is in principle equivalent to the method used originally in the implementation of NLO corrections to squark and gluino production in Prospino, see [17]. However, the actual implementation of the DS(*) scheme in a Monte Carlo event generator is quite involved. In the following the different building blocks required for both the original and the modified DS scheme are summarized. Note that the actually subtracted quantity is in both schemes identical, as mandatory for an unambiguous subtraction scheme. For more details on the implementation of the (original) DS scheme see [92].

The general form of the subtraction term for the DS method applied to a resonance in s_{2g} can be written as[6]

$$\mathrm{d}\sigma_{\mathrm{sub}} = \Theta(\sqrt{\hat{s}} - m_{\tilde{g}} - m_1)\,\Theta(m_{\tilde{g}} - m_2)\,|\mathcal{M}_{\mathrm{r},s_{2g}}(\tilde{\Phi}_3)|^2\,\frac{m_{\tilde{g}}^2\Gamma_{\tilde{g}}^2}{s_{2g}^2 + m_{\tilde{g}}^2\Gamma_{\tilde{g}}^2}\,\mathrm{d}\tilde{\Phi}_3. \tag{3.26}$$

Correspondingly this term reads for the DS* scheme

$$\mathrm{d}\sigma_{\mathrm{sub}} = \Theta(\sqrt{\hat{s}} - m_{\tilde{g}} - m_1)\,\Theta(m_{\tilde{g}} - m_2)\,\frac{f_0(\tilde{\Phi}_3)}{s_{2g}^2 + m_{\tilde{g}}^2\Gamma_{\tilde{g}}^2}\,\mathrm{d}\tilde{\Phi}_3. \tag{3.27}$$

The different elements of the equations guarantee the following properties:

- The case of on-shell intermediate gluinos can only occur if the energy in the partonic centre-of-mass system is sufficient to generate both an on-shell gluino and the squark not originating from the 'gluino decay'. This is ensured by the first step function, $\Theta(\sqrt{\hat{s}} - m_{\tilde{g}} - m_1)$.
- Only the case $m_{\tilde{g}} > m_2$ requires a subtraction, which is ensured by the factor $\Theta(m_{\tilde{g}} - m_2)$. For squark pair production this is a non-trivial restriction only in the case of same-flavour squarks with different chiralities for a hierarchy like $m_{\tilde{q}_1} < m_{\tilde{g}} < m_{\tilde{q}_2}$. In all other cases there is either only one type of squarks involved, or flavour conservation dictates which squark can originate from the on-shell gluino. For squark antisquark production there is always at most one possible singular configuration, either for the antisquark (for qg-channels) or the squark (for $\bar{q}g$-channels).
- The choice $\mathrm{d}\sigma_{\mathrm{sub}} \propto |\mathcal{M}_{\mathrm{r},s_{2g}}|^2$ ensures the exact cancellation of the $\tilde{q}\tilde{g}$ contribution in the limit $s_{2g} \to 0$. In this limit this term reproduces the term $\propto f_0$ in the analytical expansion, see Eq. (3.22), i.e. the subtraction term in both approaches is indeed identical. Moreover, using the full amplitude squared retains spin-correlations.

[6] Only the case of one singular region is discussed here, the generalization to two singular configurations as needed in case of same-flavour squarks is straightforward.

- The subtraction term is supposed to remove only contributions with $(k_2+k_3)^2 = m_{\tilde{g}}^2$. An arbitrary phase space point in the three-particle phase space Φ_3 will usually not fulfil this criterion. Therefore, the kinematics has to be adapted appropriately by a mapping $\Phi_3 \to \tilde{\Phi}_3$. Besides putting the gluino on its mass shell, this momentum reshuffling has to respect energy-momentum conservation. Furthermore, it should preserve the on-shell conditions for the final-state squarks and become an identity transformation for $(k_2+k_3)^2 = m_{\tilde{g}}^2$. This situation is similar to the construction of the transformed kinematics in the Catani-Seymour formalism. Therefore, the formulae for the case where both the spectator and the emitter are final-state massive particles could be adopted from [67] to construct the momenta of the $\tilde{q}_1$ and of the intermediate gluino, which are denoted $\tilde{k}_1$ and $\tilde{p}_{\tilde{g}}$ in $\tilde{\Phi}_3$.

  With
  $$\begin{aligned} p_{\tilde{g}}^\mu &= k_2^\mu + k_3^\mu \,, \\ m_{23}^2 &= (k_2+k_3)^2 = m_2^2 + 2k_2\cdot k_3 \,, \\ Q^\mu &= k_1^\mu + k_2^\mu + k_3^\mu \end{aligned} \tag{3.28}$$
  one obtains for the reshuffled momenta of the 'spectator' squark and the intermediate gluino
  $$\begin{aligned} \tilde{k}_1^\mu &= \frac{\lambda^{1/2}\left(Q^2, m_{\tilde{g}}^2, m_1^2\right)}{\lambda^{1/2}\left(Q^2, m_{23}^2, m_1^2\right)} \left(k_1^\mu - \frac{Q\cdot k_1}{Q^2} Q^\mu\right) + \frac{Q^2 + m_1^2 - m_{\tilde{g}}^2}{2Q^2} Q^\mu \,, \\ \tilde{p}_{\tilde{g}}^\mu &= Q^\mu - \tilde{k}_1^\mu \,, \end{aligned} \tag{3.29}$$
  where the Källén function $\lambda(x,y,z) = x^2+y^2+z^2-2xy-2xz-2yz$ has been introduced.

  To construct the remaining two transformed momenta, $\tilde{k}_2$ and $\tilde{k}_3$, the original momentum k_2 is boosted to the rest frame of the gluino, i.e. with $\vec{\beta} = -\vec{p}_{\tilde{g}}/p_{\tilde{g}}^0$, to obtain the direction of the second squark (respectively the antisquark), i.e. its polar and azimuthal angle in this frame. The new momenta in the gluino restframe are constructed preserving this direction and adapting the energies of the two particles by applying the kinematics for a $1 \to 2$ decay of an on-shell gluino (see e.g. [77]), i.e.
  $$\begin{aligned} k_2^{0\prime} &= \frac{m_{\tilde{g}}^2 + m_2^2}{2m_{\tilde{g}}}, \quad |\vec{k}_2'| = \frac{m_{\tilde{g}}^2 - m_2^2}{2m_{\tilde{g}}} \,, \\ k_3^{0\prime} &= m_{\tilde{g}} - k_2^{0\prime}, \quad \vec{k}_3' = -\vec{k}_2'. \end{aligned} \tag{3.30}$$
  Finally, k_2' and k_3' are boosted from the gluino restframe with $\vec{\beta} = \vec{\tilde{p}}_{\tilde{g}}/\tilde{p}_{\tilde{g}}^0$ to obtain $\tilde{k}_2$ and $\tilde{k}_3$.

- In the limit $\Gamma_{\tilde{g}} \to 0$ the subtracted term has to reduce to
  $$\hat{\sigma}_{\tilde{q}\bar{q}\tilde{g}}\, BR(\tilde{g} \to \tilde{q}\bar{q}) \quad \text{respectively} \quad \hat{\sigma}_{\bar{\tilde{q}}q\tilde{g}}\, BR(\tilde{g} \to \bar{\tilde{q}}q)\,. \tag{3.31}$$
  This requirement is met by the Breit-Wigner form of the (squared) gluino propagator, since
  $$\frac{m_{\tilde{g}}\Gamma_{\tilde{g}}}{s_{2g}^2 + m_{\tilde{g}}^2\,\Gamma_{\tilde{g}}^2} \overset{\Gamma_{\tilde{g}}\to 0}{\longrightarrow} \pi\delta\left(s_{2g}\right) \tag{3.32}$$
  leads to $(k_2+k_3)^2 = m_{\tilde{g}}^2$ upon integration over $(k_2+k_3)^2 \equiv s_2$.[7] The reshuffling procedure obviously destroys this form in $|M_\mathrm{r}|^2$, hence it has to be explicitly restored in the DS

[7] Note that this holds strictly speaking only if the range of integration for s_2 comprises the complete real axis. The physical phase space boundaries for s_2, however, are finite. For a discussion of the size of these (usually small) effects see Appendix D of [19].

scheme. As already mentioned above, the actual value used for $\Gamma_{\tilde{g}}$ is not the physical width. This parameter is considered here as a pure regularization parameter, which is chosen such that the result is independent of its value. Moreover, terms linear in $\Gamma_{\tilde{g}}$ which appear in the interference term $\mathcal{M}_{\mathrm{r}}\,\mathcal{M}^*_{\mathrm{nr}}$ are discarded, as only the leading term in an expansion in $\Gamma_{\tilde{g}}/m_{\tilde{g}}$ shall be reproduced, i.e. the limit $\Gamma_{\tilde{g}} \to 0$ is considered. In the DS* scheme the terms containing $\Gamma_{\tilde{g}}$ are unambiguously determined by the construction of the expansion.

- The last subtlety in the implementation is the form of the Jacobian for the numerical integration over the three-particle phase space. While the applied formalism for the reshuffling of the final-state kinematics guarantees that the transformed momenta lie within a 'restricted' phase space, i.e. they fulfil $(k_2 + k_3)^2 = m_{\tilde{g}}^2$ by construction, a naïve implementation of the subtraction term in the integral over the whole phase space would not only remove on-shell contributions, but also off-shell terms, if the integration limits are not adapted appropriately. To clarify this point, consider a specific parametrization of the three-particle phase space with two invariants (chosen as $s_2 = (k_2+k_3)^2$ and $t_1 = (p_g-k_1)^2$) and two angles which describe the gluino decay, see [94]. In terms of these integration variables the phase space element takes the form

$$\frac{\mathrm{d}\Phi_3}{\mathrm{d}\Omega} \propto \int_{s_2^-}^{s_2^+} \mathrm{d}s_2 \int_{t_1^-(s_2)}^{t_1^+(s_2)} \mathrm{d}t_1 \frac{s_2 - m_1^2}{s_2} = \int_{s_2^-}^{s_2^+} \mathrm{d}s_2 \int_0^1 \mathrm{d}x \frac{s_2 - m_1^2}{s_2} \sqrt{\lambda(\hat{s}, s_2, m_1^2)} \tag{3.33}$$

with $\hat{s}$ denoting the partonic centre-of-mass energy squared and the integration ranges given by

$$\begin{aligned} t_1^{\pm}(s_2) &= m_1^2 - \frac{1}{2}\left[\left(\hat{s} - s_2 + m_1^2\right) \mp \sqrt{\lambda\left(\hat{s}, s_2, m_1^2\right)}\right], \\ s_2^- &= m_2^2, \quad s_2^+ = \left(\sqrt{\hat{s}} - m_1\right)^2. \end{aligned} \tag{3.34}$$

The integration over t_1 has been mapped on the interval $[0,1]$ as required for a Monte Carlo integration[8], i.e. $t_1(s_2) = (t_1^+(s_2) - t_1^-(s_2))\,x + t_1^-(s_2)$. Using the same parametrization for the phase space integration of the subtraction term with its reshuffled kinematics $\tilde{\Phi}_3$, one has to take into account that in the 'restricted' phase space with $s_2 = m_{\tilde{g}}^2$ the Jacobian has to be rescaled according to the replacement $s_2 \to m_{\tilde{g}}^2$ in Eq. (3.33):

$$\mathrm{d}\tilde{\Phi}_3 = \mathrm{d}\Phi_3 \frac{\sqrt{\lambda(\hat{s}, m_{\tilde{g}}^2, m_1^2)}}{\sqrt{\lambda(\hat{s}, s_2, m_1^2)}} \frac{(m_{\tilde{g}}^2 - m_1^2)\, s_2}{(s_2 - m_1^2)\, m_{\tilde{g}}^2}. \tag{3.35}$$

[8] Considering the Breit-Wigner form of the integrand, the integration over s_2 should be mapped such that the resonant region is probed efficiently. A convenient way to achieve this is the Breit-Wigner-mapping:
$s_2 = m_{\tilde{g}}^2 + m_{\tilde{g}}\Gamma_{\tilde{g}} \tan(y)$ with $y = \left[\tan^{-1}\left(\frac{s_2^+ - m_{\tilde{g}}^2}{m_{\tilde{g}}\Gamma_{\tilde{g}}}\right) - \tan^{-1}\left(\frac{s_2^- - m_{\tilde{g}}^2}{m_{\tilde{g}}\Gamma_{\tilde{g}}}\right)\right] x + \tan^{-1}\left(\frac{s_2^- - m_{\tilde{g}}^2}{m_{\tilde{g}}\Gamma_{\tilde{g}}}\right)$, $x \in [0,1]$.

3.1.4. Checks and comparisons

To ensure the correctness of the calculation, the different building blocks described in the previous sections have been subject to numerous self consistency checks and comparisons with the older calculation in [17]. However, a comparison of the results for squark antisquark production with the publicly available program Prospino2 turns out to be difficult. In this newer version of the original Prospino code, which is based on [17], it is possible to obtain exact LO results for individual channels, keeping the full mass dependence. The NLO results for these subchannels, however, are obtained by calculating the total LO and NLO cross section for the sum of all channels with an averaged squark mass $\overline{m}_{\tilde{q}}$ (which is calculated taking into account the masses of only the light-flavour squarks). Each channel is then rescaled with the such obtained global K-factor

$$K^{\text{avg}} = \frac{\sigma_{\text{NLO}}(\overline{m}_{\tilde{q}})}{\sigma_{\text{LO}}(\overline{m}_{\tilde{q}})}. \tag{3.36}$$

In the calculation of $\sigma_{(\text{N})\text{LO}}(\overline{m}_{\tilde{q}})$ the bottom quark PDFs are explicitly set to zero, thus the contributions $b\bar{b} \to \tilde{b}\bar{\tilde{b}}$ are neglected, whereas the channels $gg \to \tilde{b}\bar{\tilde{b}}$ and $q\bar{q} \to \tilde{b}\bar{\tilde{b}}$ with $q = u, d, c, s$ are kept. Moreover, at NLO the contributions $qg \to \tilde{q}\bar{\tilde{b}}b$ and the charge conjugate processes are taken into account. Hence Prospino2 implicitly includes some $\tilde{b}$ production modes in the evaluation of the K-factors. These additional terms can be sizeable (for the benchmark scenario 10.3.6* defined in Sec. 3.1.5.1 they amount at NLO to roughly 7%) and render a comparison with the calculation performed here (which strictly takes into account the first two generations only) impossible.

Therefore the results for the NLO cross section have been compared with a different, non-public implementation of the original results from [17], which is completely equivalent to Prospino, but allows for an easy disentanglement of the number of squark flavours in the final state.[9] This program is denoted Prospino* in the following.

In detail, the following checks have been performed:

- **Born contributions:** The analytical results for the LO processes specified in Eqs. (3.3) through (3.8) have been known for some time (see [14–16] for the first calculations) and have been compared with those given in [95]. To test the correct implementation of the corresponding routines, the gg-routines have been checked numerically against those obtained from MadGraph for a multitude of phase space points. Moreover, both the gg- and the $q\bar{q}$-routines have been compared with the outcome of the Born matrix elements squared extracted from the FormCalc routines, which have been generated for the virtual contributions. Besides checking the correctness of the amplitudes squared, the results for total LO cross sections have been compared for individual channels with Prospino2 and for a combination of all channels with degenerate squark masses with Prospino*. This automatically provides a cross check for the correct combinatorics regarding the occurring flavour/chirality structures.
- **Real contributions:** As already mentioned in Sec. 3.1.3, the calculation of the real corrections has been conducted in two different gauges. The gauge independence of the total matrix elements squared can thus be easily checked by comparing the numerical results obtained in both approaches. Moreover, the real amplitudes for all production modes involving $\tilde{u}_L\bar{\tilde{u}}_L$, $\tilde{u}_L\bar{\tilde{u}}_R$ and $\tilde{u}_L\bar{\tilde{d}}_L$ (i.e. $ug \to \tilde{u}_L\bar{\tilde{u}}_L u$, $\bar{u}g \to \tilde{u}_L\bar{\tilde{u}}_L\bar{u}$ and $u\bar{u} \to \tilde{u}_L\bar{\tilde{u}}_L g$ etc.)

[9] I thank M.Spira for providing me this code.

have been generated with MadGraph and used to validate the results of the analytical calculation numerically for individual phase space points. Besides testing the full matrix elements squared, all amplitudes squared (and the resulting interference terms) in Fig. 3.7 have been compared individually with the MadGraph output (these contributions are not gauge invariant, thus this comparison is only possible using the same lightcone gauge as MadGraph, see Eq. (3.14)).

The correct expansion of the real matrix elements squared needed for the subtraction of the contributions with on-shell intermediate gluinos as defined in Eqs. (3.22) and (3.24) has been checked by comparing the results for the full and the expanded expression, both analytically and numerically. The gauge invariance of the expansion coefficients has been verified by testing their equivalence for the gauges considered in the calculation. Moreover, as discussed in Sec. 3.1.3.3, the subtraction schemes DS and DS* should yield identical results for $\Gamma_{\tilde{g}} \to 0$. Furthermore, in this limit the result should become independent of this regularization parameter. This behaviour is illustrated for a specific benchmark scenario in the next section. Finally, the contribution of the qg-channels to the total cross section has been compared individually with Prospino* for a multitude of mass combinations, both with $m_{\tilde{q}} > m_{\tilde{g}}$ and $m_{\tilde{q}} < m_{\tilde{g}}$.

The cancellation of the IR divergences against the FKS counterterms is tested in the Powheg-Box automatically by constructing for every possible singular region a set of momenta such that the soft and/or collinear limit is probed. The real matrix elements squared are then evaluated for these points and checked against their soft/collinear approximations. These depend on the process-dependent spin and colour-correlated Born amplitudes, see App. A.2. Thus testing the IR limits automatically provides a check for the correct implementation of those, too.

- **Virtual contributions:** The correctly renormalized results for the virtual corrections have to be free of UV divergences. In the framework of FormCalc/Looptools this can be tested at the level of the analytical Mathematica output by replacing the occurring loop integrals with their respective UV-divergent part. Moreover, the Looptools routines allow for a direct numerical test of the UV finiteness of the virtual contributions by setting $\Delta \equiv \frac{1}{\epsilon} - \gamma_E + \log(4\pi)$ (which is by default set to zero) to an arbitrary numerical value. Varying this value over a large range does not alter the outcome of a UV-finite result. However, note that the original Looptools routines do not distinguish between UV and IR poles. In order to directly assess either one of them the code had to be adapted. To this end, the routine used for the calculation of the two-point integrals has been modified correspondingly, including also the special case $B_0(0,0,0) = \Delta_{\mathrm{UV}} - \Delta_{\mathrm{IR}}$. Both tests have been conducted successfully. The finite parts of the counterterms obtained from FormCalc have been compared numerically with the analytical results from [44]. Note that the results given there are based on the assumption of a degenerate squark mass spectrum and had to be generalized accordingly.

Besides the UV divergences, the virtual terms contain also IR divergent parts. These divergences cancel those present in the real contributions, see Sec. 2.2.2.2. Their general

structure is process-independent and takes the form (see [96])

$$\begin{aligned}\mathcal{V} = \frac{\alpha_s}{2\pi}\frac{(4\pi)^\epsilon}{\Gamma(1-\epsilon)}\left(\frac{\mu_R^2}{Q^2}\right)^\epsilon \Bigg[\Bigg(&-\frac{1}{\epsilon^2}\sum_{k\in\mathcal{I}_l} C_k - \frac{1}{\epsilon}\sum_{k\in\mathcal{I}_l}\gamma_k - \frac{1}{\epsilon}\sum_{k\in\mathcal{I}_m} C_k\Bigg)\mathcal{B} \\ &+ \frac{2}{\epsilon}\sum_{k,l\in\mathcal{I}_l,k>l}\log\frac{2k_k\cdot k_l}{Q^2}\mathcal{B}_{kl} + \frac{2}{\epsilon}\sum_{k\in\mathcal{I}_l,l\in\mathcal{I}_m}\left(\log\frac{2k_k\cdot k_l}{Q^2} - \frac{1}{2}\log\frac{m_l^2}{Q^2}\right)\mathcal{B}_{kl} \\ &+ \frac{1}{\epsilon}\sum_{k,l\in\mathcal{I}_m,k>l}\frac{1}{\beta_{kl}}\log\frac{1+\beta_{kl}}{1-\beta_{kl}}\mathcal{B}_{kl} + \mathcal{V}_{\text{fin}}\Bigg],\end{aligned} \tag{3.37}$$

where $\mathcal{V}_{\text{fin}}$ subsumes the finite contributions and

$$\begin{aligned}\gamma_g &= \frac{11}{6}C_A - \frac{2}{3}T_F n_f, \quad \gamma_q = \frac{3}{2}C_F, \\ \beta_{kl} &= \sqrt{1-\frac{k_k^2 k_l^2}{(k_k\cdot k_l)^2}}.\end{aligned} \tag{3.38}$$

The Ellis-Sexton scale Q is not introduced in the calculation of the virtuals, thus $Q = \mu_R$ in Eq. (3.37). The set $\mathcal{I}_l$ comprises all external massless coloured particles, i.e. here only the initial-state partons. Correspondingly, $\mathcal{I}_m$ denotes the massive coloured particles, i.e. the final-state squarks. As usual, C_k are the Casimir invariants for the respective colour representation of the k^{th} particle. The normalization of the colour matrices is such that $T_F = 1/2$ and the number of massless partons is $n_f = 5$. Note that all terms in Eq. (3.37) involving the colour-correlated Born amplitudes $\mathcal{B}_{kl}$ are multiplied by a factor 2 compared to [96] to be compliant with the definition of the $\mathcal{B}_{kl}$ in Eq. (A.7). The prefactors of the $1/\epsilon^2$ and $1/\epsilon$ terms can be obtained numerically from the virtual routines generated with FormCalc for every phase space point and are in turn compared with the values evaluated according to Eq. (3.37).

Besides the divergent structures of the virtual amplitudes, the finite parts for the virtual contributions, expressed in terms of scalar loop integrals, have been compared to the results implemented in Prospino*. In detail, the prefactors of the B_0, C_0 and D_0 functions have been isolated and checked numerically, again for a multitude of different (degenerate) squark and gluino masses.

The generalization of the masses in the virtual routines for arbitrary squark antisquark pairs in the final state as described in Sec. 3.1.2 has been tested by generating the code for different combinations of final-state squarks. Specifically, this check has been performed by constructing the virtual contributions to both $gg \to \tilde{u}_L\bar{\tilde{u}}_L$ and $gg \to \tilde{d}_L\bar{\tilde{d}}_L$, generalizing in both cases the generated routines and comparing their outcome numerically for different final-state squarks with same flavour and chirality. Likewise, this procedure has been used to check the results of the other channels.

- **Total and differential cross section:** The computation of the total cross section has been checked by comparing the three production modes gg, $q\bar{q}$ and qg for the case of a degenerate mass spectrum with Prospino*. Moreover, the distributions for the transverse momenta of the squarks, $p_T^{\tilde{q}}$, and the rapidities $y^{\tilde{q}}$ have been compared to the distributions shown in [17] for $m_{\tilde{q}} = 600\,\text{GeV}$ and $m_{\tilde{g}} = 500\,\text{GeV}$.

Scenario	m_0	$m_{1/2}$	A_0	$\tan(\beta)$	$\mathrm{sgn}(\mu)$
10.3.6*	825 GeV	550 GeV	0 GeV	10	+1
10.4.5	1150 GeV	690 GeV	0 GeV	10	+1

Table 3.1.: The input parameters for the considered scenarios.

Similar checks have been performed for the NLO results of squark pair production. Moreover, in this case a comparison with the independent calculation presented in [28] could be performed, including detailed checks of all building blocks for a multitude of individual phase space points and a comparison of both total rates and numerous differential distributions, which were all found to agree within the statistical errors of the Monte Carlo integration. Furthermore, a comparison with the recently published results of the calculations presented in [19] and [20] has been conducted.

3.1.5. Results

3.1.5.1. Setup

For the following considerations two mSUGRA scenarios have been chosen which are not yet excluded by data, see e.g. [33, 54]. The scenarios are based on the CMSSM points 10.3.6*[10] and 10.4.5 from [97]. The input parameters of these scenarios are summarized in Tab. 3.1. The mass spectrum of the SUSY particles has been generated with SOFTSUSY 3.3.4 [98], the resulting on-shell masses are then used as input parameters. For the SM parameters the following values are used [77]:

$$\begin{aligned} m_Z = 91.1876\,\mathrm{GeV}, \quad G_F = 1.16637 \cdot 10^{-5}\,\mathrm{GeV}^{-2}, \\ \alpha_{em}(m_Z) = 1/127.934, \quad \alpha_s(m_Z) = 0.118, \\ m_b^{\overline{\mathrm{MS}}}(m_b) = 4.25\,\mathrm{GeV}, \quad m_t = 174.3\,\mathrm{GeV}, \quad m_\tau = 1.777\,\mathrm{GeV}. \end{aligned} \tag{3.39}$$

As SOFTSUSY implements non-vanishing Yukawa corrections, there is a small difference between the masses of the second-generation squarks and the corresponding first-generation ones, i.e. $m_{\tilde{u}_L} \neq m_{\tilde{c}_L}$ etc. To simplify the analysis and save computing time these masses are replaced by the mean of the mass pairs, i.e. $m_{\tilde{u}_L}$ and $m_{\tilde{c}_L}$ are replaced by $(m_{\tilde{u}_L} + m_{\tilde{c}_L})/2$ and so on. The obtained masses for the squarks of the first two generations are summarized in Tab. 3.2. In the virtual parts there are also contributions involving third-generation squarks. The masses of the $\tilde{t}$ and $\tilde{b}$ are not modified, they are listed in Tab. 3.3. Note that for the point 10.3.6* the mass hierarchy is $m_{\tilde{q}} > m_{\tilde{g}}$, while for 10.4.5 $m_{\tilde{q}} < m_{\tilde{g}}$, i.e. this point requires the subtraction of contributions with on-shell intermediate gluinos as described in Sec. 3.1.3.3. If not stated otherwise, the DS* method is used as subtraction scheme, with a default value for the regulator $\Gamma_{\tilde{g}} = 1\,\mathrm{GeV}$ (recall that this regulator is only needed if a subtraction is required, thus in all other cases it is set to zero).

The renormalization (μ_R) and factorization (μ_F) scales are chosen to $\mu_R = \mu_F = \overline{m}_{\tilde{q}}$, with $\overline{m}_{\tilde{q}}$ representing the average of the squark masses of the first two generations. For the two scenarios defined above one obtains $\overline{m}_{\tilde{q}}^{10.3.6^*} = 1779.31\,\mathrm{GeV}$ and $\overline{m}_{\tilde{q}}^{10.4.5} = 1714.25\,\mathrm{GeV}$, respectively. All subchannels for the production of first- and second-generation squarks are taken into account

[10] For the point 10.3.6 m_0 has been modified to get a mass spectrum consistent with the latest exclusion bounds.

Scenario	$m_{\tilde{u}_L} = m_{\tilde{c}_L}$	$m_{\tilde{u}_R} = m_{\tilde{c}_R}$	$m_{\tilde{d}_L} = m_{\tilde{s}_L}$	$m_{\tilde{d}_R} = m_{\tilde{s}_R}$	$m_{\tilde{g}}$
10.3.6*	1799.53	1760.21	1801.08	1756.40	1602.96
10.4.5	1746.64	1684.31	1748.25	1677.82	1840.58

Table 3.2.: The squark masses in [GeV] obtained with the parameters from Tab. 3.1 after averaging the masses of the first two generations as described in the text.

Scenario	$m_{\tilde{b}_1}$	$m_{\tilde{b}_2}$	$m_{\tilde{t}_1}$	$m_{\tilde{t}_2}$
10.3.6*	1585.94	1745.59	1288.84	1605.84
10.4.5	1590.12	1669.76	1336.02	1617.27

Table 3.3.: The $\tilde{t}$ and $\tilde{b}$ masses in [GeV] obtained with the parameters from Tab. 3.1.

for the results, i.e. if not stated otherwise all results presented in the rest of this chapter are obtained by adding up the subchannels.

The PDFs are taken from the LHAPDF package [99]. For the LO results shown in the following the LO set CTEQ6L1 [100] is used, while the NLO results are calculated with the NLO set CT10NLO with $\alpha_s(m_Z) = 0.118$ [101]. The strong coupling constant for the LO results is correspondingly computed using the one-loop RGEs, while the value used in the NLO results is obtained from the two-loop equations.

All results are calculated for the LHC, i.e. a pp-collider with $\sqrt{s} = 14\,\text{TeV}$. The error bars shown in the following are the statistical errors of the Monte Carlo integration, for all derived quantities like ratios of cross sections the errors have been calculated using Gaussian error propagation.

3.1.5.2. Phenomenological results

Scale dependence

The renormalization and factorization scales introduced in the calculation are unphysical and would drop out if all orders in perturbation theory could be calculated. Varying the numerical values used in the evaluation of the (N)LO results and comparing the resulting total and differential cross sections gives a rough estimate for the quality of the convergence of the perturbative series and allows for an estimation of the remaining theoretical uncertainty due to missing higher-order terms. To illustrate the effect of the scale variation for squark antisquark production the CMSSM point 10.3.6* is considered in the following. With the setup described in the previous section one obtains for the LO and NLO cross section (using $\mu_R = \mu_F = \overline{m}_{\tilde{q}}$)

$$\sigma_{\text{LO}} = 2.319\,\text{fb}, \qquad \sigma_{\text{NLO}} = 3.218\,\text{fb}\,, \tag{3.40}$$

which implies a K-factor

$$K = \frac{\sigma_{\text{NLO}}}{\sigma_{\text{LO}}} = 1.39\,. \tag{3.41}$$

To assess the scale dependence, μ_R and μ_F are varied around the central scale by considering $\mu_R = \mu_F = \xi\,\overline{m}_{\tilde{q}}$ with $\xi \in [0.1, 5.5]$. The rather awkward upper limit for ξ has been chosen as the CTEQ6L1 PDF set is only valid for scales $Q \leq 10\,\text{TeV}$, i.e. it is not sensible to consider

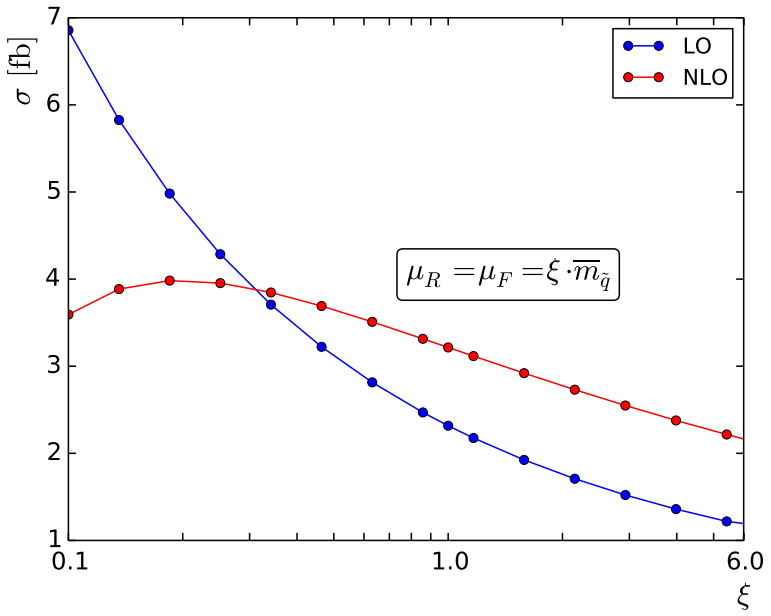

Figure 3.9.: The scale dependence of the LO and NLO cross section for $\mu_R = \mu_F = \xi\,\overline{m}_{\tilde{q}}$, using the CMSSM point 10.3.6*.

values $\xi \gtrsim 5.6$. The results obtained for the total cross section with these scale choices are shown in Fig. 3.9. Comparing the ranges covered by the LO and NLO results it is obvious that the NLO cross section exhibits a drastically reduced scale dependence compared to the LO one. Quantitatively, varying ξ by a factor two one finds

$$\begin{aligned} \sigma_{\mathrm{LO}}(\xi = 0.5) &= 3.117\,\mathrm{fb}, \qquad \sigma_{\mathrm{LO}}(\xi = 2) = 1.758\,\mathrm{fb}\,, \\ \sigma_{\mathrm{NLO}}(\xi = 0.5) &= 3.649\,\mathrm{fb}, \qquad \sigma_{\mathrm{NLO}}(\xi = 2) = 2.776\,\mathrm{fb} \end{aligned} \tag{3.42}$$

and thus (note the monotonic behaviour of the cross section $\sigma(\xi)$ in this range) at NLO a range of about $\pm 13\%$ and at LO a range of $^{+34\%}_{-24\%}$.

Varying μ_R and μ_F individually while keeping one of them at a fixed value one observes that both of them affect the total scale dependence, see Fig. 3.10. The influence of μ_R tends to be stronger, but the dependence on μ_F is by far not negligible. This is illustrated in Tab. 3.4, where for both the LO and the NLO results the spread in the results is given, which is defined as $\Delta\sigma \equiv \sigma^{\max} - \sigma^{\min}$ with the maximal/minimal cross sections $\sigma^{\max/\min}$ in the scopes considered in Fig. 3.10.

Besides comparing the scale dependence of total cross sections it is also interesting to consider LO and NLO results for differential distributions and the corresponding differential scale dependence.

Scales	$\mu_R = \xi\,\overline{m}_{\tilde{q}}$			$\mu_F = \xi\,\overline{m}_{\tilde{q}}$		
	$\mu_F = 0.1\,\overline{m}_{\tilde{q}}$	$\mu_F = \overline{m}_{\tilde{q}}$	$\mu_F = 5.5\,\overline{m}_{\tilde{q}}$	$\mu_R = 0.1\,\overline{m}_{\tilde{q}}$	$\mu_R = \overline{m}_{\tilde{q}}$	$\mu_R = 5.5\,\overline{m}_{\tilde{q}}$
$\Delta\sigma^{\mathrm{LO}}$ [fb]	4.11	2.44	1.78	3.88	2.18	1.55
$\Delta\sigma^{\mathrm{NLO}}$ [fb]	0.55	1.55	1.93	0.58	1.07	1.26

Table 3.4.: The spread in the total cross sections as defined in the text, obtained for different scale choices with $\xi \in [0.1, 5.5]$.

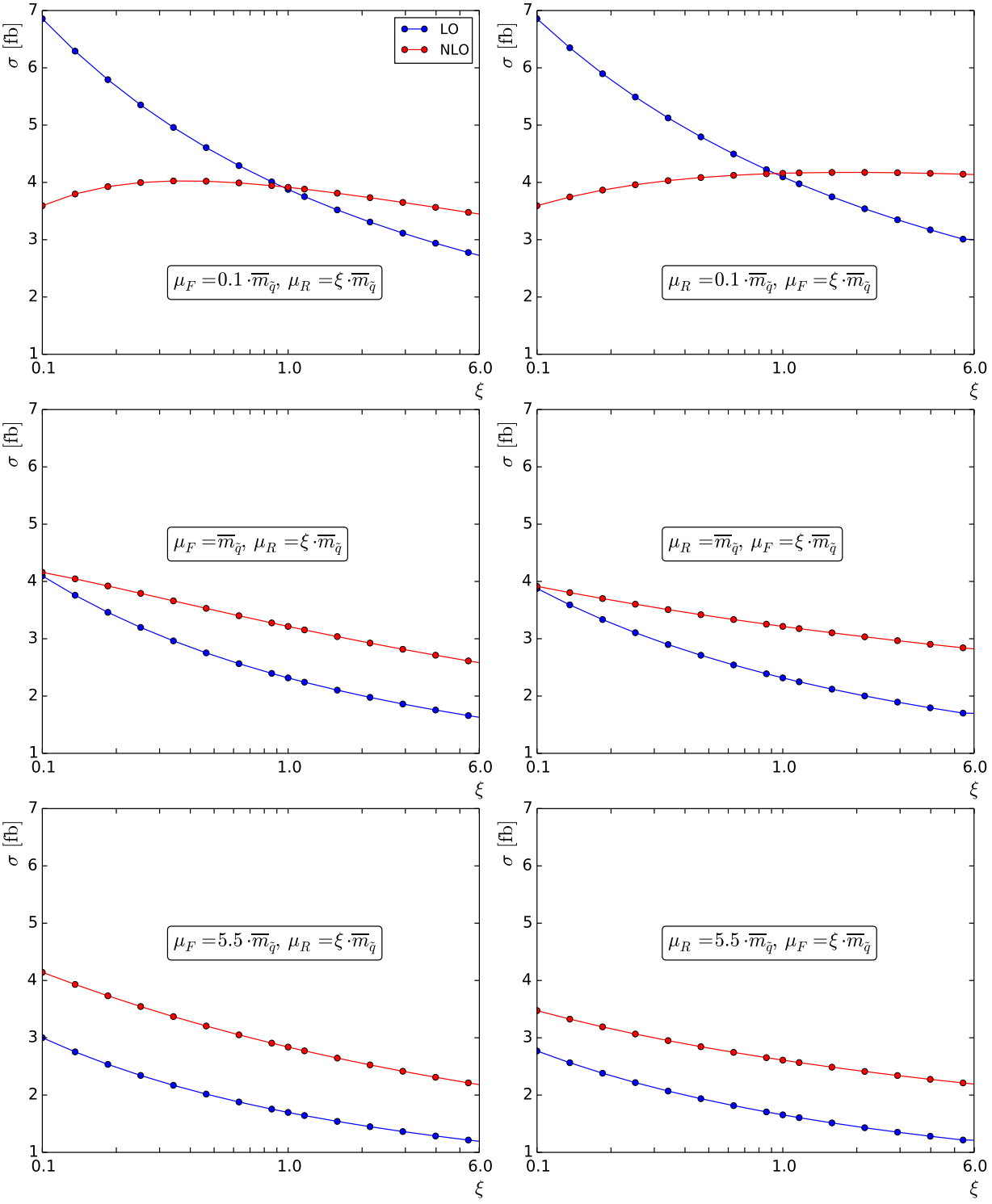

Figure 3.10.: The dependence of the total cross section on an individual variation of μ_R (left column) and μ_F (right column) with μ_F respectively μ_R set to the fixed values (from top to bottom) $\mu = 0.1\,\overline{m}_{\tilde{q}}\,, \overline{m}_{\tilde{q}}\,, 5.5\,\overline{m}_{\tilde{q}}$.

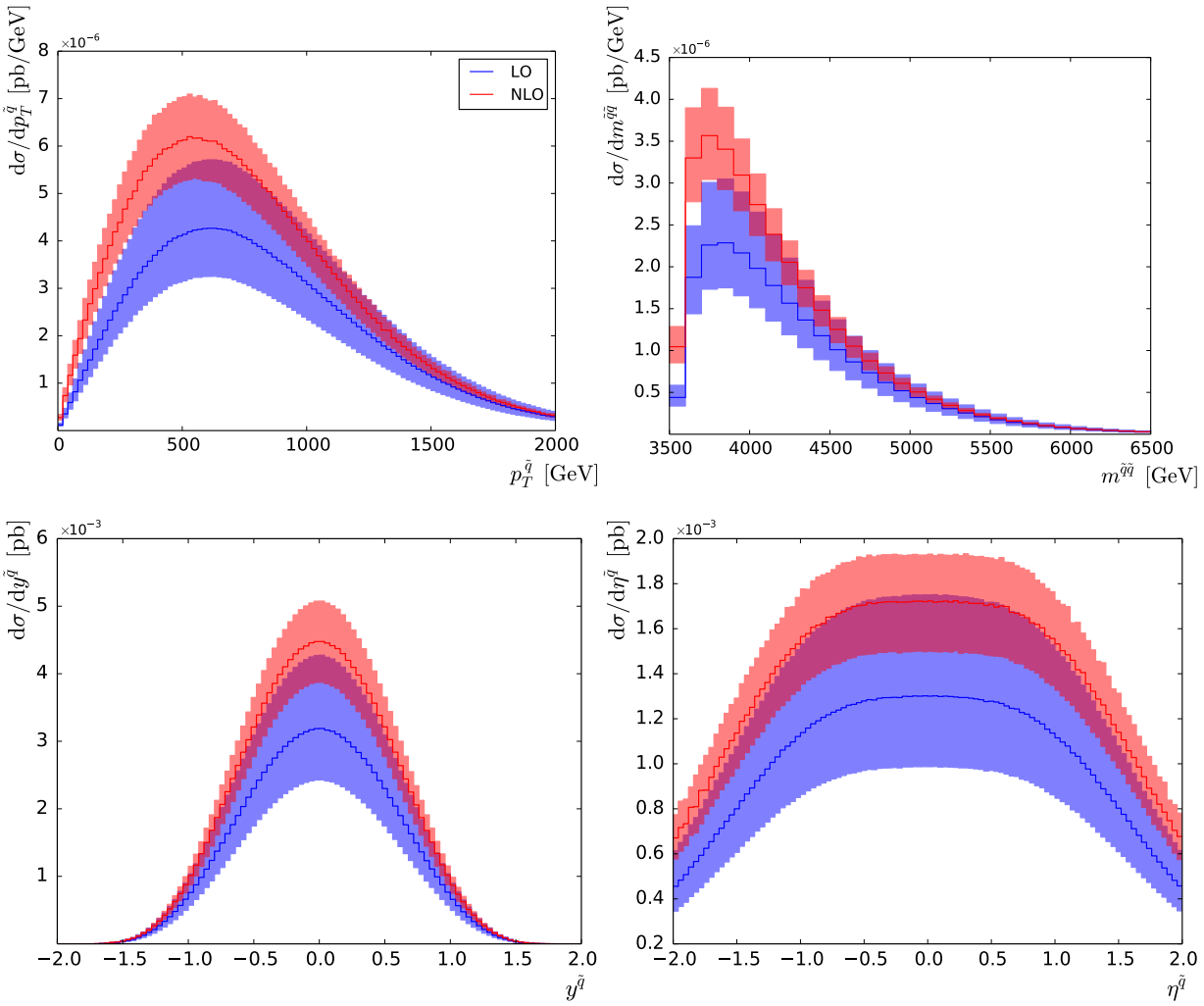

Figure 3.11.: The differential scale dependence for the transverse momentum $p_T^{\tilde{q}}$, the invariant mass $m^{\tilde{q}\bar{\tilde{q}}}$, the rapidity $y^{\tilde{q}}$ and the pseudorapidity $\eta^{\tilde{q}}$ for the scale choices $\mu_R = \mu_F = \xi\,\overline{m}_{\tilde{q}}$ with $\xi \in [0.5, 2]$, obtained for the CMSSM point 10.3.6*. The solid lines show the case $\xi = 1$.

To this end the LO and NLO results for the distributions of the transverse momentum $p_T^{\tilde{q}} \equiv \sqrt{p_x^2 + p_y^2}$, the rapidity $y^{\tilde{q}} \equiv \frac{1}{2}\log\frac{E+p_z}{E-p_z}$, the pseudorapidity $\eta^{\tilde{q}} \equiv -\log\left(\tan\frac{\Theta}{2}\right)$, where Θ is the angle between the beam axis and the squark momentum, and the invariant mass $m^{\tilde{q}\bar{\tilde{q}}} \equiv \sqrt{(p_{\tilde{q}} + p_{\bar{\tilde{q}}})^2}$ are shown in Fig. 3.11. The depicted results for $p_T^{\tilde{q}}$, $y^{\tilde{q}}$ and $\eta^{\tilde{q}}$ have been obtained by summing the contributions of the squark and the antisquark. To estimate the scale dependence the scales have been chosen equal again, $\mu_R = \mu_F = \xi\,\overline{m}_{\tilde{q}}$. The solid lines in Fig. 3.11 correspond to the case $\xi = 1$, the shaded areas have been obtained by varying ξ in the range $\xi \in [0.5, 2]$.

Comparing the size of the shaded areas for the LO and the NLO curves one notes again a reduction of the scale dependence when going from LO to NLO. For the $y^{\tilde{q}}$ and $\eta^{\tilde{q}}$ distribution the NLO bands overlap significantly with the estimated uncertainty range obtained for the LO predictions. Close to the production threshold, i.e. for small values of $p_T^{\tilde{q}}$ and $m^{\tilde{q}\bar{\tilde{q}}}$, however, the bands are far apart from each other and the NLO curve is strongly enhanced compared to the

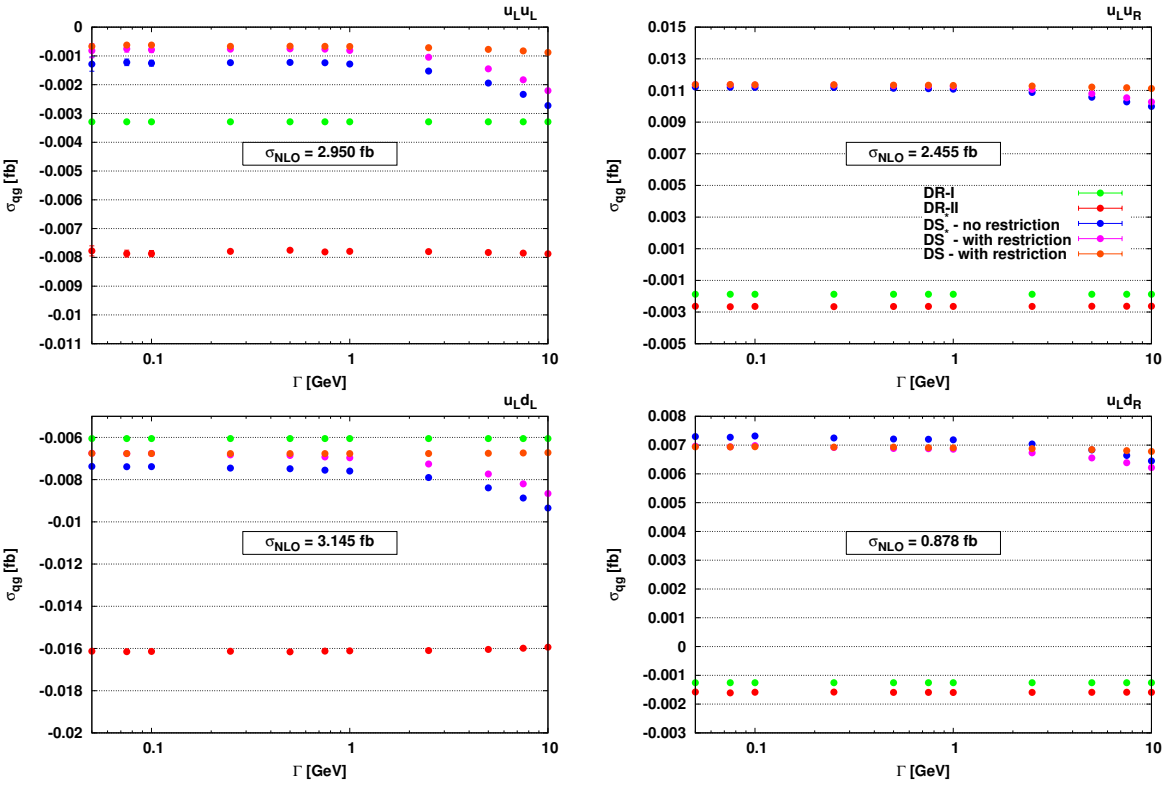

Figure 3.12.: The qg contributions as obtained by using the different subtraction schemes for the four representative $\tilde{q}\tilde{q}$-channels $\tilde{u}_L\tilde{u}_L$, $\tilde{u}_L\tilde{u}_R$, $\tilde{u}_L\tilde{d}_L$ and $\tilde{u}_L\tilde{d}_R$ with different choices for the regularization parameter $\Gamma_{\tilde{g}}$. For 'DS*–with restriction' the Jacobian has been modified according to Eq. (3.35), while 'DS*–no restriction' shows the (incorrect) results without applying this factor. To illustrate the differences between the (not gauge-invariant) DS and the DS* scheme the results obtained with the DS method (with restriction) are plotted, too. Also given is the full NLO cross section for the respective channels as obtained with the DS* scheme with the corrected Jacobian. This figure has been published in [91].

LO result. This enhancement is a well known effect and was already observed in the first NLO calculation of squark antisquark production (see [17]). It could be attributed to the exchange of Coulomb gluons between the (close to threshold slowly moving) final-state particles and the large corrections due to the radiation of soft gluons. These corrections can be resummed to all orders, see e.g. [102–110]. Further away from threshold, however, the NLO bands move entirely inside the LO bands, indicating a good convergence of perturbation theory.

On-shell intermediate gluinos

For scenarios with a mass hierarchy $m_{\tilde{q}} < m_{\tilde{g}}$ a subtraction of the contributions with on-shell intermediate gluinos is necessary. In Sec. 3.1.3.3 several methods already described in the literature and one new approach have been discussed. To illustrate the effect of the different approximations used in these approaches they are applied for the CMSSM point 10.4.5 specified in Tab. 3.1. For the numerical discussion the real contributions are evaluated in the lightcone gauge defined in Eq. (3.14) (recall that only the DS* scheme is not gauge dependent). As squark antisquark and squark pair production are affected by this subtraction, results for both process types will be shown in the following.

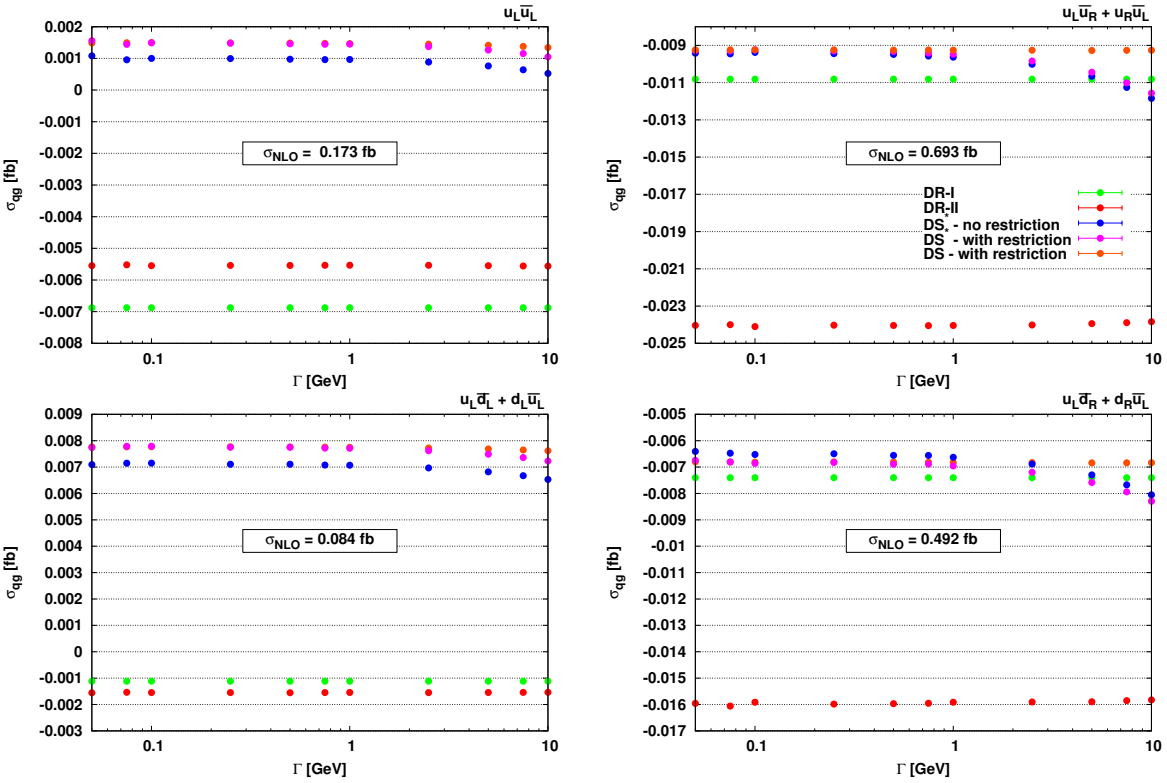

Figure 3.13.: Same as Fig. 3.12 for squark antisquark. For the plots both the qg and $\bar{q}g$-channels are taken into account.

In Fig. 3.12 the results for the qg contributions, σ_{qg}, to the specific subchannels $\tilde{u}_L\tilde{u}_L$, $\tilde{u}_L\tilde{u}_R$, $\tilde{u}_L\tilde{d}_L$ and $\tilde{u}_L\tilde{d}_R$ are shown as functions of the regulator $\Gamma_{\tilde{g}}$. Recall that the DR-I scheme does not require a regulator, the results obtained with this method are thus constant. These combinations of flavour and chirality represent all possible categories for squark pair production. The qg contributions comprise only the $2 \to 3$ parts of the respective processes, i.e. the real amplitudes squared with a qg initial state and the FKS counterterms for the subtraction of the IR divergences. Thus the differences visible in this quantity (which is not a physical observable) can be attributed directly to the neglected terms in the different subtraction schemes. The scales for these subchannels are set to the average of the respective final-state particles, i.e. $\mu_R = \mu_F = (m_{\tilde{q}_1} + m_{\tilde{q}_2})/2$. The curves for 'DS*–with restriction' and 'DS*–no restriction' have been obtained by including/excluding the correction factor to the Jacobian as defined in Eq. (3.35).

In Fig. 3.13 the corresponding results are depicted for squark antisquark production, again for a representative set of flavour/chirality combinations. Note that the shown results include the charge conjugate channels and both the qg and $\bar{q}g$ initiated processes, i.e. $\tilde{u}_L\bar{\tilde{d}}_L + \tilde{d}_L\bar{\tilde{u}}_L$ includes the processes $ug \to \tilde{u}_L\bar{\tilde{d}}_L d$, $\bar{d}g \to \tilde{u}_L\bar{\tilde{d}}_L\bar{u}$, $dg \to \tilde{d}_L\bar{\tilde{u}}_L u$ and $\bar{u}g \to \tilde{d}_L\bar{\tilde{u}}_L\bar{d}$.

Comparing the results one notes for both squark production processes the following:

- All predictions are essentially insensitive to the choice of the regularizing gluino width for $\Gamma_{\tilde{g}} \lesssim 1\,\text{GeV}$. For larger values the influence of $\Gamma_{\tilde{g}}$ becomes visible, as can be deduced from the plots for the DS* scheme for $\Gamma_{\tilde{g}} > 1\,\text{GeV}$. Using $\Gamma_{\tilde{g}} \lesssim 0.01\,\text{GeV}$ the results get numerically unstable. This region is excluded from the plots.

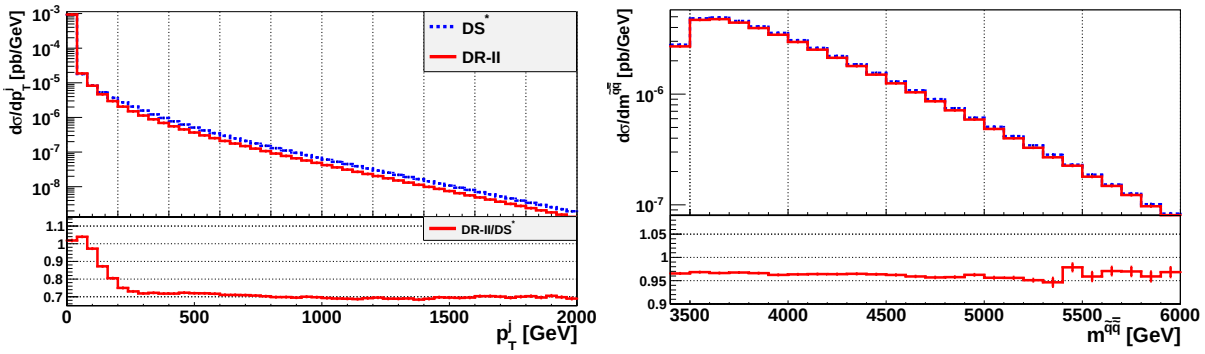

Figure 3.14.: The distributions for squark antisquark production of the transverse momentum of the radiated parton generated in the real contributions, p_T^j, (left) and the invariant mass $m^{\bar{q}\bar{q}}$ (right) for the subtraction methods DS* and DR-II. The lower panels show the respective ratio of the DR-II and the DS* result.

- The DS and DS* scheme become equivalent for $\Gamma_{\tilde{g}} \lesssim 1\,\text{GeV}$, as expected from the discussion in Sec. 3.1.3.3.
- The discrepancies in σ_{qg} between the DR schemes and the DS method are in general large and completely process-dependent.
- The influence of the modified Jacobian as defined in Eq. (3.35) is small, but not negligible.

Relating the results for σ_{qg} to the full NLO cross section, σ_{NLO}, one observes that in case of squark pair production this contribution plays only a minor role, at the sub-percent level, i.e. the observed discrepancies for the different subtraction methods hardly affect the full results. The values for σ_{NLO} are also depicted in the plots, they have been obtained by applying the DS* scheme with the corrected Jacobian. However, this statement holds only for the production of squarks of the first generation. If second-generation squarks are involved, the discrepancies in the results for the total cross sections of the different subchannels obtained with the different subtraction schemes can become rather large. Comparing e.g. the DS* and the DR-II method, deviations up to $\mathcal{O}(20\%)$ occur for channels including second-generation squarks. These large effects can be explained by the fact that in these cases the qg contributions gain in relative importance due to larger PDF factors f, e.g. $f_u f_g > f_u f_c$. Nevertheless, the impact of these channels on the total cross section after summing all subchannels is very small.

For squark antisquark production, however, the qg contributions can play a more significant role. To quantify the effect of the different subtraction methods on the full NLO cross section, the results for the individual subchannels are listed in the first columns of Tab. 3.5 for the DS* and the DR-II method. The charge conjugate channels have been combined in the table. The differences in the individual predictions cover a large range, from below 1% to more than 20%. In contrast to squark pair production, the impact of the channels with large differences on the total cross section is not negligible, resulting in a 3.5% discrepancy for the two methods applied here. The reason for this stronger sensitivity on the applied subtraction method lies simply in the fact that the qg (and $\bar{q}g$) channels contribute in general with $\mathcal{O}(\%)$ to the full NLO cross section, whereas their contribution in case of squark pair production amounts only to a per-mille effect for the relevant channels. For completeness the results for σ_{qg} and their percental contribution to σ_{NLO} are given in the last four columns of Tab. 3.5, again for each individual subchannel.

Besides the rather large effects on the total NLO cross section, the discrepancies in the individual

Process	σ^{DS^*}[fb]	$\sigma^{\text{DR-II}}$[fb]	Δ_σ[%]	$\sigma_{qg}^{\mathrm{DS}^*}$[fb]	$\frac{\sigma_{qg}^{\mathrm{DS}^*}}{\sigma^{\mathrm{DS}^*}}$[%]	$\sigma_{qg}^{\text{DR-II}}$[fb]	$\frac{\sigma_{qg}^{\text{DR-II}}}{\sigma^{\text{DR-II}}}$[%]
$\tilde{d}_R\bar{\tilde{u}}_R$	$1.09 \cdot 10^{-1}$	$1.00 \cdot 10^{-1}$	8.33	$7.47 \cdot 10^{-3}$	6.83	$-1.64 \cdot 10^{-3}$	−1.64
$\tilde{c}_R\bar{\tilde{s}}_R$	$8.28 \cdot 10^{-4}$	$6.02 \cdot 10^{-4}$	27.2	$1.83 \cdot 10^{-4}$	22.1	$-4.29 \cdot 10^{-5}$	−7.12
$\tilde{c}_L\bar{\tilde{d}}_R$	$4.47 \cdot 10^{-2}$	$4.19 \cdot 10^{-2}$	6.34	$-1.62 \cdot 10^{-3}$	−3.61	$-4.43 \cdot 10^{-3}$	−10.6
$\tilde{u}_L\bar{\tilde{d}}_R$	$4.92 \cdot 10^{-1}$	$4.83 \cdot 10^{-1}$	1.88	$-6.90 \cdot 10^{-3}$	−1.4	$-1.60 \cdot 10^{-2}$	−3.3
$\tilde{s}_L\bar{\tilde{u}}_R$	$2.12 \cdot 10^{-1}$	$2.03 \cdot 10^{-1}$	3.93	$-4.34 \cdot 10^{-3}$	−2.05	$-1.27 \cdot 10^{-2}$	−6.24
$\tilde{s}_R\bar{\tilde{c}}_L$	$3.23 \cdot 10^{-3}$	$2.98 \cdot 10^{-3}$	7.86	$-2.09 \cdot 10^{-4}$	−6.46	$-4.61 \cdot 10^{-4}$	−15.5
$\tilde{s}_L\bar{\tilde{s}}_L$	$9.11 \cdot 10^{-2}$	$9.10 \cdot 10^{-2}$	0.17	$-5.66 \cdot 10^{-3}$	−6.21	$-5.80 \cdot 10^{-3}$	−6.38
$\tilde{s}_L\bar{\tilde{d}}_L$	$1.35 \cdot 10^{-2}$	$1.11 \cdot 10^{-2}$	17.9	$2.03 \cdot 10^{-3}$	15.0	$-4.03 \cdot 10^{-4}$	−3.63
$\tilde{u}_L\bar{\tilde{c}}_L$	$2.79 \cdot 10^{-2}$	$2.08 \cdot 10^{-2}$	25.6	$5.97 \cdot 10^{-3}$	21.4	$-1.19 \cdot 10^{-3}$	−5.73
$\tilde{c}_R\bar{\tilde{c}}_R$	$1.27 \cdot 10^{-1}$	$1.27 \cdot 10^{-1}$	0.07	$-8.07 \cdot 10^{-3}$	−6.36	$-8.16 \cdot 10^{-3}$	−6.43
$\tilde{s}_L\bar{\tilde{d}}_R$	$7.37 \cdot 10^{-2}$	$7.08 \cdot 10^{-2}$	3.9	$-1.66 \cdot 10^{-3}$	−2.25	$-4.52 \cdot 10^{-3}$	−6.38
$\tilde{d}_R\bar{\tilde{d}}_R$	$1.64 \cdot 10^{-1}$	$1.62 \cdot 10^{-1}$	1.37	$-6.02 \cdot 10^{-3}$	−3.66	$-8.25 \cdot 10^{-3}$	−5.09
$\tilde{u}_L\bar{\tilde{d}}_L$	$8.42 \cdot 10^{-2}$	$7.49 \cdot 10^{-2}$	11.1	$7.80 \cdot 10^{-3}$	9.27	$-1.55 \cdot 10^{-3}$	−2.07
$\tilde{c}_R\bar{\tilde{d}}_R$	$1.15 \cdot 10^{-2}$	$9.13 \cdot 10^{-3}$	20.7	$1.94 \cdot 10^{-3}$	16.8	$-4.31 \cdot 10^{-4}$	−4.71
$\tilde{c}_R\bar{\tilde{u}}_L$	$1.26 \cdot 10^{-1}$	$1.19 \cdot 10^{-1}$	5.34	$-5.25 \cdot 10^{-3}$	−4.17	$-1.18 \cdot 10^{-2}$	−9.9
$\tilde{s}_L\bar{\tilde{s}}_R$	$5.18 \cdot 10^{-3}$	$4.88 \cdot 10^{-3}$	5.73	$-2.61 \cdot 10^{-4}$	−5.03	$-5.54 \cdot 10^{-4}$	−11.4
$\tilde{d}_L\bar{\tilde{c}}_L$	$9.20 \cdot 10^{-3}$	$6.82 \cdot 10^{-3}$	25.9	$1.98 \cdot 10^{-3}$	21.5	$-3.94 \cdot 10^{-4}$	−5.78
$\tilde{u}_L\bar{\tilde{s}}_R$	$2.15 \cdot 10^{-1}$	$2.08 \cdot 10^{-1}$	3.14	$-5.47 \cdot 10^{-3}$	−2.55	$-1.20 \cdot 10^{-2}$	−5.78
$\tilde{c}_R\bar{\tilde{u}}_R$	$3.41 \cdot 10^{-2}$	$2.70 \cdot 10^{-2}$	20.8	$5.80 \cdot 10^{-3}$	17.0	$-1.26 \cdot 10^{-3}$	−4.66
$\tilde{d}_R\bar{\tilde{d}}_L$	$2.41 \cdot 10^{-1}$	$2.36 \cdot 10^{-1}$	1.91	$-3.41 \cdot 10^{-3}$	−1.42	$-8.15 \cdot 10^{-3}$	−3.45
$\tilde{c}_L\bar{\tilde{c}}_L$	$9.16 \cdot 10^{-2}$	$9.15 \cdot 10^{-2}$	0.11	$-5.77 \cdot 10^{-3}$	−6.3	$-5.86 \cdot 10^{-3}$	−6.4
$\tilde{u}_R\bar{\tilde{u}}_L$	$6.94 \cdot 10^{-1}$	$6.79 \cdot 10^{-1}$	2.12	$-9.44 \cdot 10^{-3}$	−1.36	$-2.40 \cdot 10^{-2}$	−3.54
$\tilde{u}_R\bar{\tilde{c}}_L$	$1.27 \cdot 10^{-1}$	$1.18 \cdot 10^{-1}$	6.57	$-4.32 \cdot 10^{-3}$	−3.41	$-1.26 \cdot 10^{-2}$	−10.6
$\tilde{c}_R\bar{\tilde{d}}_L$	$4.35 \cdot 10^{-2}$	$4.13 \cdot 10^{-2}$	4.98	$-1.90 \cdot 10^{-3}$	−4.37	$-4.06 \cdot 10^{-3}$	−9.82
$\tilde{u}_R\bar{\tilde{d}}_L$	$4.84 \cdot 10^{-1}$	$4.74 \cdot 10^{-1}$	2.09	$-6.03 \cdot 10^{-3}$	−1.25	$-1.63 \cdot 10^{-2}$	−3.44
$\tilde{c}_R\bar{\tilde{s}}_L$	$3.16 \cdot 10^{-3}$	$2.92 \cdot 10^{-3}$	7.43	$-2.10 \cdot 10^{-4}$	−6.65	$-4.43 \cdot 10^{-4}$	−15.2
$\tilde{s}_R\bar{\tilde{d}}_R$	$1.76 \cdot 10^{-2}$	$1.52 \cdot 10^{-2}$	13.6	$1.93 \cdot 10^{-3}$	11.0	$-4.37 \cdot 10^{-4}$	−2.88
$\tilde{u}_L\bar{\tilde{u}}_L$	$1.74 \cdot 10^{-1}$	$1.67 \cdot 10^{-1}$	4.09	$1.60 \cdot 10^{-3}$	0.92	$-5.46 \cdot 10^{-3}$	−3.27
$\tilde{s}_R\bar{\tilde{s}}_R$	$1.32 \cdot 10^{-1}$	$1.32 \cdot 10^{-1}$	0.11	$-8.31 \cdot 10^{-3}$	−6.3	$-8.45 \cdot 10^{-3}$	−6.42
$\tilde{s}_R\bar{\tilde{d}}_L$	$7.33 \cdot 10^{-2}$	$7.12 \cdot 10^{-2}$	2.94	$-2.01 \cdot 10^{-3}$	−2.74	$-4.20 \cdot 10^{-3}$	−5.9
$\tilde{c}_L\bar{\tilde{c}}_R$	$1.96 \cdot 10^{-3}$	$1.77 \cdot 10^{-3}$	9.73	$-1.60 \cdot 10^{-4}$	−8.15	$-3.50 \cdot 10^{-4}$	−19.7
$\tilde{d}_L\bar{\tilde{d}}_L$	$1.15 \cdot 10^{-1}$	$1.13 \cdot 10^{-1}$	2.02	$-3.38 \cdot 10^{-3}$	−2.94	$-5.67 \cdot 10^{-3}$	−5.03
$\tilde{u}_L\bar{\tilde{s}}_L$	$4.13 \cdot 10^{-2}$	$3.41 \cdot 10^{-2}$	17.4	$6.01 \cdot 10^{-3}$	14.6	$-1.20 \cdot 10^{-3}$	−3.51
$\tilde{s}_L\bar{\tilde{c}}_L$	$6.63 \cdot 10^{-4}$	$4.29 \cdot 10^{-4}$	35.3	$1.95 \cdot 10^{-4}$	29.5	$-3.86 \cdot 10^{-5}$	−8.99
$\tilde{s}_R\bar{\tilde{u}}_R$	$5.22 \cdot 10^{-2}$	$4.52 \cdot 10^{-2}$	13.4	$5.70 \cdot 10^{-3}$	10.9	$-1.26 \cdot 10^{-3}$	−2.78
$\tilde{u}_R\bar{\tilde{u}}_R$	$2.31 \cdot 10^{-1}$	$2.24 \cdot 10^{-1}$	3.06	$-5.71 \cdot 10^{-4}$	−0.25	$-7.56 \cdot 10^{-3}$	−3.38
Sum	4.37	4.21	3.57	-0.0424	-0.97	-0.198	-4.69

Table 3.5.: The NLO cross sections for squark antisquark production obtained for the CMSSM point 10.4.5 applying the DS* scheme (second column) and the DR-II method (third column), with $\Delta_\sigma \equiv \left(\sigma^{\mathrm{DS}^*} - \sigma^{\text{DR-II}}\right)/\sigma^{\mathrm{DS}^*}$. The last four columns contain the numerical values for the quantity σ_{qg} as defined in the text and the respective contribution to the full NLO cross section, again for both the DS* and the DR-II method.

channels can play a significant role if the decays of the squarks are taken into account, see the discussion in the next paragraph. Moreover, the impact on differential distributions which are sensitive to the emitted parton of the real contributions and thus to the real amplitudes squared can be much larger compared to the effects on the total cross section. As an example Fig. 3.14 shows the distributions of the transverse momentum of the emitted parton, p_T^j, and the invariant mass $m^{\tilde{q}\bar{\tilde{q}}}$ for squark antisquark production. While the $m^{\tilde{q}\bar{\tilde{q}}}$ distribution essentially reflects the difference in the overall normalization, the p_T^j predictions differ for $p_T^j > 200\,\text{GeV}$ by about 30%. Considering the same distributions for squark pair production, the discrepancy in p_T^j amounts to about 7%, while the $m^{\tilde{q}\tilde{q}}$ distribution is affected only at the sub-percent level.

The remainder of this section is devoted to a comparison of the results obtained with the fully differential NLO calculation, taking into account the full mass dependence, and the 'status quo ante', i.e. the predictions obtained in a similar way as implemented in Prospino2. All results in the following are obtained with the implementation of squark antisquark production in the Powheg-Box, mimicking for comparison the way Prospino2 calculates NLO results. This is achieved by maintaining the full mass dependence for the LO results, but approximating the NLO effects by rescaling the individual LO results with a common K-factor, obtained from the ratio of the NLO and LO results with averaged squark masses. Concerning differential distributions at NLO accuracy there is no publicly available program to produce those. Hitherto, they have been only approximated by rescaling the LO results with a constant K-factor calculated with Prospino(2).[11]

To check the underlying assumptions of these approximations the following questions will be investigated:

- Is it sufficient to calculate the LO results for individual channels with the full mass dependence and approximate the NLO contributions by multiplying them with a common K-factor, i.e. is it sufficient to take the dominant kinematic effects into account and approximate all other mass effects by using an averaged squark mass?
- Is it justified to rescale LO histograms with a global K-factor, i.e. are the differential K-factors flat?
- How sensitive are these approximations to the differences in the squark masses?

Individual channels

To assess the numerical effect of individual K-factors for the different subchannels the benchmark scenario CMSSM 10.3.6* is considered again. The LO and NLO results for all channels contributing to the production of a squark antisquark pair involving squarks of the first two generations are summarized in the first columns of Tab. 3.6. Note that the final states which are charge conjugate to each other have been combined, i.e. $\tilde{q}_i\bar{\tilde{q}}_j$ is the sum of $\tilde{q}_i\bar{\tilde{q}}_j + \tilde{q}_j\bar{\tilde{q}}_i$ $(i \neq j)$.

The LO results have been reproduced with Prospino2. Considering the concrete values for the individual K-factors one notices that they differ significantly for the different channels. Moreover, the K-factors for the channels involving strange and charm quark PDFs (i.e. $\tilde{s}$ and $\tilde{c}$ squarks in the final state) are unnaturally large. This effect has already been observed in the context of squark pair production and could be traced back to large differences in the strange

[11] This is not entirely true, as Prospino(2) can be used to obtain the NLO distributions for the transverse momentum and the rapidity of the squarks. However, this is only possible for degenerate squark masses and thus not fully general.

Process	σ_{LO}[fb]	σ_{NLO}[fb]	K-factor	$\sigma_{\mathrm{LO}}^{\mathrm{CT10}}$[fb]	K-factor (CT10)
$\tilde{d}_R\bar{\tilde{u}}_R$	$8.36 \cdot 10^{-2}$	$9.54 \cdot 10^{-2}$	1.14	$5.69 \cdot 10^{-2}$	1.68
$\tilde{u}_L\bar{\tilde{c}}_L$	$1.20 \cdot 10^{-2}$	$2.34 \cdot 10^{-2}$	1.95	$1.40 \cdot 10^{-2}$	1.67
$\tilde{c}_R\bar{\tilde{s}}_R$	$2.14 \cdot 10^{-4}$	$6.07 \cdot 10^{-4}$	2.84	$3.41 \cdot 10^{-4}$	1.78
$\tilde{c}_L\bar{\tilde{d}}_R$	$1.58 \cdot 10^{-2}$	$3.17 \cdot 10^{-2}$	2.01	$1.94 \cdot 10^{-2}$	1.63
$\tilde{u}_L\bar{\tilde{d}}_R$	$2.98 \cdot 10^{-1}$	$3.54 \cdot 10^{-1}$	1.19	$2.08 \cdot 10^{-1}$	1.70
$\tilde{u}_L\bar{\tilde{s}}_R$	$1.19 \cdot 10^{-1}$	$1.55 \cdot 10^{-1}$	1.30	$9.35 \cdot 10^{-2}$	1.66
$\tilde{s}_R\bar{\tilde{c}}_L$	$9.10 \cdot 10^{-4}$	$2.20 \cdot 10^{-3}$	2.42	$1.34 \cdot 10^{-3}$	1.64
$\tilde{s}_L\bar{\tilde{d}}_L$	$8.04 \cdot 10^{-3}$	$1.20 \cdot 10^{-2}$	1.49	$7.12 \cdot 10^{-3}$	1.69
$\tilde{u}_R\bar{\tilde{s}}_L$	$1.17 \cdot 10^{-1}$	$1.53 \cdot 10^{-1}$	1.31	$9.23 \cdot 10^{-2}$	1.66
$\tilde{c}_R\bar{\tilde{c}}_R$	$4.44 \cdot 10^{-2}$	$8.20 \cdot 10^{-2}$	1.85	$5.55 \cdot 10^{-2}$	1.48
$\tilde{u}_R\bar{\tilde{c}}_R$	$1.43 \cdot 10^{-2}$	$2.78 \cdot 10^{-2}$	1.94	$1.65 \cdot 10^{-2}$	1.68
$\tilde{d}_R\bar{\tilde{d}}_R$	$6.89 \cdot 10^{-2}$	$1.11 \cdot 10^{-1}$	1.61	$7.30 \cdot 10^{-2}$	1.52
$\tilde{u}_L\bar{\tilde{d}}_L$	$6.98 \cdot 10^{-2}$	$7.89 \cdot 10^{-2}$	1.13	$4.72 \cdot 10^{-2}$	1.67
$\tilde{c}_R\bar{\tilde{d}}_R$	$4.10 \cdot 10^{-3}$	$9.24 \cdot 10^{-3}$	2.25	$5.42 \cdot 10^{-3}$	1.70
$\tilde{c}_R\bar{\tilde{u}}_L$	$5.20 \cdot 10^{-2}$	$9.18 \cdot 10^{-2}$	1.77	$5.67 \cdot 10^{-2}$	1.62
$\tilde{s}_L\bar{\tilde{c}}_L$	$1.70 \cdot 10^{-4}$	$4.85 \cdot 10^{-4}$	2.85	$2.77 \cdot 10^{-4}$	1.75
$\tilde{d}_L\bar{\tilde{c}}_L$	$3.35 \cdot 10^{-3}$	$7.63 \cdot 10^{-3}$	2.28	$4.51 \cdot 10^{-3}$	1.69
$\tilde{d}_R\bar{\tilde{d}}_L$	$1.41 \cdot 10^{-1}$	$1.70 \cdot 10^{-1}$	1.21	$9.88 \cdot 10^{-2}$	1.72
$\tilde{c}_L\bar{\tilde{c}}_R$	$3.68 \cdot 10^{-4}$	$1.35 \cdot 10^{-3}$	3.67	$8.43 \cdot 10^{-4}$	1.60
$\tilde{s}_R\bar{\tilde{s}}_L$	$2.21 \cdot 10^{-3}$	$3.51 \cdot 10^{-3}$	1.59	$2.10 \cdot 10^{-3}$	1.67
$\tilde{u}_R\bar{\tilde{s}}_R$	$3.37 \cdot 10^{-2}$	$4.46 \cdot 10^{-2}$	1.32	$2.66 \cdot 10^{-2}$	1.68
$\tilde{u}_R\bar{\tilde{u}}_L$	$3.75 \cdot 10^{-1}$	$5.12 \cdot 10^{-1}$	1.37	$3.07 \cdot 10^{-1}$	1.67
$\tilde{d}_L\bar{\tilde{d}}_L$	$5.50 \cdot 10^{-2}$	$8.79 \cdot 10^{-2}$	1.60	$5.83 \cdot 10^{-2}$	1.51
$\tilde{c}_R\bar{\tilde{d}}_L$	$1.55 \cdot 10^{-2}$	$3.13 \cdot 10^{-2}$	2.02	$1.91 \cdot 10^{-2}$	1.64
$\tilde{u}_R\bar{\tilde{d}}_L$	$2.94 \cdot 10^{-1}$	$3.49 \cdot 10^{-1}$	1.19	$2.05 \cdot 10^{-1}$	1.70
$\tilde{d}_R\bar{\tilde{s}}_L$	$3.66 \cdot 10^{-2}$	$5.23 \cdot 10^{-2}$	1.43	$3.12 \cdot 10^{-2}$	1.68
$\tilde{c}_R\bar{\tilde{s}}_L$	$8.95 \cdot 10^{-4}$	$2.17 \cdot 10^{-3}$	2.42	$1.32 \cdot 10^{-3}$	1.64
$\tilde{u}_L\bar{\tilde{s}}_L$	$2.82 \cdot 10^{-2}$	$3.71 \cdot 10^{-2}$	1.32	$2.23 \cdot 10^{-2}$	1.66
$\tilde{s}_R\bar{\tilde{d}}_R$	$9.89 \cdot 10^{-3}$	$1.47 \cdot 10^{-2}$	1.49	$8.68 \cdot 10^{-3}$	1.69
$\tilde{s}_L\bar{\tilde{s}}_L$	$3.61 \cdot 10^{-2}$	$6.63 \cdot 10^{-2}$	1.84	$4.52 \cdot 10^{-2}$	1.47
$\tilde{u}_R\bar{\tilde{u}}_R$	$1.14 \cdot 10^{-1}$	$1.72 \cdot 10^{-1}$	1.51	$1.12 \cdot 10^{-1}$	1.54
$\tilde{s}_R\bar{\tilde{d}}_L$	$3.66 \cdot 10^{-2}$	$5.23 \cdot 10^{-2}$	1.43	$3.12 \cdot 10^{-2}$	1.68
$\tilde{u}_L\bar{\tilde{u}}_L$	$9.51 \cdot 10^{-2}$	$1.43 \cdot 10^{-1}$	1.50	$9.30 \cdot 10^{-2}$	1.54
$\tilde{u}_R\bar{\tilde{c}}_L$	$5.20 \cdot 10^{-2}$	$9.17 \cdot 10^{-2}$	1.76	$5.67 \cdot 10^{-2}$	1.62
$\tilde{s}_R\bar{\tilde{s}}_R$	$4.55 \cdot 10^{-2}$	$8.40 \cdot 10^{-2}$	1.85	$5.68 \cdot 10^{-2}$	1.48
$\tilde{c}_L\bar{\tilde{c}}_L$	$3.61 \cdot 10^{-2}$	$6.66 \cdot 10^{-2}$	1.84	$4.54 \cdot 10^{-2}$	1.47
Sum	2.32	3.22	1.39	1.97	1.63

Table 3.6.: Results for the LO and NLO cross section for individual channels. The charge conjugate channels have been combined and the CMSSM point 10.3.6* has been used. The results for σ_{LO} and the first K-factor have been obtained with the CTEQ6L1 PDF set and one-loop running α_s, while the results $\sigma_{\mathrm{LO}}^{\mathrm{CT10}}$ and the second K-factor have been calculated with the NLO set CT10NLO and two-loop running α_s.

Scenario	BR($\tilde{u}_L \to u\tilde{\chi}_1^0$)	BR($\tilde{u}_R \to u\tilde{\chi}_1^0$)	BR($\tilde{d}_L \to d\tilde{\chi}_1^0$)	BR($\tilde{d}_R \to d\tilde{\chi}_1^0$)
10.3.6*	0.0095	0.573	0.0117	0.260
10.4.5	0.013	0.998	0.015	0.999

Table 3.7.: The LO branching ratios for the decay $\tilde{q} \to \tilde{\chi}_1^0 q$ for the two scenarios considered here. For the calculation see Sec. 3.2.

and charm PDFs for the sets used in the numerical evaluation there, CTEQ6L1 and CTEQ6mE, for large x-values (for an extensive discussion see [28])). The same explanation holds here in case of the t-channel graphs for the modes $q_i\,\bar{q}_j \to \tilde{q}_k^{c1}\,\bar{\tilde{q}}_l^{c2}$. Using the same set for both the LO and NLO results eliminates this effect, as can be concluded from the last two columns of Tab. 3.6, where the LO cross sections obtained with the CT10NLO PDFs and the resulting K-factors are shown. Note that the resulting values for $\sigma_{\text{LO}}^{\text{CT10}}$ are smaller than those obtained with the CTEQ6L1 set. The observation that individual K-factors differ significantly from the total K-factor, however, is still valid.

Using the exact NLO results for the individual channels may be important if the decays of the squarks are taken into account and the branching ratios for the different squarks differ significantly. To be more quantitative, consider the case of both the squark and the antisquark decaying into the lightest neutralino and an (anti)quark. The LO branching ratios are defined as

$$\text{BR}^{\text{LO}}\left(\tilde{q} \to \tilde{\chi}_1^0 q\right) = \frac{\Gamma_{\text{LO}}^{\tilde{q}\to\tilde{\chi}_1^0 q}}{\Gamma_{\text{tot,LO}}^{\tilde{q}}}\,, \tag{3.43}$$

with the partial width for these decays, $\Gamma_{\text{LO}}^{\tilde{q}\to\tilde{\chi}_1^0 q}$, and the total squark width $\Gamma_{\text{tot,LO}}^{\tilde{q}}$. The branching ratios are summarized in Tab. 3.7, for a discussion of the calculation of the relevant widths see Sec. 3.2.

Multiplying the NLO production results with the LO decay results and adding up all subchannels yields

$$\sum_{\text{channels}} \sigma_{\text{NLO}} \cdot \text{BR}^{\text{LO}}\left(\tilde{q} \to \tilde{\chi}_1^0 q\right) \cdot \text{BR}^{\text{LO}}\left(\bar{\tilde{q}} \to \tilde{\chi}_1^0 \bar{q}\right) = 0.139\,\text{fb}. \tag{3.44}$$

To mimic the way PROSPINO obtains the individual NLO results a common K-factor has to be calculated, using an averaged squark mass $m_{\tilde{q}} = 1779.31\,\text{GeV}$. In the case at hand this leads to

$$\begin{aligned} \sigma_{\text{LO}}^{\text{avg}} = 2.315\,\text{fb}, \qquad \sigma_{\text{NLO}}^{\text{avg}} = 3.218\,\text{fb} \\ \Rightarrow K^{\text{avg}} = 1.39\,, \end{aligned} \tag{3.45}$$

with the LO result obtained again using the CTEQ6L1 set. Note that the difference compared to the full calculation given in Eq. (3.40) is marginal. This is due to the fact that the spread in the squark masses is rather small. For larger $\Delta m_{\tilde{q}}$ the differences in the K-factor can be larger, as will be discussed in the next paragraph.

Multiplying the LO result for each subchannel with this common K-factor and the corresponding branching ratios gives

$$\sum_{\text{channels}} \sigma_{\text{LO}} \cdot K^{\text{avg}} \cdot \text{BR}^{\text{LO}}\left(\tilde{q} \to \tilde{\chi}_1^0 q\right) \cdot \text{BR}^{\text{LO}}\left(\bar{\tilde{q}} \to \tilde{\chi}_1^0 \bar{q}\right) = 0.126\,\text{fb}\,. \tag{3.46}$$

Thus the rate obtained with the approximation relying on a constant K-factor for all subchannels is roughly 10% smaller for this special case.

Repeating this procedure for the benchmark scenario CMSSM 10.4.5 one obtains for the PROSPINO-like K-factor

$$\begin{aligned} \sigma_{\mathrm{LO}}^{\mathrm{avg}} = 3.090\,\mathrm{fb}, \qquad \sigma_{\mathrm{NLO}}^{\mathrm{avg}} = 4.356\,\mathrm{fb} \\ \Rightarrow K^{\mathrm{avg}} = 1.41\,. \end{aligned} \tag{3.47}$$

Again, comparing this result to the full calculation, which yields $\sigma_{\mathrm{LO}} = 3.098\,\mathrm{fb}$ and $\sigma_{\mathrm{NLO}} = 4.366\,\mathrm{fb}$, the discrepancy is only tiny.

Considering the individual subchannels with the correct individual NLO corrections yields

$$\sum_{\text{channels}} \sigma_{\mathrm{NLO}} \cdot \mathrm{BR}^{\mathrm{LO}}\left(\tilde{q} \to \tilde{\chi}_1^0 q\right) \cdot \mathrm{BR}^{\mathrm{LO}}\left(\bar{\tilde{q}} \to \tilde{\chi}_1^0 \bar{q}\right) = 0.916\,\mathrm{fb}, \tag{3.48}$$

while the approximation of the common K-factor gives

$$\sum_{\text{channels}} \sigma_{\mathrm{LO}} \cdot K^{\mathrm{avg}} \cdot \mathrm{BR}^{\mathrm{LO}}\left(\tilde{q} \to \tilde{\chi}_1^0 q\right) \cdot \mathrm{BR}^{\mathrm{LO}}\left(\bar{\tilde{q}} \to \tilde{\chi}_1^0 \bar{q}\right) = 0.807\,\mathrm{fb} \tag{3.49}$$

and thus again a discrepancy of about 10%.

Differential K-factors

In order to test the effect of the NLO contributions on differential distributions the LO and NLO results for the four representative observables already shown in Fig. 3.11, i.e. $p_T^{\tilde{q}}$, $m^{\tilde{q}\bar{\tilde{q}}}$, $\eta^{\tilde{q}}$ and $y^{\tilde{q}}$ evaluated for the scenario 10.3.6*, are depicted in Fig. 3.15. Again, the distributions for $p_T^{\tilde{q}}$, $y^{\tilde{q}}$ and $\eta^{\tilde{q}}$ have been obtained by adding those for the squark and the antisquark. The lower part of each plot shows the ratio of the NLO result over the LO prediction, i.e. the differential K-factor (full), and the global K-factor (dashed).

The differences between the differential and the global K-factors can be sizeable. For the $y^{\tilde{q}}$ and $\eta^{\tilde{q}}$ distributions the deviations are smaller than 10% in the central region, where the bulk of the squarks is produced, in agreement with the observations in [111] for the rapidity distribution. The NLO corrections to the $p_T^{\tilde{q}}$ and $m^{\tilde{q}\bar{\tilde{q}}}$ distributions, however, are strongly enhanced in the threshold region (see the comments following Fig. 3.11) and approach the LO results far away from threshold. The global K-factor is thus a mere average of this shape, which is by far not flat.[12]

So far the fixed scale $\mu_R = \mu_F = \overline{m}_{\tilde{q}}$ has been used for the numerical evaluation. To assess the influence of a dynamic scale the calculation has been repeated for $\mu_R = \mu_F = \overline{m}_T$, with $\overline{m}_T$ defined as the average of the two transverse masses of the squarks,

$$\overline{m}_T = \frac{1}{2}\left(\sqrt{m_{\tilde{q}}^2 + p_{T,\tilde{q}}^2} + \sqrt{m_{\bar{\tilde{q}}}^2 + p_{T,\bar{\tilde{q}}}^2}\right). \tag{3.50}$$

With this scale choice the total cross sections change to

$$\sigma_{\mathrm{LO}} = 2.212\,\mathrm{fb}, \qquad \sigma_{\mathrm{NLO}} = 3.157\,\mathrm{fb}\,, \tag{3.51}$$

[12] Using the CT10NLO PDFs for the LO distributions does not change this observation, i.e. it is a genuine effect of the NLO calculation.

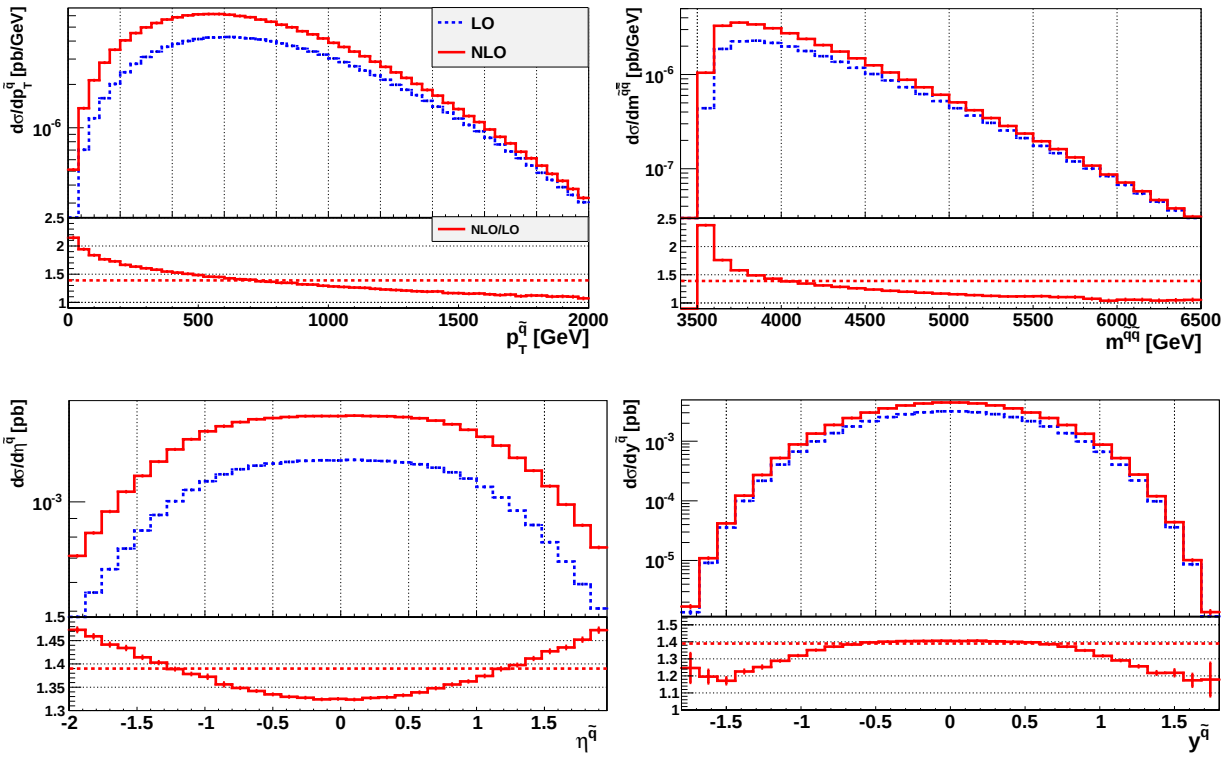

Figure 3.15.: The LO and NLO distributions for the transverse momentum $p_T^{\tilde{q}}$, the invariant mass $m^{\tilde{q}\bar{\tilde{q}}}$, the pseudorapidity $\eta^{\tilde{q}}$ and the rapidity $y^{\tilde{q}}$ for the scale choice $\mu_R = \mu_F = \overline{m}_{\tilde{q}}$. In the lower plot the differential (full) and global (dashed) K-factors are shown. The CMSSM point 10.3.6* has been used.

which implies

$$K = 1.43\,. \tag{3.52}$$

Considering the LO and NLO distributions for this scale choice in Fig. 3.16 one observes close to threshold a similar behaviour as in case of the fixed scale used before, as in this region $\overline{m}_T$ approaches the average of the respective squark masses (which is slightly different for the individual subchannels, but due to the small mass spread in the considered scenario the difference to the averaged squark mass $\overline{m}_{\tilde{q}}$ is small). Far away from threshold, the behaviour tends to be a bit flatter compared to the results obtained for the fixed scale. However, the deviation from the global K-factor is still of $\mathcal{O}(20\%)$ for both the $p_T^{\tilde{q}}$ and $m^{\tilde{q}\bar{\tilde{q}}}$ distribution. This is a consequence of the fact that the value of the global K-factor is driven by the size of the NLO corrections close to threshold.

Influence of mass splittings

The results shown so far have been based on the benchmark scenarios defined in Sec. 3.1.5.1. For both points the differences in the masses of the squarks of the first two generations are rather small (up to $\approx 45\,\text{GeV}$ for the point 10.3.6* and $\approx 70\,\text{GeV}$ for 10.4.5). To assess the influence of a larger mass spread the mass spectrum of 10.3.6* is taken as a starting point. The squark masses are then varied in the range $[1605.0\,\text{GeV}, 2000.0\,\text{GeV}]$. Thus only cases with $m_{\tilde{q}} > m_{\tilde{g}}$ are considered and no subtraction of on-shell intermediate gluino contributions is necessary. To simplify the following considerations all left and right chiral squarks are set to equal masses m_L

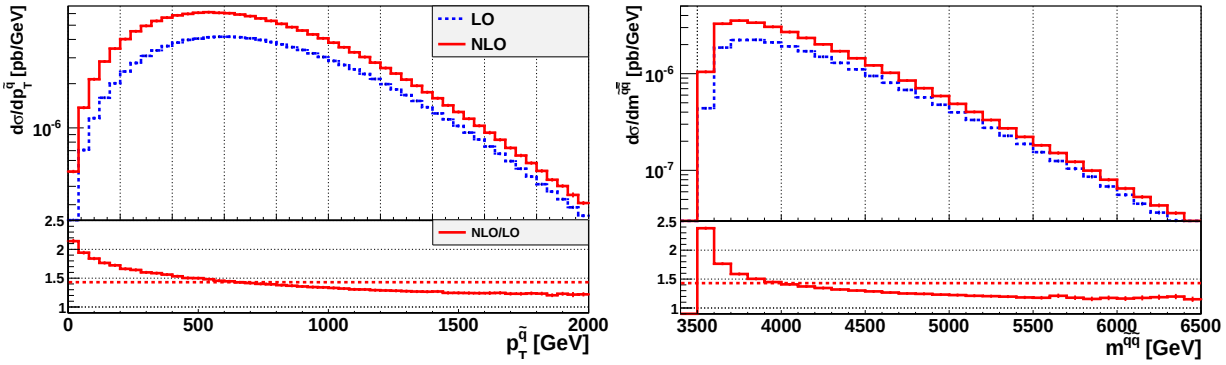

Figure 3.16.: The LO and NLO distributions for the transverse momentum $p_T^{\tilde{q}}$ and the invariant mass $m^{\tilde{q}\bar{\tilde{q}}}$ for the dynamic scale $\mu_R = \mu_F = \overline{m}_T$ defined in the text. In the lower panels the differential (full) and global (dashed) K-factors are shown.

and m_R. For the sake of simplicity the stop and sbottom masses are set to either one of these values, too, similar to what is done in PROSPINO(2). This choice is not completely ad hoc, as the mass differences (in mSUGRA models) tend to be larger between squarks of different chirality compared to e.g. the differences between different flavours. Adapting the mass spectrum this way the total rates change significantly due to the changed kinematics. In order not to bias the following considerations by this effect only the K-factors are considered here. The results calculated in this manner are then compared to those obtained for a completely degenerate mass spectrum, i.e. setting all squark masses to a value $\overline{m}_{\tilde{q}} = (m_L + m_R)/2$, and thus mimicking the way PROSPINO2 calculates the total K-factors. The scales are in both cases set to $\overline{m}_{\tilde{q}}$, i.e. the comparison is not affected by a different scale choice.

The resulting K-factors are depicted in Fig. 3.17 for the choices $m_L = 1605\,\text{GeV}$, $1800\,\text{GeV}$, $2000\,\text{GeV}$ as functions of m_R. Comparing the results obtained with the full calculation and the approximation based on the averaged squark masses one observes that the effect of the mass splitting is indeed rather small. For a splitting of $m_R - m_L = 200\,\text{GeV}$ the difference in the K-factor amounts to about 0.02. Only for larger mass splittings the discrepancy gets more pronounced, for $|m_L - m_R| \approx 400\,\text{GeV}$ the two curves differ by about 0.06. Thus the assumption that the influence of a non-degenerate mass spectrum can be taken into account by considering the LO prediction for the correct mass spectrum and multiplying the result with a K-factor obtained for a degenerate mass spectrum is at least for the case considered here valid, as long as $|m_L - m_R| \lesssim 100\,\text{GeV}$. For larger mass splittings, however, it is mandatory to take into account the full mass dependence. Moreover, this consideration is only relevant for the discussion of total production rates. As soon as decays and/or differential distributions are considered it is inevitable to calculate the K-factors for the individual channels in a fully differential way, i.e. a global K-factor is not suitable at all, as has been shown in the paragraphs before.

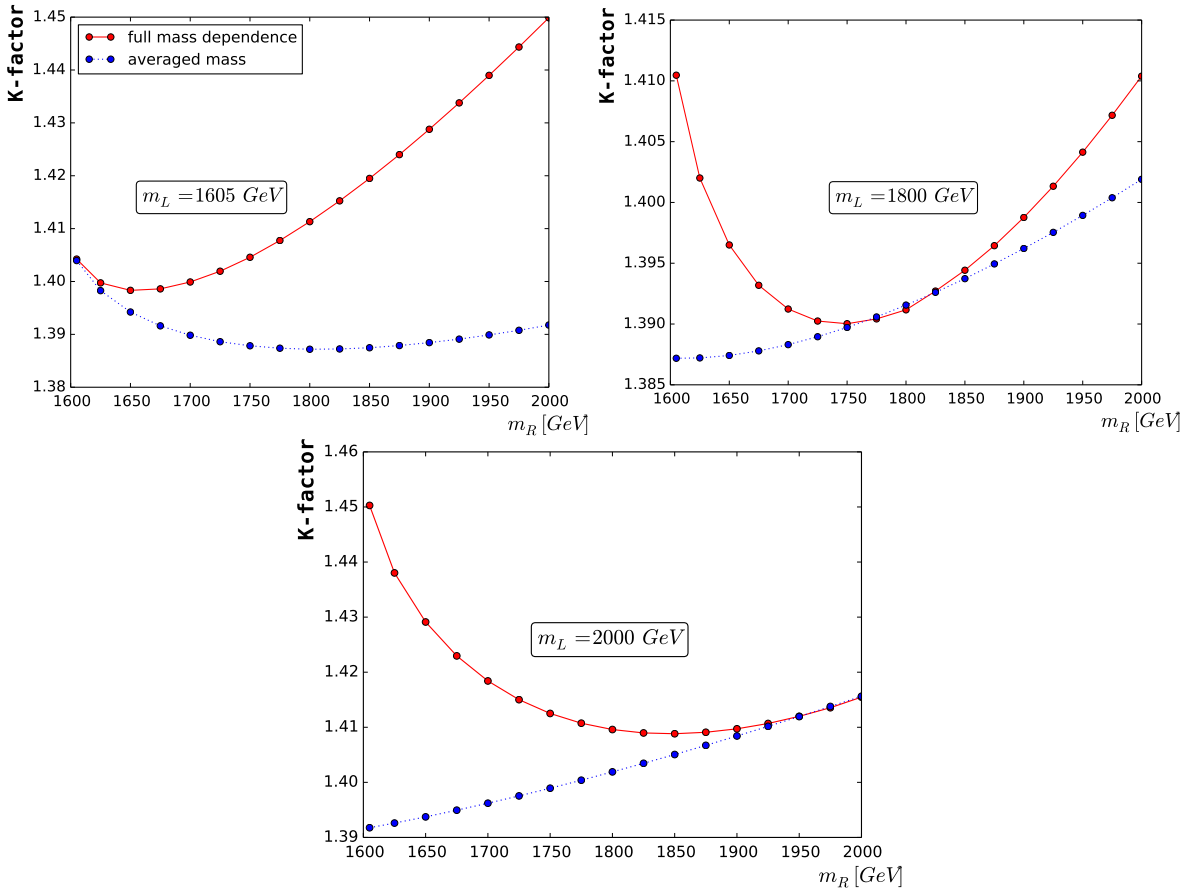

Figure 3.17.: The total K-factors for different mass spectra obtained by modifying the spectrum of the scenario 10.3.6* as described in the text. The mass of the left chiral squarks, m_L, is set to the fixed values given in the boxes, the mass of the right chiral squarks, m_R, is varied. The dashed curves show the results for a completely degenerate mass spectrum with $\overline{m}_{\tilde{q}} = (m_L + m_R)/2$.

3.2. Squark decays

The calculation of higher-order contributions to the production processes of supersymmetric particles is only the first step towards a precise prediction of what to expect at a hadron collider like the LHC. The next step in a realistic simulation requires a description of the decays of these particles into partons, leptons and invisible particles like neutrinos and neutralinos. In case of squark decays there are several modes possible (if kinematicly allowed):

- $\tilde{q}_i \to q_i \tilde{\chi}_k^0$, $k = 1, 2, 3, 4$: The decays into neutralinos are mediated by the electroweak interaction. In many SUSY scenarios the lightest neutralino, $\tilde{\chi}_1^0$, is the lightest supersymmetric particle and (if R-parity conservation is assumed) stable. For the heavier neutralinos, $\tilde{\chi}_k^0$ ($k = 2, 3, 4$), the decay pattern is more involved, as these particles decay further in cascade decays until only stable SM particles and the LSP are left.
- $\tilde{q}_i \to q_j \tilde{\chi}_k^\pm$, $k = 1, 2$: The electroweak decays into charginos are only possible for left chiral squarks. The charginos decay further in cascade decays.
- $\tilde{q}_i \to q_i \tilde{g}$: This decay mode is the only strong process. The gluino decays further into a quark and a (potentially off-shell) antisquark, which decays in turn via one of the electroweak modes.

In the following only the decay mode $\tilde{q} \to q\tilde{\chi}_1^0$ will be taken into account, as this mode has the simplest final-state structure: in case of squark (anti)squark production this leads to two partons and two neutralinos, which corresponds at tree level to an experimental signature of two jets and missing transverse energy.

3.2.1. Decay width for $\tilde{q} \to q\tilde{\chi}_1^0$ at NLO

The SUSY-QCD corrections to the decay $\tilde{q} \to q\tilde{\chi}_1^0$ at NLO have been known for several years. However, the original calculation in [21] provides only the results for the partial width of this mode, thus a differential description is not possible. Therefore the calculation for this decay has been repeated in the context of this thesis and combined with the squark antisquark and squark pair production processes, see Sec. 3.3.

The LO contribution

At LO only one Feynman graph contributes, which is shown in Fig. 3.18 (a). The corresponding matrix element squared takes the form

$$\begin{aligned} |\mathcal{M}_B|^2 &= 8\pi\alpha\, p_q \cdot p_{\tilde{\chi}_1^0}\, G_{L/R}^2 \\ &= g^2 \left(m_{\tilde{q}}^2 - m_{\tilde{\chi}_1^0}^2\right) G_{L/R}^2 \end{aligned} \tag{3.53}$$

with the electromagnetic coupling constant $g = \sqrt{4\pi\alpha}$ and the momenta of the final-state particles in an obvious notation. The couplings $G_{L/R}$ depend on the chirality and the flavour of the decaying squark. They are given by

$$\begin{aligned} G_L &= -\sqrt{2}\left[I_3^L \frac{N_{12}}{\sin\theta_W} + \frac{N_{11}}{6\cos\theta_W}\right], \\ G_R &= \sqrt{2} e_q \frac{N_{11}}{\cos\theta_W}, \end{aligned} \tag{3.54}$$

where e_q denotes the charge of the squark in units of the elementary charge, i.e. $e_q = +2/3$ for up-type and $e_q = -1/3$ for down-type squarks. The weak isospin I_3^L takes the values $+1/2$ for up-type and $-1/2$ for down-type squarks. The factors N_{ij} are the matrix elements of the neutralino mixing matrix, θ_W is the Weinberg mixing angle.

Integrating this result over the full phase space for a $1 \to 2$ process yields for the partial width

$$\begin{aligned} \Gamma_{\mathrm{LO}}^{\tilde{q}\to q\tilde{\chi}_1^0} &= \int \frac{\left(m_{\tilde{q}}^2 - m_{\tilde{\chi}_1^0}^2\right)}{64\pi^2 m_{\tilde{q}}^3} |\mathcal{M}_B|^2 d\Omega \\ &= \frac{\alpha}{4} m_{\tilde{q}} \left(1 - \frac{m_{\tilde{\chi}_1^0}^2}{m_{\tilde{q}}^2}\right)^2 G_{L/R}^2, \end{aligned} \tag{3.55}$$

in accordance with the results given in [21].

Virtual corrections

The calculation of the virtual contributions (shown in Fig. 3.18 (b)) proceeds in a similar manner as described for the production case, see Sec. 3.1.2. For the calculation the FeynArts/FormCalc framework has been used. The numerical evaluation of the loop integrals is performed with

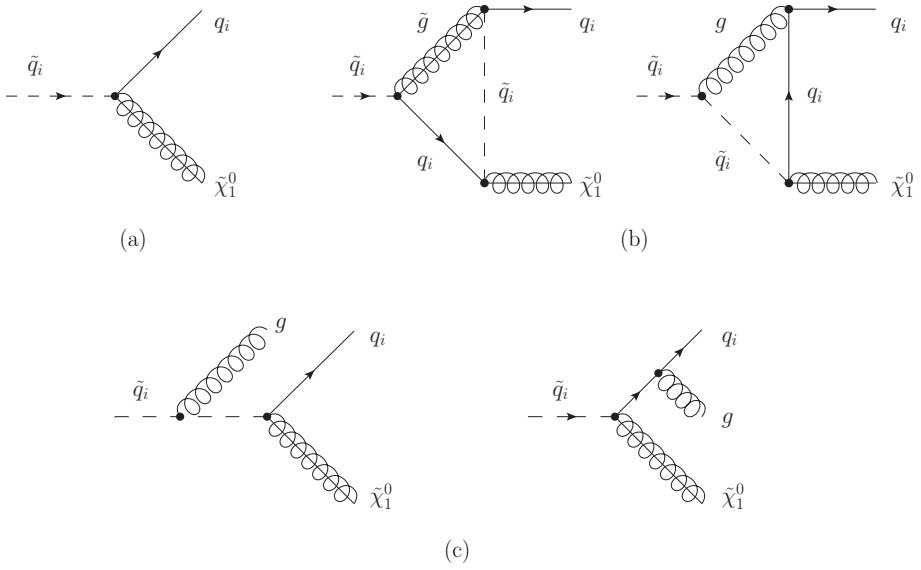

Figure 3.18.: Feynman diagrams contributing to the decay $\tilde{q}_i \to q_i \tilde{\chi}_1^0$ at NLO: Born (a), virtual (b) and real gluon radiation (c).

LOOPTOOLS. The external squark and quark fields are renormalized on shell, correcting again the field renormalization constant δZ_q by removing the incorrect rational term already mentioned in Sec. 3.1.2. The calculation is performed in Dimensional Regularisation, which breaks SUSY explicitly as described in Sec. 2.2.2. This affects the squark-quark-neutralino Yukawa coupling $\hat{g}$ (similar to the squark-quark-gluino vertex in the NLO calculation for the production process). Restoring SUSY at the one-loop level requires a finite counterterm for the Yukawa coupling $\hat{g}$ and leads to the following relation with the gauge coupling g, see [63]:

$$\hat{g} = g\left[1 - \alpha_s \frac{C_F}{8\pi}\right] = g\left[1 - \frac{\alpha_s}{6\pi}\right]. \tag{3.56}$$

This amounts to adapting the NLO result as follows (neglecting for the moment the real contributions, which are not affected):

$$|\mathcal{M}_{\mathrm{NLO}}|^2 = \mathcal{B} + \alpha_s \mathcal{V} = \hat{g}^2\left(\tilde{\mathcal{B}} + \alpha_s \tilde{\mathcal{V}}\right) = g^2\left(\tilde{\mathcal{B}} + \alpha_s\left(\tilde{\mathcal{V}} - \frac{\tilde{\mathcal{B}}}{3\pi}\right)\right) + \mathcal{O}(\alpha_s^2)\,. \tag{3.57}$$

Here, $\mathcal{B} = \hat{g}^2\tilde{\mathcal{B}} = |\mathcal{M}_B|^2$ is the Born matrix element squared, $\alpha_s\mathcal{V} = \hat{g}^2\alpha_s\tilde{\mathcal{V}} = 2\mathrm{Re}(\mathcal{M}_B\mathcal{M}_V^*)$ corresponds to the virtual contribution with a factor α_s factored out and in the last step the relation Eq. (3.56) has been used. All in all, it is sufficient to subtract the term $\alpha_s\frac{\mathcal{B}}{3\pi}$ from the calculated virtual contribution $\alpha_s\mathcal{V}$.

Noting that the Born result $|\mathcal{M}_B|^2$ can be factorized completely from $\mathcal{V}$ and that the remainder does not depend on the squark flavour or chirality, it is sufficient to perform the calculation for one specific squark, e.g. $\tilde{u}_L$. All other results are then obtained by inserting the respective Born matrix element squared and replacing the squark masses in the loops.

Real corrections

The real contributions to $\tilde{q} \to q\tilde{\chi}_1^0$ involve an additional gluon, emitted either from the squark or the quark, see Fig. 3.18 (c). The matrix elements squared for these two diagrams can be cast

into the form

$$|\mathcal{M}_R|^2 = \frac{128}{3}\pi^2\alpha\alpha_s G_{L/R}^2 \left[\frac{p_{\tilde{\chi}_1^0}\cdot p_q \left(p_{\tilde{q}}\cdot p_g - m_{\tilde{q}}^2\right)}{(p_{\tilde{q}}\cdot p_g)^2} + \frac{p_{\tilde{\chi}_1^0}\cdot p_g}{p_q\cdot p_g} - \frac{p_{\tilde{q}}\cdot p_{\tilde{\chi}_1^0}\ p_q\cdot p_g - p_{\tilde{\chi}_1^0}\cdot p_g\ p_{\tilde{q}}\cdot p_q + p_{\tilde{\chi}_1^0}\cdot p_q\ (p_q\cdot p_g - 2p_{\tilde{q}}\cdot p_q - p_{\tilde{q}}\cdot p_g)}{p_{\tilde{q}}\cdot p_g\ p_q\cdot p_g} \right], \tag{3.58}$$

where the momenta of the external particles are denoted $p_{\tilde{q}}$ for the squark, $p_{\tilde{\chi}_1^0}$ for the neutralino, p_q for the quark and p_g for the gluon.

This result contains again IR divergences, which are obvious here if the scalar products are expressed in terms of the gluon energy E_g and the angle θ_{qg},

$$\begin{aligned} p_q\cdot p_g &= E_g E_q(1-\cos\theta_{qg})\,, \\ p_{\tilde{q}}\cdot p_g &= E_g(E_{\tilde{q}} - |\vec{p}_{\tilde{q}}|\cos\theta_{\tilde{q}g})\,. \end{aligned} \tag{3.59}$$

In the soft limit, $E_g \to 0$, both expressions vanish, while only the first one gives rise to a collinear singularity for $\theta_{qg} \to 0$. These divergences cancel due to the KLN theorem against the corresponding ones in the virtual routines. As the decay will be combined with the production process and implemented in the POWHEG-BOX to allow for a simultaneous description of both production and decay (see Sec. 3.3) the cancellation of these divergences is achieved automatically via the FKS method implemented there. The only further ingredient required is the colour-correlated Born amplitude squared, which reads in the POWHEG-BOX convention (see Eq. (A.7))

$$\mathcal{B}_{\tilde{q}q} = C_F\mathcal{B}. \tag{3.60}$$

Checks

The different elements of the calculation have been tested extensively:

- **Born contributions:** The result for the partial width in Eq. (3.55) has been compared to the analytical results in [21]. Moreover, the implementation has been checked against the result obtained from SDECAY 1.3 [24].
- **Virtual contributions:** The virtual results have been tested by checking the cancellation of the UV divergences as described for the production case in Sec. 3.1.4. Moreover, the correct IR structure has been tested by comparing the poles in ϵ obtained from LOOPTOOLS with the general pole structure given in Eq. (3.37) adapted to the decay case,

  $$\mathcal{V} = \frac{\alpha_s}{2\pi}\frac{(4\pi)^\epsilon}{\Gamma(1-\epsilon)}\left[-\frac{1}{\epsilon^2}C_F\mathcal{B} - \frac{1}{\epsilon}\left((\gamma_q + C_F)\,\mathcal{B} - \mathcal{B}_{\tilde{q}q}\left(2\log\frac{2p_q\cdot p_{\tilde{q}}}{\mu_R^2} - \log\frac{m_{\tilde{q}}^2}{\mu_R^2}\right)\right) + \mathcal{V}_{\text{fin}}\right] \tag{3.61}$$

  with $\gamma_q = \frac{3}{2}C_F$ and $C_F = 4/3$. Furthermore, the finite virtual results have been compared to an independent calculation.
- **Real contributions:** The real matrix elements squared have been tested numerically for a multitude of phase space points against the corresponding routines obtained with MADGRAPH. The correct cancellation of the IR poles in the implementation in the POWHEG-BOX has been tested again by checking the soft/collinear limit.

Finally, the result for the complete partial width calculated at NLO has been compared numerically with the SDECAY implementation of the results from [21].

3.2.2. The total squark width at NLO

In order to obtain the branching ratios of the squarks the total width $\Gamma^{\tilde{q}}_{\text{tot}}$ including all possible decay modes has to be determined, too. This quantity is required to get the correct normalization when combining production and decay of squarks in the next section. However, it is not necessary to determine all partial widths differentially, as only the decay mode $\tilde{q} \to q\tilde{\chi}^0_1$ will be considered. Thus the (NLO) results can be taken from literature, respectively the implementations of the different modes in SDECAY can be extracted and adapted appropriately.

- **Electroweak decay modes:** The decays into neutralinos and charginos all have a similar structure, only the squark-quark-gaugino coupling has to be modified for the respective channels. The results for the NLO partial widths obtained for these modes can be found in [21], the corresponding routines in SDECAY could be simply adopted after adapting the conventions used to calculate the squark-quark-gaugino vertex. In addition to the typical electroweak parameters α, θ_W, the electromagnetic charge and the weak isospin of the squark, this coupling depends also on the mixing matrices of the neutralinos/charginos.
- **Strong decay into $q\tilde{g}$:** The NLO corrections to this mode have been calculated in [23]. The results given there form the basis of the implementation in SDECAY. However, it is not possible to simply adopt this implementation without the following modifications:
  1. The SDECAY routines use the strong coupling determined in the $\overline{\text{DR}}$ scheme, i.e. the implemented routines have been converted from the $\overline{\text{MS}}$ scheme used in the original calculation in [23] by subtracting a conversion factor $-\alpha_s/(4\pi)\mathcal{B}$ from the NLO result. However, throughout the following numerical evaluation α_s is determined in the $\overline{\text{MS}}$ scheme, as implemented in the POWHEG-BOX. Thus this conversion factor has been removed from the adopted routine.
  2. The heavy particles in the SDECAY implementation are decoupled from the running of α_s. However, all squark masses in the original routines are set to an equal value. The corresponding logarithms have been modified such that the full mass dependence is restored, similar to Eq. (2.23).

  With these two modifications it is possible to use $\alpha_s^{(5),\overline{\text{MS}}}$, as implemented in the POWHEG-BOX.
  3. The gluino self-energy has been evaluated in [23], assuming a degenerate squark mass spectrum. To include the full mass effects, the corresponding function in SDECAY has been adapted by generalizing the contribution of the top-stop loops, which is implemented including the correct masses for the $\tilde{t}_{1/2}$, the top quark mass and the $\tilde{t}$ mixing angle $\theta_{\tilde{t}}$ (see [22]). To this end this function is called for each squark with the correct squark masses, but with $m_t \to 0$ and $\theta_t \to 0$.

If not stated otherwise, the renormalization scale appearing in the $\tilde{q} \to q\tilde{g}$ mode is set to the average of the squark masses of the first two generations, $\mu_R = \overline{m}_{\tilde{q}}$, see Sec. 3.1.5.1. This scale is chosen as the results for the total width will be used in the combined description of squark production and decay, discussed in the next section.

Numerical evaluation of $\Gamma^{\tilde{q}}_{\text{tot}}$

The modified analytical results for the total width have been implemented in the framework of the POWHEG-BOX and are used in Sec. 3.3. To obtain the numerical values several additional (electroweak) parameters are needed, which are summarized in the following.

Scenario	$m_{\tilde{\chi}_1^0}$ [GeV]	$m_{\tilde{\chi}_2^0}$ [GeV]	$m_{\tilde{\chi}_3^0}$ [GeV]	$m_{\tilde{\chi}_4^0}$ [GeV]	$m_{\tilde{\chi}_1^\pm}$ [GeV]	$m_{\tilde{\chi}_2^\pm}$ [GeV]
10.3.6*	290.83	551.76	−844.74	856.87	551.99	856.40
10.4.5	347.71	657.84	−993.42	1003.79	856.06	1003.46

Table 3.8.: The neutralino and chargino masses for the CMSSM scenarios defined in Tab. 3.1.

The weak mixing angle θ_W is determined according to Eq. (10.11) from [77], yielding

$$\sin^2\theta_W = \frac{1}{2} - \sqrt{\frac{1}{4} - \frac{\pi\alpha(m_Z)}{\sqrt{2}G_F m_Z^2}}\,, \tag{3.62}$$

with the other SM parameters stated in Sec. 3.1.5.1. The masses of the neutralinos and charginos for the two CMSSM scenarios defined in Tab. 3.1 are given in Tab. 3.8.

The neutralino mixing matrices for the scenarios 10.3.6* and 10.4.5 read

$$N^{10.3.6^*} = \begin{pmatrix} 0.99759 & -0.00979 & 0.06292 & -0.02740 \\ 0.02329 & 0.97889 & -0.16595 & 0.11704 \\ -0.24682 & 0.03551 & 0.70512 & 0.70776 \\ -0.06044 & 0.20106 & 0.68651 & -0.69615 \end{pmatrix} \quad \text{and}$$

$$N^{10.4.5} = \begin{pmatrix} 0.98267 & -0.00716 & 0.05338 & -0.02358 \\ -0.20847 & 0.02997 & 0.70567 & 0.70760 \\ 0.01724 & 0.98393 & -0.14473 & 0.10318 \\ -0.05226 & 0.17590 & 0.69154 & -0.69865 \end{pmatrix}. \tag{3.63}$$

In order to diagonalize the chargino mass matrix two matrices are needed, one for the left-handed components (denoted U) and one for the right-handed ones (denoted V). These 2×2 mixing matrices are parametrized as ($i = U, V$)

$$\begin{pmatrix} \cos\theta_i & -\sin\theta_i \\ \sin\theta_i & \cos\theta_i \end{pmatrix}. \tag{3.64}$$

The mixing angles are given by $\cos\theta_U = 0.97213$ and $\cos\theta_V = 0.98594$ for the parameter point 10.3.6*. Likewise, those for the point 10.4.5 read $\cos\theta_U = 0.97894$ and $\cos\theta_V = 0.98914$. With these parameters the partial and total widths for the different squark types can be determined. The results for the first-generation squarks are listed in Tab. 3.9, those for the second-generation squarks are identical.

Scenario	10.3.6*		10.4.5	
Mode	$\Gamma_{\rm LO}$[GeV]	$\Gamma_{\rm NLO}$[GeV]	$\Gamma_{\rm LO}$[GeV]	$\Gamma_{\rm NLO}$[GeV]
$\tilde{u}_L \to u\tilde{\chi}_1^0$	0.216	0.206	0.210	0.204
$\tilde{u}_L \to u\tilde{\chi}_2^0$	5.972	5.715	5.242	5.115
$\tilde{u}_L \to u\tilde{\chi}_3^0$	0.0044	0.0042	0.0023	0.0022
$\tilde{u}_L \to u\tilde{\chi}_4^0$	0.162	0.156	0.091	0.089
$\tilde{u}_L \to d\tilde{\chi}_1^+$	12.01	11.49	10.52	10.27
$\tilde{u}_L \to d\tilde{\chi}_2^+$	0.251	0.242	0.142	0.139
$\tilde{u}_L \to u\tilde{g}$	4.181	5.648	0	0
$\Gamma^{\rm tot}_{\tilde{u}_L}$[GeV]	22.79	23.44	16.21	15.81
$\tilde{u}_R \to u\tilde{\chi}_1^0$	3.757	3.587	3.487	3.408
$\tilde{u}_R \to u\tilde{\chi}_2^0$	0.0018	0.0017	0.0008	0.0008
$\tilde{u}_R \to u\tilde{\chi}_3^0$	0.0014	0.0014	0.0007	0.0007
$\tilde{u}_R \to u\tilde{\chi}_4^0$	0.0085	0.0082	0.0043	0.043
$\tilde{u}_R \to u\tilde{g}$	2.793	3.819	0	0
$\Gamma^{\rm tot}_{\tilde{u}_R}$[GeV]	6.561	7.413	3.493	3.411
$\tilde{d}_L \to d\tilde{\chi}_1^0$	0.267	0.255	0.246	0.239
$\tilde{d}_L \to d\tilde{\chi}_2^0$	5.875	5.623	5.183	5.056
$\tilde{d}_L \to d\tilde{\chi}_3^0$	0.0074	0.0071	0.0038	0.0038
$\tilde{d}_L \to d\tilde{\chi}_4^0$	0.203	0.195	0.113	0.111
$\tilde{d}_L \to u\tilde{\chi}_1^-$	11.69	11.19	10.32	10.07
$\tilde{d}_L \to u\tilde{\chi}_2^-$	0.496	0.477	0.274	0.269
$\tilde{d}_L \to d\tilde{g}$	4.240	5.725	0	0
$\Gamma^{\rm tot}_{\tilde{d}_L}$[GeV]	22.78	23.45	16.14	15.74
$\tilde{d}_R \to d\tilde{\chi}_1^0$	0.937	0.895	0.868	0.848
$\tilde{d}_R \to d\tilde{\chi}_2^0$	0.0004	0.0004	0.0002	0.0002
$\tilde{d}_R \to d\tilde{\chi}_3^0$	0.0004	0.0003	0.0002	0.0002
$\tilde{d}_R \to d\tilde{\chi}_4^0$	0.0021	0.0020	0.0011	0.0011
$\tilde{d}_R \to d\tilde{g}$	2.671	3.656	0	0
$\Gamma^{\rm tot}_{\tilde{d}_R}$[GeV]	3.610	4.553	0.869	0.849

Table 3.9.: The partial and total widths for first-generation squarks at LO and NLO for the two scenarios considered here. For the parameters see the main text. The scale for α_s has been set to $\mu_R = \overline{m}_{\tilde{q}}$.

3.3. Combination of production and decay

In the last step towards a description of squark (anti)squark production and the subsequent decays into two quarks and two neutralinos the NLO results for these two steps have to be combined. The formalism and the limitations of the method applied in the following have already been discussed extensively in [112], thus the first subsection only summarizes the main points given there. This is followed by some phenomenological results obtained for both squark antisquark and squark pair production.

3.3.1. Formalism

Following closely the description in [112], this section considers the special case of squark pair production with subsequent decays. The adaption to squark antisquark production is straightforward.

Combining the results for the direct production of two on-shell squarks and their decays relies implicitly on the so-called 'double-pole approximation', i.e. only those contributions to $pp \to 2q + 2\tilde{\chi}_1^0$ are taken into account that can lead to two on-shell intermediate squarks. Taking into account all MSSM processes resulting in this final state the LO matrix element can be expanded as

$$\mathcal{M} = \frac{\mathrm{DP}(k_1, k_2, \{k_i\})}{(k_1^2 - m_{\tilde{q}_1}^2)(k_2^2 - m_{\tilde{q}_2}^2)} + \frac{\mathrm{SP}_1(k_1, \{k_i\})}{(k_1^2 - m_{\tilde{q}_1}^2)} + \frac{\mathrm{SP}_2(k_2, \{k_i\})}{(k_2^2 - m_{\tilde{q}_2}^2)} + \mathrm{NP}(\{k_i\}), \tag{3.65}$$

where $k_{1/2}$ are the momenta of the resonant squarks and $\{k_i\}$ collectively denotes all other momenta. The first term contains a double pole for $k_1^2 \to m_{\tilde{q}_1}^2$, $k_2^2 \to m_{\tilde{q}_2}^2$, while the terms SP_i (NP) have only a single (no) pole in this limit. Examples for processes contributing to the single-pole part are the direct production of a squark, a quark and a neutralino, followed by the decay $\tilde{q} \to q\tilde{\chi}_1^0$. The NP part gets contributions from the direct production of two quarks and two neutralinos, without any intermediate (potentially) resonant squarks. After introducing the finite width of the unstable intermediate squarks via a Dyson summation of self-energy contributions to the squark propagator, i.e. formally replacing

$$\frac{1}{k_i^2 - m_{\tilde{q}_i}^2} \to \frac{1}{k_i^2 - m_{\tilde{q}_i}^2 + i m_{\tilde{q}_i}\Gamma_{\tilde{q}_i}}, \tag{3.66}$$

the contribution of the double-pole part to the cross section reads

$$\sigma_{\mathrm{DP}}^{\mathrm{LO}} = \frac{1}{2\hat{s}} \int \mathrm{d}\Phi_4 \frac{|\mathrm{DP}(k_1, k_2, \{k_i\})|^2}{\left((k_1^2 - m_{\tilde{q}_1}^2)^2 + m_{\tilde{q}_1}^2\Gamma_{\tilde{q}_1}^2\right)\left((k_2^2 - m_{\tilde{q}_2}^2)^2 + m_{\tilde{q}_2}^2\Gamma_{\tilde{q}_2}^2\right)}, \tag{3.67}$$

demanding implicitly the on-shell condition $\sqrt{\hat{s}} > m_{\tilde{q}_1} + m_{\tilde{q}_2}$ to allow for the two poles. If the widths of the squarks fulfil $\Gamma_{\tilde{q}_i}/m_{\tilde{q}_i} \ll 1$ one can make use of the approximation

$$\frac{1}{(k_i^2 - m_{\tilde{q}_i}^2)^2 + m_{\tilde{q}_i}^2\Gamma_{\tilde{q}_i}^2} \overset{\Gamma_{\tilde{q}_i}\to 0}{\longrightarrow} \frac{\pi}{m_{\tilde{q}_i}\Gamma_{\tilde{q}_i}} \delta\left(k_i^2 - m_{\tilde{q}_i}^2\right). \tag{3.68}$$

After dissecting the Lorentz-invariant phase space element $\mathrm{d}\Phi_4$ for the $2 \to 4$ process into the phase space for a $2 \to 2$ process and two $1 \to 2$ processes, the two Delta-distributions in Eq. (3.67) can be integrated out and one obtains the well known result in this so-called narrow-width approximation (NWA),

$$\sigma_{\mathrm{DP}}^{\mathrm{LO}} = \sigma_{\mathrm{LO}}^{\tilde{q}_1\tilde{q}_2} \frac{\Gamma_{\mathrm{LO}}^{\tilde{q}_1 \to q\tilde{\chi}_1^0}}{\Gamma_{\mathrm{tot}}^{\tilde{q}_1}} \frac{\Gamma_{\mathrm{LO}}^{\tilde{q}_2 \to q\tilde{\chi}_1^0}}{\Gamma_{\mathrm{tot}}^{\tilde{q}_2}}. \tag{3.69}$$

The total cross section is thus the product of the production cross section and the (LO) branching ratios for the decays. This relation is easily promoted to the level of differential cross sections, yielding

$$\mathrm{d}\sigma_{\mathrm{tot}} = \mathrm{d}\sigma_{\mathrm{prod}} \frac{\mathrm{d}\Gamma^{\tilde{q}_1 \to \tilde{\chi}_1^0 q}}{\Gamma^{\tilde{q}_1}_{\mathrm{tot}}} \frac{\mathrm{d}\Gamma^{\tilde{q}_2 \to \tilde{\chi}_1^0 q}}{\Gamma^{\tilde{q}_2}_{\mathrm{tot}}} \,, \tag{3.70}$$

with an obvious generalization of the labels.

Considering the numbers for the total squark widths (Tab. 3.9) and setting them in relation to the respective squark masses (Tab. 3.2) the application of the NWA is justified for the scenarios considered in this work. Moreover, as squarks are scalar particles, there are no spin-correlations between the production and decay stages which could affect the combined results.

Narrow-width approximation at NLO

In order to promote this LO result to NLO accuracy, the factors in Eq. (3.70) have to be replaced by the corresponding NLO quantities,

$$\begin{aligned} \mathrm{d}\sigma_{\mathrm{prod}} &= \mathrm{d}\sigma_0 + \alpha_s \mathrm{d}\sigma_1 \,, \\ \mathrm{d}\Gamma^{\tilde{q}_i \to \tilde{\chi}_1^0 q} &= \mathrm{d}\Gamma_0^{\tilde{q}_i \to \tilde{\chi}_1^0 q} + \alpha_s \mathrm{d}\Gamma_1^{\tilde{q}_i \to \tilde{\chi}_1^0 q} \,, \\ \Gamma^{\tilde{q}_i}_{\mathrm{tot}} &= \Gamma^{\tilde{q}_i}_{\mathrm{tot},0} + \alpha_s \Gamma^{\tilde{q}_i}_{\mathrm{tot},1} . \end{aligned} \tag{3.71}$$

Obviously it is not possible to just insert these NLO quantities into Eq. (3.70) as this would induce contributions of $\mathcal{O}(\alpha_s^2)$. Thus the obtained expression has to be expanded appropriately in α_s. There exist two approaches for this problem, both developed in the context of (single) top production and decay:

- In the first approach (see e.g. [113]) an expansion of the complete expression is performed, i.e. both the nominator and the denominator are expanded and only terms up to $\mathcal{O}(\alpha_s)$ are kept:

$$\begin{aligned} \mathrm{d}\sigma_{\mathrm{tot}} = \frac{1}{\Gamma^{\tilde{q}_1}_{\mathrm{tot},0} \Gamma^{\tilde{q}_2}_{\mathrm{tot},0}} \Bigg[& \mathrm{d}\sigma_0 \, \mathrm{d}\Gamma_0^{\tilde{q}_1 \to \tilde{\chi}_1^0 q} \, \mathrm{d}\Gamma_0^{\tilde{q}_2 \to \tilde{\chi}_1^0 q} \left(1 - \frac{\alpha_s \Gamma^{\tilde{q}_1}_{\mathrm{tot},1}}{\Gamma^{\tilde{q}_1}_{\mathrm{tot},0}} - \frac{\alpha_s \Gamma^{\tilde{q}_2}_{\mathrm{tot},1}}{\Gamma^{\tilde{q}_2}_{\mathrm{tot},0}} \right) \\ & + \alpha_s \left(\mathrm{d}\sigma_0 \, \mathrm{d}\Gamma_1^{\tilde{q}_1 \to \tilde{\chi}_1^0 q} \mathrm{d}\Gamma_0^{\tilde{q}_2 \to \tilde{\chi}_1^0 q} + \mathrm{d}\sigma_0 \, \mathrm{d}\Gamma_0^{\tilde{q}_1 \to \tilde{\chi}_1^0 q} \mathrm{d}\Gamma_1^{\tilde{q}_2 \to \tilde{\chi}_1^0 q} + \mathrm{d}\sigma_1 \, \mathrm{d}\Gamma_0^{\tilde{q}_1 \to \tilde{\chi}_1^0 q} \mathrm{d}\Gamma_0^{\tilde{q}_2 \to \tilde{\chi}_1^0 q} \right) \Bigg] , \end{aligned} \tag{3.72}$$

  This approach has also been used for the combination of squark pair production and decays in [19] and [112]. This expression might cause some problems if the NLO corrections to the total width are positive and large, while the corrections to the partial width of the decay under consideration are small (or even negative). In this case the term proportional to the LO contribution can become small, while this change is not necessarily fully compensated by the NLO terms in the second bracket. This is especially troublesome in the context of Monte Carlo event generators like the POWHEG-BOX: recall that one of the main benefits of the POWHEG method is the generation of events with (almost exclusively) positive weights, according to the $\overline{\mathcal{B}}$ function in the POWHEG master formula, Eq. (2.52). Subtracting terms from this function, however, will increase the number of events with negative weights, as in some phase space regions $\overline{\mathcal{B}} < 0$. This is in principle no problem, as long as physical observables are positive, but it requires a larger number of events and

renders subsequent simulation steps like detector simulations rather inefficient. Nevertheless, besides its formal correctness this expansion has another advantage: Summing over all possible decay channels reproduces (for the integrated version of Eq. (3.72)) directly the NLO production cross section $\sigma_0 + \alpha_s\sigma_1$, as all other terms drop out.

- Similar to the proposal in [114] the problem of potentially negative contributions can be avoided by expanding only the numerator in α_s, but keeping the NLO total widths in the denominator, thus

$$\begin{aligned} \mathrm{d}\sigma_{\mathrm{tot}} = \frac{1}{\Gamma^{\tilde{q}_1}_{\mathrm{tot}}\Gamma^{\tilde{q}_2}_{\mathrm{tot}}}\Big[&\mathrm{d}\sigma_0\,\mathrm{d}\Gamma_0^{\tilde{q}_1\to\tilde{\chi}_1^0 q}\mathrm{d}\Gamma_0^{\tilde{q}_2\to\tilde{\chi}_1^0 q} + \alpha_s\big(\mathrm{d}\sigma_0\,\mathrm{d}\Gamma_1^{\tilde{q}_1\to\tilde{\chi}_1^0 q}\mathrm{d}\Gamma_0^{\tilde{q}_2\to\tilde{\chi}_1^0 q} \\ &+ \mathrm{d}\sigma_0\,\mathrm{d}\Gamma_0^{\tilde{q}_1\to\tilde{\chi}_1^0 q}\mathrm{d}\Gamma_1^{\tilde{q}_2\to\tilde{\chi}_1^0 q} + \mathrm{d}\sigma_1\,\mathrm{d}\Gamma_0^{\tilde{q}_1\to\tilde{\chi}_1^0 q}\mathrm{d}\Gamma_0^{\tilde{q}_2\to\tilde{\chi}_1^0 q}\big)\Big]. \end{aligned} \tag{3.73}$$

  However, summing over all decay channels in this approach does not reproduce the production cross section, i.e. in this sense unitarity is violated.

In the following section results obtained with both approaches are shown. However, in the rest of this thesis only the first expansion is used, as in the benchmark points considered here the subtracted terms in Eq. (3.72) are rather small, see Tab. 3.9 for the total widths at LO and NLO.

Separating production and decay in the NWA as outlined above does not only neglect off-shell contributions, which are suppressed by $\Gamma_{\tilde{q}_i}/m_{\tilde{q}_i}$, but also all so-called non-factorizable higher-order contributions, i.e. (gluonic) interactions between the production and decay stage or interactions between the two decays, e.g. the exchange of a gluon between the produced quarks. These effects are expected to be suppressed by $\Gamma_{\tilde{q}_i}/m_{\tilde{q}_i}$ [115, 116]. However, for soft gluons which induce a long-range interaction the results of exclusive observables could still be affected. The investigation of these effects is beyond the scope of this thesis.

3.3.2. Phenomenological results

Taking into account the decays of the produced squarks into $q\tilde{\chi}_1^0$ leads at NLO to up to three partons in the final state. These partons are clustered into jets with FASTJET 3.0.3 [117, 118]. To this end the anti-k_T algorithm [119] is adopted, using $R = 0.4$. In the following only minimal cuts are applied on the transverse momentum and the pseudorapidity of the resulting jets:

$$p_T^j > 20\,\mathrm{GeV}, \quad |\eta^j| < 2.8\,. \tag{3.74}$$

No event selection cuts are imposed.

Total cross sections

The general setup for the numerical evaluation is identical to the one outlined in Sec. 3.1.5.1. All predictions have been obtained for the production of squarks of the first two generations, treating the channels individually and considering the decays $\tilde{q} \to q\tilde{\chi}_1^0$. Both results for squark antisquark and squark pair production will be shown, where the latter ones include the charge conjugate channels, i.e. antisquark pair production.

Using first of all Eq. (3.73) to combine production and decay one obtains for squark antisquark (squark pair) production the results in Tab. 3.10 (3.11) for the two benchmark scenarios specified in Tab. 3.1. The different numbers have been calculated as follows:

Scenario	10.3.6*		10.4.5	
contribution	σ[fb]	K-factor	σ[fb]	K-factor
LO⊗LO	$7.13 \cdot 10^{-2}$		$6.00 \cdot 10^{-1}$	
LO⊗NLO	$6.09 \cdot 10^{-2}$	0.85	$5.74 \cdot 10^{-1}$	0.96
NLO⊗LO	$1.05 \cdot 10^{-1}$	1.47	$9.60 \cdot 10^{-1}$	1.60
NLO⊗NLO	$9.88 \cdot 10^{-2}$	1.39	$9.32 \cdot 10^{-1}$	1.55

Table 3.10.: Contributions to squark antisquark production and decay at NLO, combined according to Eq. (3.73).

Scenario	10.3.6*		10.4.5	
contribution	σ[fb]	K-factor	σ[fb]	K-factor
LO⊗LO	1.03		7.92	
LO⊗NLO	0.71	0.69	6.11	0.77
NLO⊗LO	1.16	1.13	9.19	1.16
NLO⊗NLO	1.09	1.06	8.89	1.12

Table 3.11.: Contributions to squark pair production and decay at NLO, combined according to Eq. (3.73).

- LO⊗LO: These results correspond to LO production and LO decays, thus essentially to Eq. (3.70). However, the 'normalization' factor is not the product of the two LO widths, but of the NLO ones. With this choice this factor drops out when calculating the K-factors, defined again as the ratio of the NLO and LO predictions, and does not blur the NLO effects in production and/or decay. The LO PDF set CTEQ6L1 has been used.
- LO⊗NLO: These contributions are obtained by taking into account only the first three summands in Eq. (3.73), i.e. only the NLO corrections to the decay of the two squarks. Here the NLO PDF set CT10NLO has been used.
- NLO⊗LO: In these terms only the NLO corrections to the production are taken into account, i.e. the first and the last term in Eq. (3.73).
- NLO⊗NLO: These numbers have been obtained by evaluating the full cross section σ_{tot} according to Eq. (3.73).

Comparing the different contributions one notices that in all cases the NLO corrections to the decays are negative (see the values for the partial widths at NLO in Tab. 3.9), while those for the production are positive (as already discussed in Sec. 3.1.5.2). The combined result is consequently somewhat smaller compared to the case where only NLO corrections to the production are taken into account.

In the next step the predictions obtained with the fully expanded version of the combination formula, Eq. (3.72), are considered. The results for the total cross sections for squark antisquark (squark pair) production are summarized in Tab. 3.12 (3.13). Due to the different form of the combination formula the meaning of the entries is slightly different:

- LO⊗LO: These numbers correspond to LO production and LO decays, using the LO total widths of the two squarks as normalization factor. Again, with this choice this factor drops

Scenario	10.3.6*		10.4.5	
contribution	σ[fb]	K-factor	σ[fb]	K-factor
LO⊗LO	$9.29 \cdot 10^{-2}$		$5.73 \cdot 10^{-1}$	
LO⊗NLO	$5.35 \cdot 10^{-2}$	0.58	$5.73 \cdot 10^{-1}$	1.00
NLO⊗LO	$1.39 \cdot 10^{-1}$	1.50	$9.16 \cdot 10^{-1}$	1.60
NLO⊗NLO	$1.03 \cdot 10^{-1}$	1.11	$9.15 \cdot 10^{-1}$	1.60

Table 3.12.: Contributions to squark antisquark production and decay at NLO, combined according to Eq. (3.72).

Scenario	10.3.6*		10.4.5	
contribution	σ[fb]	K-factor	σ[fb]	K-factor
LO⊗LO	1.34		7.57	
LO⊗NLO	0.63	0.47	6.10	0.81
NLO⊗LO	1.54	1.15	8.76	1.16
NLO⊗NLO	1.12	0.84	8.75	1.16

Table 3.13.: Contributions to squark pair production and decay at NLO combined, according to Eq. (3.72).

out when comparing these LO results with the different NLO contributions. Note that the correction factors, which are subtracted in the first bracket of Eq. (3.72), are not included here.

- LO⊗NLO: In these contributions the first three terms in Eq. (3.72) are taken into account, keeping the subtracted factors. The motivation for this approach is simply the fact that these subtraction terms guarantee the 'unitarity' of the total cross section upon summing over all possible decay modes, see the comment after Eq. (3.72).

- NLO⊗LO: These numbers are obtained from the NLO corrections to the production and the LO part of Eq. (3.72) without the correction factors, hence the first and the last terms in Eq. (3.72). Thus this quantity is nothing else than the pure NLO prediction for the production with each subchannel multiplied by the corresponding LO branching ratio.

- NLO⊗NLO: These predictions are obtained by evaluating the full cross section σ_{tot} according to Eq. (3.72).

Considering the obtained numbers for scenario 10.3.6* one notices that the corrections to the decays incorporated in LO⊗NLO lead in both cases to large negative contributions. This was to be expected considering the NLO contributions to the total widths (Tab. 3.9), as this scenario is an example for the case outlined after Eq. (3.72) with positive corrections to Γ_{tot} and negative ones to the partial widths. The full result is therefore slightly smaller compared to the case where only NLO contributions to the production part are taken into account. The scenario 10.4.5 shows a completely different behaviour: the results for LO⊗NLO are essentially identical to those obtained for LO⊗LO. The difference between the LO⊗LO and LO⊗NLO values for squark pair production in Tab. 3.13 is caused by the use of different PDF sets (CTEQ6L1 and CT10NLO, respectively). Evaluating LO⊗LO with CT10NLO PDFs yields 6.1 fb, too. This

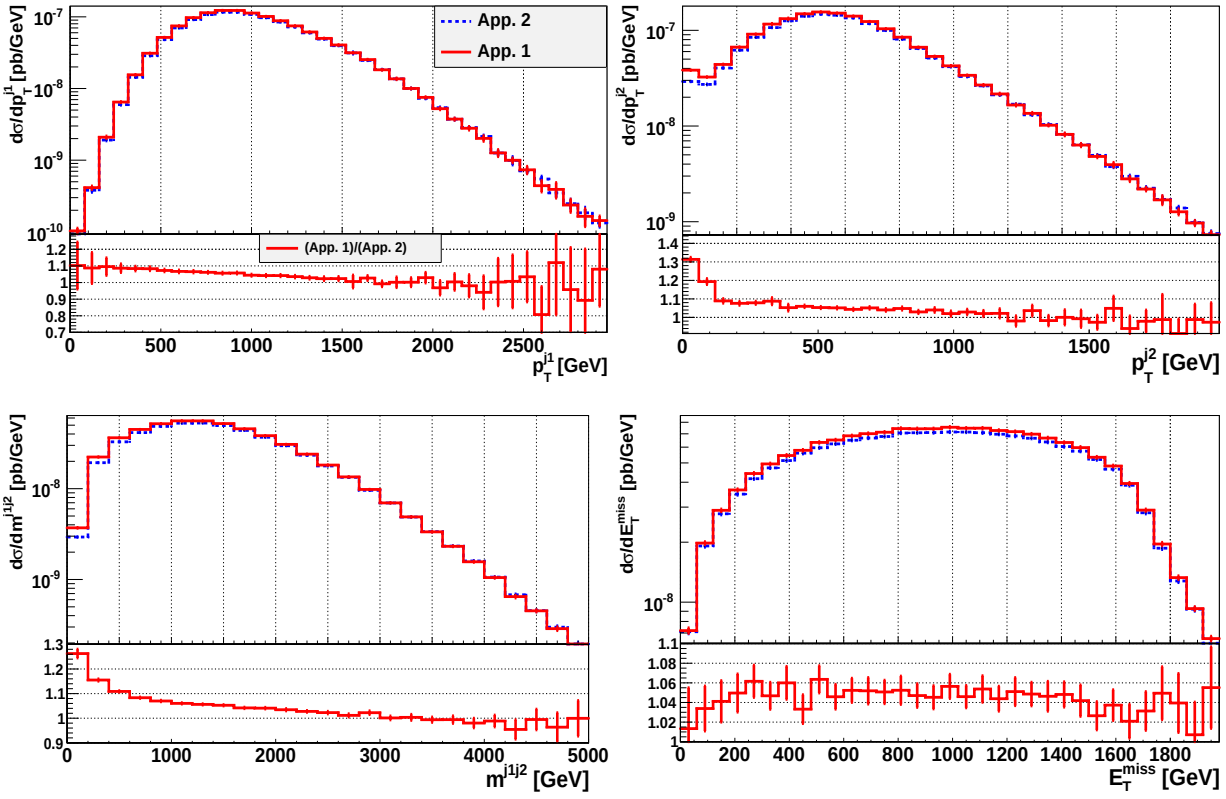

Figure 3.19.: Comparison of the two approaches for the combination of NLO corrections in production and decay according to Eq. (3.72) (denoted App. 1 in the legend) and Eq. (3.73) (App. 2). Shown are the distributions obtained for squark antisquark production and subsequent decays for the scenario 10.3.6*. All contributions according to Eqs. (3.72) and (3.73) are included. The lower panels show the differential ratios (App. 1)/(App. 2).

is in accordance with the results for the NLO corrections to the total and partial widths, which are in both cases negative and of the same order. Thus the correction factors in Eq. (3.72) and the NLO contributions to the decays balance each other.

Comparing the results obtained for σ_{tot} (including all terms) with the two approaches yields only small differences in the total cross section for the two scenarios considered here. Quantitatively, the discrepancies are in all cases $< 4\%$. The effect on differential distributions, however, can be larger. To get an impression of these discrepancies the differential cross sections for the transverse momenta of the two hardest jets $p_T^{j_1/j_2}$, their invariant mass $m^{j_1 j_2}$ and the missing transverse energy $\not{E}_T$ as defined below are shown in Fig. 3.19, including the differential ratio of the two results in the lower panels. The results have been obtained for squark antisquark production using the scenario 10.3.6*, and thus the one showing the largest discrepancy in the total rate. While the $\not{E}_T$ distribution essentially reflects the different normalization, the impact on the other distributions is larger and not flat. However, the discrepancies exceed $\mathcal{O}(10\%)$ only close to threshold, while the changes away from threshold tend to be smaller. In the rest of this section (and throughout Ch. 4) only the prescription outlined in Eq. (3.72) will be used for the combination of production and decay.

Differential K-factors

In order to assess the influence of NLO corrections in both production and decay on distributions, the LO predictions for several (in the context of SUSY searches relevant, see [33, 54]) observables are compared to the NLO ones. The LO results shown here have been calculated according to Eq. (3.70). The observables considered in the following are

- the distributions of the transverse momentum of the hardest and the second hardest jet, $p_T^{j_1}$ and $p_T^{j_2}$,
- the rapidity distribution of the hardest jet, y^{j_1} (the results for the second hardest jet are similar and not shown explicitly),
- the invariant mass of the two hardest jets, $m^{j_1 j_2}$,
- the distribution of the missing transverse energy, $\not{E}_T$, calculated from the two neutralino momenta p_1 and p_2 via

$$\not{E}_T = \not{p}_T = \sqrt{(p_{1,x} + p_{2,x})^2 + (p_{1,y} + p_{2,y})^2}\,, \tag{3.75}$$

- and the effective mass

$$m_{\text{eff}} = p_T^{j_1} + p_T^{j_2} + \not{E}_T\,. \tag{3.76}$$

Note that with this definition m_{eff} is an exclusive quantity.

The predictions obtained for these observables, using the benchmark point 10.3.6*, are depicted for squark antisquark production in Fig. 3.20, those for the point 10.4.5 display qualitatively the same behaviour and are not shown here. The lower panel of each plot shows the differential K-factor (full) and the total K-factor from Tab. 3.12 (dashed).

Considering the p_T distributions of the jets one observes qualitatively the same properties as in case of the results for $p_T^{\tilde{q}}$ without decays (see Fig. 3.15): the NLO corrections are strongly enhanced for small values of p_T, while they turn even negative for large values. Hence the spectrum of the NLO predictions is for both the hardest and the second hardest jet softer than for the LO ones. The enhancement of the NLO curve in the first few bins of $p_T^{j_2}$ is caused by events with only two jets in the final state. In this configuration the two hard jets originating from the partons of the two decays are clustered into one jet, while the parton of the real radiation forms the second hardest jet. These contributions are strongly enhanced for small p_T values of the radiated quark/gluon (and even divergent for $p_T \to 0$), see the discussions in the next chapter. It has explicitly been checked that if $n_j = 3$ jets are demanded in the final state this peak vanishes completely. In any case, a simple rescaling of the LO curves with a constant K-factor obtained from the total cross sections is in general not correct. A similar observation holds for the invariant mass of the two hardest jets: the NLO curve is dragged to smaller values of $m^{j_1 j_2}$ and the differential K-factor is far from being flat over the whole region. For the $\not{E}_T$ predictions, in contrast, the deviation of the differential K-factor from the total one is rather small, of $\mathcal{O}(5\%)$, except for events with very large missing transverse energy. Likewise, the shape of the rapidity distributions of the jets are hardly affected by the NLO corrections. The m_{eff} curve essentially reflects the behaviour of the p_T distributions, as anticipated from its definition, Eq. (3.76).

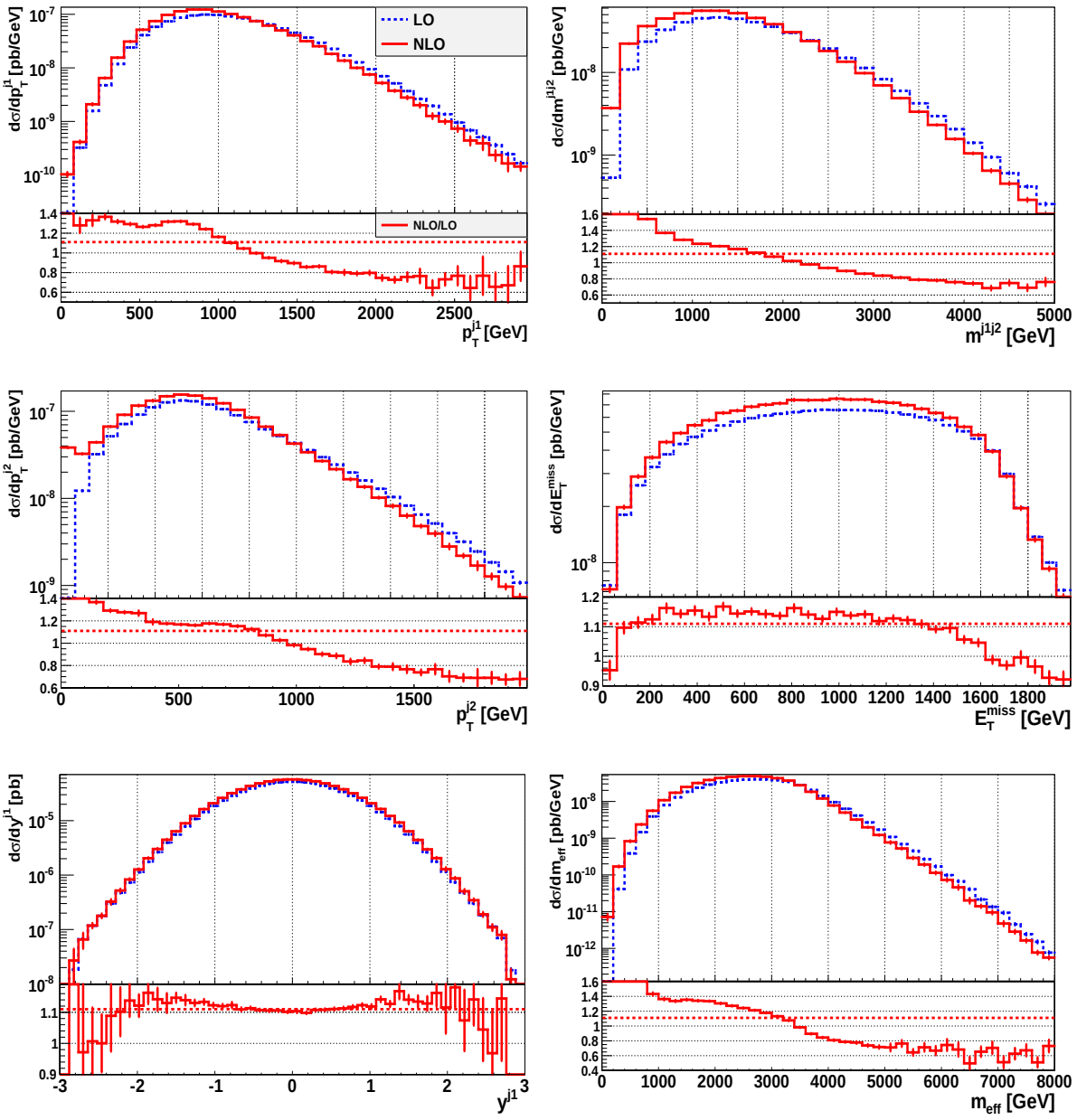

Figure 3.20.: Differential distributions as defined in the text for squark antisquark production, combined with the subsequent decay $\tilde{q} \to q\tilde{\chi}_1^0$ for the scenario 10.3.6*. Shown are the LO predictions obtained using Eq. (3.70) and the NLO results determined according to Eq. (3.72). In all plots the lower panels depict the respective differential K-factor (full) and the total K-factor from Tab. 3.12 (dashed).

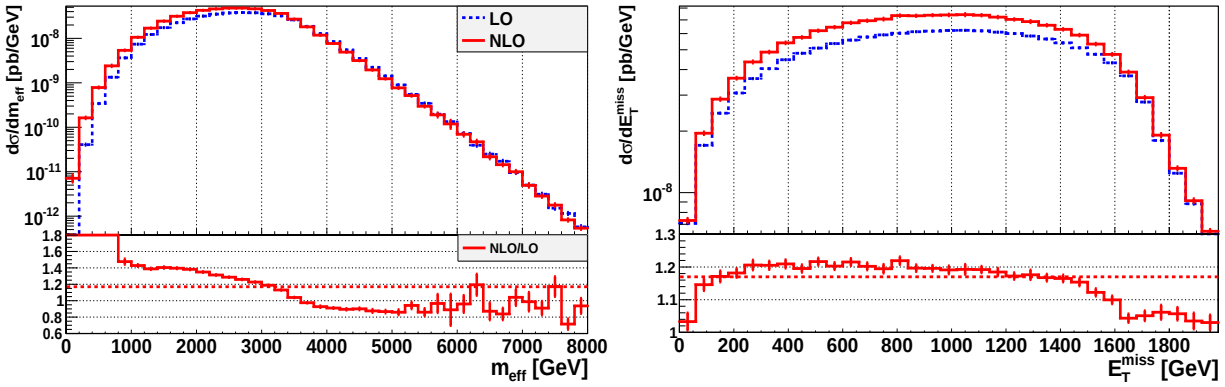

Figure 3.21.: Differential distributions for $\not{E}_T$ and m_{eff} as in Fig. 3.20, but using a dynamic scale $\mu_R = \mu_F = \overline{m}_T$.

Using a dynamic scale $\mu_R = \mu_F = \overline{m}_T$, determined from the momenta of the two squarks according to Eq. (3.50), does not alter these observations. With this scale choice the results for the total cross sections at LO and NLO are slightly different,

$$\sigma_{\text{LO}} = 0.087\,\text{fb}, \qquad \sigma_{\text{NLO}} = 0.102\,\text{fb}, \tag{3.77}$$

which implies

$$K = 1.17. \tag{3.78}$$

Fig. 3.21 shows the distributions for $\not{E}_T$ and m_{eff} with this scale choice. Comparing those to the respective distributions obtained for the fixed scale $\mu = \overline{m}_{\tilde{q}}$ in Fig. 3.20 one observes qualitatively an identical behaviour.

Next consider the same set of distributions for squark pair production with subsequent decays, this time for the scenario 10.4.5, depicted in Fig. 3.22. Again the results for 10.3.6* are qualitatively identical and not shown here. In essence, the behaviour is very much the same as for squark antisquark production in Fig. 3.20 and differs only in details. For example the differential K-factor of the rapidity distribution y^{j_1} shows slightly larger deviations from the total K-factor, whereas the one for $\not{E}_T$ is a bit flatter in the range considered here.

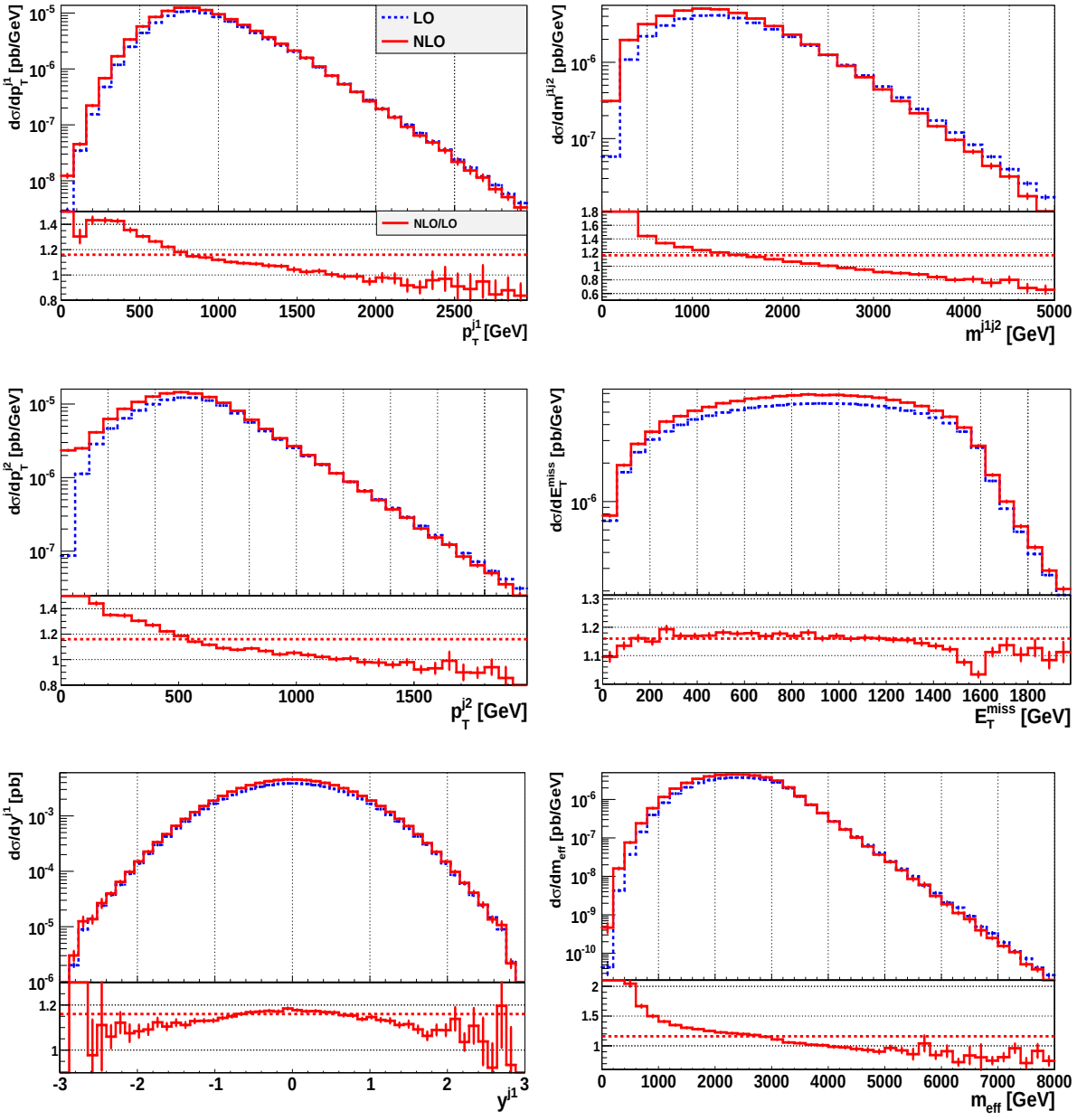

Figure 3.22.: Differential distributions as defined in the text for squark pair production, combined with the subsequent decay $\tilde{q} \to q\tilde{\chi}_1^0$ for the scenario 10.4.5. Shown are the LO predictions obtained using Eq. (3.70) and the NLO results determined according to Eq. (3.72). In all plots the lower panels depict the respective differential K-factor (full) and the total K-factor from Tab. 3.13 (dashed).

CHAPTER 4

MATCHING SQUARK PRODUCTION AND DECAY WITH PARTON SHOWERS

The implementation of squark (anti)squark production and the subsequent decay processes in the POWHEG-BOX allows not only for fixed order predictions at NLO, but also for a combination with arbitrary parton shower programs. The results obtained for this matching of the two simulation steps are presented in this chapter. After discussing the implementation of the processes in Sec. 4.1 the conducted tests are presented in Sec. 4.2. The effects of different parton shower algorithms provided in the frameworks of the Monte Carlo event generators PYTHIA 6 and HERWIG++ on these processes are investigated in Sec. 4.3. The last section contains a comparison of event rates obtained with the new tools developed in this thesis and the currently used simulation setup of the experiments at the LHC.

4.1. Implementation of the processes in the Powheg-Box

Besides the implementation of the typical process-dependent parts required by the POWHEG-BOX, which are discussed in the first part of this section, the correct treatment of contributions with on-shell intermediate gluinos has necessitated several conceptual changes in the overall organization of the event generation. Therefore, the implementation of the subtraction schemes described in Sec. 3.1.3.3 turned out to be one of the main obstacles and is described in detail in the second part of this section. The different operation modes of the developed code are steered by a multitude of flags, which can be provided in a typical POWHEG-BOX input file. For future reference, these flags are summarized and explained in App. B.

4.1.1. Process-dependent ingredients

As outlined in Sec. 2.2.4, the process-dependent ingredients required by the POWHEG-BOX consist of the following parts:

- **Flavour structures:** Both squark antisquark and squark pair production exhibit a non-trivial combinatorics when calculating all contributions to the production of light-flavour squarks. Nonetheless, as already discussed in Sec. 3.1, the matrix elements of many of these individual channels are identical. Thus they differ only with respect to the occurring

PDFs and the masses of the final-state squarks (which affect of course also the internal squark masses in the virtual and real contributions). An efficient organization of the evaluation leads to a considerable reduction of the required CPU time. The POWHEG-BOX already provides an option called `smartsig` to calculate identical amplitudes only once per iteration and to reuse the results. If the corresponding flag is set the program compares, before performing the main run, the results for the Born, virtual and real contributions, calculated without PDFs, for all implemented Born and real flavour structures. If some of them are found to be identical, or proportional to each other, they are calculated only once for each phase space point in the main run. The PDFs and the proportionality factors for the respective flavour structures are then attached to the cached results. However, the structure of the POWHEG-BOX is not designed for the evaluation of processes involving flavour structures with different combinations of final-state masses, i.e. for a $2 \to 2$ process only processes with at most two different final-state masses can be calculated in a single run. Hence for squark production with an arbitrary mass spectrum in principle each combination of flavour/chirality has to be evaluated separately. This requires 36 runs for squark pair production and additionally the same number for antisquark pair production. However, the contributions to the latter ones differ from the squark pair production processes only in the PDFs and can thus easily be obtained by applying the `smartsig` option. For squark antisquark production 64 individual subchannels have to be evaluated. The number of required single runs can be reduced if the considered mass spectrum is such that some of the individual production channels share identical mass combinations for the final-state squarks, as e.g. in case of the two scenarios defined in Sec. 3.1.5.1.

In order to minimize the computational cost as much as possible the following three options for the initialization of the flavour structures have been implemented in the POWHEG-BOX:

1. Individual calculation: In the `powheg.input` card the two final-state particles are entered directly. With this option only the flavour structures contributing to the specific subchannel are generated (which include in case of squark pair production the charge conjugate modes if the flag `withcc` is set, see App. B).

2. Partial combination: Here an input file has to be provided by the user, which specifies the final states sharing identical masses (e.g. $\tilde{u}_L\tilde{u}_L$, $\tilde{u}_L\tilde{c}_L$ and $\tilde{c}_L\tilde{c}_L$ in the two scenarios defined in Sec. 3.1.5.1). The resulting flavour structures for each set are then created automatically.

3. Full combination: If all squarks are assumed to be degenerate in mass, all possible flavour structures can be evaluated in one run. Applying the `smartsig` option automatically sorts out those which are fundamentally distinct and have to be calculated explicitly.

If the decays of the squarks are taken into account, the flavour structures have to be extended to include the decay products. For the decay $\tilde{q} \to q\tilde{\chi}_1^0$ considered here this is trivial, since the flavour of the quark corresponds to the one of the decaying squark.

- **Born phase space:** The definition of the Born phase space is fairly standard: for both production processes a $2 \to 2$ phase space with massive particles in the final-state is required (see e.g. [120]). As no resonant structures occur in the Born processes, no sophisticated mapping of the integration variables is needed here. For the decays of the produced squarks in the NWA the phase space for the $2 \to 4$ process completely factorizes,

as discussed in Ch. 3, and only the parametrization of a $1 \to 2$ phase space has to be implemented.

- **Matrix elements squared:** The implementation of both the Born amplitudes squared and the colour- and spin-correlated amplitudes, calculated as described in the previous chapter, is straightforward. The results for the virtual contributions created with FORMCALC can be used without further modifications, since the overall factor $\frac{\Gamma(1-\epsilon)}{(4\pi)^\epsilon}$ is already factored out in the LOOPTOOLS routines, as required by the convention used in the POWHEG-BOX for the FKS method. The implementation of the real contributions, in contrast, is more complicated due to the treatment of the contributions with on-shell intermediate gluinos in the qg-channels and is discussed in the next section.
- **Colour flows:** The colour flows for the Born processes are determined in the colour flow decomposition [121], see App. A.3. The colour flows for events with real emissions generated according to the POWHEG master formula, Eq. (2.52), are built automatically by the POWHEG-BOX in an approximate manner. The implemented algorithm starts from the colour flow determined for the underlying Born configuration of a specific event and constructs the colour of the emitter and the emitted parton according to the performed splitting, see [27] for further details.

4.1.2. Implementation of the subtraction schemes for on-shell intermediate gluinos

The considerations presented in this subsection have been partly published in [91].

The main problem in the implementation of the subtraction schemes for on-shell intermediate gluinos is the way the phase space for the real radiation is constructed. The process-independent definitions used in the POWHEG-BOX are adjusted to the structure of the automated version of the FKS method, hence changing them would require a complete reimplementation of this subtraction algorithm. To be more concrete, the POWHEG-BOX starts from a phase space point for the $2 \to n$ Born-like configuration and constructs the one-particle phase space for the additional radiation using the rescaled energy of the emitted parton and two angles relative to the emitter. Comparing this setup to the way the different subtraction schemes defined in Sec. 3.1.3.3 work two problems are evident. First of all, it is not possible to perform a mapping of the integration such that the Breit-Wigner form of the intermediate gluino propagator is efficiently probed. Using a small value for the regulator $\Gamma_{\tilde{g}}$, which is desirable to reduce the effect of this unphysical parameter to a minimum, worsens the convergence of the integration further. The second problem concerns the restriction of the phase space for the subtraction terms as defined in Eq. (3.35). In the parametrization used in the POWHEG-BOX the required modification of the Jacobian is not straightforward.

Further problems occur in all schemes, except for the simple DR-I method, since after the subtractions the real contributions are no longer positive definite. This increases the fraction of events with negative weights, as the number of phase space points for which the $\overline{\mathcal{B}}$ function in Eq. (2.52) is negative increases (see also the discussion in Sec. 4.3.1). Moreover, the algorithm used in the POWHEG-BOX for the generation of the hardest emission is based on the assumption that the ratio $\mathcal{R}_s/\mathcal{B}$ in the POWHEG Sudakov form factor is positive. Both these problems have already been observed in the context of the implementation of tW production in the POWHEG-BOX, see [122]. While the larger fraction of events with negative weights can be reduced by means of a folded integration over the radiation variables, see Eq. (4.6) below, the second problem

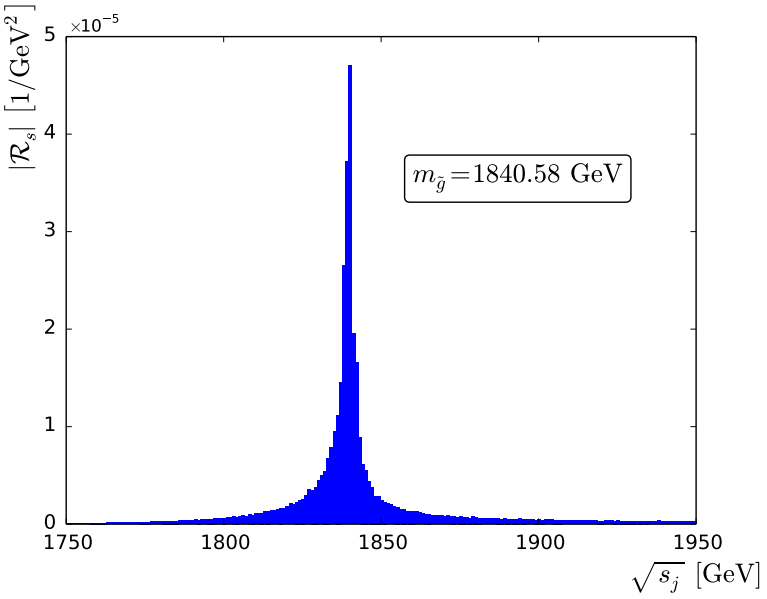

Figure 4.1.: The envelope for the absolute values $|\mathcal{R}_s|$ with $\mathcal{R}_s < 0$ as a function of the invariant mass of the intermediate gluino, $\sqrt{s_j}$, as defined in the text. The results have been obtained for the benchmark scenario 10.4.5, applying the DS* scheme. All contributing qg-channels to squark antisquark production are taken into account

cannot be solved directly. The proposal of [122], adapted to the processes considered here, consists in introducing a cut on the invariant mass $\sqrt{s_j}$ of the intermediate gluino close to the resonant region,

$$\mathcal{R}_s \to \mathcal{R}_s\, \Theta(|m_{\tilde{g}} - \sqrt{s_j}| - \Delta)\,, \tag{4.1}$$

with $\Delta = \mathcal{O}(\Gamma_{\tilde{g}})$. The motivation for this procedure was based on the observation that the negative ratio, $\mathcal{R}_s/\mathcal{B} < 0$, occurs mostly close to the resonant region. This holds also in case of the implemented squark production processes. In order to justify this statement quantitatively the points with negative values for $\mathcal{R}_s$ in the qg-channels of squark antisquark production are shown in Fig. 4.1 as a function of $\sqrt{s_j}$, with s_j corresponding to either $s_1 = (k_{\tilde{q}} + k_3)^2$ (for the $\tilde{q}\bar{\tilde{q}}\bar{q}$-channels) or $s_2 = (k_{\bar{\tilde{q}}} + k_3)^2$ (for the $\tilde{q}\bar{\tilde{q}}q$-channels). Here, k_3 is the momentum of the final-state (anti)quark. The depicted results for $|\mathcal{R}_s|$ comprise all contributing qg-subchannels and have been obtained for the benchmark scenario 10.4.5 defined in Sec. 3.1.5.1, applying the DS* scheme as defined in Sec. 3.1.3.3 for the subtraction of on-shell intermediate gluinos. The figure shows the envelope for the absolute values $|\mathcal{R}_s|$, i.e. all points with $\mathcal{R}_s < 0$ lie in the blue area. The depicted curve is clearly peaked around $\sqrt{s_j} = m_{\tilde{g}}$, a behaviour which can be explained by the (negative) contribution of the interference terms between resonant and non-resonant diagrams. These terms have an integrable resonant structure, which is not subject to any subtraction procedure and can thus dominate the remaining terms close to the resonant region.

In view of all these problems a 'direct' implementation of the DS scheme as presented in [122] for tW production is not very promising. Instead, the most general version of the POWHEG master formula, Eq. (2.52), has been taken as a starting point. For the qg-channels, which contain the singularities arising from on-shell intermediate gluinos, the real amplitude squared has been split such that the different building blocks for the actual subtraction mechanism are no longer used in the generation of the hardest emission, but are treated as regular remnants.

These remnants correspond to the term $\mathcal{R} - \mathcal{R}_s$ in Eq. (2.52). They are integrated separately, using a phase space parametrization tailored to the resonant structure. However, this splitting must not destroy the leading-log accuracy of the POWHEG formalism, i.e. all terms involving soft/collinear singularities have to be contained in $\mathcal{R}_s$, which corresponds to the part actually used for the POWHEG-like event generation. The different ways of splitting the real amplitudes can be summarized as follows:

- $\mathcal{R}_s = |M_{\text{tot}}|^2$: This choice corresponds to the original DS method also used in the implementation of tW production, i.e. the real amplitudes squared are actually not split. However, this quantity is only gauge invariant if the regularizing gluino width is introduced after the analytical expansion in the poles, as discussed in Sec. 3.1.3.3. This option is denoted DS*-I in the following.
- $\mathcal{R}_s = |M_{\text{nr}}|^2$: For this choice the interference terms and the resonant part of the amplitude squared, i.e. $2\,\text{Re}(M_{\text{r}} M_{\text{nr}}^*) + |M_{\text{r}}|^2$ in Eq. (3.18), and the subtraction term for the on-shell intermediate gluino, Eq. (3.26), are treated as regular remnant. These terms do not contain any IR divergences, thus the leading-log accuracy of the POWHEG method is not spoiled. For their integration a mapping of the integration variables on the Breit-Wigner structure of the gluino propagator is straightforward and the Jacobian for the subtracted term can be easily adapted. Moreover, the artificial cut introduced in Eq. (4.1) is not necessary, as $\mathcal{R}_s = |M_{\text{nr}}|^2 > 0$. However, it is not possible to introduce the regularizing gluino width in a gauge-invariant way by expanding the expressions.[13] This option is called DS-II in the following.
- $\mathcal{R}_s = \frac{f_1}{s_{2g}} + f_2(s_{2g})$ (see Eq. (3.22) for the definition of f_1, f_2): With this choice gauge independence is guaranteed by construction. Again, the leading-log accuracy of the POWHEG method is preserved, as all IR-divergent contributions are contained in f_2. However, in this approach $\mathcal{R}_s < 0$ is possible, requiring again the introduction of the artificial cut on the invariant mass of the resonant gluino described above. The points with $\mathcal{R}_s < 0$ occur again most often close to the region where $\sqrt{s_j} \approx m_{\tilde{g}}$. This option is denoted DS*-III in the following.

Note that this splitting procedure is only applied if the considered mass spectrum actually allows for intermediate resonant gluinos, i.e. $m_{\tilde{q}} < m_{\tilde{g}}$.

Splitting the real amplitudes squared and treating parts of them as regular remnants requires an explicit implementation of the colour flows for the remnant contributions $\mathcal{R} - \mathcal{R}_s$, as the approximate algorithm implemented in the POWHEG-BOX cannot be applied to these terms. Therefore, all possible colour flows (in the planar limit) have to be calculated, similar to the Born case. As described in App. A.3, they can be constructed by applying the colour flow decomposition for the amplitudes and choosing a specific colour flow according to its relative contribution. The actual calculation of the different contributions is rather involved, as the subtraction of on-shell intermediate gluinos has to be performed in the respective colour flow expressions, too. The approach followed here is essentially identical to the colour assignment procedure used in MADGRAPH, which has been used to perform a multitude of cross checks for the different topologies. A further drawback of all DS schemes with $\mathcal{R}_s \neq |M_{\text{tot}}|^2$ is the fact that the regular remnants $\mathcal{R} - \mathcal{R}_s$ are not positive definite, since they comprise only parts of the full matrix elements squared and the subtracted contributions. In the original POWHEG-BOX code,

[13] As these terms are treated differently in the event generation (see Eq. (2.52)), a residual gauge dependence is left even for $\Gamma_{\tilde{g}} \to 0$.

Method	BW-mapping	phase space restr.	cut for radiation	gauge invariance
DR-I	unnecessary	unnecessary	unnecessary	violated
DR-II	unnecessary	unnecessary	yes	violated
DS*-I	not possible	not possible	yes	preserved
DS-II	possible	possible	unnecessary	violated
DS*-III	possible	possible	yes	preserved

Table 4.1.: Summary of the advantages and disadvantages of the different subtraction methods. Both Diagram Removal (DR) methods are discussed in Sec. 3.1.3.3. The Diagram Subtraction (DS) methods listed here are only distinct w.r.t. the actual implementation: for DS*-I the subtraction is performed on the complete real amplitude squared (i.e. $\mathcal{R}_s = \mathcal{R}$ in Eq. (2.52)). For DS-II and DS*-III the real contributions are split as described in the text. This table has been published in [91].

regular remnants are supposed to be positive, as they usually comprise the full matrix elements squared for flavour structures which do not contain any IR divergences. Therefore, the parts of the code concerning the integration and event generation for these contributions have had to be adapted accordingly.

The implementation of both DR methods defined in Sec. 3.1.3.3 is rather straightforward, as they solely consist in neglecting certain terms in the real matrix elements squared. In Tab. 4.1 the advantages/disadvantages of all the aforementioned methods are summarized. Comparing the different implementations one is lead to conclude that there is no optimal choice regarding speed, numerical stability and conceptual correctness: while the simple but incomplete DR-I method is the fastest and most stable one, the more involved solutions based on the DS(*) scheme either require the introduction of an artificial cut for the radiation generation or are not gauge invariant. Moreover, the implementation of these methods is way more involved and has required major modifications of the code and additionally the explicit calculation of the expressions for the remnant colour flows in the colour flow decomposition.

4.2. Checks of the implementation

In order to check the correct implementation of the processes discussed in the previous chapter in the POWHEG-BOX several aspects of the results have to be tested. First of all, the NLO predictions obtained as a by-product during the integration of the $\overline{\mathcal{B}}$-function in Eq. (2.52) have to reproduce any results available from stand-alone NLO programs. This point has already been discussed extensively in Sec. 3.1.4. A second important check consists in the verification of the basic properties of the POWHEG method for inclusive and exclusive quantities, see Sec. 2.2.4. Moreover, as discussed in the previous section, the implementation of the different schemes for the subtraction of intermediate on-shell gluinos has required major modifications in the main code and should therefore be checked carefully. To this end the outcome for the implemented schemes is compared at the end of this section.

The checks presented in the following have been conducted for both squark antisquark and squark pair production. The results are essentially the same, therefore only those obtained for squark antisquark production are presented here. A nearly identical set of distributions has been published for squark pair production in [91].

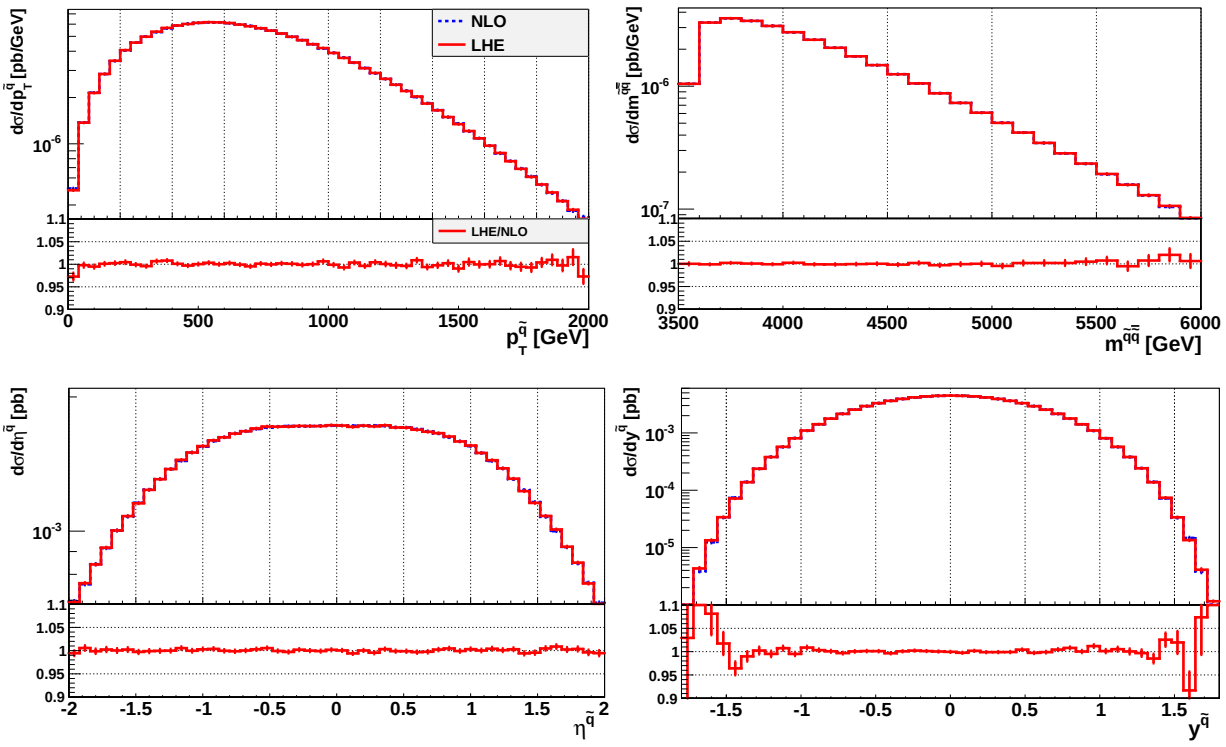

Figure 4.2.: Distributions for squark antisquark production at NLO accuracy compared to the predictions obtained after generation of the first radiation according to Eq. (2.52). Here the benchmark scenario 10.3.6* is used. Note that the NLO and LHE curves are essentially identical and thus hardly distinguishable.

Setup

The benchmark scenarios considered here are identical to those defined in Tab. 3.1. All results in the following have been obtained for the LHC with $\sqrt{s} = 14\,\text{TeV}$, using a fixed scale $\mu_R = \mu_F = \overline{m}_{\tilde{q}}$ and the PDF set CT10NLO with the two-loop RGEs for α_s. For the investigation of inclusive and exclusive observables the NLO predictions for these quantities are compared with the distributions at the level of the generated POWHEG events, i.e. after generating the first emission according to Eq. (2.52), but before adding any subsequent radiation from parton showers. These events are by default written to an LHE file and thus denoted LHE. In the following predictions for both decayed and undecayed samples are shown. In the undecayed case no cuts are applied, except for demanding $p_T^j > 1\,\text{GeV}$ for the emitted parton. If the decays are taken into account, the jet identification cuts used in Ch. 3.3,

$$p_T^j > 20\,\text{GeV}, \quad |\eta^j| < 2.8, \tag{4.2}$$

are applied, but no event selection cuts are used. Consequently the total cross section for inclusive quantities remains unaltered. The jets are clustered again with the anti-k_T algorithm, using $R = 0.4$. If not stated explicitly otherwise all plots in the following include again the statistical errors of the Monte Carlo integration. The error bars for the ratios shown in the lower panels of the respective figures have been calculated using Gaussian error propagation.

Considering first the case of undecayed squarks, the NLO and LHE curves for the transverse momentum $p_T^{\tilde{q}}$, the invariant mass $m^{\tilde{q}\bar{\tilde{q}}}$, the pseudorapidity $\eta^{\tilde{q}}$ and the rapidity $y^{\tilde{q}}$ are shown in

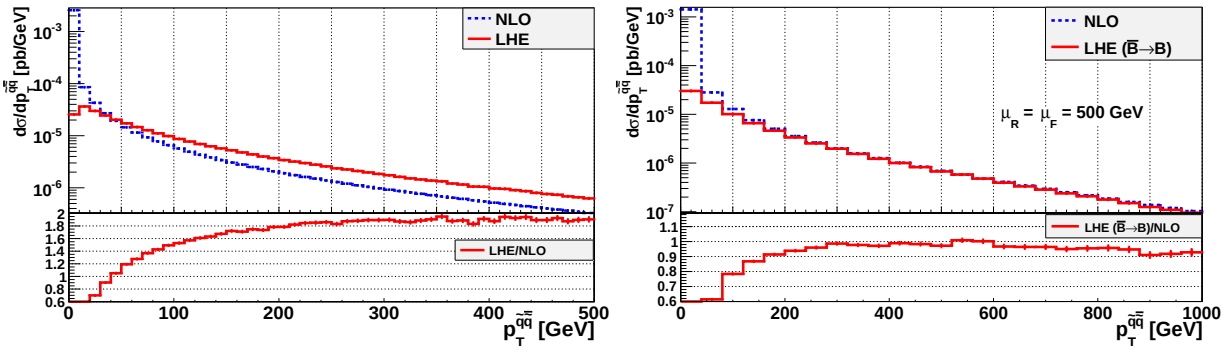

Figure 4.3.: Comparison of the NLO result and the LHE outcome for $p_T^{\tilde{q}\bar{\tilde{q}}}$ with the default scales $\mu_R = \mu_F = \overline{m}_{\tilde{q}}$ and a full POWHEG simulation (left) and for the scale choice $\mu_R = \mu_F = 500\,\text{GeV}$ with the replacement $\mathcal{B} \to \overline{\mathcal{B}}$ in the POWHEG event generation (right).

Fig. 4.2. The results for $p_T^{\tilde{q}}$, $y^{\tilde{q}}$ and $\eta^{\tilde{q}}$ have been obtained again by summing the contributions of the squark and the antisquark. Here the benchmark scenario 10.3.6* has been used, for the scenario 10.4.5 the output is qualitatively the same. As can be inferred from the depicted distributions, the NLO and the LHE results are in perfect agreement, as expected for these inclusive observables.

Turning next to exclusive quantities, which are expected to be more sensitive to the additional emission of partons, the p_T distribution of the $\tilde{q}\bar{\tilde{q}}$ system, $p_T^{\tilde{q}\bar{\tilde{q}}}$, is considered. At fixed NLO this observable is identical to the p_T distribution of the radiated parton. The predictions for this observable are shown in the left plot of Fig. 4.3. Here the NLO result differs significantly from the POWHEG outcome after generation of the first emission over the whole p_T range. The disagreement for small values of p_T is to be expected, as the NLO result is actually divergent in this limit, whereas the LHE curve shows the Sudakov damping inherent in the way the hardest emission is generated in the POWHEG method. For large p_T, however, the two predictions should coincide, as in the limit $p_T^{\tilde{q}\bar{\tilde{q}}} = p_T^j \gg 1$ the NLO result should be recovered in the POWHEG master formula, Eq. (2.52). However, in this region the LHE curve overshoots the NLO one by roughly a factor 1.9.

A similar discrepancy for large p_T values of the radiated parton has also been observed in other POWHEG implementations, e.g. Higgs boson production in gluon fusion [123] or the pair production of vector bosons [124]. The studies performed in these publications revealed that it is caused by two effects. First of all, the K-factors are sizable in both cases. Recalling the structure of the POWHEG master formula in the limit of large p_T (see Eq. (2.55)),

$$\mathrm{d}\sigma_{PWG} = \left(\frac{\overline{\mathcal{B}}}{\mathcal{B}}\mathcal{R}_s + (\mathcal{R} - \mathcal{R}_s)\right)\mathrm{d}\Phi_{n+1}\,, \tag{4.3}$$

the presence of a large NLO K-factor clearly enhances the first contribution. This is formally an effect of higher orders and yields only negligible modifications for comparatively small values of the ratio $\overline{\mathcal{B}}/\mathcal{B}$. However, in the processes investigated here the NLO corrections amount to several tens of percent. The second point causing this enhancement is the use of different scales in the $\overline{\mathcal{B}}$ function and in $\mathcal{B}$. In $\overline{\mathcal{B}}$ the fixed scale of the NLO calculation is used, whereas $\mathcal{B}$ is evaluated at the scale used in the generation of the hardest emission and thus depends on the p_T of the radiated parton.

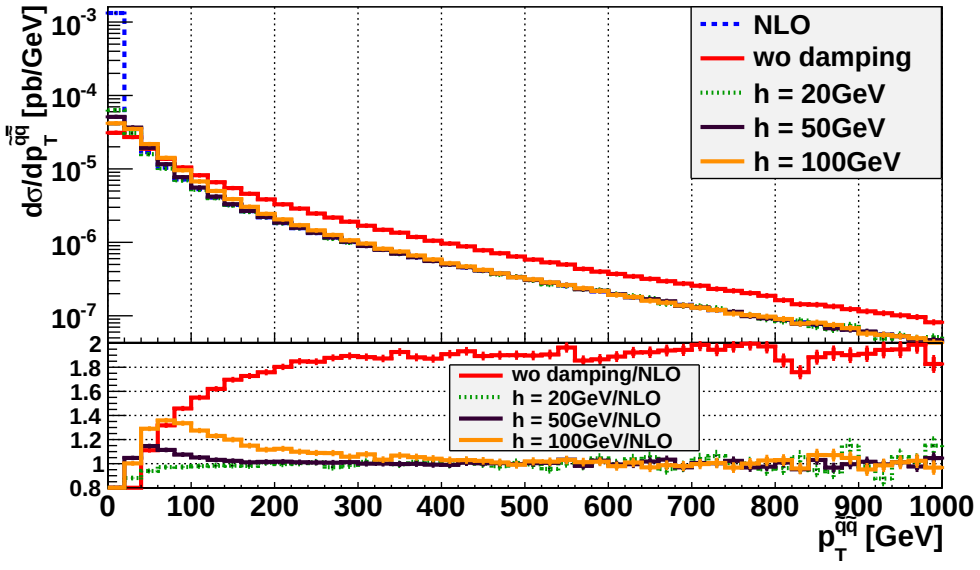

Figure 4.4.: The $p_T^{\tilde{q}\bar{\tilde{q}}}$ distribution as obtained for the NLO case, the POWHEG simulation without any damping of non-singular regions (formally $h \to \infty$ in Eq. (4.4)) and for different values of h.

In the context of the implementation of [123] a simple test for the validity of these arguments has been proposed: in order to eliminate the effect of the large K-factor, the event generation is performed by replacing the $\overline{\mathcal{B}}$ function with the Born amplitude squared, $\mathcal{B}$. Moreover, the effect of the different scales can be reduced by lowering the scale used in the replaced $\overline{\mathcal{B}}$ function and comparing the LHE outcome with the pure NLO prediction for p_T values in the vicinity of this new scale. To this end, the scales have been set to $\mu_R = \mu_F = 500\,\text{GeV}$. The thus obtained results are depicted in the right panel of Fig. 4.3. With these modifications the LHE outcome reproduces the NLO result for $p_T^{\tilde{q}\bar{\tilde{q}}} \gtrsim 300\,\text{GeV}$. Hence the enhancement observed in the left plot of Fig. 4.3 is indeed caused by the two points discussed above.

This artificial enhancement can be reduced by applying the generalized POWHEG master formula given in Eq. (2.52) with $\mathcal{R} \neq \mathcal{R}_s$. Instead of the full real contribution only the soft/collinear part of the real matrix element squared is used for the event generation. Following the proposal of [123], this part is isolated by multiplying $\mathcal{R}$ with a function $\mathcal{F}$ constructed such that $\mathcal{F} \to 1$ in the limit of soft/collinear radiation and $\mathcal{F} \to 0$ for large p_T values of the emitted parton. A possible choice for this function is

$$\mathcal{F} = \frac{h^2}{p_T^2 + h^2}\,. \tag{4.4}$$

This form is implemented in the POWHEG-BOX and therefore used in the following. The parameter h controls the 'damping' of the enhancement caused by the factor $\overline{\mathcal{B}}/\mathcal{B}$. The choice $h \to \infty$ reproduces the case $\mathcal{R} = \mathcal{R}_s$ (thus no damping), while smaller values lead to a stronger damping. The effects for different choices of h can be inferred from Fig. 4.4, where the $p_T^{\tilde{q}\bar{\tilde{q}}}$-distribution is shown for different values of h. As expected from the definition, h determines the value of $p_T^{\tilde{q}\bar{\tilde{q}}}$ where the LHE outcome reproduces the NLO behaviour.

The ad hoc introduction of this additional parameter might seem to introduce a certain amount of arbitrariness into the simulation. However, one should recall here that all results obtained with the POWHEG method outlined in Sec. 2.2.4 are only determined modulo effects beyond

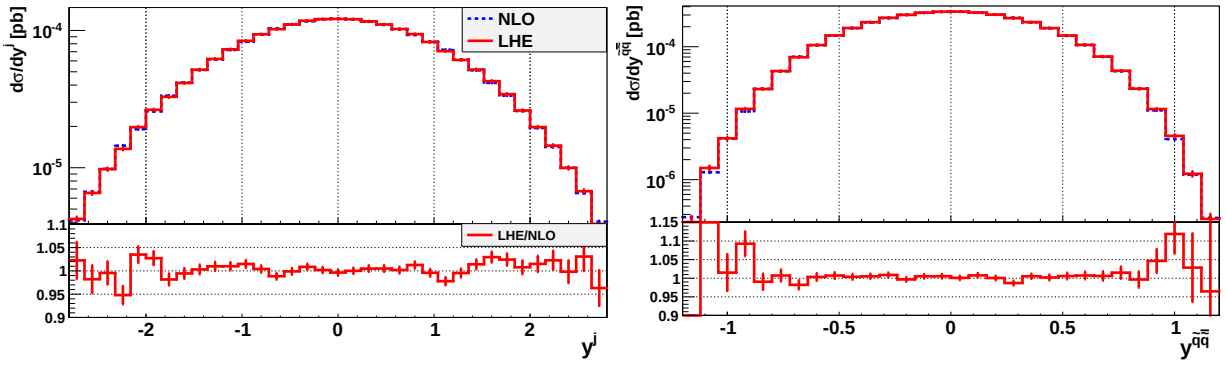

Figure 4.5.: The rapidity distributions of the emitted parton, y^j, and of the $\tilde{q}\bar{\tilde{q}}$ system, $y^{\tilde{q}\bar{\tilde{q}}}$ after applying a cut $p_T^{\tilde{q}\bar{\tilde{q}}} > 200\,\text{GeV}$. Shown are the NLO results and the LHE outcome, using the scenario 10.3.6*.

NLO. Moreover, this parameter does not affect the predictions for inclusive observables as those shown in Fig. 4.2.

In the following all results are calculated for $h = 50\,\text{GeV}$, which ensures that the $p_T^{\tilde{q}\bar{\tilde{q}}}$-distributions at NLO and after the generation of the POWHEG radiation coincide for $p_T^{\tilde{q}\bar{\tilde{q}}} \gtrsim 200\,\text{GeV}$. This agreement is of course not limited to this specific observable. Considering other distributions which are sensitive to the emission of an additional parton one observes a similar behaviour, if a lower cut on $p_T^{\tilde{q}\bar{\tilde{q}}}$ is applied. To illustrate this point the rapidity distributions for the radiated parton, y^j, and for the $\tilde{q}\bar{\tilde{q}}$-system, $y^{\tilde{q}\bar{\tilde{q}}}$, are shown in Fig. 4.5, applying a cut $p_T^{\tilde{q}\bar{\tilde{q}}} > 200\,\text{GeV}$.

Adding the decay of the squarks into a quark and the lightest neutralino and combining the NLO contributions to both production and decay as described in Eq. (3.72) yields for the p_T distributions of the resulting jets, the missing transverse energy $\not{E}_T$, the pseudorapidity of the second hardest jet η^{j_2}, the invariant mass of the two hardest jets $m^{j_1 j_2}$ and the observable m_{eff} defined in Eq. (3.76) the results depicted in Fig. 4.6. Considering the p_T distributions of the three jets one observes an excellent agreement for large p_T values in all cases. The predictions for the two hardest jets, especially the second one, which originate predominantly from the parton generated in the squark decay, show some discrepancies in the low-p_T region. The same effect has already been observed and explained in the discussion of the differential K-factors in Sec. 3.3.2. The $p_T^{j_3}$ distribution reflects again the Sudakov damping, as discussed above. By construction m_{eff} inherits the behaviour of the p_T distributions. The NLO and LHE predictions for the invariant mass agree perfectly away from the threshold region, while for small values of $m^{j_1 j_2}$ the difference in the two simulation steps already observed for $p_T^{j_2}$ shows up again. Last but not least, the results for $\not{E}_T$ and η^{j_2} are nearly identical.

Comparison of different subtraction schemes

In order to test the correctness of the implementations of the different subtraction schemes described in Sec. 4.1.2, the outcome for benchmark scenarios with $m_{\tilde{q}} < m_{\tilde{g}}$ has to be considered. As outlined above, especially the different versions of the DS approach have required major modifications in the code. Moreover, all DS schemes require the introduction of unphysical regularization parameters, which should not alter the results.

The results shown in the following have been obtained throughout at the level of LHE files for

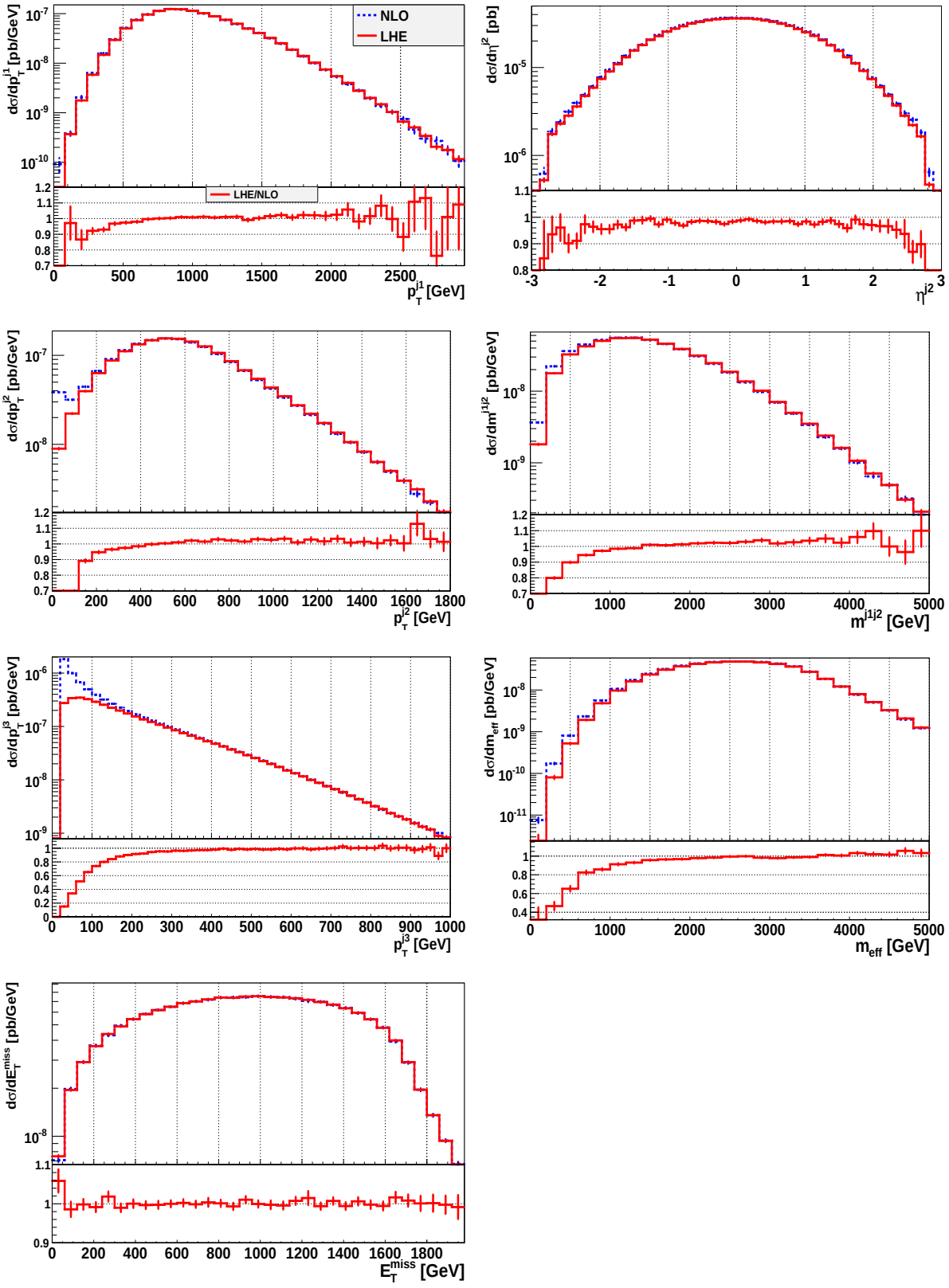

Figure 4.6.: Distributions of NLO results for squark antisquark production compared to the predictions obtained after generation of the first radiation according to Eq. (2.52). The NLO decays $\tilde{q} \to q\tilde{\chi}_1^0$ are included and the benchmark scenario 10.3.6* is used.

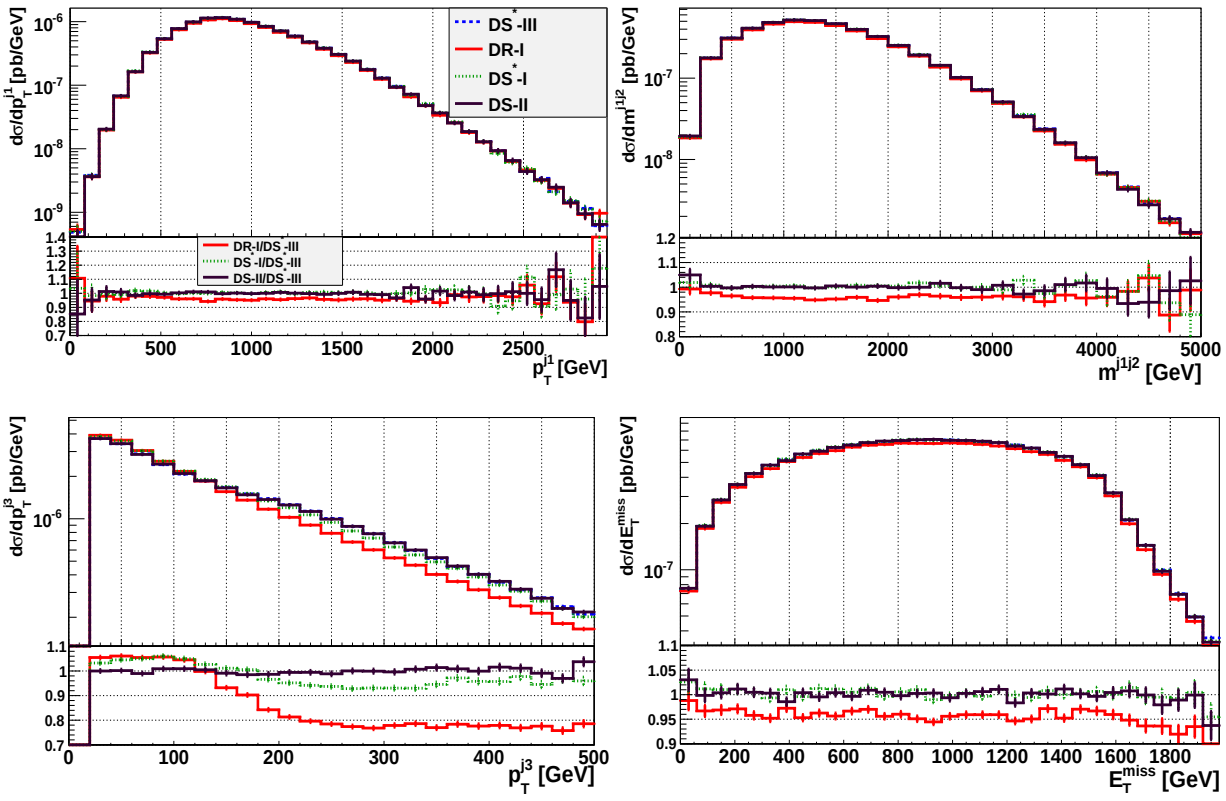

Figure 4.7.: Comparison of the different subtraction schemes for the subtraction of intermediate on-shell gluinos implemented in the POWHEG-BOX. The results include the decays $\tilde{q} \to q\tilde{\chi}_1^0$ at NLO and have been obtained for squark antisquark production using the benchmark scenario 10.4.5. All curves depicted have been determined at the level of LHE files, i.e. after performing the POWHEG-like event generation. The lower panels show the ratios of the DR-I, the DS-II and the DS*-I results to the DS*-III prediction.

the benchmark scenario 10.4.5 and squark antisquark production. The squark decays $\tilde{q} \to q\tilde{\chi}_1^0$ at NLO are included. The rest of the setup has been outlined at the beginning of this section.

In a first step the results for the subtraction schemes DR-I, DS*-I, DS*-III and DS-II are compared with each other. All DS schemes need a regularizing width for the intermediate gluino, which is chosen to $\Gamma_{\tilde{g}} = 1\,\text{GeV}$. Moreover, for the DS* methods a cut on the invariant mass $\sqrt{s_j}$ of the gluino as specified in Eq. (4.1) is used, which is set to $\Delta = 10\,\text{GeV}$. The obtained predictions for the p_T distributions of the first and third hardest jet, $p_T^{j_1}$ and $p_T^{j_3}$, the invariant mass of the two hardest jets, $m^{j_1 j_2}$, and the missing transverse energy $\not{E}_T$ are shown in Fig. 4.7. In each plot the lower panel depicts the ratio of the respective subtraction scheme and the method DS*-III.

The dependence of the $p_T^{j_1}$, $m^{j_1 j_2}$ and $\not{E}_T$ distribution on the concrete scheme used for the subtraction is rather small and reflects essentially the difference in the total cross section in case of the DR-I scheme. The residual gauge dependence introduced in the DS-II scheme is negligible in the scenario considered here (recall that the 'size' of the gauge dependence is directly proportional to the regularizing width, see the discussion in Sec. 3.1.3.3). In contrast, the prediction for $p_T^{j_3}$ shows for the DR-I scheme large discrepancies, whereas the DS*-I scheme deviates by less than 5% from the other two implementations of the DS scheme, which agree

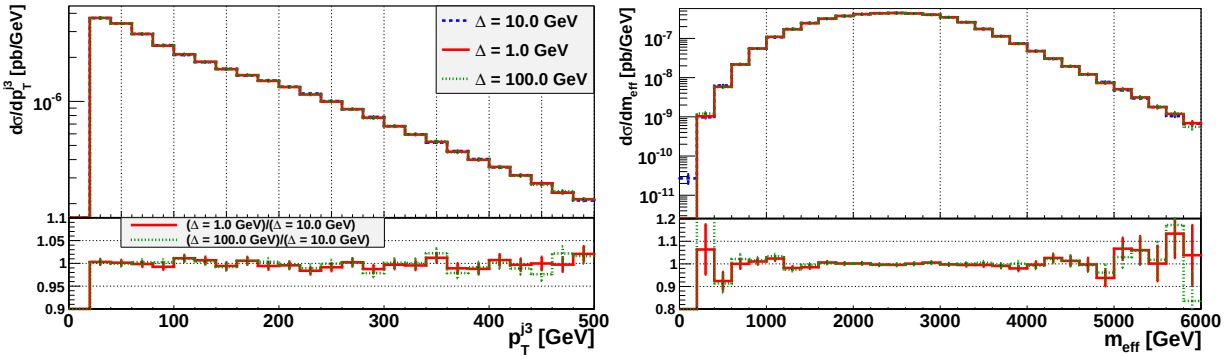

Figure 4.8.: Dependence of the LHE results for the benchmark scenario 10.4.5 obtained with the DS*-III method on the parameter Δ used in the generation of the hardest emission. The lower panels show the ratios of the results for $\Delta = 1\,\text{GeV}$ or $\Delta = 100\,\text{GeV}$ and $\Delta = 10\,\text{GeV}$.

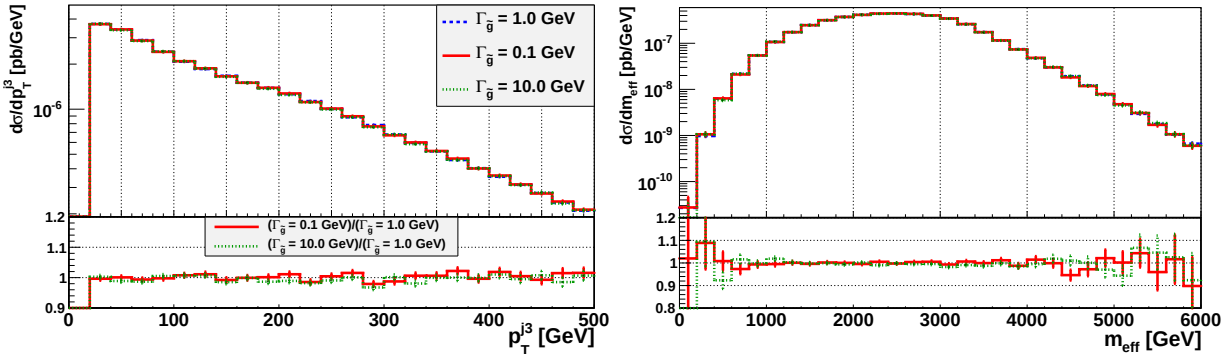

Figure 4.9.: Dependence of the LHE results for the benchmark scenario 10.4.5 obtained with the DS*-III method on the parameter $\Gamma_{\tilde{g}}$. The lower panels show the ratios of the results for $\Gamma_{\tilde{g}} = 0.1\,\text{GeV}$ or $\Gamma_{\tilde{g}} = 10.0\,\text{GeV}$ and $\Gamma_{\tilde{g}} = 1.0\,\text{GeV}$.

perfectly.

In order to assess the influence of the unphysical parameters $\Gamma_{\tilde{g}}$ and Δ, the predictions for the DS*-III scenario have been evaluated for different (reasonable) values of these parameters. In Fig. 4.8 the results for p_T^{j3} and m_{eff} are shown for three exemplary values $\Delta \in \{1\,\text{GeV}, 10\,\text{GeV}, 100\text{GeV}\}$, using in all cases $\Gamma_{\tilde{g}} = 1\,\text{GeV}$. The lower panels show the ratios with respect to the central value $\Delta = 10\,\text{GeV}$. The depicted curves delineate the independence of the actual Δ value. Other observables do not depend either on this parameter.

Similarly, the dependence on the regularizing gluino width is investigated by comparing the results obtained with the DS*-III method for different values of $\Gamma_{\tilde{g}}$ (using always $\Delta = 10\,\text{GeV}$), $\Gamma_{\tilde{g}} \in \{0.1\,\text{GeV}, 1.0\,\text{GeV}, 10.0\text{GeV}\}$. The results for p_T^{j3} and m_{eff} are depicted in Fig. 4.9, where again the lower panels show the ratios with respect to the central value $\Gamma_{\tilde{g}} = 1.0\,\text{GeV}$. As can be inferred from the different curves, the outcome of the simulation does not significantly depend on the actual value used for $\Gamma_{\tilde{g}}$. Again, this observation holds for other distributions, too.

4.3. Effects of different parton shower algorithms

The next step in a full simulation chain consists in processing the generated events with a parton shower, succeeded by a hadronization model and supplemented by a simulation of the underlying event. In the following section the effects induced by different parton shower algorithms are investigated. After introducing in Sec. 4.3.1 the utilized Monte Carlo shower programs and discussing some peculiarities arising in the context of the processes considered here, the subsequent sections address shower effects in event samples with undecayed (Sec. 4.3.2) and decayed (Sec. 4.3.3) squarks.

4.3.1. Setup and general remarks

The general setup concerning PDFs, scales, centre-of-mass energy and the applied jet algorithm to cluster final-state partons is identical to the one used in Sec. 4.2. Again, only jets passing the cuts specified in Eq. (4.2) are considered. The damping parameter introduced in Eq. (4.4) is set to $h = 50\,\text{GeV}$. All results are based on the two benchmark scenarios defined in Tab. 3.1. Using these scenarios five million events have been generated for squark antisquark and squark pair production, both with and without consideration of the squark decays into the lightest neutralino and a quark. The created event samples for squark pair production include always the (tiny) contributions of antisquark pair production. The event generation in the POWHEG-BOX can be performed either including or neglecting events with negative weights, a point which demands some discussion.

Events with negative weights and how to deal with them

One of the basic properties of the POWHEG method is the positivity of the event weights, which is guaranteed by the positivity of the $\overline{\mathcal{B}}$-function in Eq. (2.52). However, the evaluation of this function for a specific point in the phase space of the underlying Born configuration, Φ_n, requires in principal an integration over the phase space of the extra emission, Φ_{rad}. The implementation in the POWHEG-BOX circumvents this problem by projecting the three radiation variables forming Φ_{rad} onto a unit hyper cube $X_{\text{rad}} \equiv \{x^1_{\text{rad}}, x^2_{\text{rad}}, x^3_{\text{rad}}\}$ and integrating instead the function

$$\tilde{\mathcal{B}}(\Phi_n, X_{\text{rad}}) = \mathcal{B}(\Phi_n) + \mathcal{V}(\Phi_n) + \left|\frac{\partial \Phi_{\text{rad}}}{\partial X_{\text{rad}}}\right| [\mathcal{R}_s(\Phi_n, X_{\text{rad}}) - \mathcal{C}(\Phi_n, X_{\text{rad}})] \tag{4.5}$$

over (Φ_n, X_{rad}), see [26] for details. However, the positivity of $\tilde{\mathcal{B}}$ in this enlarged phase space is not guaranteed for every single phase space point. The fraction of points with negative $\tilde{\mathcal{B}}$ values, and hence events with negative weights, increases even further if $\mathcal{R}_s \neq \mathcal{R}$, as required in the squark production processes (see the discussion in the previous section). This is simply a consequence of the choice $\mathcal{R}_s = \mathcal{F}\mathcal{R}$, with $\mathcal{F}$ defined in Eq. (4.4), as in this case $\mathcal{R}_s < \mathcal{R}$ and consequently $\mathcal{R}_s - \mathcal{C} < 0$ in a larger region of phase space.

In order to reduce the fraction of negatively weighted events the $\tilde{\mathcal{B}}$-function can be redefined by averaging over more points X_{rad} while keeping the Born variables Φ_n fixed, i.e.

$$\tilde{\mathcal{B}} \to \mathcal{B}(\Phi_n) + \mathcal{V}(\Phi_n) + \frac{1}{n_1 n_2 n_3} \sum_{f_1=1}^{n_1} \sum_{f_2=1}^{n_2} \sum_{f_3=1}^{n_3} \left|\frac{\partial \Phi_{\text{rad}}}{\partial X'_{\text{rad}}}\right| \left[\mathcal{R}_s(\Phi_n, X'_{\text{rad}}) - \mathcal{C}(\Phi_n, X'_{\text{rad}})\right] , \tag{4.6}$$

with $X'_{\text{rad}} \equiv \{x^1_{\text{rad},f_1}, x^2_{\text{rad},f_2}, x^3_{\text{rad},f_2}\}$. This procedure is called folding (see [125]) and is also implemented in the POWHEG-BOX. An obvious drawback of this approach is the increased

run time, which grows proportional to the number of performed folding operations (modulo the evaluation of $\mathcal{B}$ and $\mathcal{V}$, which is of course performed only once per iteration), hence it is mandatory to make a reasonable choice for the n_i.

The results shown in the following sections have been obtained by setting the folding parameters of the POWHEG-BOX to the values

$$n_\xi = 5, \quad n_y = 5, \quad n_\phi = 1. \tag{4.7}$$

The subscripts refer to the respective radiation variables in the parametrization of the real emission phase space used in the POWHEG-BOX, which correspond to the rescaled energy of the emitted parton (ξ), the cosine of the splitting angle (y) and the azimuthal angle (ϕ). With this choice the fraction of negative events in case of squark antisquark production, using the benchmark scenario 10.3.6* and the damping parameter $h = 50\,\text{GeV}$, is reduced from 7% to 1‰.

However, in the context of squark production and decay processes two further sources of negative events can occur. The first one originates from the way production and decay are combined in Eq. (3.72), see the discussion in Sec. 3.3. It is not possible to apply the folding procedure described above in this case, since the negative contributions to $\overline{\mathcal{B}}$ are directly related to the (modified) Born contribution. Using a different expansion of the combination formula as in Eq. (3.73) would remedy this point, however this approach violates unitarity (see the remarks after Eq. (3.73)) and should therefore be avoided.

The implemented subtraction schemes described in Sec. 4.1.2 present another source of contributions with negative weights. While these are completely absent for the DR-I method and their number can be reduced again by means of folding for the DS*-I and the DR-II method, they inevitably occur for the methods relying on a splitting of $\mathcal{R}$, i.e. in particular for the DS*-III method applied in the following.

All in all, using the (for conceptual reasons preferable) DS*-III subtraction scheme and Eq. (3.72) for the combination of production and decay leads unavoidably to events with negative weights, which cannot be neglected. Therefore, they are kept in the LHE files by setting the POWHEG-BOX flag `withnegweights=1`, see [126] for details. In essence, with this choice the program writes out events with negative weights to the LHE, setting the individual weights `XWGTUP` to the respective sign times the absolute value of the cross section. Hence, averaging over all events yields for sufficiently large samples the physical total cross section.

Shower Monte Carlo programs

The generated event samples have been showered with two Monte Carlo event generators, using three different parton shower algorithms implemented in these programs. The individual settings are summarized in the following.

- **Pythia 6:** This event generator includes both a virtuality-ordered and a p_T-ordered shower. Only the latter one is applied here, as appropriate for the POWHEG method. In the following the version 6.4.28 [29] is used. All results have been obtained with the Perugia 0 tune [127], invoked by setting `MSTP(5) = 320`. A comparison with the Perugia 11 tune (`MSTP(5) = 350`) yields only tiny discrepancies.[14] In order to study only effects of the

[14] To be more precise, for squark antisquark production, including the decays and using the benchmark scenario 10.3.6*, of all observables considered in this section only the p_T^{j3} distribution shows with $\mathcal{O}(5\%)$ a deviation larger than 1%.

parton shower, hadronization and MPI effects have been turned off by setting `MSTP(111) = 0` and `MSTP(81) = 20`. Note that the rather awkward choice for the flag controlling the MPI simulation (20/21 for MPI off/on) is crucial in order to invoke the p_T-ordered shower. If this flag is set to 0 or 1 the virtuality-ordered shower is used instead. Moreover, electromagnetic γ-radiation off the quarks has been switched off via `MSTJ(41) = 11`.

However, in the simulation of the full process, including NLO corrections to the production and the decays, a further subtle difficulty arises when using Pythia, which is related to the way the starting scales for the shower are chosen. Recall that the Powheg approach relies on the assumption that the p_T of the additional final-state parton, which is emitted according to the master formula Eq. (2.52), is larger than the transverse momentum of any subsequent splitting generated by the parton shower. This requires the application of a p_T veto in the parton shower. In principle this is achieved in Pythia by reading the `SCALUP` entry in the individual event records written to the LHE file, which corresponds to the maximum p_T allowed for any branching, and using this value as starting scale for the evolution of the external partons. However, if final-state resonances are present (indicated by status codes `ISTUP=2` in the LHE file) the mass of those has to be preserved by the reshuffling operations performed in the shower algorithm. Therefore, the showering of partons originating from the decays of these resonances, i.e. in the processes considered here the produced squarks, is performed separately. The starting scale for these shower contributions is set to the invariant mass of all decay products, hence in the case at hand to the mass of the respective squark. In the scenarios considered here this scale is typically an order of magnitude larger than the `SCALUP` value, leading to much more radiation and thus to a strong bias of the results. In order to correct for this effect, the Pythia routines had to be adapted to use the scale specified in the LHE file as starting scale in all individual contributions to the parton shower. This amounted mainly to several changes concerning the `QMAX` variable in the `PYADSH` routine. The influence of this different choice for the starting scale is sizeable, as can be inferred from the sample results shown in Fig. 4.10. The depicted distributions have been calculated for squark pair production, using the benchmark scenario 10.3.6*, both with the original version of Pythia (green curve, denoted 'Pythia') and the modified one with the adapted starting scale $p_T^{\max} = p_T^{\mathrm{PWG}}$ (red curve), where p_T^{PWG} corresponds to the `SCALUP` value read from the LHE file. The lower panels depict the ratio of these results and the NLO prediction. In the following the modified Pythia version is used throughout.

- **Herwig++:** The default shower of Herwig++ [32] is ordered in the angles of the branchings. Applying this shower to an event sample generated according to the Powheg method requires again the use of a p_T veto. However, as already discussed in Ch. 2.2.3, this combination lacks the emission of soft wide-angle partons, as the first emission in an angular-ordered shower is not necessarily the hardest one. In principle these missing parts have to be simulated in an extra step via a so-called vetoed truncated shower, which is not provided by Herwig++ and thus not taken into account in the following. The effect of this missing part will be estimated by comparing the results to those obtained with the p_T-ordered Dipole-Shower [30, 31], which is also part of the Herwig++ framework. The results presented in the following sections have been obtained using the version 2.6.1 [128].

  The parameters controlling the different elements of the two Herwig++ showers have to be provided in a special input file, an example containing the most relevant ones is

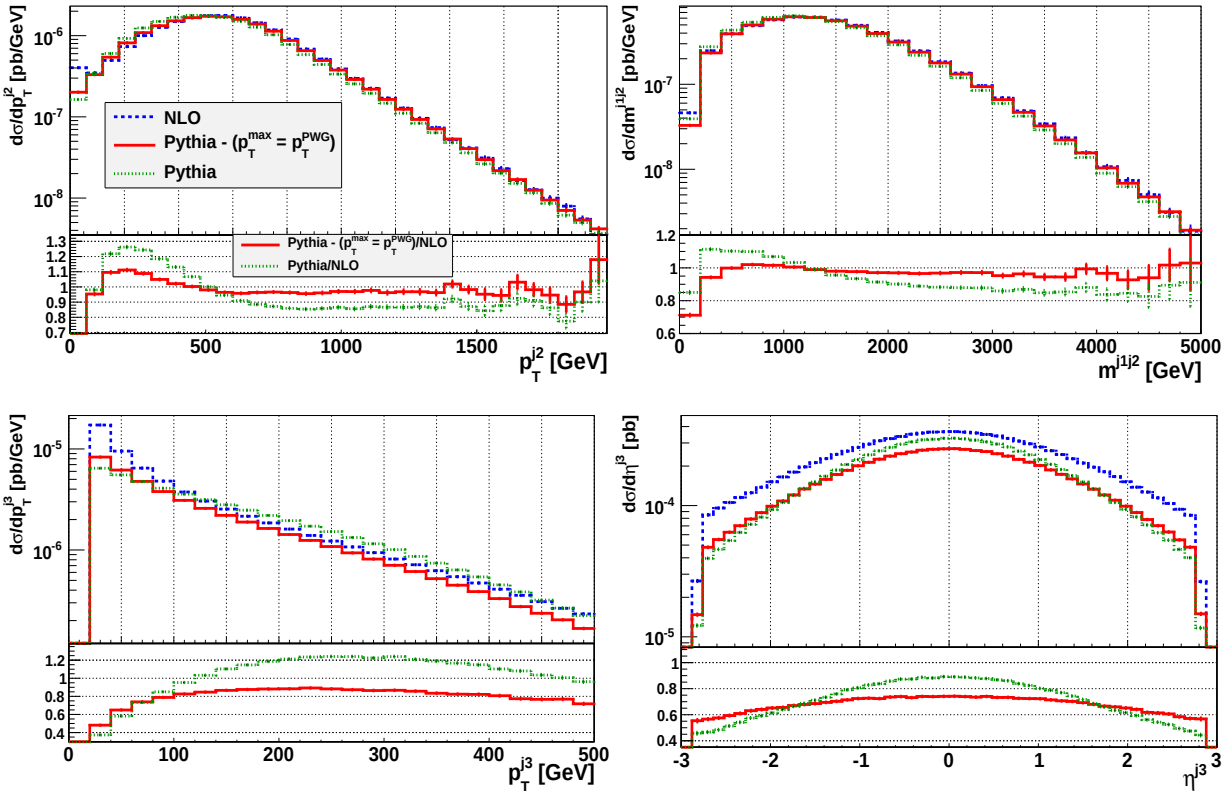

Figure 4.10.: Some differential distributions for squark pair production and decay with subsequent parton shower illustrating the effects of the modified starting scale in PYTHIA, as described in the text. The depicted results have been calculated for the scenario 10.3.6*, using the original version of PYTHIA (green) and the adapted one with $p_T^{\max} = p_T^{\mathrm{PWG}}$ (red). The lower panels show the ratios of the thus obtained predictions and the NLO results.

given in App. C. There are two further noteworthy points: First of all, the version of the DIPOLE-SHOWER used here does not include the dipole splitting kernels involving massive scalar particles. Hence it is not possible to use this parton shower for the showering of event samples with undecayed squarks in Sec. 4.3.2. Second, the problem of different starting scales arising for PYTHIA is not present in HERWIG++, as the imposed p_T veto is a global one in the sense that all radiated partons are guaranteed to have $p_T < p_T^{\mathrm{PWG}}$, regardless of their origin. In the following HERWIG++ refers only to the default shower, while the results labeled DIPOLE-SHOWER or, for the sake of brevity, DIPOLE refer to the DIPOLE-SHOWER included in the HERWIG++ framework.

4.3.2. Results for undecayed squarks

In a first step the decays of the produced squarks are not included, hence additional radiation induced by the parton showers can only originate from the initial-state partons or the final-state parton generated according to the POWHEG method. This procedure is obviously not suitable for phenomenologically relevant studies, however, it allows for an investigation of the parton shower effects solely at production level.

Figure 4.11 shows several distributions obtained for squark antisquark production using the scenario 10.3.6* (the results for the scenario 10.4.5 are qualitatively the same and not shown

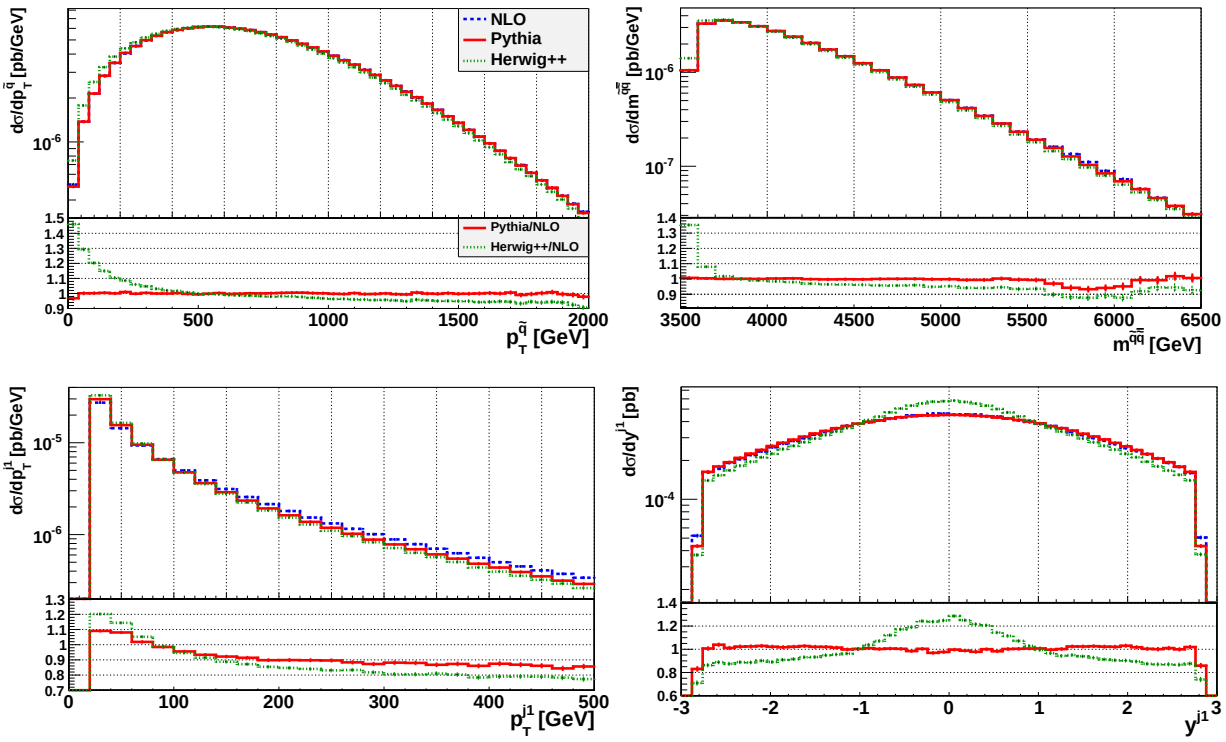

Figure 4.11.: Distributions obtained for squark antisquark production using the scenario 10.3.6*. The NLO result and the outcome of the parton showers PYTHIA and HERWIG++ for $p_T^{\tilde{q}}$, $m^{\tilde{q}\bar{\tilde{q}}}$ and $p_T^{j_1}$, y^{j_1} of the hardest jet are shown. The decays of the squarks are not simulated. In the lower part of each plot the ratio of the shower results and the NLO prediction is shown.

explicitly). The depicted curves comprise the predictions of the pure NLO calculation and the results after applying the parton showers of PYTHIA and HERWIG++, respectively. The lower panels show the ratios to the NLO outcome. Considering first the $p_T^{\tilde{q}}$ distributions (which comprise again the combined distributions for both squarks) and the $m^{\tilde{q}\bar{\tilde{q}}}$ predictions one notices that PYTHIA reproduces the NLO curve, whereas the HERWIG++ results are shifted to slightly smaller values, i.e. the squarks are softer. Away from threshold, however, the difference between the NLO and the HERWIG++ outcome is smaller than 10%.

Considering next observables describing the hardest jet, more distinct differences between the two shower programs are visible. Comparing the p_T distributions depicted in the lower left panel of Fig. 4.11 one notices that both parton showers predict for $p_T^{j_1} > 100\,\text{GeV}$ smaller rates than the pure NLO simulation, whereas the rates in the region $20\,\text{GeV} < p_T^{j_1} < 100\,\text{GeV}$ are slightly enhanced. This behaviour is caused by additional radiation generated in the showering stage, which may be too hard and/or develop too large angles to be clustered together with the original parton into the hardest jet. Contrasting the outcome of the two shower simulations one notes that HERWIG++ predicts a softer spectrum, with deviations of $\mathcal{O}(10\%)$ to PYTHIA. Comparing next the rapidity distribution of the hardest jet, y^{j_1}, it is apparent that PYTHIA essentially reproduces the NLO prediction, whereas the HERWIG++ result is enhanced in the central detector region. The same behaviour can be observed in the PYTHIA and HERWIG++ predictions for the rapidity distributions of the subleading jets, which are not present in the NLO calculation and hence only simulated by the respective parton shower. In these observables, which are not shown here, the HERWIG++ result is always strongly peaked in the central region, whereas the jets generated

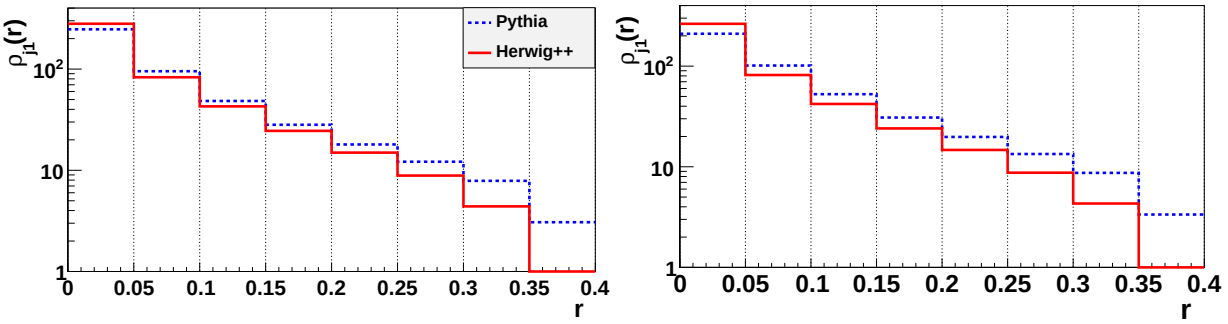

Figure 4.12.: The shapes $\rho_{j_1}(r)$ of the hardest jets obtained with PYTHIA and HERWIG++. The results have been obtained for squark antisquark (left) and squark pair production (right) without decays, using the scenario 10.3.6*. The error bars are not shown.

in the PYTHIA simulation are distributed rather uniformly. A possible explanation for this difference is the fact that PYTHIA is known to produce more soft, wide-angle radiation and therefore 'pulls' the jets away from the central region. A similar behaviour has been observed in a recent study on parton shower effects in vector boson fusion [129]. To confirm this statement it is useful to compare the structure of the (hardest) jets. Using the definition of [130] the shape of the i^{th} jet is defined as

$$\rho_{j_i}(r) = \frac{1}{\Delta r} \frac{p_T^{j_i}(r - \Delta r/2, r + \Delta r/2)}{p_T^{j_i}(0, R)}, \quad \Delta r/2 \leq r \leq R - \Delta r/2\,, \tag{4.8}$$

with the distance $r = \sqrt{\Delta y^2 + \Delta\phi^2}$ relative to the jet-axis. The quantity $p_T^{j_i}(r_1, r_2)$ corresponds to the summed transverse momenta of all partons which are clustered into the jet under consideration and lie in an annulus with inner/outer radius r_1/r_2 around the jet axis, i.e. have a distance $r_1 \leq r \leq r_2$ to the jet axis. In the following analysis the resolution parameter $\Delta r = r_2 - r_1$ is set to $\Delta r = 0.05$.

The thus obtained results for the hardest jet obtained with PYTHIA and HERWIG++ are depicted in the left panel of Fig. 4.12. Comparing the two curves it is obvious that the PYTHIA jet is significantly broader than the HERWIG++ one, thus indeed the partons produced by the PYTHIA shower are more diluted compared to the HERWIG++ result.

Considering the same set of observables for squark pair production (see Fig. 4.13), one notices that in this case the HERWIG++ predictions for $p_T^{\tilde{q}}$ and $m^{\tilde{q}\bar{q}}$ reproduce the respective NLO curves. The $p_T^{j_1}$ distributions obtained with the two shower programs essentially agree for $p_T^{j_1} > 200\,\text{GeV}$, for very soft jets the HERWIG++ outcome shows again a small enhancement. The rapidity distribution obtained with PYTHIA is identical to the NLO prediction, whereas the hardest jet in the HERWIG++ simulation is more central. However, the discrepancy is less pronounced compared to squark antisquark production.[15] Again, the consideration of the shape of the hardest jet, which is shown in the right panel of Fig. 4.12, suggests the difference in the way the two shower programs populate the available phase space as possible explanation for this observation.

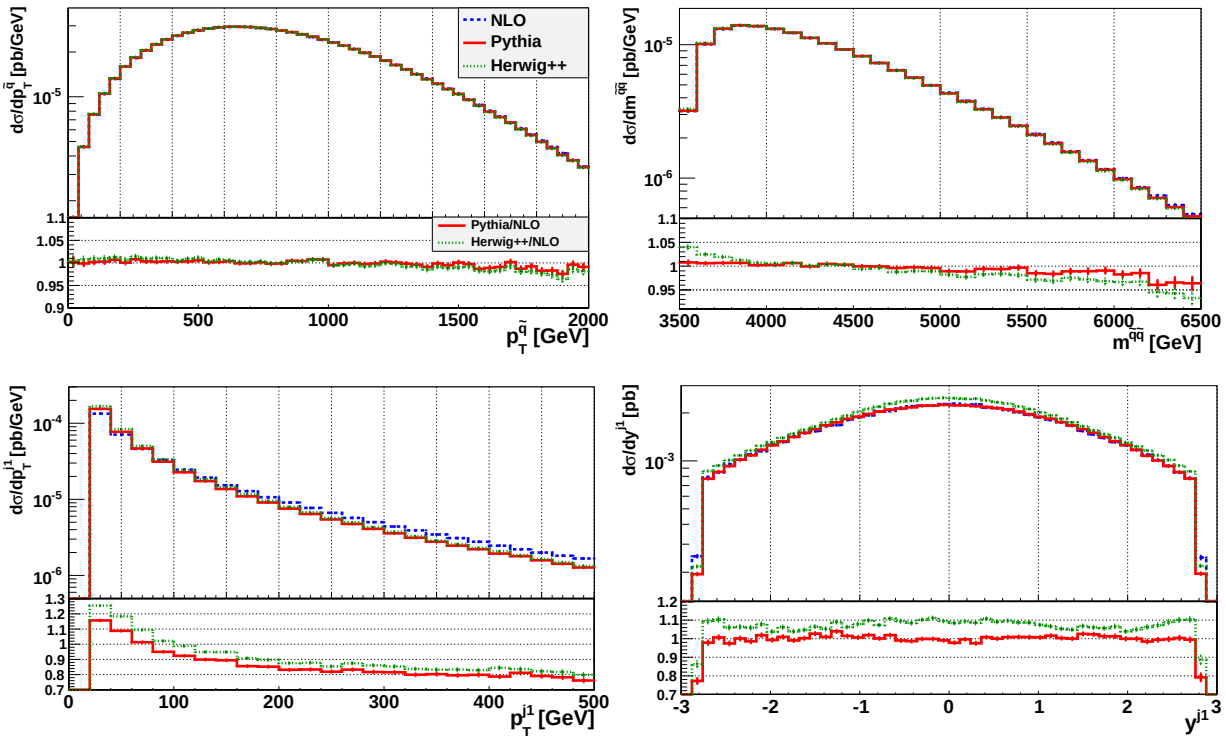

Figure 4.13.: Same as Fig. 4.11 for squark pair production. This figure has been published in [91].

4.3.3. Including the decays $\tilde{q} \to q\tilde{\chi}_1^0$

While investigating shower effects on event samples with undecayed squarks in the final state is interesting in order to compare different shower implementations, a phenomenologically relevant study additionally requires the consideration of squark decays. To this end the three parton showers introduced in Sec. 4.3.1 are applied to event samples which include the decays $\tilde{q} \to q\tilde{\chi}_1^0$. In order to assess the effects of the parton showers their predictions for different observables are shown for squark antisquark production in Fig. 4.14, using the scenario 10.3.6*. Likewise, Fig. 4.15 depicts the results for squark pair production, obtained with the scenario 10.4.5. All plots show the outcome of the three parton showers introduced in Sec. 4.3.1 and the NLO prediction, which serves as normalization in the respective ratio plots shown in the lower panels. The results for squark pair production using scenario 10.3.6* and squark antisquark production with scenario 10.4.5 do not reveal any new features compared to the depicted combinations and are therefore not shown here.

Comparing the predictions for the individual observables shown in the two figures the effects of the parton showers can be summarized as follows:

- $\boldsymbol{p_T^{j_1}}$: In all cases considered here the HERWIG++ result is in the low-p_T region slightly ($\mathcal{O}(10\%)$) enhanced compared to the other parton showers, whereas the DIPOLE-SHOWER and PYTHIA essentially agree here. At the other end of the spectrum, however, both the HERWIG++ and the DIPOLE-SHOWER predict $\mathcal{O}(10\%)$ smaller rates than PYTHIA, which is almost in accordance with the NLO result for large values of $p_T^{j_1}$. The outcome of HERWIG++ and the DIPOLE-SHOWER is identical for hard jets.

[15] Note that the total rate for the HERWIG++ result obtained by integrating the y^{j_1} distribution is larger than the NLO prediction. This is a consequence of the exclusive nature of this observable.

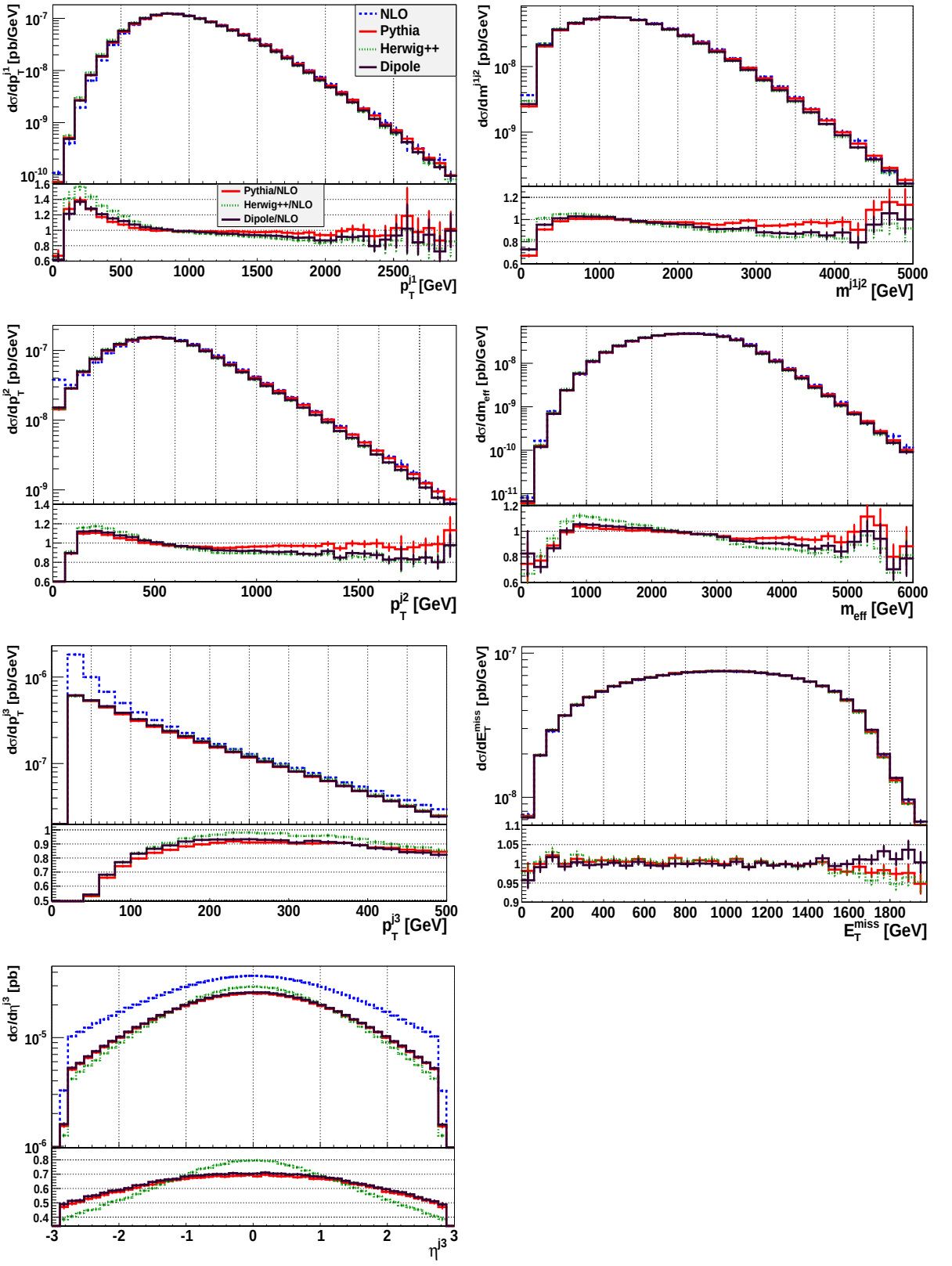

Figure 4.14.: Differential distributions for squark antisquark production combined with the decays $\tilde{q} \to q\tilde{\chi}_1^0$. Depicted are the results obtained at NLO and after applying the PYTHIA shower, the default shower of HERWIG++ and the DIPOLE-SHOWER. The benchmark scenario 10.3.6* has been used. In the lower panels the ratios of the results obtained with the three parton showers and the pure NLO prediction are shown.

- $\boldsymbol{p_T^{j_2}}$: The distributions for the transverse momentum of the second hardest jet show a similar behaviour. The HERWIG++ prediction is now almost exactly identical to the one obtained with the DIPOLE-SHOWER over the whole range considered. In the low-p_T region, all three parton showers yield within $\mathcal{O}(5\%)$ identical results, whereas PYTHIA predicts again more hard jets with nearly the same rate as the NLO result. The discrepancy compared to the other parton showers amounts again to $\mathcal{O}(10\%)$ for jets with large transverse momentum. Comparing the p_T distributions for the two hardest jets to the NLO result all parton showers predict a softer spectrum, caused by the additional radiation generated in the showering stage.

- $\boldsymbol{p_T^{j_3}}$: As already expected from the discussion of the undecayed samples in the last section, the distributions describing the third hardest jet show more pronounced differences. Comparing first the results of HERWIG++ and the DIPOLE-SHOWER one notices that they agree within $\mathcal{O}(5-10\%)$. The rate for the third jet obtained with PYTHIA is in all cases smaller compared to the other two parton showers. While the discrepancy using the benchmark scenario 10.3.6* is for both squark antisquark and squark pair production smaller than 10%, it amounts to 10-15% for the scenario 10.4.5 in both cases.

- $\boldsymbol{\eta^{j_3}}$: The largest differences in the three shower predictions emerge in the results for the pseudorapidity of the third hardest jet. While PYTHIA and the DIPOLE-SHOWER agree within 5% for all cases and differ in case of squark pair production only in the overall normalization, but not in the shape of the distributions, HERWIG++ predicts evidently more jets in the central region $\left|\eta^{j_3}\right| \lesssim 1$. Comparing the HERWIG++ result and the PYTHIA outcome for squark antisquark production, this enhancement amounts to a 20% higher rate in the centre and a reduction of the same magnitude for $\left|\eta^{j_3}\right| \approx 2.8$. In case of squark pair production, this effect is somewhat smaller, of $\mathcal{O}(10\%)$, but still clearly visible. This result is in accordance with the observation made in the context of undecayed squarks in the previous section.

- $\boldsymbol{m^{j_1 j_2}}$: The invariant mass of the two hardest jets shows a similar behaviour in all cases considered here: away from threshold, HERWIG++ and the DIPOLE-SHOWER are in good agreement, whereas the PYTHIA prediction is shifted to higher values and essentially reproduces the NLO results within $\mathcal{O}(5\%)$. The discrepancy between PYTHIA and the two other parton showers amounts to $\pm 10\%$ for small/large values of $m^{j_1 j_2}$ in the range considered here.

- $\boldsymbol{m_{\text{eff}}}$: The effective mass in the exclusive definition used here ($m_{\text{eff}} = \not{E}_T + p_T^{j_1} + p_T^{j_2}$, see Eq. (3.76)) inherits the behaviour of $\not{E}_T$ and the p_T distributions of the jets. The result obtained with PYTHIA reproduces almost the NLO prediction, whereas the HERWIG++ outcome is slightly enhanced for small values. The prediction of the DIPOLE-SHOWER agrees with the HERWIG++ one for large m_{eff} and deviates here by roughly -10% from PYTHIA. For squark pair production the results show qualitatively the same behaviour, however the discrepancies are even smaller and amount to $\mathcal{O}(5\%)$.

- $\boldsymbol{\not{E}_T}$: The predictions for the missing transverse energy agree very well and essentially reproduce the NLO result. Tiny deviations are only visible in the tails of the distributions, however they are smaller than 5% in all cases.

Summarizing these observations one is lead to conclude that the predictions of the different parton showers for the considered observables depending solely on the two hardest jet agree within $\mathcal{O}(10\%)$ or better. Comparing the showered results with the outcome of a pure NLO simulation

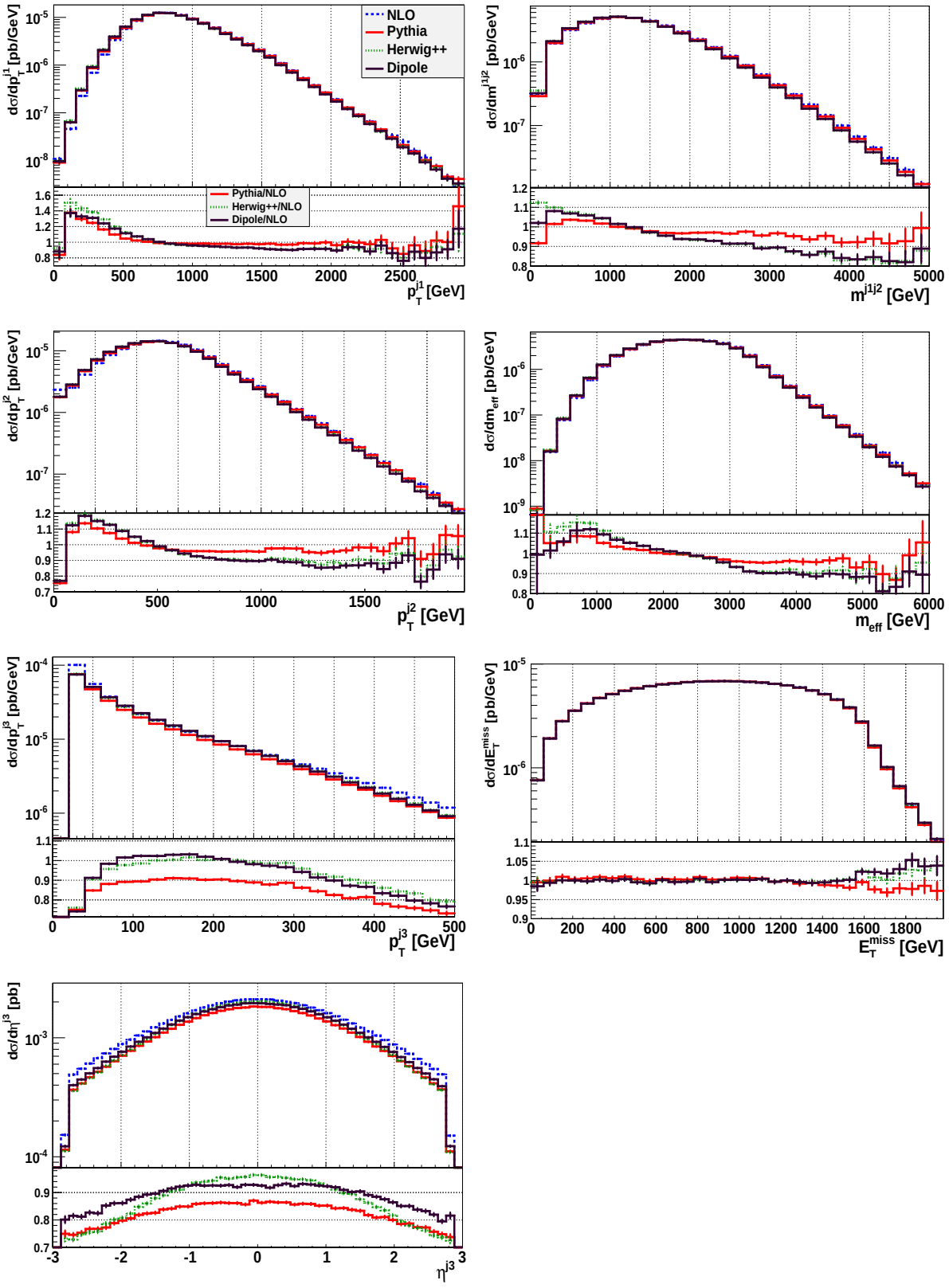

Figure 4.15.: Same as Fig. 4.14 for the benchmark scenario 10.4.5 and squark pair production.

the effects of the parton showers on these observables are at most of $\mathcal{O}(10-20\%)$, except for the threshold region, where only very few events occur. By and large, the two HERWIG++ showers yield larger deviations from the NLO outcome for these observables, whereas PYTHIA reproduces the NLO curves within $\mathcal{O}(10\%)$. The $\not{E}_T$ distribution is in all cases hardly affected by parton shower effects.

Larger deviations between the different parton showers emerge in the predictions for the third hardest jet, which is formally described only at LO in the hard process. Especially the HERWIG++ prediction differs significantly from the other two showers and predicts more jets in the central region of the detector. At this point it is not possible to decide ultimately if this discrepancy is an effect of the missing truncated shower or simply a relict of the way the phase space is populated in the different shower algorithms. This would require the actual implementation of a vetoed truncated shower, which is beyond the scope of this thesis. However, comparing the outcomes of the DIPOLE-SHOWER and HERWIG++ reveals only very small discrepancies in the other observables. Hence the overall effect of the neglected truncated shower seems to be small. Comparing the showered results with the NLO predictions the Sudakov damping in the low $p_T^{j_3}$ region is clearly visible for all three parton showers, especially in case of squark antisquark production.

4.4. Results for total rates

In the last step the created event samples are analysed using a realistic set of event selection cuts, which corresponds to the definition of the signal region 'A-loose' for the SUSY searches in two-jet events performed by the ATLAS collaboration [33]. Essentially, these cuts are designed such that events with two hard jets and large missing transverse energy are selected. For the reconstruction of jet candidates the anti-k_T algorithm with $R = 0.4$ is used. Only jets fulfilling $p_T^j > 20\,\text{GeV}$ and $|\eta^j| < 2.8$ are kept for the further analysis. The event selection cuts used in the analysis are

$$\begin{aligned} p_T^{j_1} > 130\,\text{GeV}, \quad p_T^{j_2} > 60\,\text{GeV}, \quad \not{E}_T > 160\,\text{GeV}, \quad \frac{\not{E}_T}{m_{\text{eff}}} > 0.2, \quad m_{\text{eff}}^{\text{incl}} > 1\,\text{TeV}, \\ \Delta\phi(j_{1/2}, \vec{\not{E}}_T) > 0.4, \quad \Delta\phi(j_3, \vec{\not{E}}_T) > 0.4 \quad \text{if} \quad p_T^{j_3} > 40\,\text{GeV}\,. \end{aligned} \tag{4.9}$$

Here, the effective mass m_{eff} is defined as the sum of the p_T of the two hardest jets and $\not{E}_T$ (see Eq. (3.76)), whereas the inclusive definition of this observable includes all jets with $p_T^j > 40\,\text{GeV}$:

$$m_{\text{eff}}^{\text{incl}} = \sum_{i=1}^{n_j} p_T^{j_i} + \not{E}_T\,. \tag{4.10}$$

Moreover, $\Delta\phi(j_i, \vec{\not{E}}_T)$ denotes the minimal azimuthal separation between the direction of the missing transverse energy, $\vec{\not{E}}_T$, and the i^{th} jet. The additional cut $\Delta\phi(j_3, \vec{\not{E}}_T) > 0.4$ is only applied if a third jet with $p_T^{j_3} > 40\,\text{GeV}$ is present.

Applying these cuts at the level of a pure NLO simulation yields for the total cross sections for squark (anti)squark production combined with the subsequent decays $\tilde{q} \to q\tilde{\chi}_1^0$ in the two benchmark scenarios 10.3.6* and 10.4.5 the results given in the first row of Tab. 4.2. Matching these NLO results with a parton shower hardly affects the outcome after using the cuts defined in Eq. (4.9), as can be inferred from the results obtained with PYTHIA and the HERWIG++ default

	10.3.6*		10.4.5	
	$\tilde{q}\tilde{q}$	$\tilde{q}\bar{\tilde{q}}$	$\tilde{q}\tilde{q}$	$\tilde{q}\bar{\tilde{q}}$
NLO	0.871 fb	0.0781 fb	6.809 fb	0.696 fb
PYTHIA	0.883 fb	0.0797 fb	6.854 fb	0.704 fb
HERWIG++	0.895 fb	0.0807 fb	6.936 fb	0.711 fb

Table 4.2.: Total cross sections after applying the event selection cuts defined in Eq. (4.9) for the different production modes in the two benchmark scenarios. The decays of the squarks to $q\tilde{\chi}_1^0$ are included at NLO. The given results have been obtained at the level of a pure NLO simulation and including parton shower effects with PYTHIA and HERWIG++, respectively.

Scenario	BR($\tilde{u}_L \to u\tilde{\chi}_1^0$)	BR($\tilde{u}_R \to u\tilde{\chi}_1^0$)	BR($\tilde{d}_L \to d\tilde{\chi}_1^0$)	BR($\tilde{d}_R \to d\tilde{\chi}_1^0$)
10.3.6*	0.00879	0.484	0.0109	0.197
10.4.5	0.0129	0.999	0.0152	0.999

Table 4.3.: The NLO branching ratios for the decay $\tilde{q} \to \tilde{\chi}_1^0 q$ for the two scenarios considered here, as obtained from the NLO widths in Tab. 3.9.

shower listed in the second and third row, respectively. Note that due to the mixture of cuts on inclusive and exclusive quantities the rates predicted by the two showers are slightly larger compared to the NLO case. Moreover, the two parton showers yield identical rates within 1-2%.

In order to assess the impact of the calculations and implementations performed in the context of this thesis it is interesting to compare these results with those used e.g. by the ATLAS collaboration for the theoretical prediction of the event rates. In the analysis performed in [33] these are obtained by calculating the production processes at LO, using the LO PDF set CTEQ6L1, and rescaling them with a common K-factor obtained from PROSPINO. In order to include higher-order corrections in the decays the individual channels are multiplied with the NLO branching ratios calculated with SDECAY.[16] Subsequent parton shower effects, hadronization etc. are then simulated with either HERWIG++ or PYTHIA 6. To mimic the way these predictions are obtained, event samples with five million events for undecayed (anti)squarks have been generated with LO accuracy. The subsequent simulation, i.e. the decays $\tilde{q} \to q\tilde{\chi}_1^0$ and the showering, are performed with HERWIG++ and PYTHIA, neglecting again effects of hadronization, MPI etc. For the branching ratios of the individual decays the NLO results calculated in Sec. 3.2.2 are used, the relevant NLO branching ratios are summarized in Tab. 4.3. The K-factors for the NLO corrections to the production processes are determined in an analogous manner as in PROSPINO, i.e. the squark masses are averaged and all channels are summed up, see the discussion in Sec. 3.1.5.2. For the LO cross section the CTEQ6L1 PDF set has been used, whereas the NLO results have been obtained with the NLO set used throughout this chapter, CT10NLO. The results for squark antisquark and squark pair production are summarized in Tab. 4.4.

The results obtained with this approximate setup after applying the event selection cuts defined in Eq. (4.9) are summarized in Tab. 4.5. Comparing these numbers with those obtained in the full

[16] In fact, in the ATLAS analysis [33] the effects of NLL soft gluon resummation are also included via a modified global K-factor. However, as these effects are not part of the calculations presented here this step would modify all results only by a constant factor.

	10.3.6*		10.4.5	
	$\tilde{q}\tilde{q}$	$\tilde{q}\bar{\tilde{q}}$	$\tilde{q}\tilde{q}$	$\tilde{q}\bar{\tilde{q}}$
σ_{LO}	14.46 fb	2.32 fb	17.43 fb	3.09 fb
σ_{NLO}	17.43 fb	3.22 fb	20.28 fb	4.36 fb
K-factor	1.21	1.39	1.16	1.41

Table 4.4.: Summary of the K-factors obtained for the averaged squark masses, using the CT10NLO set for the NLO and the CTEQ6L1 set for the LO results. No decays are included here.

	10.3.6*		10.4.5	
	$\tilde{q}\tilde{q}$	$\tilde{q}\bar{\tilde{q}}$	$\tilde{q}\tilde{q}$	$\tilde{q}\bar{\tilde{q}}$
Pythia	0.855 fb	0.0664 fb	6.844 fb	0.617 fb
Herwig++	0.858 fb	0.0667 fb	6.876 fb	0.620 fb

Table 4.5.: Total cross sections after applying the cuts defined in Eq. (4.9), obtained by rescaling LO events after application of the Pythia/Herwig++ shower with the constant K-factors given in Tab. 4.4 and the individual NLO branching ratios of Tab. 4.3.

simulation in Tab. 4.2 one notes that the discrepancy in case of squark pair production is almost negligible, whereas the total rates for squark antisquark production differ in both scenarios by 15-20%. In order to obtain precise predictions it is therefore not in all cases sufficient to use this approximate approach.

However, it should be noted at this point that comparing the results for two randomly chosen scenarios certainly allows not for a universal statement on the validity of the approximations used so far in the experimental analyses. Nevertheless, the examples considered here show that the effects can be large. Hence to obtain as precise predictions as possible a full NLO calculation for both the production and the decay stage, combined consistently with the subsequent steps of the event simulation, is mandatory.

CHAPTER 5

SUMMARY AND OUTLOOK

Despite the non-observation of any indications of SUSY until now, the hunt for sparticles is far from being finished and still one of the main tasks on the physical agenda of the LHC. For the interpretation of the data taken in the experiments predictions as precise as possible are required. On the one hand, a higher precision can be achieved by taking into account higher-order corrections. On the other hand, these fixed-order predictions should be supplemented by the all-order effects of parton showers to obtain a realistic simulation of the event structure observed in the detectors.

The work presented in this thesis contributes to this effort by providing the full calculation of squark antisquark production at NLO SUSY-QCD for squarks of the first two generations. This production process has been combined with the decay $\tilde{q} \to q\tilde{\chi}_1^0$, using the narrow-width approximation. The calculations have been performed for an arbitrary mass spectrum, treating each subchannel individually and allowing for predictions of arbitrary differential distributions. Moreover, an independent calculation of the NLO corrections to squark pair production has been performed and compared to [28], sharing only the virtual contributions with the results presented there. This process has been combined with the squark decay, too.

For the calculation of the virtual contributions the packages FeynArts, FormCalc and LoopTools have been used. The UV divergences have been canceled by applying an on-shell renormalization scheme for the masses and fields. The strong coupling has been renormalized in the $\overline{\text{MS}}$ scheme, decoupling the heavy particles from the RGE running of α_s and introducing a SUSY restoring counterterm. The cancellation of the IR divergences between the virtual and the real contributions is achieved by means of a subtraction formalism, the FKS method. This method is automated in the program package Powheg-Box, which has served as the basis for the implementation of all processes considered in this thesis. A further type of singularities emerges in the real contributions for scenarios with $m_{\tilde{q}} < m_{\tilde{g}}$. Both for squark antisquark and for squark pair production one of the final state squarks can originate from an intermediate gluino, which can be produced on shell for this mass configuration. These contributions occur also in the LO production of a squark and a gluino, followed by the gluino decay into a squark and an antiquark, and have to be subtracted consistently in order to avoid a double counting. Several methods proposed in the literature for similar cases have been used in order to perform this subtraction. Moreover, a new approach has been introduced, which guarantees gauge invariance

by construction. The implementation of these subtraction schemes extends the results presented in [28] to scenarios with $m_{\tilde{q}} < m_{\tilde{g}}$.

In order to assess the impact of the higher-order contributions to squark antisquark production, two mSUGRA scenarios have been considered. The corrections induced by these contributions are large and lead to $K \approx 1.4$ for the two scenarios. The scale dependence both for the total cross section and for distributions is substantially reduced at NLO. Comparing the numerical results of this new calculation to those obtained with the approximations used in PROSPINO2 reveals large discrepancies: The K-factors of the individual subchannels differ significantly from the total K-factor for the sum of all contributing channels. Taking into account the individual K-factors is especially important if the branching ratios of the squarks differ considerably. For the specific decay mode $\tilde{q} \to q\tilde{\chi}_1^0$ the results obtained by rescaling the LO results for the contributing channels with the averaged K-factor and the individual K-factors, respectively, differ by roughly 10% for the two scenarios considered here. Moreover, differential K-factors have been found to vary in general substantially, implying that the rescaling of LO results with a total K-factor is not sufficient to achieve NLO accuracy for arbitrary distributions. The differences in the total K-factors obtained with the full mass spectrum and after averaging the light-flavour squark masses are marginal in the considered cases, as long as the masses differ by less than 100 GeV.

The combination of the squark production and decay processes, both calculated at NLO accuracy, requires in the narrow-width approximation an expansion in α_s. To this end two approaches originally proposed in the context of (single) top production have been investigated. The total rates obtained with these approaches agree within 4% in all cases considered here. However, the deviations in distributions can be of $\mathcal{O}(10\%)$ and even larger in the threshold region. The differential K-factors for the combined production and decay processes inherit the behaviour of the pure production results and are in general far from being flat. Moreover, in the scenarios considered here, the influence of the NLO corrections to the squark decays is sizeable.

The fixed-order results for both squark production processes, combined with the subsequent decays, have been matched with parton showers by applying the POWHEG method. To this end, the individual contributions have been implemented in the program package POWHEG-BOX. The correctness of the implementation has been extensively checked by testing the properties inherent in the POWHEG method. In this context an artificial enhancement in the p_T distribution of the additional parton, which is emitted according to the POWHEG formalism, has been found. This effect could be traced back to the large K-factors and the use of different scales in the individual parts of the POWHEG master formula, Eq. (2.52). In order to correct for this enhancement a damping factor has been introduced, similar to the proposal in [123]. The implementation of the subtraction schemes for the contributions with on-shell intermediate gluinos turned out to be rather involved and required profound changes in the general structure of the main code.

In order to estimate the influence of a parton shower on the results three different shower algorithms have been applied to the event samples generated with the POWHEG-BOX: the p_T-ordered shower of PYTHIA 6, the angular-ordered default shower of HERWIG++ and the p_T-ordered DIPOLE-SHOWER, which is also implemented in the HERWIG++ framework. In general, the observed differences between the parton showers amount to at most $\mathcal{O}(10\%)$. The only distribution showing a notable discrepancy is the pseudorapidity of the third hardest jet, which is in the prediction of the HERWIG++ default shower distinctly more central compared to the other two showers. At this point it is not clear if this is merely an effect of the way the parton showers populate the available phase space, or a result of the missing vetoed truncated shower. Comparing the results obtained at fixed NLO with the outcome of the different showers reveals

at most differences in the range $\mathcal{O}(10-20\%)$, except for observables describing the third hardest jet. However, one should keep in mind that these observables have formally only LO accuracy and are moreover influenced by the Sudakov damping of the parton showers.

In the last part a cut-based analysis of the total cross sections obtained for two benchmark scenarios has been conducted, using realistic event selection cuts taken from an analysis of the ATLAS collaboration. The numerical results for the total rates have been calculated using the new implementations in the POWHEG-BOX and the approximate approach used so far by the experimental collaborations. Comparing the results obtained with the two setups revealed only small discrepancies for squark pair production, but up to 20% difference for squark antisquark production in the scenarios considered here. The consideration of two randomly chosen benchmark scenarios is of course not sufficient to make a universal statement on the validity of the approximations used so far in the experimental analyses. Nevertheless, these examples show that the effects can be large and precise theoretical predictions should take into account the full NLO calculation for the production processes, consistently combined with the squark decays at NLO. To this end the code developed in the course of this thesis will be made public in the POWHEG-BOX in the near future.

The next step towards a description of all production modes for strongly interacting sparticles consists in the implementation of squark gluino and gluino pair production into the POWHEG-BOX. The strategy for the implementation of these processes is basically identical to the procedure for squark production described in this thesis. However, the combination of the production and decay stages is slightly more involved due to the fermionic nature of the gluino, which requires the consideration of spin correlations. Moreover, the implementation of decay modes leading to final states with higher multiplicities would be interesting for phenomenological studies. If the neutralinos and charginos produced in the first decay step decay only into leptons, neutrinos and the LSP, the structure of the NLO corrections in SUSY-QCD is essentially identical to the simplest mode, $\tilde{q} \to q\tilde{\chi}_1^0$, considered here and requires no fundamental changes. In this sense, the calculations and implementations presented in this thesis have hopefully provided the next step towards high precision predictions for SUSY processes at the LHC.

APPENDIX A

CALCULATIONAL TECHNIQUES

A.1. Ghost subtraction

In calculations involving more than one external on-shell gluon the analytical summation over the (physical) transverse gluon polarizations often leads to rather complex expressions. In the calculation of squark antisquark production this problem occurs in the $gg \to \tilde{q}_i^c \bar{\tilde{q}}_i^c$ channels, which have the general structure

$$|\mathcal{M}_{gg}|^2 = \mathcal{M}_{\mu\nu}\mathcal{M}^*_{\mu'\nu'} P_1^{\mu\mu'} P_2^{\nu\nu'}, \tag{A.1}$$

where μ (ν) is the index associated with the first (second) gluon and P_i denotes the sum over the transverse polarizations of the respective gluon.

In QCD calculations it is usually not possible to apply the simple formula known from QED calculations,

$$P_i^{\mu\nu} = \sum \epsilon_T^{\mu\,*}(p_i)\epsilon_T^{\nu}(p_i) = -g^{\mu\nu}, \tag{A.2}$$

as in this expression the unphysical longitudinal degrees of freedom of the gluons are not properly subtracted.

Instead, one has to use the rather lengthy expression

$$P_i^{\mu\nu} = \sum \epsilon_T^{\mu\,*}(p_i)\epsilon_T^{\nu}(p_i) = -g^{\mu\nu} + \frac{n_i^\mu p_i^\nu + n_i^\nu p_i^\mu}{n_i \cdot p_i} - \frac{n_i^2 p_i^\mu p_i^\nu}{(n_i \cdot p_i)^2} \tag{A.3}$$

with n_i being an arbitrary four vector defined such that $n_i \neq p_i$, with the momentum p_i of the first/second gluon.[17] This expression indeed fulfils the transversality conditions

$$p_{i,\mu} P_i^{\mu\nu} = p_{i,\nu} P_i^{\mu\nu} = 0 \tag{A.4}$$

[17] Recall that in QED, the Ward identities guarantee that for any process involving an external on-shell photon the replacement $\epsilon_\mu(k) \to k_\mu$ leads to $\epsilon_\mu(k)\mathcal{M}^\mu \to k_\mu \mathcal{M}^\mu = 0$, hence the additional terms in Eq. (A.3) simply vanish after contraction with the matrix elements and Eq. (A.2) can be used instead, see e.g. [131].

for on-shell gluons, i.e. only the transverse degrees of freedom give a non-zero contribution. In a gauge-independent result the dependence on the arbitrary n_i drops out in the end. However, in intermediate steps this four-vector is present.

In order to use the simpler expression given in Eq. (A.2) for the polarization sum the longitudinal degrees of freedom have to be subtracted explicitly. This can be achieved by applying the Slavnov-Taylor identities for on-shell external particles (see [131]),

$$p_1^\mu \mathcal{M}_{\mu\nu} = \mathcal{M}_\nu^{\text{ghost}} \propto p_{2,\nu}\,, \tag{A.5}$$

and likewise for p_2. The ghost contributions $\mathcal{M}_\nu^{\text{ghost}}$ contain only the unphysical longitudinal degrees of freedom and thus correspond exactly to the terms which have to be removed. Inserting (A.3) in (A.1) and using these identities immediately leads to the conclusion that an easier way to calculate the matrix element squared amounts to neglecting all terms $\propto p_{1,\mu}$ and $\propto p_{2,\nu}$ and using the simpler relation (A.2) for the polarization sums. This procedure is called 'ghost subtraction', see [17].

A simple cross-check for the correct application of this formalism consists in performing the full calculation (i.e. without neglecting any terms) and using (A.2) for the polarization sums, hence including the longitudinal polarization states in a first step. The longitudinal parts can be obtained explicitly by calculating the ghost contributions directly (i.e. in the calculation of squark antisquark production the unphysical process of two ghost particles producing the squark antisquark pair). For squark antisquark production this contribution reads

$$|\mathcal{M}_{\text{ghost}}|^2 = 2\frac{g_s^4}{4\cdot 64} F_3 \frac{(u-t)^2}{4s^2}\,, \tag{A.6}$$

where $F_3 = 12$, see Eq. (3.9). Subtracting this term from the matrix element squared of the full process yields indeed the same result as obtained with 'ghost subtraction'.

A.2. Colour- and spin-correlated Born amplitudes squared

The subtraction methods used to cancel the infrared divergences between the real and virtual contributions in NLO (SUSY)-QCD calculations require the calculation of the so-called colour- and spin-correlated Born amplitudes squared, which represent the process-dependent building blocks in the general subtraction formulae. The following section contains some comments on the calculation of these quantities and the results for squark antisquark production.

Colour-correlated Born amplitudes squared

The colour-correlated Born amplitudes squared occur in the soft approximation of the real matrix elements squared, see Eq. (2.34). They are defined as

$$\mathcal{B}_{ij} = -\frac{1}{F} \sum_{\substack{\text{spin,}\\ \text{colour}}} \mathcal{M}_{\{c_k\}} \left(\mathcal{M}^\dagger_{\{c_k\}}\right)_{\substack{c_i \to c_i' \\ c_j \to c_j'}} T^a_{c_i, c_i'} T^a_{c_j, c_j'}\,, \tag{A.7}$$

where $\{c_k\}$ denotes all colour indices in the Born matrix elements $\mathcal{M}$, F subsumes the factors from averaging over spin/colour of the initial-state partons and possible symmetry factors, and the sum runs over all spin/colour combinations of external particles. The summation over repeated indices is implicitly assumed. Note that the minus sign is pure convention, rendering

the results for the $\mathcal{B}_{ij}$ consistent with the choice made in the POWHEG-BOX, see [27]. The colour factors $T^a_{c_i,\,c'_i}$ depend on the $SU(3)$ representation of the i^{th} external particle. For particles of the adjoint representation (e.g. gluons, gluinos) they read $T^a_{cb} = if_{cab}$ with the structure constants f_{abc} of $SU(3)$. Incoming particles and outgoing antiparticles of the fundamental representation (e.g. quarks, squarks) have $T^a_{\alpha\beta} = t^a_{\alpha\beta}$, where $t^a_{\alpha\beta}$ are the colour matrices of the fundamental representation. For incoming antiparticles and outgoing particles they read $T^a_{\alpha\beta} = -t^a_{\beta\alpha}$.

In actual calculations the relations to the Born amplitudes squared $\mathcal{B}$,

$$\sum_{i,i\neq j} \mathcal{B}_{ij} = C_i \mathcal{B} \tag{A.8}$$

following from colour conservation are very useful. The index i runs over all external coloured particles and C_i are the Casimir invariants for the respective $SU(3)_C$ representation of the i^{th} particle, i.e. $C_i = C_F = 4/3$ for (s)quarks and $C_i = C_A = 3$ for gluons and gluinos. Moreover, by construction $\mathcal{B}_{ij}$ is symmetric.

For a general $2 \to 2$ process with four external coloured particles, $\mathcal{B}_{ij}$ forms a 4×4 matrix. Due to the symmetric form and the fact that only entries with $i \neq j$ are relevant this leaves a priori six entries which have to be calculated. Taking into account Eq. (A.8) this number can be further reduced by solving the following four linear equations, expressing all matrix entries in terms of $\mathcal{B}_{12}$ and $\mathcal{B}_{13}$:

$$\begin{aligned}
\mathcal{B}_{14} &= C_1\mathcal{B} - \mathcal{B}_{12} - \mathcal{B}_{13}\,, \\
\mathcal{B}_{23} &= \frac{1}{2}(C_1 + C_2 + C_3 - C_4)\mathcal{B} - \mathcal{B}_{12} - \mathcal{B}_{13}\,, \\
\mathcal{B}_{24} &= \frac{1}{2}(-C_1 + C_2 - C_3 + C_4)\mathcal{B} + \mathcal{B}_{13}\,, \\
\mathcal{B}_{34} &= \frac{1}{2}(-C_1 - C_2 + C_3 + C_4)\mathcal{B} + \mathcal{B}_{12}\,.
\end{aligned} \tag{A.9}$$

In case of squark antisquark production, the Casimir invariants are either all given by C_F (for the $q\bar{q}$-channels) or by $C_1 = C_2 = C_A$, $C_3 = C_4 = C_F$ (for the gg-channels). The calculation of the matrix elements is identical to the calculation of the Born amplitudes squared, only the colour factors have to be recalculated. For the $q\bar{q}$-channels (depicted in the upper row of Fig. 3.1) this leads to the following expressions:

$$\begin{aligned}
\mathcal{B}_{12} &= -\frac{g_s^4}{4\cdot 9}\left\{ T_1 \frac{A_1}{(t-m_{\tilde{g}}^2)^2} + T_2 \frac{A_2}{s^2} + T_3 \frac{A_3}{s(t-m_{\tilde{g}}^2)} \right\}, \\
\mathcal{B}_{13} &= -\frac{g_s^4}{4\cdot 9}\left\{ T_2 \frac{A_1}{(t-m_{\tilde{g}}^2)^2} + T_1 \frac{A_2}{s^2} + T_3 \frac{A_3}{s(t-m_{\tilde{g}}^2)} \right\},
\end{aligned} \tag{A.10}$$

with the trace expressions for the colour factors

$$\begin{aligned}
T_1 &= -\mathrm{Tr}\left[T^a\,T^c\,T^b\right]\mathrm{Tr}\left[T^a\,T^c\,T^b\right] = -\frac{7}{3}\,, \\
T_2 &= -\mathrm{Tr}\left[T^a\,T^c\,T^b\,T^c\right]\mathrm{Tr}\left[T^a\,T^b\right] = \frac{1}{3}\,, \\
T_3 &= -\mathrm{Tr}\left[T^a\,T^c\,T^b\,T^a\,T^b\,T^c\right] = -\frac{1}{9}\,.
\end{aligned} \tag{A.11}$$

For the evaluation of these trace factors a FORM-package has been used [132, 133]. The form of the coefficients A_i depends only on the masses and the Mandelstam variables, they can be deduced from the Born results for the different flavour/chirality combinations given in Eqns. (3.3), (3.4) and (3.5) by replacing the factors F_i with the corresponding T_j in those equations and keeping only the non-zero terms.

Likewise, the $\mathcal{B}_{ij}$ can be calculated for the gg-channels. Again, only the part concerning the colour factors has to be changed, thus the result given for $|\mathcal{M}_{gg}|^2$ in Eq. (3.8) can easily be adapted by replacing the colour factors F_i with the appropriate expressions and multiplying the full term with -1 to match the sign convention in Eq. (A.7). These new colour factors can be expressed in terms of two different structures after evaluating all colour structures:

$$\begin{aligned} T_4 &= -\frac{N_c C_A^2 C_F}{4} = -9 \\ T_5 &= -\frac{N_c C_A C_F^2}{2} = -8, \end{aligned} \tag{A.12}$$

with $N_c = 3$.

The required replacements can be summarized as follows:

- For $\mathcal{B}_{12}$:
$$F_{3,6,10,11} \to 2T_4, \quad F_{4,5} \to T_4, \quad F_{7,8} \to -T_4, \quad F_9 \to 0 \tag{A.13}$$
- For $\mathcal{B}_{13}$:
$$\begin{aligned} &F_3 \to T_4, \quad F_4 \to T_5, \quad F_{5,9} \to (T_5 - T_4), \quad F_6 \to (4T_5 - 3T_4), \\ &F_7 \to -T_4, \quad F_8 \to 0, \quad F_{10} \to (2T_5 - T_4), \quad F_{11} \to (2T_5 - 2T_4) \end{aligned} \tag{A.14}$$
Moreover, $\mathcal{B}_{13}$ contains an additional term which vanishes in $\mathcal{B}$ due to the colour structure, namely the interference term between the s-channel gluon diagram and the four point vertex in Fig. 3.1. This contribution results in
$$-\frac{g_s^4}{4 \cdot 64} T_4 \frac{6(t-u)}{s}. \tag{A.15}$$
Note that the sign has already been adapted to the convention used in (3.8), i.e. this term is simply added to $\mathcal{B}_{13}$.

Spin-correlated Born amplitudes squared

The spin-correlated Born amplitudes occur in the collinear limits of the real contributions. If the j^{th} leg of the underlying Born flavour structure is a gluon, the corresponding spin-correlated amplitude is defined as

$$\mathcal{B}_j^{\mu\nu} = \frac{1}{F} \sum_{\substack{\{s\},\, s_j,\, s_j', \\ \text{colour}}} \mathcal{M}(\{s\}, s_j) \mathcal{M}^\dagger(\{s\}, s_j') \epsilon^{\mu,*}(s_j) \epsilon^\nu(s_j') \,, \tag{A.16}$$

where s_j is the spin of the gluon and $\{s\}$ denotes collectively all other spins. The explicit calculation of the $\mathcal{B}_j^{\mu\nu}$ amounts to simply leaving the indices of the j^{th} gluon uncontracted. Since the polarization vectors $\epsilon^\mu(s_j)$ are normalized as $g_{\mu\nu} \epsilon^{\mu,*}(s_j) \epsilon^\nu(s_j') = -\delta_{s_j s_j'}$ the spin-correlated amplitudes fulfil

$$g_{\mu\nu} \mathcal{B}_j^{\mu\nu} = -\mathcal{B}, \tag{A.17}$$

which provides a simple check for the correctness of the calculation.

In the context of squark antisquark production the spin-correlated amplitudes are non-zero only for the gg-channels, as these are the only ones involving external gluons. There are in principle two contributions for the two gluons. However, it is sufficient to calculate only one of them for an arbitrarily chosen gluon. The result for the second amplitude is then obtained by interchanging both the momenta $p_1 \leftrightarrow p_2$ of the gluons and the momenta $k_1 \leftrightarrow k_2$ of the squark and the antisquark. For the explicit calculation the 'ghost subtraction' formalism as explained in Sec. A.1 has been applied, i.e. for the summation over the polarization of the second gluon Eq. (A.2) can be used. This results in

$$
\begin{aligned}
B_1^{\mu\nu} = \frac{g_s^4}{4\cdot 64}\Bigg[& \frac{3\left(12(s-4m_{\tilde{q}}^2)p_2^\mu p_2^\nu - 3(t-u)\left((t-u)g^{\mu\nu} + 2p_1^\mu(k_1^\nu - k_2^\nu) + 2p_1^\nu(k_1^\mu - k_2^\mu)\right)\right)}{s^2} \\
& - \frac{8(m_{\tilde{q}}^2+t)(2k_1^\mu - p_1^\mu)(2k_1^\nu - p_1^\nu)}{(t-m_{\tilde{q}}^2)^2} - \frac{8(m_{\tilde{q}}^2+u)(2k_2^\mu - p_1^\mu)(2k_2^\nu - p_1^\nu)}{(u-m_{\tilde{q}}^2)^2} - 7g^{\mu\nu} \\
& + \frac{9(2k_1^\nu - p_1^\nu)\left((t-u)(k_1^\mu + k_2^\mu) + 2p_2^\mu(4m_{\tilde{q}}^2 - s)\right)}{s(m_{\tilde{q}}^2 - t)} \\
& + \frac{9(2k_2^\nu - p_1^\nu)\left((u-t)(k_1^\mu + k_2^\mu) + 2p_2^\mu(4m_{\tilde{q}}^2 - s)\right)}{s(m_{\tilde{q}}^2 - u)} \\
& + \frac{7(2k_1^\mu - p_1^\mu)(2k_2^\nu - p_2^\nu)}{m_{\tilde{q}}^2 - t} + \frac{7(2k_2^\mu - p_1^\mu)(2k_1^\nu - p_2^\nu)}{m_{\tilde{q}}^2 - u} \\
& - \frac{(4m_{\tilde{q}}^2 - s)(2k_1^\mu - p_1^\mu)(2k_2^\nu - p_1^\nu)}{(t-m_{\tilde{q}}^2)(u-m_{\tilde{q}}^2)}\Bigg].
\end{aligned}
\tag{A.18}
$$

A.3. Colour flow decomposition

The implementation of any process in the POWHEG-BOX requires a prescription for the assignment of the 'flow of colour' in the planar limit for the created events, see Sec. 2.2.4. A very convenient way for the calculation of the relative contribution of each colour flow is the so-called colour flow decomposition of the amplitudes (see [121, 134]). This approach consists in a reorganization of the colour algebra. On the one hand this allows for a more efficient calculation of the colour factors of complicated processes at tree level (e.g. the n-gluon amplitude, see [121] for some examples) or of one-loop amplitudes with a large number of external legs in recent automated approaches (see e.g. [135]). On the other hand, this approach is interesting in the context of Monte Carlo event generators, as it allows by construction for a physical interpretation of the different contributions to a specific process in terms of the 'flow of colour'.

The basic idea of the colour flow decomposition consists in treating the $SU(N_c)$ gluon field A_μ (and correspondingly the gluino field) as $N_c \times N_c$ matrix $(A_\mu)^i_j$ with $i,j \in [1,\ldots,N_c]$ rather than a one-index field A_μ^a with $a = 1,\ldots,N_c^2-1$. Following closely the original proposition in [121] these two quantities are connected via

$$
(A_\mu)^i_j = \frac{(\lambda^a)^i_j}{\sqrt{2}} A_\mu^a\,, \tag{A.19}
$$

with the fundamental representation matrices λ^a of the group $SU(N_c)$, normalized as $\mathrm{Tr}\left[\lambda^a\lambda^b\right] = \delta^{ab}$. The upper indices (i) transform hereby under the fundamental representation of $SU(N_c)$, the lower ones (j) under the antifundamental one. Using this different decomposition affects only the colour algebra in the Feynman rules for (S)QCD used in the actual calculation of the matrix elements, the Dirac and kinematic structure remain essentially the same. The thus obtained Feynman rules for the vertices and propagators no longer contain the generators or structure constants of $SU(N_c)$, but only factors of Kronecker deltas with indices i, j which allow for an unambiguous interpretation in terms of a 'flow of colour'. In this decomposition the gluon propagator has a more complicated colour structure,

$$\left\langle (A_\mu)^{i_1}_{j_1} (A_\nu)^{i_2}_{j_2} \right\rangle \propto \delta^{i_1}_{j_2}\delta^{i_2}_{j_1} - \frac{1}{N_c}\delta^{i_1}_{j_1}\delta^{i_2}_{j_2}\,, \tag{A.20}$$

compared to the usual result $\left\langle (A_\mu)^a (A_\nu)^b \right\rangle \propto \delta^{ab}$. This structure can easily be interpreted in terms of the colour flow: while the first term actually represents a 'colour exchange' between the two particles coupled to the gluon, the second term provides no such exchange. Pictorially, this interpretation has the following form:

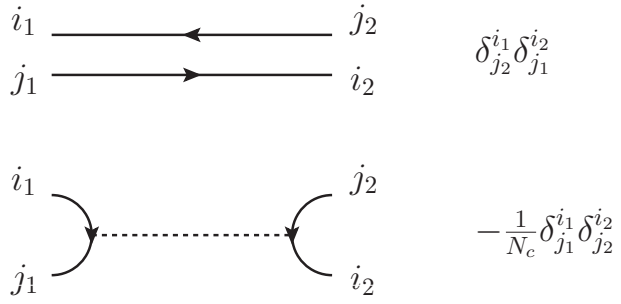

The second term can be considered as an (unphysical) QED like $U(1)$ gluon, which does not couple to gluons, see [134]. The full set of Feynman rules for QCD vertices can be found in [121] and [134]. Formally, a connection to the calculations performed in Ch. 3 with the Feynman rules defined in [44] can be achieved by replacing in the $gq\bar{q}$ (and the $g\tilde{q}\bar{\tilde{q}}$ respectively the $\tilde{g}\tilde{q}\bar{q}$) vertex the generators of the fundamental representation of $SU(N_c)$

$$(T^a)^i_j \to \frac{1}{\sqrt{2}}\delta^i_{j_1}\delta^{i_1}_j\,, \tag{A.21}$$

where i_1 and j_1 are the 'colour indices' of the gluon (respectively the gluino). Moreover, for the calculation of the colour flows contributing to the process $gg \to \tilde{q}^c_i\bar{\tilde{q}}^c_i$ the three-gluon vertex is needed, which yields a contribution to two colour flows with a relative minus sign. Formally, it can be obtained from the three-gluon vertex rule in the convention of [44] by replacing

$$f_{abc} \to \frac{-i}{\sqrt{2}}\left(\delta^{i_3}_{j_1}\delta^{i_1}_{j_2}\delta^{i_2}_{j_3} - \delta^{i_3}_{j_2}\delta^{i_2}_{j_1}\delta^{i_1}_{j_3}\right). \tag{A.22}$$

The 'numbering' of the gluons has been chosen such that the indices (i_3, j_3) correspond to the internal gluon in the first diagram depicted in Fig. 3.1, while the external gluons are denoted 1 and 2, respectively. The two resulting colour flows are depicted in Fig. A.1. The other diagrams occurring in the calculation of $gg \to \tilde{q}^c_i\bar{\tilde{q}}^c_i$ contribute either to the first colour flow (the t-channel graph in Fig. 3.1), to the second one (the u-channel diagram) or to both of them (the diagram

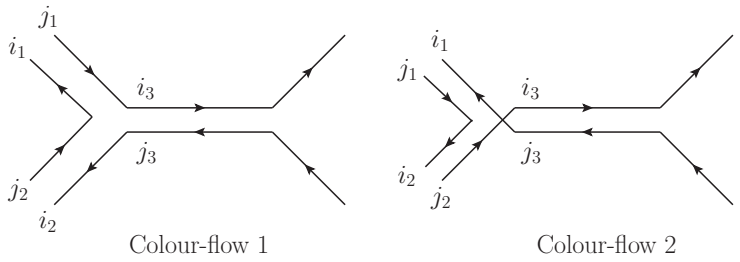

Figure A.1.: The two colour flows contributing to the gg-channels.

involving the $gg\tilde{q}_i^c\bar{\tilde{q}}_i^c$ vertex). Recalling the invariance of the $gg\tilde{q}_i^c\bar{\tilde{q}}_i^c$ vertex under exchange of the two gluons no relative minus sign has to be introduced in this case.

Performing these replacements and using Eq. (A.20) in the calculation of the matrix elements contributing to the different squark production channels allows for an attribution of each matrix element to one (or several) colour flows. The choice of a colour flow for a given kinematic configuration, i.e. a specific event, can then be performed according to its respective relative weight. This choice is performed in the planar limit, i.e. no interference terms between different colour flows are taken into account (these are suppressed by inverse powers of N_c). In detail, the planar colour flow contributions for squark (anti)squark production are obtained as follows (see [134]):

1. Find all possible planar colour flow diagrams, starting from the usual Feynman diagrams for the processes and adding those diagrams where $U(1)$ gluons (gluinos) can replace the original ones (keeping in mind that the couplings of physical gluons with this auxiliary particle vanish).
2. For each $U(1)$ gluon (gluino) contained in an amplitude squared an additional factor $-\frac{1}{N_c}$ has to be attached.
3. Each $gq\bar{q}$, $g\tilde{q}\bar{\tilde{q}}$ and $\tilde{g}\tilde{q}\bar{q}$ vertex gets a factor $\frac{1}{\sqrt{2}}$, each 3-gluon vertex a factor $\frac{-i}{\sqrt{2}}$.
4. Forming the matrix elements squared for each colour flow separately and evaluating the occurring Kronecker deltas yields a factor N_c for every closed 'colour loop'.

It is obvious from this approach that it is not necessary to calculate the kinematic parts of the matrix elements squared again, i.e. the results obtained for the Born (and the real) contributions can be reused after replacing the colour factors accordingly.

Born colour flows for the $q\bar{q}$-channels

To illustrate this approach consider the simplest non-trivial case occurring in the context of the calculation of squark antisquark production, the determination of the colour flows for the Born contributions to the $q\bar{q}$-channels (depicted in the upper row of Fig. 3.1). The two possible flows for these processes are sketched in Fig. A.2. Following the prescription given above both colour flows get in total a factor 1/4, which drops out when determining the relative 'weight' of each flow and can thus be neglected from the very beginning. Upon squaring the respective matrix elements for the first configuration shown in Fig. A.2 and counting the number of closed 'colour loops' and intermediate $U(1)$ propagators one obtains

- for the s-channel squared a factor N_c^2,

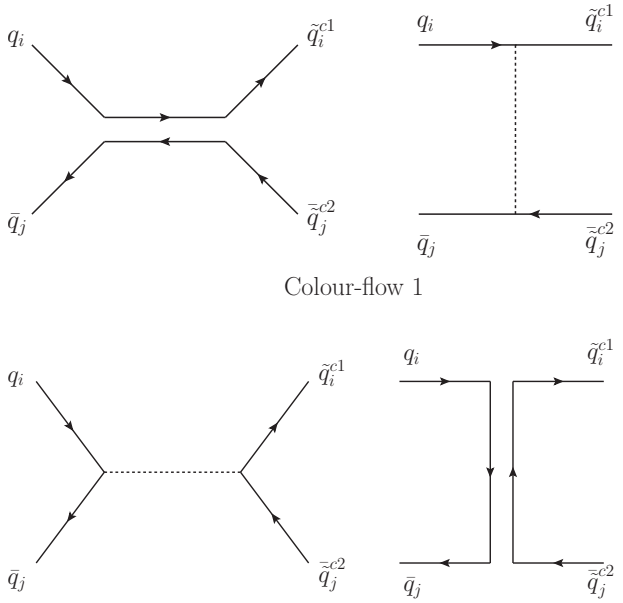

Figure A.2.: The two colour flows contributing to $q_i\bar{q}_j \to \tilde{q}_i^{c1}\bar{\tilde{q}}_j^{c2}$

- for the t-channel squared a factor $\frac{N_c^2}{N_c^2} = 1$
- and for the interference term $\left(-\frac{1}{N_c}\right) N_c^2 = -N_c$.

The contributions to the second colour flow are identical after interchanging $s \leftrightarrow t$. Using the results for the matrix elements squared from Eq. (3.5) yields for the special case $q_i\bar{q}_i \to \tilde{q}_i^c\bar{\tilde{q}}_i^c$ for the two colour flows (leaving out a common factor $\frac{g_s^4}{4 \cdot 9}$)

$$\begin{aligned} J_1^2 &= N_c^2 \frac{8\left(tu - m_{\tilde{q}}^2 m_{\bar{\tilde{q}}}^2\right)}{s^2} - N_c \frac{8\left(tu - m_{\tilde{q}}^2 m_{\bar{\tilde{q}}}^2\right)}{s\left(t - m_{\tilde{g}}^2\right)} + \frac{4\left(tu - m_{\tilde{q}}^2 m_{\bar{\tilde{q}}}^2\right)}{\left(t - m_{\tilde{g}}^2\right)^2}, \\ J_2^2 &= \frac{8\left(tu - m_{\tilde{q}}^2 m_{\bar{\tilde{q}}}^2\right)}{s^2} - N_c \frac{8\left(tu - m_{\tilde{q}}^2 m_{\bar{\tilde{q}}}^2\right)}{s\left(t - m_{\tilde{g}}^2\right)} + N_c^2 \frac{4\left(tu - m_{\tilde{q}}^2 m_{\bar{\tilde{q}}}^2\right)}{\left(t - m_{\tilde{g}}^2\right)^2}. \end{aligned} \tag{A.23}$$

For all other flavour/chirality combinations these formulae have to be adapted according to the results given in Sec. 3.1.1 by leaving out either the s-channel or the t-channel contribution.

A specific colour flow i is then chosen with the probability

$$P_i = \frac{J_i^2}{J_1^2 + J_2^2}. \tag{A.24}$$

APPENDIX B

INPUT PARAMETERS FOR THE POWHEG-BOX

In the course of the implementation of squark (anti)squark production and the combination with the decay $\tilde{q} \to \tilde{\chi}_1^0 q$ several new parameters and flags have been introduced, which can be set in the usual input file for the POWHEG-BOX, `powheg.input`. For future reference these are listed and explained in the following. The syntax in each case is identical to the usual POWHEG-BOX convention:

```
keyword    value  ! comments .
```

The parameters controlling the general behaviour of the POWHEG-BOX are not specified here, they are explained in detail in the POWHEG-BOX manual [126].

- **Spectrum file:** The user has to provide a file containing the masses, mixing matrices etc. of the considered scenario according to the SUSY Les Houches accord (SLHA) [136]:

  ```
  SLHA-File  input.slha !  name of the SLHA input-file
  ```

- **Process choice:** As explained in Sec. 4.1 there are three different ways to operate the code. The first option consists in specifying one specific final-state configuration by setting

  ```
  part1      uL    ! first squark: e.g. uL for sup-left and so on
  part2      uL    ! second squark (for antisquarks: uLbar)
  withcc     1     ! for squark pair production: consider also antisquarks
  ```

  where the flag `withcc` is only used for squark pair production. In the second option a list of Born flavour structures, which shall be considered in one run, is read from an external file:

  ```
  partialsumup 0      ! if set to 1: read in a user-provided file
  SUMFLST  flst.input ! input file containing the flavour structures
  ```

  In this case the masses in all given combinations have to be identical, otherwise the program stops. Moreover, the flag `smartsig` should be set in order to benefit from the considerable speed up. In the third operation mode all squarks are treated as mass degenerate and all channels are summed up. This mode is invoked by setting

```
debug_sumup  0  ! sum up all contributions using degenerate mass-spectrum
avgslhamass  0  ! if set: read SLHA-file, but form average of sq-masses
msquark  500.0  ! mass of the degenerate squarks
mgluino  500.0  ! gluino-mass
mtop     175.0  ! top-mass
```

If the flag `avgslhamass` is set, the common squark mass is calculated by averaging the masses of all squarks occurring in the final state, using the masses provided in the SLHA file. In this case the top and gluino mass are read from this file, too. Otherwise the specified masses are used. Again, the flag `smartsig` should be set. In this mode it is possible to refine the flavours of the squarks considered in the final state by setting

```
nextfla    4 ! number of external flavours
```

for squark pair production and

```
nextflaIS  4 ! number of external flavours in the IS
nextflaFS  4 ! number of external flavours in the FS
```

for squark antisquark production. Note that in this case the number of quark flavours considered in the initial state is not necessarily the same as the number of squark flavours due to the s-channel contributions in Fig. 3.1.

- **Scale settings:** The renormalization and factorization scales, which are in any case identical, can be either set to a fixed value or a dynamic scale can be used.

```
fixedscale      1     ! fixed (1) or dynamic (0) scale
setscale        500.0 ! set mur=muf to a specific value
dynscalechoice  1     ! 1: average of m_T, 2: m_sq1sq2
```

The fixed scale can be set to any value. If the `setscale` keyword is not present in the input file, the average mass of the two final-state squarks is used as default value. Possible choices for dynamic scales are the average of the transverse masses of the two squarks, see Eq. (3.50), or their invariant mass.

- **Decays:** The flags specifying the decays of the produced squarks are the following:

```
decay       0  ! perform decays of squarks (1) or not (0)
decchan1    1  ! decay-channel for first squark, (1): sq->q chi^0_1
decchan2    1
NLOwhich    3  ! NLO only in prod.(1), only in decay (2) or in both (3)
CalcGatot   1  ! calculate Gamma^sq_tot (1) or read from SLHA file (0)
NWAapproach 2  ! 1: do not expand NLO width in denominator, 2: expand all
```

At the moment only the decay mode $\tilde{q} \to q\tilde{\chi}_1^0$ is implemented, hence `decchan1` and `decchan2` have to be set to 1. The NLO corrections can be calculated for either only the production process, only the decay processes, or both (see Sec. 3.3). The total width used in the combination formulae for production and decay can be either calculated as described in Sec. 3.2.2 or read from the specified SLHA file. Setting the flag `NWAapproach` to 1 (2) invokes the use of Eq. (3.73) (Eq. (3.72)) for the combination of production and decay.

- **Cuts and jet parameters:** In the NLO analysis performed during the integration of the $\overline{\mathcal{B}}$ function some cuts on the jets, $\not{E}_T$ etc. can be applied, which have to be specified in a separate file:

```
cuts      0        ! apply cuts in NLO-plots (1) or not (0)
CUTS-File cuts.dat ! name of the file where the cuts are specified
```

Moreover, if the decays of the squarks are taken into account a jet algorithm has to be applied to cluster the resulting partons. As mentioned in Sec. 3.3.2 the FASTJET package is used. For the choice of the jet algorithm, the jet radius parameter (if required by the algorithm) and the minimal transverse momentum of the jets the following parameters have to be set:

```
jetalgo  2     ! 1:kt, 2: antikt, 3: Cambridge-Aachen
Rpara    0.7   ! jet radius parameter for the (anti)kt-algorithm
ptjmin   1.0   ! minimal pt requested for the jets
```

- **Subtraction of on-shell gluinos:** As described in Sec. 4.1.2 several different schemes for the subtraction of contributions with intermediate on-shell gluinos have been implemented. In order to choose a specific scheme the following parameters have to be modified:

```
flagsubmethod 1 ! 1: DS, 2: DR-I, 3: DR-II
! in order to choose a specific DS scheme:
flagsplit     3 ! 0: DS(*)-I, 2: DS-II, 3: DS*-III
flagunexp     0 ! distinguish DS*-I (0) and DS-I (1)

flagrestrict  1 !modify Jacobian for the subtracted residuum (1) or not (0)
```

The meaning of the different schemes can be inferred from the discussion in Sec. 4.1.2. The option `flagsplit = 1` has not been discussed there, this setting is in principle equivalent to the DS-II approach, however, with this choice only the resonant amplitude squared, $|M_{\mathrm{r}}|^2$, is treated as regular remnant. If the flag `flagunexp` is set to 1, the analytical expansion in the poles is not performed for the DS-I scheme. In order to neglect the modification of the Jacobian in Eq. (3.35) for the reshuffled phase space, the flag `flagrestrict` has to be set to 0. The parameters required for the different schemes are set as follows (for the meaning of `radcut` see the discussion after Eq. (4.1)):

```
widthgluino  0.1 ! the regularizing width for the gluino
radcut       1.0 ! radiation cut applied to avoid negative R-values
```

The number of points and iterations for the integration of the remnant terms can be chosen differently from the settings for the $\overline{\mathcal{B}}$ integration:

```
ncall1split  100000
itmx1split   8
ncall2split  300000
itmx2split   5
```

These settings are only relevant if the DS scheme is used and `flagsplit` $\neq 0$.

- **Miscellaneous options:** The colour flow for events with real emissions can be either determined according to the approximate algorithm implemented in the POWHEG-BOX, or using the colour flow decomposition for the real amplitude squared:

```
flagownRCF 0 ! 0: POWHEG-BOX algorithm to assign real colour flows
             ! 1: use colour flow decomposition
```

The real amplitudes can be either evaluated using the lightcone gauge or the Feynman gauge for the external gluons.

```
flaggauge  1 ! in the real routines: use lightcone (1) or Feynman (2) gauge
```

Both choices yield of course identical results. Finally, in order to calculate (differential) cross sections at LO, using one-loop-running for the strong coupling and LO PDF sets, the flag `bornxs` has been introduced:

```
bornxs       0     ! calculate LO xs with LO alphas and LO pdfs
lhans1_born  10042 ! born-pdf set for hadron 1 (LHA numbering)
lhans2_born  10042 ! born-pdf set for hadron 2 (LHA numbering)
```

The PDF sets for these LO simulations have to be specified by setting `lhans1_born` and `lhans2_born` to the LHAPDF value of the desired set.

APPENDIX C

SAMPLE INPUT FILE FOR HERWIG++

In order to run Herwig++ an input file including the settings for some parameters, file names, PDFs etc. has to be read in first. As the processing of LHE files for BSM processes with events of both positive and negative weight turned out to be rather involved, an example input file is briefly discussed in the following. The given statements have to be saved in a text file `test.in`, which is read in turn by running `Herwig++ read test.in`.

- In order to invoke the Dipole-Shower the corresponding input files have to be loaded first:

  ```
  read Matchbox.in
  read DipoleShower.in
  read DipoleShowerParameters-NLO.in
  ```

  These are part of the Herwig++ package and have been left unaltered.

- The following statements load a PDF set `SETNAME.LHgrid` provided by the LHAPDF package [99] and initialize the strong coupling constant for two-loop running:

  ```
  cd /Herwig/Partons
  create ThePEG::LHAPDF PDFset ThePEGLHAPDF.so
  set PDFset:PDFName SETNAME.LHgrid
  set PDFset:RemnantHandler HadronRemnants
  set /Herwig/Particles/p+:PDF PDFset
  set /Herwig/Particles/pbar-:PDF PDFset

  cd /Herwig/Generators
  create Herwig::O2AlphaS AlphaS
  set /Herwig/Generators/LHCGenerator:StandardModelParameters:\\
      QCD/RunningAlphaS AlphaS
  ```

- For the simulation of processes within the MSSM it is necessary to load the corresponding model file `MSSM.model`, which is also part of the Herwig++ package. The specified particles, vertices etc. are relevant if the (LO) decays of produced sparticles are performed

with HERWIG++. Moreover, reading the events from an LHE file requires an explicit removal of the constructors for the internal hard processes:

```
read MSSM.model

erase /Herwig/NewPhysics/NewModel:HardProcessConstructors[0]
erase /Herwig/NewPhysics/NewModel:HardProcessConstructors[0]
erase /Herwig/NewPhysics/NewModel:HardProcessConstructors[0]
erase /Herwig/NewPhysics/NewModel:HardProcessConstructors[0]
erase /Herwig/NewPhysics/NewModel:HardProcessConstructors[0]
```

- The centre-of-mass energy and the primordial k_T of the partons extracted from the protons can be set via

```
cd /Herwig/Generators
set LHCGenerator:EventHandler:LuminosityFunction:Energy 14000
set /Herwig/Shower/Evolver:IntrinsicPtGaussian 2.2*GeV
```

- As described in Ch. 4.3.1, a p_T veto has to be applied, using the value of the `SCALUP` variable provided for each event in the LHE file. This is accomplished by the following settings:

```
set /Herwig/Shower/Evolver:HardVetoMode Yes
set /Herwig/Shower/Evolver:HardVetoScaleSource Read
set /Herwig/Shower/Evolver:HardVetoReadOption PrimaryCollision
set /Herwig/Shower/Evolver:MECorrMode No
```

- In order to read events from a specific LHE file `LHENAME.lhe`, an instance of the `LesHouchesFileReader` class has to be created and initialized as follows:

```
library LesHouches.so
cd /Herwig/EventHandlers
create ThePEG::LesHouchesFileReader pwgReader

set pwgReader:FileName LHENAME.lhe
set pwgReader:CacheFileName cache.tmp
set pwgReader:AllowedToReOpen No
set pwgReader:MaxScan 1

set pwgReader:InitPDFs 0
set pwgReader:PDFA /Herwig/Partons/PDFset
set pwgReader:PDFB /Herwig/Partons/PDFset
```

  The settings for the parameters `AllowedToReOpen` and `MaxScan` ensure that HERWIG++ processes each event exactly once, without performing any sampling.

- The actual processing of the events is performed by the `LesHouchesEventHandler`, which is set up as follows:

```
create ThePEG::LesHouchesEventHandler pwghandler
insert pwghandler:LesHouchesReaders 0 pwgReader
```

```
insert pwghandler:PreCascadeHandlers 0 \\
    /Herwig/NewPhysics/DecayHandler

set pwghandler:CascadeHandler /Herwig/Shower/ShowerHandler
#set pwghandler:CascadeHandler \\
     /Herwig/DipoleShower/DipoleShowerHandler

set pwghandler:PartonExtractor /Herwig/Partons/QCDExtractor
set pwghandler:StatLevel 2
set pwghandler:WeightOption VarNegWeight

set pwghandler:DecayHandler /Herwig/Decays/DecayHandler
```

Here, the `PreCascadeHandlers` is required if the decays of the sparticles are performed with Herwig++. The `CascadeHandler` is set to either the Herwig++ default shower or (commented in the block above) to the Dipole-Shower. The option `VarNegWeight` allows for the processing of events with arbitrary (positive or negative) weights.

- In order to switch off MPI and hadronization the corresponding handlers have to be initialized as follows (again using the commented statement for the Dipole-Shower):

```
set pwghandler:HadronizationHandler NULL
set /Herwig/Shower/ShowerHandler:MPIHandler NULL
#set /Herwig/DipoleShower/DipoleShowerHandler:MPIHandler NULL
```

- The default shower allows for an individual choice of initial/final-state radiation (ISR/FSR):

```
set /Herwig/Shower/SplittingGenerator:ISR Yes
set /Herwig/Shower/SplittingGenerator:FSR Yes
```

- If the decays of the produced sparticles are performed with Herwig++, the parameters of the considered SUSY scenario have to be provided according to the SUSY Les Houches accord (SLHA) [136] in a file `SLHAFILE.slha`:

```
cd /Herwig/NewPhysics
setup MSSM/Model SLHAFILE.slha
```

It is possible to disable specific decay modes. This can be achieved by adding the corresponding tag to the `DisableModes` interface of the `DecayConstructor`, e.g. disabling the decay $\tilde{u}_L \to \tilde{\chi}_2^0 u$ amounts to including the line

```
insert DecayConstructor:DisableModes 0 ~u_L->~chi_20,u;
```

in the input file.

- Last but not least some general parameters and settings should be set:

```
create ThePEG::Cuts /Herwig/Cuts/NoCuts
set /Herwig/Cuts/NoCuts:MHatMin 0.1 GeV
cd /Herwig/EventHandlers
set pwgReader:Cuts /Herwig/Cuts/NoCuts
```

```
cd /Herwig/Analysis
set Basics:CheckQuark 0

cd /Herwig/Generators
cp LHCGenerator pwgLesHouchesGenerator
set pwgLesHouchesGenerator:EventHandler /Herwig/EventHandlers/pwghandler

cd /Herwig/Generators
set pwgLesHouchesGenerator:NumberOfEvents NEVENTS
set pwgLesHouchesGenerator:PrintEvent 0
set pwgLesHouchesGenerator:MaxErrors 30
set pwgLesHouchesGenerator:DebugLevel 1

saverun RUNNAME pwgLesHouchesGenerator
```

The first block of statements prevents the application of any cuts during the event generation, the second one removes the warnings raised if quarks occur in the final state (which is the case if no hadronization is considered). The number of requested events `NEVENTS` should be identical to the number of events in the LHE file. The generated run-file is saved as `RUNNAME` and can be processed by calling `Herwig++ run RUNNAME`.

BIBLIOGRAPHY

[1] M. Gell-Mann, *A Schematic Model of Baryons and Mesons*. Phys. Lett. **8** (1964) 214–215.

[2] H. Fritzsch, M. Gell-Mann, and H. Leutwyler, *Advantages of the Color Octet Gluon Picture*. Phys. Lett. **B47** (1973) 365–368.

[3] S. Glashow, *Partial Symmetries of Weak Interactions*. Nucl. Phys. **22** (1961) 579–588.

[4] A. Salam, *in Proceedings of the 8th Nobel Symposium*. Almqvist and Wiksell, Stockholm, 1968.

[5] S. Weinberg, *A Model of Leptons*. Phys. Rev. Lett. **19** (1967) 1264–1266.

[6] **ATLAS Collaboration** , G. Aad *et al.*, *Observation of a new particle in the search for the Standard Model Higgs boson with the ATLAS detector at the LHC*. Phys. Lett. **B716** (2012) 1–29, `arXiv:hep-ex/1207.7214`.

[7] **CMS Collaboration** , S. Chatrchyan *et al.*, *Observation of a new boson at a mass of 125 GeV with the CMS experiment at the LHC*. Phys. Lett. **B716** (2012) 30–61, `arXiv:hep-ex/1207.7235`.

[8] P. W. Higgs, *Broken symmetries, massless particles and gauge fields*. Phys. Lett. **12** (1964) 132–133.

[9] P. W. Higgs, *Broken Symmetries and the Masses of Gauge Bosons*. Phys. Rev. Lett. **13** (1964) 508–509.

[10] F. Englert and R. Brout, *Broken Symmetry and the Mass of Gauge Vector Mesons*. Phys. Rev. Lett. **13** (1964) 321–323.

[11] G. S. Guralnik, C. R. Hagen, and T. W. B. Kibble, *Global Conservation Laws and Massless Particles*. Phys. Rev. Lett. **13** (1964) 585–587.

[12] R. Haag, J. T. Lopuszanski, and M. Sohnius, *All Possible Generators of Supersymmetries of the s Matrix*. Nucl. Phys. **B88** (1975) 257.

[13] G. L. Kane and J. Leveille, *Experimental Constraints on Gluino Masses and Supersymmetric Theories*. Phys. Lett. **B112** (1982) 227.

[14] P. Harrison and C. Llewellyn Smith, *Hadroproduction of Supersymmetric Particles*. Nucl. Phys. **B213** (1983) 223.

[15] E. Reya and D. Roy, *Supersymmetric Particle Production at p anti-p Collider Energies*. Phys. Rev. **D32** (1985) 645.

[16] S. Dawson, E. Eichten, and C. Quigg, *Search for Supersymmetric Particles in Hadron - Hadron Collisions*. Phys. Rev. **D31** (1985) 1581.

[17] W. Beenakker, R. Hopker, M. Spira, and P. Zerwas, *Squark and gluino production at hadron colliders*. Nucl. Phys. **B492** (1997) 51–103, arXiv:hep-ph/9610490.

[18] W. Beenakker, R. Hopker, and M. Spira, *PROSPINO: A Program for the production of supersymmetric particles in next-to-leading order QCD*. arXiv:hep-ph/9611232.

[19] W. Hollik, J. M. Lindert, and D. Pagani, *NLO corrections to squark-squark production and decay at the LHC*. JHEP **1303** (2013) 139, arXiv:hep-ph/1207.1071.

[20] D. Goncalves-Netto, D. Lopez-Val, K. Mawatari, T. Plehn, and I. Wigmore, *Automated Squark and Gluino Production to Next-to-Leading Order*. Phys. Rev. **D87** (2013) 014002, arXiv:hep-ph/1211.0286.

[21] A. Djouadi, W. Hollik, and C. Junger, *QCD corrections to scalar quark decays*. Phys. Rev. **D55** (1997) 6975–6985, arXiv:hep-ph/9609419.

[22] W. Beenakker, R. Hopker, T. Plehn, and P. Zerwas, *Stop decays in SUSY QCD*. Z. Phys. **C75** (1997) 349–356, arXiv:hep-ph/9610313.

[23] W. Beenakker, R. Hopker, and P. Zerwas, *SUSY QCD decays of squarks and gluinos*. Phys. Lett. **B378** (1996) 159–166, arXiv:hep-ph/9602378.

[24] M. Muhlleitner, A. Djouadi, and Y. Mambrini, *SDECAY: A Fortran code for the decays of the supersymmetric particles in the MSSM*. Comput. Phys. Commun. **168** (2005) 46–70, arXiv:hep-ph/0311167.

[25] P. Nason, *A New method for combining NLO QCD with shower Monte Carlo algorithms*. JHEP **0411** (2004) 040, arXiv:hep-ph/0409146.

[26] S. Frixione, P. Nason, and C. Oleari, *Matching NLO QCD computations with Parton Shower simulations: the POWHEG method*. JHEP **0711** (2007) 070, arXiv:hep-ph/0709.2092.

[27] S. Alioli, P. Nason, C. Oleari, and E. Re, *A general framework for implementing NLO calculations in shower Monte Carlo programs: the POWHEG BOX*. JHEP **1006** (2010) 043, arXiv:hep-ph/1002.2581.

[28] E. Popenda, *Higher Order Corrections to Supersymmetric Production and Decay Processes*. Dissertation, Karlsruher Institut für Technologie, 2012.

[29] T. Sjostrand, S. Mrenna, and P. Z. Skands, *PYTHIA 6.4 Physics and Manual*. JHEP **0605** (2006) 026, arXiv:hep-ph/0603175.

[30] S. Platzer and S. Gieseke, *Coherent Parton Showers with Local Recoils*. JHEP **1101** (2011) 024, arXiv:hep-ph/0909.5593.

[31] S. Platzer and S. Gieseke, *Dipole Showers and Automated NLO Matching in Herwig++*. Eur. Phys. J. **C72** (2012) 2187, arXiv:hep-ph/1109.6256.

[32] M. Bahr, S. Gieseke, M. Gigg, D. Grellscheid, K. Hamilton, *et al.*, *Herwig++ Physics and Manual*. Eur. Phys. J. **C58** (2008) 639–707, arXiv:hep-ph/0803.0883.

[33] **ATLAS Collaboration** , *Search for squarks and gluinos with the ATLAS detector in final states with jets and missing transverse momentum and 20.3 fb^{-1} of $\sqrt{s} = 8$ TeV proton-proton collision data*. ATLAS-CONF-2013-047.

[34] S. P. Martin, *A Supersymmetry primer*. arXiv:hep-ph/9709356.

[35] Y. Golfand and E. Likhtman, *Extension of the Algebra of Poincare Group Generators and Violation of p Invariance*. JETP Lett. **13** (1971) 323–326.

[36] J. Wess and B. Zumino, *Supergauge Transformations in Four-Dimensions*. Nucl. Phys. **B70** (1974) 39–50.

[37] H. P. Nilles, *Supersymmetry, Supergravity and Particle Physics*. Phys. Rept. **110** (1984) 1–162.

[38] H. E. Haber and G. L. Kane, *The Search for Supersymmetry: Probing Physics Beyond the Standard Model*. Phys. Rept. **117** (1985) 75–263.

[39] M. Sohnius, *Introducing Supersymmetry*. Phys. Rept. **128** (1985) 39–204.

[40] D. Volkov and V. Akulov, *Is the Neutrino a Goldstone Particle?* Phys. Lett. **B46** (1973) 109–110.

[41] S. R. Coleman and J. Mandula, *All Possible Symmetries of the S Matrix*. Phys. Rev. **159** (1967) 1251–1256.

[42] H. Kalka and G. Soff, *Supersymmetrie*. Teubner, Stuttgart, 1997.

[43] G. R. Farrar and P. Fayet, *Phenomenology of the Production, Decay, and Detection of New Hadronic States Associated with Supersymmetry*. Phys. Lett. **B76** (1978) 575–579.

[44] M. Weber, *Tests of Supersymmetric Couplings at High Energy Colliders*. Dissertation, Universität Hamburg, 2001.

[45] **ATLAS Collaboration** , G. Aad *et al.*, *Search for squarks and gluinos using final states with jets and missing transverse momentum with the ATLAS detector in $\sqrt{s} = 7$ TeV proton-proton collisions*. Phys. Lett. **B710** (2012) 67–85, arXiv:hep-ex/1109.6572.

[46] **ATLAS Collaboration** , G. Aad *et al.*, *Hunt for new phenomena using large jet multiplicities and missing transverse momentum with ATLAS in 4.7 fb^{-1} of $\sqrt{s} = 7$ TeV proton-proton collisions*. JHEP **1207** (2012) 167, arXiv:hep-ex/1206.1760.

[47] **ATLAS Collaboration** , *Search for squarks and gluinos with the ATLAS detector using final states with jets and missing transverse momentum and 5.8 fb^{-1} of $\sqrt{s}$=8 TeV proton-proton collision data*. ATLAS-CONF-2012-109, ATLAS-COM-CONF-2012-140.

[48] **ATLAS Collaboration** , G. Aad *et al.*, *Search for new phenomena in final states with large jet multiplicities and missing transverse momentum at sqrt(s)=8 TeV proton-proton collisions using the ATLAS experiment.* JHEP **1310** (2013) 130, arXiv:hep-ex/1308.1841.

[49] **CMS Collaboration** , S. Chatrchyan *et al.*, *Search for New Physics with Jets and Missing Transverse Momentum in pp collisions at* $\sqrt{s} = 7$ *TeV.* JHEP **1108** (2011) 155, arXiv:hep-ex/1106.4503.

[50] **CMS Collaboration** , S. Chatrchyan *et al.*, *Search for supersymmetry in hadronic final states using MT2 in pp collisions at* $\sqrt{s} = 7$ *TeV.* JHEP **1210** (2012) 018, arXiv:hep-ex/1207.1798.

[51] **CMS Collaboration** , S. Chatrchyan *et al.*, *Search for new physics in the multijet and missing transverse momentum final state in proton-proton collisions at* $\sqrt{s} = 7$ *TeV.* Phys. Rev. Lett. **109** (2012) 171803, arXiv:hep-ex/1207.1898.

[52] **CMS Collaboration** , S. Chatrchyan *et al.*, *Search for supersymmetry in hadronic final states with missing transverse energy using the variables AlphaT and b-quark multiplicity in pp collisions at 8 TeV.* Eur. Phys. J. **C73** (2013) 2568, arXiv:hep-ex/1303.2985.

[53] **CMS Collaboration** , S. Chatrchyan *et al.*, *Search for gluino mediated bottom- and top-squark production in multijet final states in pp collisions at 8 TeV.* arXiv:hep-ex/1305.2390.

[54] **CMS Collaboration** , S. Chatrchyan *et al.*, *Search for new physics in the multijet and missing transverse momentum final state in proton-proton collisions at* $\sqrt{s} = 8$ *TeV.* arXiv:hep-ex/1402.4770.

[55] **ATLAS Collaboration** , J. Boyd, *Overview of SUSY results from the ATLAS experiment.* Talk at the SUSY conference (2013) .

[56] R. K. Ellis, W. J. Stirling, and B. Webber, *QCD and collider physics.* Camb. Monogr. Part. Phys. Nucl. Phys. Cosmol. **8** (1996) 1–435.

[57] G. 't Hooft and M. Veltman, *Regularization and Renormalization of Gauge Fields.* Nucl. Phys. **B44** (1972) 189–213.

[58] W. Siegel, *Supersymmetric Dimensional Regularization via Dimensional Reduction.* Phys. Lett. **B84** (1979) 193.

[59] D. Capper, D. Jones, and P. van Nieuwenhuizen, *Regularization by Dimensional Reduction of Supersymmetric and Nonsupersymmetric Gauge Theories.* Nucl. Phys. **B167** (1980) 479.

[60] A. Denner, *Techniques for calculation of electroweak radiative corrections at the one loop level and results for W physics at LEP-200.* Fortsch. Phys. **41** (1993) 307–420, arXiv:hep-ph/0709.1075.

[61] W. A. Bardeen, A. Buras, D. Duke, and T. Muta, *Deep Inelastic Scattering Beyond the Leading Order in Asymptotically Free Gauge Theories.* Phys. Rev. **D18** (1978) 3998.

[62] R. Harlander, L. Mihaila, and M. Steinhauser, *Two-loop matching coefficients for the strong coupling in the MSSM*. Phys. Rev. **D72** (2005) 095009, arXiv:hep-ph/0509048.

[63] S. P. Martin and M. T. Vaughn, *Regularization dependence of running couplings in softly broken supersymmetry*. Phys. Lett. **B318** (1993) 331–337, arXiv:hep-ph/9308222.

[64] T. Kinoshita, *Mass singularities of Feynman amplitudes*. J.Math.Phys. **3** (1962) 650–677.

[65] T. Lee and M. Nauenberg, *Degenerate Systems and Mass Singularities*. Phys. Rev. **133** (1964) B1549–B1562.

[66] S. Catani and M. Seymour, *A General algorithm for calculating jet cross-sections in NLO QCD*. Nucl. Phys. **B485** (1997) 291–419, arXiv:hep-ph/9605323.

[67] S. Catani, S. Dittmaier, M. H. Seymour, and Z. Trocsanyi, *The Dipole formalism for next-to-leading order QCD calculations with massive partons*. Nucl. Phys. **B627** (2002) 189–265, arXiv:hep-ph/0201036.

[68] S. Frixione, Z. Kunszt, and A. Signer, *Three jet cross-sections to next-to-leading order*. Nucl. Phys. **B467** (1996) 399–442, arXiv:hep-ph/9512328.

[69] G. Altarelli and G. Parisi, *Asymptotic Freedom in Parton Language*. Nucl. Phys. **B126** (1977) 298.

[70] A. Buckley, J. Butterworth, S. Gieseke, D. Grellscheid, S. Hoche, *et al.*, *General-purpose event generators for LHC physics*. Phys. Rept. **504** (2011) 145–233, arXiv:hep-ph/1101.2599.

[71] F. Ambroglini, R. Armillis, P. Azzi, G. Bagliesi, A. Ballestrero, *et al.*, *Proceedings of the Workshop on Monte Carlo's, Physics and Simulations at the LHC. Part I*. arXiv:hep-ph/0902.0293.

[72] G. Marchesini and B. Webber, *Simulation of QCD Jets Including Soft Gluon Interference*. Nucl. Phys. **B238** (1984) 1.

[73] G. Marchesini and B. Webber, *Monte Carlo Simulation of General Hard Processes with Coherent QCD Radiation*. Nucl. Phys. **B310** (1988) 461.

[74] S. Frixione and B. R. Webber, *Matching NLO QCD computations and parton shower simulations*. JHEP **0206** (2002) 029, arXiv:hep-ph/0204244.

[75] S. Hoeche, F. Krauss, M. Schonherr, and F. Siegert, *A critical appraisal of NLO+PS matching methods*. JHEP **1209** (2012) 049, arXiv:hep-ph/1111.1220.

[76] J. Alwall, A. Ballestrero, P. Bartalini, S. Belov, E. Boos, *et al.*, *A Standard format for Les Houches event files*. Comput. Phys. Commun. **176** (2007) 300–304, arXiv:hep-ph/0609017.

[77] **Particle Data Group** , J. Beringer *et al.*, *Review of Particle Physics (RPP)*. Phys. Rev. **D86** (2012) 010001.

[78] B. Jager, A. von Manteuffel, and S. Thier, *Slepton pair production in the POWHEG BOX*. JHEP **1210** (2012) 130, arXiv:hep-ph/1208.2953.

[79] M. Klasen, K. Kovarik, P. Nason, and C. Weydert, *Associated production of charged Higgs bosons and top quarks with POWHEG*. Eur. Phys. J. **C72** (2012) 2088, arXiv:hep-ph/1203.1341.

[80] T. Hahn, *Generating Feynman diagrams and amplitudes with FeynArts 3*. Comput. Phys. Commun. **140** (2001) 418–431, arXiv:hep-ph/0012260.

[81] T. Hahn and C. Schappacher, *The Implementation of the minimal supersymmetric standard model in FeynArts and FormCalc*. Comput. Phys. Commun. **143** (2002) 54–68, arXiv:hep-ph/0105349.

[82] T. Hahn, *A Mathematica interface for FormCalc-generated code*. Comput. Phys. Commun. **178** (2008) 217–221, arXiv:hep-ph/0611273.

[83] T. Hahn and M. Perez-Victoria, *Automatized one loop calculations in four-dimensions and D-dimensions*. Comput. Phys. Commun. **118** (1999) 153–165, arXiv:hep-ph/9807565.

[84] G. van Oldenborgh, *FF: A Package to evaluate one loop Feynman diagrams*. Comput. Phys. Commun. **66** (1991) 1–15.

[85] R. Mertig, M. Böhm, and A. Denner, *Feyn Calc - Computer-algebraic calculation of Feynman amplitudes*. Computer Physics Communications **64** (1991) 345–359.

[86] G. Leibbrandt, *Introduction to Noncovariant Gauges*. Rev. Mod. Phys. **59** (1987) 1067.

[87] J. Alwall, P. Demin, S. de Visscher, R. Frederix, M. Herquet, *et al.*, *MadGraph/MadEvent v4: The New Web Generation*. JHEP **0709** (2007) 028, arXiv:hep-ph/0706.2334.

[88] T. Stelzer and W. Long, *Automatic generation of tree level helicity amplitudes*. Comput. Phys. Commun. **81** (1994) 357–371, arXiv:hep-ph/9401258.

[89] J. Alwall, M. Herquet, F. Maltoni, O. Mattelaer, and T. Stelzer, *MadGraph 5 : Going Beyond*. JHEP **1106** (2011) 128, arXiv:1106.0522 [hep-ph].

[90] H. Murayama, I. Watanabe, and K. Hagiwara, *HELAS: HELicity Amplitude Subroutines for Feynman Diagram Evaluations* Tech. Rep. KEK-91-11, KEK, 1992.

[91] R. Gavin, C. Hangst, M. Krämer, M. Mühlleitner, M. Pellen, E. Popenda, and M. Spira, *Matching Squark Pair Production at NLO with Parton Showers*. JHEP **10** (2013) 187, arXiv:hep-ph/1305.4061.

[92] S. Frixione, E. Laenen, P. Motylinski, B. R. Webber, and C. D. White, *Single-top hadroproduction in association with a W boson*. JHEP **0807** (2008) 029, arXiv:hep-ph/0805.3067.

[93] R. G. Stuart, *General renormalization of the gauge invariant perturbation expansion near the Z0 resonance*. Phys. Lett. **B272** (1991) 353–358.

[94] E. Byckling and K. Kajantie, *Particle kinematics*. A Wiley-Interscience Publication. Wiley, London [u.a.], 1973.

[95] H. Baer and X. Tata, *Weak Scale Supersymmetry: From Superfields to Scattering Events*. Cambridge University Press, 2006.

[96] R. Frederix, S. Frixione, F. Maltoni, and T. Stelzer, *Automation of next-to-leading order computations in QCD: The FKS subtraction*. JHEP **0910** (2009) 003, arXiv:hep-ph/0908.4272.

[97] S. AbdusSalam, B. Allanach, H. Dreiner, J. Ellis, U. Ellwanger, *et al.*, *Benchmark Models, Planes, Lines and Points for Future SUSY Searches at the LHC*. Eur. Phys. J. **C71** (2011) 1835, arXiv:hep-ph/1109.3859.

[98] B. Allanach, *SOFTSUSY: a program for calculating supersymmetric spectra*. Comput. Phys. Commun. **143** (2002) 305–331, arXiv:hep-ph/0104145.

[99] M. Whalley, D. Bourilkov, and R. Group, *The Les Houches accord PDFs (LHAPDF) and LHAGLUE*. arXiv:hep-ph/0508110.

[100] J. Pumplin, D. Stump, J. Huston, H. Lai, P. M. Nadolsky, *et al.*, *New generation of parton distributions with uncertainties from global QCD analysis*. JHEP **0207** (2002) 012, arXiv:hep-ph/0201195.

[101] H.-L. Lai, M. Guzzi, J. Huston, Z. Li, P. M. Nadolsky, *et al.*, *New parton distributions for collider physics*. Phys. Rev. **D82** (2010) 074024, arXiv:hep-ph/1007.2241.

[102] U. Langenfeld and S.-O. Moch, *Higher-order soft corrections to squark hadro-production*. Phys. Lett. **B675** (2009) 210–221, arXiv:hep-ph/0901.0802.

[103] A. Kulesza and L. Motyka, *Threshold resummation for squark-antisquark and gluino-pair production at the LHC*. Phys. Rev. Lett. **102** (2009) 111802, arXiv:hep-ph/0807.2405.

[104] A. Kulesza and L. Motyka, *Soft gluon resummation for the production of gluino-gluino and squark-antisquark pairs at the LHC*. Phys. Rev. **D80** (2009) 095004, arXiv:hep-ph/0905.4749.

[105] W. Beenakker, S. Brensing, M. Kramer, A. Kulesza, E. Laenen, and I. Niessen, *Soft-gluon resummation for squark and gluino hadroproduction*. JHEP **0912** (2009) 041, arXiv:hep-ph/0909.4418.

[106] W. Beenakker, S. Brensing, M. Kramer, A. Kulesza, E. Laenen, and I. Niessen, *NNLL resummation for squark-antisquark pair production at the LHC*. JHEP **1201** (2012) 076, arXiv:hep-ph/1110.2446.

[107] M. Beneke, P. Falgari, and C. Schwinn, *Threshold resummation for pair production of coloured heavy (s)particles at hadron colliders*. Nucl. Phys. **B842** (2011) 414–474, arXiv:hep-ph/1007.5414.

[108] P. Falgari, C. Schwinn, and C. Wever, *NLL soft and Coulomb resummation for squark and gluino production at the LHC*. JHEP **1206** (2012) 052, arXiv:hep-ph/1202.2260.

[109] W. Beenakker, T. Janssen, S. Lepoeter, M. Kramer, A. Kulesza, E. Laenen, I. Niessen, S. Thewes, and T. Van Daal, *Towards NNLL resummation: hard matching coefficients for squark and gluino hadroproduction*. arXiv:hep-ph/1304.6354.

[110] W. Beenakker, T. Janssen, S. Lepoeter, M. Krämer, A. Kulesza, *et al.*, *Towards NNLL resummation: hard matching coefficients for squark and gluino hadroproduction*. JHEP **1310** (2013) 120, arXiv:hep-ph/1304.6354.

[111] W. Beenakker, M. Kramer, T. Plehn, and M. Spira, *SUSY particle production at the Tevatron*. arXiv:hep-ph/9810290.

[112] J. M. R. Lindert, *Aspects of SUSY Phenomenology at the LHC*. Dissertation, Technische Universität München, 2013.

[113] K. Melnikov and M. Schulze, *NLO QCD corrections to top quark pair production and decay at hadron colliders*. JHEP **0908** (2009) 049, arXiv:hep-ph/0907.3090.

[114] J. M. Campbell, R. K. Ellis, and F. Tramontano, *Single top production and decay at next-to-leading order*. Phys. Rev. **D70** (2004) 094012, arXiv:hep-ph/0408158.

[115] V. S. Fadin, V. A. Khoze, and A. D. Martin, *How suppressed are the radiative interference effects in heavy instable particle production?* Phys. Lett. **B320** (1994) 141–144, arXiv:hep-ph/9309234.

[116] V. S. Fadin, V. A. Khoze, and A. D. Martin, *Interference radiative phenomena in the production of heavy unstable particles*. Phys. Rev. **D49** (1994) 2247–2256.

[117] M. Cacciari and G. P. Salam, *Dispelling the N^3 myth for the k_t jet-finder*. Phys. Lett. **B641** (2006) 57–61, arXiv:hep-ph/0512210.

[118] M. Cacciari, G. P. Salam, and G. Soyez, *FastJet User Manual*. Eur. Phys. J. **C72** (2012) 1896, arXiv:hep-ph/1111.6097.

[119] M. Cacciari, G. P. Salam, and G. Soyez, *The Anti-k(t) jet clustering algorithm*. JHEP **0804** (2008) 063, arXiv:hep-ph/0802.1189.

[120] S. Frixione, P. Nason, and G. Ridolfi, *A Positive-weight next-to-leading-order Monte Carlo for heavy flavour hadroproduction*. JHEP **0709** (2007) 126, arXiv:hep-ph/0707.3088.

[121] F. Maltoni, K. Paul, T. Stelzer, and S. Willenbrock, *Color flow decomposition of QCD amplitudes*. Phys. Rev. **D67** (2003) 014026, arXiv:hep-ph/0209271.

[122] E. Re, *Single-top Wt-channel production matched with parton showers using the POWHEG method*. Eur. Phys. J. **C71** (2011) 1547, arXiv:hep-ph/1009.2450.

[123] S. Alioli, P. Nason, C. Oleari, and E. Re, *NLO Higgs boson production via gluon fusion matched with shower in POWHEG*. JHEP **0904** (2009) 002, arXiv:hep-ph/0812.0578.

[124] T. Melia, P. Nason, R. Rontsch, and G. Zanderighi, *W+W-, WZ and ZZ production in the POWHEG BOX*. JHEP **1111** (2011) 078, arXiv:hep-ph/1107.5051.

[125] P. Nason, *MINT: A Computer program for adaptive Monte Carlo integration and generation of unweighted distributions*. arXiv:hep-ph/0709.2085.

[126] S. Alioli, P. Nason, C. Oleari, and E. Re, *The POWHEG BOX user manual: common features*.

[127] P. Z. Skands, *Tuning Monte Carlo Generators: The Perugia Tunes*. Phys. Rev. **D82** (2010) 074018, arXiv:hep-ph/1005.3457.

[128] K. Arnold, L. d'Errico, S. Gieseke, D. Grellscheid, K. Hamilton, *et al.*, *Herwig++ 2.6 Release Note*. hep-ph/arXiv:1205.4902.

[129] F. Schissler and D. Zeppenfeld, *Parton Shower Effects on W and Z Production via Vector Boson Fusion at NLO QCD*. JHEP **04** (2013) 057, arXiv:hep-ph/1302.2884.

[130] **Atlas Collaboration** , G. Aad *et al.*, *Study of Jet Shapes in Inclusive Jet Production in pp Collisions at $\sqrt{s} = 7$ TeV using the ATLAS Detector*. Phys. Rev. **D83** (2011) 052003, arXiv:hep-ex/1101.0070.

[131] M. E. Peskin and D. V. Schroeder, *An Introduction to quantum field theory*. Addison-Wesley, 1997.

[132] J. Vermaseren, *New features of FORM*. arXiv:math-ph/0010025.

[133] T. van Ritbergen, A. Schellekens, and J. Vermaseren, *Group theory factors for Feynman diagrams*. Int. J. Mod. Phys. **A14** (1999) 41–96, arXiv:hep-ph/9802376.

[134] W. Kilian, T. Ohl, J. Reuter, and C. Speckner, *QCD in the Color-Flow Representation*. JHEP **1210** (2012) 022, arXiv:hep-ph/1206.3700.

[135] S. Actis, A. Denner, L. Hofer, A. Scharf, and S. Uccirati, *Recursive generation of one-loop amplitudes in the Standard Model*. JHEP **1304** (2013) 037, arXiv:hep-ph/1211.6316.

[136] P. Z. Skands, B. Allanach, H. Baer, C. Balazs, G. Belanger, *et al.*, *SUSY Les Houches accord: Interfacing SUSY spectrum calculators, decay packages, and event generators*. JHEP **0407** (2004) 036, arXiv:hep-ph/0311123.

ACKNOWLEDGMENTS

In erster Linie gebührt mein Dank natürlich meiner "Doktormutter" Prof. Dr. Margarete Mühlleitner: nicht nur für die Vergabe dieses interessanten und vielschichtigen Themas, sondern auch für die Bereitschaft, jederzeit Fragen und Probleme zu diskutieren. Bedanken möchte ich mich an dieser Stelle auch dafür, dass sie mir den Besuch einiger Konferenzen und Schulen ermöglicht hat.

Prof. Dr. Matthias Steinhauser danke ich für die bereitwillige Übernahme des Korreferats.

Für die gute und konstruktive Zusammenarbeit im Rahmen des Squark-Squark Projekts möchte ich mich bei Dr. Eva Popenda bedanken, Dr. Michael Spira danke ich in diesem Zusammenhang für die Hilfe beim Vergleich mit Prospino und die diversen Einladungen an das Paul-Scherrer-Institut.

Für das Korrekturlesen dieser Arbeit danke ich Johannes Bellm, Bastian Feigl, Eva Popenda, Christian Röhr, Franziska Schissler und Kathrin Walz.

Ich habe meine Zeit am Institut für Theoretische Physik immer als sehr angenehm empfunden. Für die angenehme Arbeitsatmosphäre, die interessanten Diskussionen (auch abseits der Physik) und die zahllosen Kaffeepausen danke ich nicht nur meinen Bürokollegen Hamzeh Alavirad, Johannes Bellm, Bastian Feigl, Eva Popenda und Kathrin Walz, sondern auch allen gegenwärtigen und ehemaligen Institutsmitgliedern.

Dem Graduiertenkolleg "GRK 1694: Elementarteilchenphysik bei höchster Energie und höchster Präzision" und der "Karlsruher Schule für Elementarteilchen- und Astroteilchenphysik: Wissenschaft und Technologie (KSETA)" danke ich für die finanzielle Unterstützung in den letzten drei Jahren.

Mein größter Dank gilt meiner Familie und meinen Freunden, die mich auch in schwierigen Phasen dieser Arbeit immer unterstützt haben. Besonders danke ich meinen Eltern für den bedingungslosen Rückhalt während meines gesamten Studiums und der Promotion, durch den mir diese überhaupt erst ermöglicht wurden.